Modelling and Simulation of materials for Photovoltaic applications

Murugesan Rasukkannu

Thesis for the Degree of Philosophiae Doctor (PhD)
University of Bergen, Norway

UNIVERSITY OF BERGEN

Modelling and Simulation of materials for Photovoltaic applications

Murugesan Rasukkannu

Thesis for the Degree of Philosophiae Doctor (PhD)
at the University of Bergen

2019

Date of defence: 09.01 2019

Year: 2019

Title: Modelling and Simulation of materials for Photovoltaic applications

Name: Murugesan Rasukkannu

Print: Skipnes Kommunikasjon / University of Bergen

TO APPA, AMMA, AKKA, MAMA, ANJALI, SUGAN,
ARAVIND, KAVINAYA, AND GAYATHRI

Preface and Acknowledgement

This thesis is written to fulfil the requirements for a Doctor of Philosophy degree at University of Bergen. This thesis would not have been able to be completed without the help and support of many people. First, I would like to thank my thesis supervisor, Professor Dhayalan Velauthapillai, for his help and support throughout my graduate career. I was greatly impressed by his deep insight in photovoltaic applications and broad knowledge in various research areas, and I am very grateful for the collaboration opportunities with University of Oslo, Coimbatore Institute of Technology, India and University of Jaffna, Sri Lanka that he provided during the past years. His generous contributions in ideas, skillful guidance, in particular for devoting his valuable time to discussions of all aspects of the project, including formulations in publications, and for making my academic career run smoothly without problems are deeply appreciated. I render my sincere gratitude to Professor Dhayalan for his many insightful discussions and helping to write the PhD thesis. I also really appreciate his helpful advice and warm support on my future career plans.

My sincere and special thanks goes to co-supervisor, Dr. Ponniah Vajeeston, for his kind help in formulating the ideology of the research work, suggesting new ideas, for assistance in interpreting the results, insightful suggestions, and continuous motivation in journal writing and in particular contributions with practical working tools during the whole project period. I kindly acknowledge him for actively participating in discussions and continuously motivating me to use different tools to bring out the efficient results.

I also extend my thanks to, Professor Lars Egil Helseth from University of Bergen, for his helpful advice, fruitful scientific discussions and guiding me the right direction.

I also gratefully acknowledge the Western Norway University of Applied Sciences for financially supporting the project (23300) and UNINETT Sigma2 for computing facilities of project numbers NN2867K and NN2875K, which have been used to conduct the calculations presented in publications.

I also extend my thanks to Dr. Federico Bianchini for spending his valuable time for scientific discussions and help with critical reading of manuscripts and thesis. I also acknowledge, Dr. Vishnukanthan Venkatachalapathy for scientific discussions.

Last but not least, I would like to thank my parents, my sisters, my uncle, my nephew and my fiancée Gayathri. Without their love and support, completion of my PhD would not have been possible. I am truly blessed to have such an amazing, warm, and caring family. This thesis is dedicated to you.

Abstract

The global need for energy is predicted to double by 2050 and triple by the end of the 21st century. Today, fossil fuels are the primary source for energy supply in the world. However, the excessive consumption of fossil fuels has led to global warming and has resulted in severe environmental impacts. Growing population demands a lot of energy in the future, and there will be limited fossil fuels resources available. Thus, alternative clean energy resources will be the hour of need.

Solar energy is probably the most promising source of clean and abundant energy that we have now. An enormous technological and political effort has been undertaken to harness the solar energy more directly. However, the challenge is that solar energy technologies should become cheaper, flexible, energy effective and harmless to the environment. This research focuses on materials for new generation solar cell technologies that fulfil these demands. Third generation solar cells such as intermediate band solar cells and non-silicon solar cells are a newer type of solar cells. They have attained considerable attention in the last two decades, as a potentially cost-effective alternative to conventional costly silicon solar cells. Intermediate band solar cells and non-silicon solar cells are complex devices, which is relied on the interplay of several key components. The unique architecture of intermediate band solar cells provides balance-limiting efficiencies of 63.2%. As a result, an extensive and increasing amount of research effort has been devoted to design and synthesize novel materials. However, most of such efforts have been expensive and time-consuming synthesis procedure. To overcome this drawback, modelling and simulation of new materials is a better method to study and verify the properties of the materials for photovoltaic applications.

This thesis has focussed on a theoretical calculation of properties like structural prediction, electronic structure, optical properties, structural stability and mechanical stability behaviour of photovoltaic materials. The aim of the study is fivefold: The first is to study and gain knowledge on the fundamental properties of the matter governed by the electronic structure of a variety of bulk materials. The second is to study novel materials and determine the adaptability and the applicability of theoretical calculation as an accompaniment to experiments for the material scientist in his/her search for novel photovoltaic materials. The third is to investigate materials numerically with intermediate bandgaps that could pave the way for higher cell efficiencies than the theoretically limited efficiency of 32%. Fourth is to carry out an in-depth analysis of low-cost, direct band gap, non-silicon materials for PV

applications. Fifth is to implement efficient approximations, methods and algorithms to derive accurate numerical results for electronic and optical properties of a variety of novel materials for PV applications. We expect these findings of novel materials in this thesis will lead to immediate concern and interest to an extensive audience in the scientific society.

List of Publications

The following publications are part of the thesis.

I. **Computational modeling of novel bulk materials for the intermediate-band solar cells**
Murugesan Rasukkannu, Dhayalan Velauthapillai, Ponniah Vajeeston
ACS Omega 2, no. 4 (2017): 1454-1462.

II. **Hybrid density functional study of $Au_2Cs_2I_6$, Ag_2GeBaS_4, Ag_2ZnSnS_4 and $AgCuPO_4$ for the Intermediate band solar cells**
Murugesan Rasukkannu, Dhayalan Velauthapillai, Ponniah Vajeeston. *Submitted to Advanced Energy Materials (ACS).*

III. **A first-principle study of the electronic, mechanical and optical properties of inorganic perovskite Cs_2SnI_6 for intermediate-band solar cells**
Murugesan Rasukkannu, Dhayalan Velauthapillai, Ponniah Vajeeston
Materials Letters 218 (2018): 233-236.

IV. **Properties of novel non-silicon materials for the photovoltaic applications: A first-principle insight**
Murugesan Rasukkannu, Dhayalan Velauthapillai, Federico Bianchini, Ponniah Vajeeston. *Materials* 11 (2018): 2006.

V. **A promising high-efficiency photovoltaic alternative non-silicon material: A first-principle investigation**
Murugesan Rasukkannu, Dhayalan Velauthapillai, Ponniah Vajeeston
Scripta Materialia 156 (2018): 134-137.

VI. **First-principle calculation of high absorption-$TlGaTe_2$ for photovoltaic application**
Murugesan Rasukkannu, Dhayalan Velauthapillai, Federico Bianchini, Ponniah Vajeeston. *Submitted to Scripta Materialia (Elsevier).*

VII. **Bandgap engineering in $CsSn_xPb_{(1-x)}I_3$ and their influence on light absorption**
Murugesan Rasukkannu, Dhayalan Velauthapillai, Ponniah Vajeeston
Materials Letters 218 (2018): 253-256.

Contents

Chapter 1

Introduction

"When the sun is shining I can do anything;

No mountain is too high, no trouble too difficult to overcome." Wilma Rudolph

1.1 Energy requirements and the role of renewable energy sources

World population is steadily increasing. Ensuring the standard of the living and energy security are the two main challenges humanity faces today. Energy demand has increased by 50% in the last ten years. More than 80% of energy needs are satisfied by non-renewable energy sources such as fossil fuels. The fossil fuels as the energy source have been used for so long is perishable. Non-renewable fossil fuels take around a million years to form and store under the earth surface. Fossil fuels that create air pollutants such as nitrogen oxides, sulphur dioxide, volatile organic compounds. These are major contributors to global warming. This is one of the major demerits of fossil fuels. Today, about $20X10^{12}$ kg of carbon dioxide is put into the atmosphere every year, mainly by burning fossil fuels[1]. The plants are unable to absorb this vast amount of extra carbon dioxide (CO_2). As a result, the enormous amounts of CO_2 is released into the earth's atmosphere, intensifying the greenhouse effect. The greenhouse effect arises when certain gases accumulate in the earth's atmosphere known as greenhouse gases (GHG). As shown in Figure 1.1, 68 % use of energy indicates by far the largest source of GHG emissions [2]. By far the biggest of these anthropogenic GHGs are carbon dioxide from the energy portion. Smaller shares of GHG emissions correspond to industrial processes, agriculture, and others (biomass burning, post-burn decay, peat decay). Figure 1.2 demonstrates the increasing trend in the yearly CO_2 emissions [2]. Therefore, it is clear that something needs to be done in order to avoid the increasing trend in CO_2 emissions.

This is an alarming trend, it will not only continue reliance on these non-renewable resources harming the climate, but it will eventually run out. Because of this, renewable energy sources become important. The term renewable energy is applied to all the energy sources that will not exhaust or change significantly in millions of years to come. There are several

renewable energy sources existing today such as wind hydroelectric, biomass, geothermal, and solar.

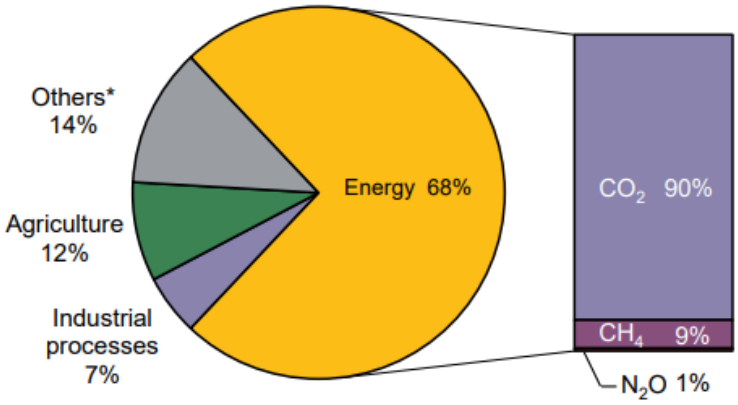

Figure 1.1. Estimated shares of global anthropogenic GHG. The figure is taken from [2].

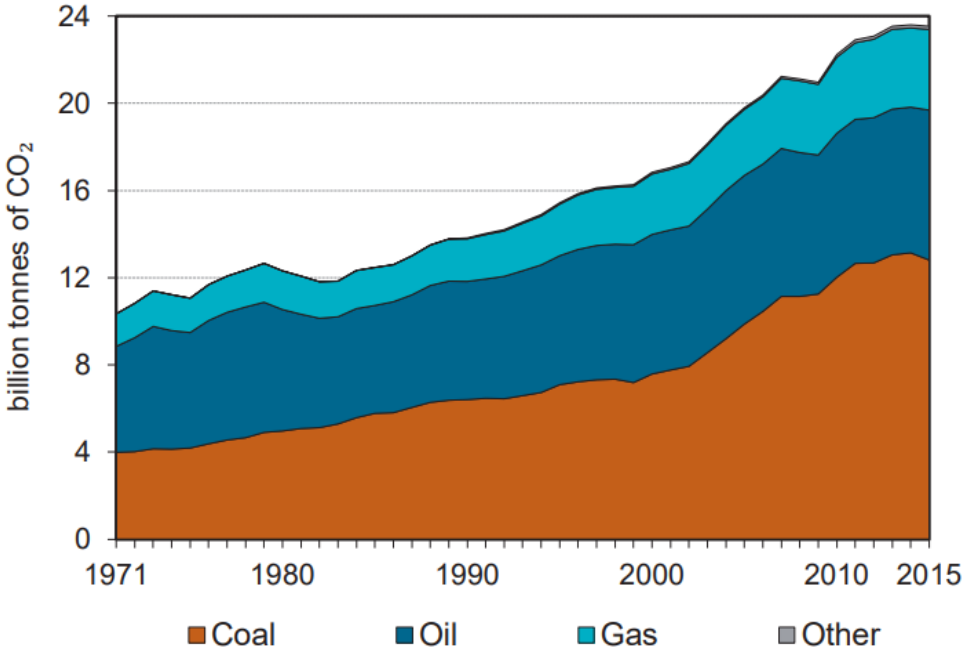

Figure 1.2. Historical data of CO_2 emissions per year, divided by sources. The figure is taken from [2].

Today, wind energy is one of the significant candidates to the world energy production. Turbines located in windy areas can adventure the atmospheric kinetic energy with the benefit of being a straightforward implementation. Due to some issues like noise, landscape damage and wind fickleness, wind energy are not likely to able to reach that enormous amount of power even if a substantial increase in marine plants and wind farms. The predictions in the DNV GL report [3], shown in Figure 1.3 and Figure 1.4, indicates that wind energy will become one of the most significant sources of electricity after 2020.

Another renewable is hydroelectric energy, and it is already a primarily used buffering mechanism where water basins or high flow rivers are available. Due to there is no demand to start a thermal engine, but it is sufficient to let the waterfall then drive turbines for generating electrical energy. Therefore, hydroelectric energy looks more like a kind of gravitational storage mechanism than other resources. From Figure 1.3 and Figure 1.4, the usage of hydroelectric power was the dominant renewable resource in the year 2000. The prediction in the DNV GL report [3] indicates that hydroelectric energy will become insignificant than wind and solar energy as shown in Figure 1.3 and Figure 1.4. It is due to the risk of hydrogeological instability and need of building huge plants. However, it needs to be acknowledged that carbon emissions are not attributed to hydroelectric energy. Biomass and waste burning are inherent to the life cycle of our planet and the human activity itself, and sometimes, they are included among the renewable energy. As of 2013, they contribute more to the source of electricity shown in Figure 1.3 and Figure 1.4 [3]. However, it cannot be treated as the clean energy source since it produces CO_2 in the burning process. Geothermal energy could be an exciting source in countries with significant sub-volcanic and volcanic activity. Geothermal energy is related to the presence of high-temperature regions. The exploitation of the internal heat capacity of the earth seems to have no time constraints. As discussed among the renewable sources, solar is the most abundant source of clean energy that is readily available.

Solar energy is probably the most promising source of clean and abundant energy that we have now. Solar energy dramatically surmounts all the other energy sources. An enormous technological and political effort has been undertaken to harness the solar energy more directly. Therefore, there are intense efforts in the scientific community to find new and more efficient ways of maximising its potential. Solar energy is utilized in three different ways, namely as passive heat, solar thermal and photovoltaic energy. Passive heat is the form where the sunlight is used without a mechanical system. Sunlight is directly converted into usable heat. There are applications related to passive heat such as solar water heating, solar cookers, and earth

sheltering. Solar thermal energy is another way to exploit solar energy. It is a technology for harnessing solar energy to produce thermal energy or electrical energy. With a high concentration in sunlight regions, it is easily possible to heat water to several tens of degrees, and the heat is saved as thermal energy. Thermal energy produces high pressure that can be used to power up turbines and generate electricity. The third way is to use the solar energy on PV structures such that sunlight is converted into electric current.

Now, we have entered a new photovoltaic age. The predictions in the DNV GL report [3], shown in Figure 1.3 and Figure 1.4, indicates that photovoltaic energy will become one of the most significant sources of electricity after 2020. Furthermore, in 2050, renewable energy will beat fossil fuels as the main supplier of primary energy, and it will be by far the most significant electricity source. If these predictions prove right, photovoltaic energy will play a significant role in supplying primary energy and in mollifying climate change. Photovoltaics effect deals with the direct conversion of photons into electrical energy. Solar cells exploit this photovoltaic effect, thanks to its competence of generating and collecting electric charges when illuminated with light. This electric charge flow constitutes a direct current flow through photovoltaic (PV) cell as long as the illumination is steady. The current flow and potential difference are strongly related to the absorption spectrum and material, respectively. Hence, PV cells act as DC generators without any demand for additional thermal cycles to generate electricity and photovoltaic solar energy. It has several merits over the other renewable energy sources.

Photovoltaic energy sources which neither run out nor have any significant harmful effects on our environment. Photovoltaic solar cells have gone through drastic improvements and developments thanks to its reliability, convenience, and versatility to comply with the different needs of power generation. This Ph.D. thesis is dedicated to studying novel photovoltaic materials that can be used mainly in the so-called ‘third generation’ solar cells.

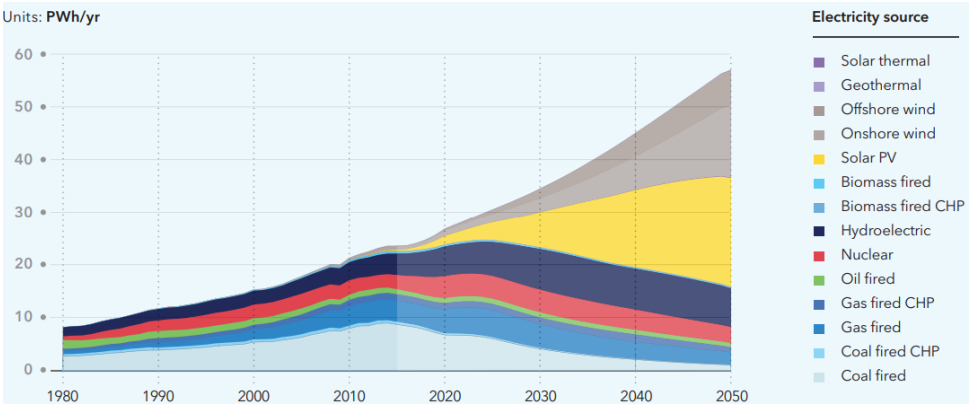

Figure 1.3. Forecast of the world's electricity generation by source. The figure is taken from [3].

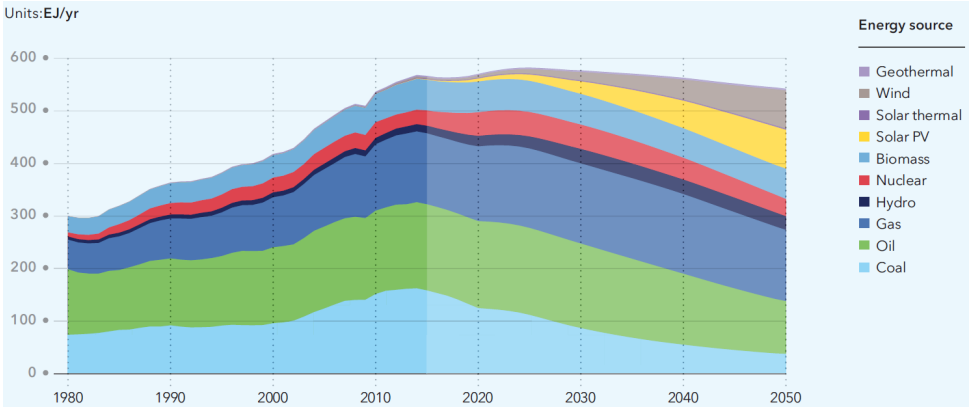

Figure 1.4. Forecast of the world's primary energy supply by source. The figure is taken from [3].

1.2 Historical Development of Photovoltaic solar cell

In 1839, Edmond Becquerel discovered that when a semiconductor device is exposed to light, it will result in the generation of voltage, and this effect is called photovoltaic (PV) effect [4] [5]. Until 1940, there was not much development on PV effects. First in 1941 Ohl [6] investigated the PV effect in silicon and Benzer in germanium in 1946 [7]. Until 1954, the solar cell research received limited interest among the researchers. Chapin *et al.,*[8] discovered the first single-crystal silicon solar cells and then Reynolds *et al.,* [9] investigated the cadmium sulphide solar cell. Growth in space research made the research community to look for

alternatives to conventional resources like fuel, high field batteries because the spacecraft needed continues fuel and energy supply for an extended period away from the earth. Scientists began looking for alternative sources including solar energy [5].

Bell Laboratories were the first to develop the practical photovoltaic solar cell based in 1954, and they observed an initial conversion efficiency of 6% [5, 10]. After this, using solar cells for practical applications, especially in the space industry gathered momentum. Solar energy was accepted as a reliable power source for satellites or spacecraft. Polycrystalline, monocrystalline and amorphous thin-film silicon have been dominating the solar cell technologies for a long time. Gallium Arsenide (GaAs) is another material that is suitable for PV applications because of its light absorption coefficient. This makes GaAs solar cell more efficient than the Si-based solar cells, but GaAs require epitaxial crystal growth techniques that make it more expensive than Si.

Research community has been taken considerable interest in developing solar cell technologies that become compatible with fossil energy sources. For a long period, oil and coal have been much cheaper than solar cell technologies. The environmental issues related to coal and oil has forced people to realize the importance of alternative energy resources like solar energy. Considering the catastrophic impact on the environment, the use of fossil fuels has to be minimized. For the past 25 years, the nations and organizations have started supporting the development of clean energy resources, and this has helped the solar energy research to go forward. In the last ten years, the solar energy industry as has exponential growth. High-quality research and market developments have now made the solar energy technologies to be very attractive and competitive compared to fossil fuels. Research community is striving to develop better solar energy technologies that can be cheap, flexible and efficient.

Green [11] has described the three generations of solar cells with characteristic cell costs and efficiency. The different photovoltaic technologies can be divided into three generations [11, 12] as shown in Figure 1.5. The first generation includes single-crystalline, multicrystalline Si-wafers, primarily made of silicon. Crystalline silicon has touched a record efficiency of 25 % [12, 13]. The second generation is thin film technologies. Thin film solar cells have comparable and lower efficiency to first-generation cells. Green forecasts first and second generation solar cells are cheap to fabricate, but it is very hard to achieve high efficiency due to the detailed balance limit [13]. The third generation of PVs is a compilation of all new concepts that aim for higher efficiency by capturing more photons that are available according

to the Shockley-Queisser [14]. Green forecasts first and second generation solar cells are cheap to fabricate, but it is very hard to achieve high efficiency. These have fundamentally different designs that the first and second generation, each harvesting a more significant fraction of the sunlight, and thus achieve efficiencies above 30 % [15]. They are currently too expensive to be used with normal sunlight intensity (1 sun illumination). To achieve the predicted cost reduction, they are mounted at the focus of cheap lenses or mirrors known as concentrators or collectors that maximize the amount of sunlight harvested by each cell, effectively increasing the cell efficiency. One can then allow for expensive solar cells since a smaller cell area is needed.

One of the proposed third generation solar cell concepts that could result in higher cell efficiency is intermediate band solar cell (IBSC). This is one of the focus areas of this PhD study. In this study, we also focus on non-conventional solar cell materials that can be flexible and cheap.

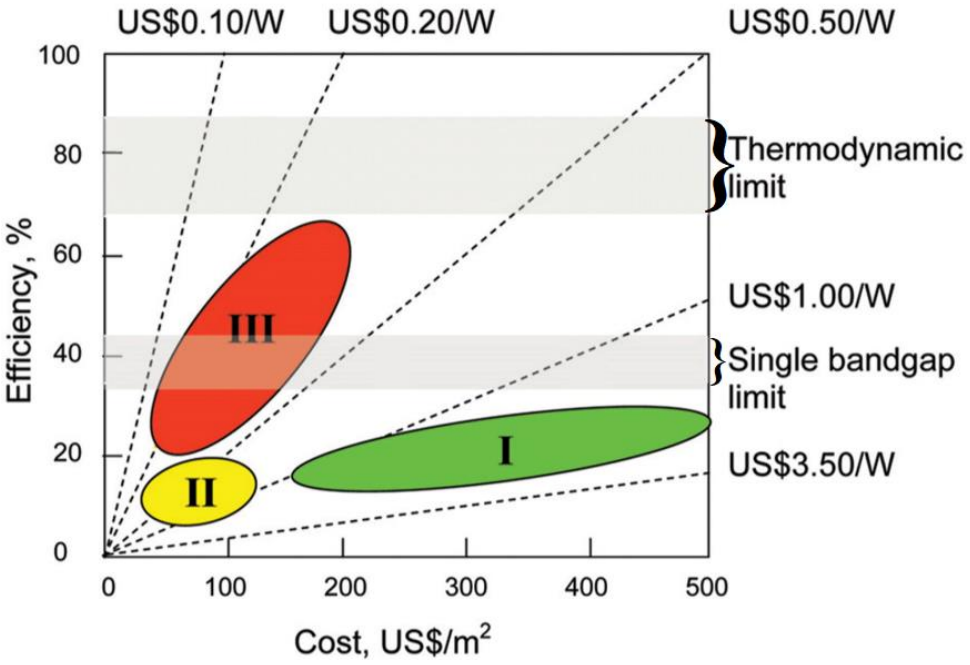

Figure 1.5. The cost and efficiency of the first, second and third-generation solar cells. The figure is taken from [11]

1.3 Working Principle of Photovoltaic solar cell

The general working principle of PV solar cells is described in this section. A PV cell exploits electromagnetic radiation in the form of photons to produce electrical energy through the photovoltaic effect. This photovoltaic effect is created by arranging a semiconductor material in a junction and combining it with an external circuit. The majority of PV cells use a PN junction [16]. When the PV solar cell is exposed to the solar spectrum (sunlight), if the photon has less energy than the energy band gap, no electron will be emitted. If the photon has more energy than the energy band gap, the electron will be exited from the valence band to conduction band and create a negatively charged carrier and a positively charged carrier referred to an electron-hole pair [5]. The electron-hole pair will then move in different directions due to the electric field in the PV cell that drives the hole towards the anode contact and the electron towards the cathode contact. Then the electron arriving at the cathode will travel through the external circuit or load. A cross-section of the basic silicon solar cell is shown in Figure 1.6 [16].

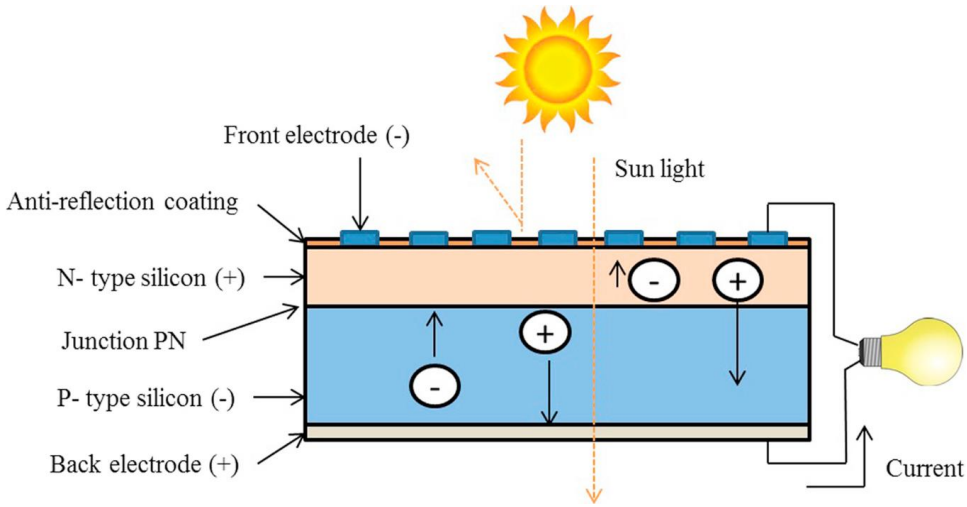

Figure 1.6. Cross-section of basic silicon solar cell. The figure is taken from [16]

A semiconductor is a material with specific electrical characteristics, semiconductors act as an insulator at low temperature, and it acts as conductor at room temperature. As it is well known, when the semiconductor material is doped acceptor impurities, it is said to be a p-type semiconductor, whereas when it is doped with donor impurities materials, then the material is

called as n-type semiconductor. A p-n junction is formed when p-type and n-type semiconductors are connected.

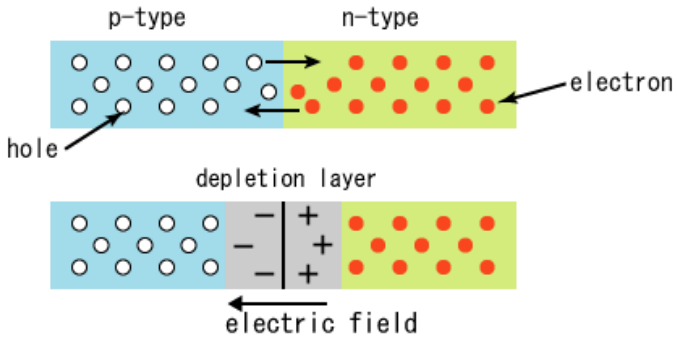

Figure 1.7. Schematic diagram of PN junctions

1.4 Limits of PV solar cells.

Solar cells are not 100% efficient. Loss mechanism exists, and it decreases the energy available for extraction. If an incoming photon has less energy than the energy band gap of the material, there are no allowed states for electrons to be excited to the valence band. Therefore, the photon is not absorbed. The semiconductor material is effectively transparent for photon energies less than the energy band gap. This means that the part of the solar spectrum (effectively visible light region) cannot be used for energy production.

Conversely, if the photon has energy higher than the band gap of the material, the excess kinetic energy is lost in collisions with the crystal lattice. Energy losses in the PV solar cells are attributed to thermalisation loss, junction loss, contact loss, and recombination loss. Recombination is the process in which an excited electron falls to the valence band. This type of loss can be divided into radiative recombination and non-radiative recombination. Radiative recombination is band-to-band recombination where electron releases energy as a photon. This process is unavoidable; emitted photons can be reabsorbed. Non-radiative recombination is a process where an electron releases energy as heat in collisions with crystal lattice. By tuning single junction solar cells to one specific wavelength of light, these losses are minimised [17].

Detailed balanced model is one of the models for calculating theoretical solar cell efficiency. By detailed balance arguments, Shockley-Queisser could account for the entropy generation mechanism in solar cells and calculated the ultimate theoretical efficiency limit of

nearly 32% for the irradiance level to AM (air mass) 1.5 and 41% for fully concentrated sunlight [14, 18, 19]. PV solar cells do not only absorb photons but also emit photons. For example, in the dark, the absorbed and emitted photon flux is the same with no applied voltage. Single junction PV devices poorly match the sunlight for all the reasons mentioned above. So-called third generation PV solar cell technology is a collection of new physical concepts such as nanotechnology and photonic approach to overcome the Shockley-Queisser limit.

1.5 Solutions for the detailed balance limit

As the basis of the versatile PV solar cell, the nanomaterials have attracted huge attention due to its exclusive ability to employ light and control energy flow at approximately the atomic level. The energy density of fossil fuels (measured per unit mass) is higher than the energy density of sunlight (measured per unit area). It is essential to cover massive areas with PV devices to produce suitable current levels for large-scale applications. Therefore, the production and implementation cost of PV solar cells is high. As mentioned earlier, the other challenge with the conventional solar cells is the efficiency limit of 32%. To overcome the high cost of PV solar cells, stability issues, and the efficiency limits, there are three ways how appropriate nanomaterials can contribute to the betterment of solar cell technologies. First, the fabrication of thin film solar cells of a few microns will decrease the amount of the materials used in solar cells. Second, semiconductor materials with lattice dynamic stability and mechanical stability will increase the stability and life cycle of the PV device. Third, the fabrication of multi-junction and intermediate band solar cells will lead to increase in the efficiency of the devices.

Rapid development in the field of nanotechnology has paved the way for the synthesis of advanced nanomaterials that can be used in a variety of new type of solar cell technologies. Doing a trial and error method on experimental counts in checking the suitability of materials for PV applications is rather time-consuming, costly and ineffective. Theoretical modelling and simulation will give enough information on the properties of the materials, and the experimental variation of the applicability of these materials can then be verified using the experimental methods. Rapid growth in computer processing and the use of parallel computing has allowed higher and more complex numerical simulations to be viable. After experiment and theory, computer simulation methods have now become a reliable and effective way to explore nature. In nanomaterial research, numerical simulations can lead the way to identify the appropriate materials for relevant purposes. Numerical simulations can provide a connection

between the perceiving of experimental data and theoretical models while remaining interdependent to both.

This thesis will focus on the application of numerical simulations in investigating photovoltaic properties in condensed matter systems. Specifically, we will emphasize density functional theory (DFT), one of the most common methods for solving the many-electron problem. We can apply DFT to study the physical properties of matter from first principles, providing accurate simulations of matter without intolerance from expectations associated with the understanding of experimental results. As mentioned, the merit of such simulation is that bulk material that may be acutely expensive to yield for the experiment can be investigated computationally. Also, some physical conditions that cannot be produced in the laboratory can be simulated.

1.6 Thesis Objectives

Today, it is possible to accomplish ab initio calculation to study the behaviour of materials for specific applications. This thesis copes with the theoretical calculation of properties like structural prediction, electronic structure, optical, structural stability and mechanical stability behaviour of photovoltaic materials. The aim of the study is fivefold: The first is to study and gain knowledge on the fundamental properties of the matter governed by the electronic structure of a variety of bulk materials. The second is to study novel materials and determine the adaptability and the applicability of theoretical calculation as an accompaniment to experiments for the material scientist in his/her search for novel photovoltaic materials. The third is to investigate materials numerically with intermediate band gaps that could pave the way for higher cell efficiencies than the theoretically limited efficiency of 32% [14]. Fourth is to carry out an in-depth analysis of low-cost, direct band gap, non-silicon materials for PV applications. Fifth is to implement efficient approximations, methods and algorithms to derive accurate numerical results for electronic and optical properties of a variety of novel materials for PV applications. We expect these findings of novel materials in this thesis will lead to immediate concern and interest to an extensive audience in the scientific society.

1.7 Summary

The whole study has resulted in seven research articles. In order to make it easier for the reader to follow, the thesis is divided into two essential parts. The first part is of general nature where we discuss state of the art, the motivation factors, and shed light on theoretical

methodology, computational methods, fundamental properties of materials for photovoltaic applications. In this part, we also present a literature review on intermediate band solar cells and non-silicon solar cells. The second part comes with an accumulation of individual research articles resulting from our entire study on novel materials for intermediate band solar cells and non-silicon solar cells. Because of the page strain in publishing journal articles, these research articles are written in a compact manner avoiding additional information and confirming results obtained during the study. We have included such supporting information at the end of each article.

The organization of the thesis is as follows: Chapter 2 presents the theoretical methodology related to the solid-state physics and materials science. Specifically, it will focus on one of the more popular approaches, density functional theory (DFT), for solving the many-body problem. This method is utilised to study or investigate the physical properties of matter from first principles, yielding more accurate simulations of matter without bias from belief related to knowledge of experimental results. It is a conventional method that can be practiced on many condensed matter systems of interest. This contains, but it is not limited to, semiconductors, pharmaceuticals, biological chemistry, and magnetic materials.

Precisely, the theoretical methodology for the solar cell bulk materials through density functional theory is thoroughly discussed in chapter 2. Our emphasis in this whole study is restricted to bulk materials. This means that possible surface effects are excluded, and the research considered the bulk to be an infinite crystal. To study the properties of a given material, the so-called Schrödinger equation has become the primary tool that the solid-state theorists work with. The Hamiltonian for the whole bulk system is tough to solve. In order to deal with the real bulk system (which contains the substantial number of particles), we have to make some approximations and simplifications. This chapter discusses a different type of approximations such as the Hartree approximation, Hartree-Fock approximation, and density functional theory in order to solve the Hamiltonian.

Chapter 3 outlines a brief note on the computational methods. It is essential to be aware that there are limitations to the applicability of DFT or exchange-correlation function in which is discussed in chapter 2. It brings the main problem into the forefront. The solving of the equations given from density functional theory (DFT) is not as straightforward as may be presumed. In chapter 3, we briefly explain some of the mechanics of solving the single-particle equations in a crystal and outline the difference between the methods that have been used in

this thesis to solve the Schrödinger equations. Further, we discus different methods such as electronic structure method, linear-muffin-tin orbital (LMTO), full potential LMTO and projected augmented wave method.

Chapter 4 presents a brief introduction to the photovoltaic properties, both electronic and optical properties of the semiconductor materials. Since the efficiency of solar cell is highly dependent on the band gap of material, it is important to employ accurate and efficient methods to calculate the band gap accurately, and this will present a promising opportunity for engineering the material for the photovoltaic applications. We discuss the need for accurate and complicated calculation methods to investigate the electronic and optical properties of photovoltaic materials. Details of the hybrid functional method, the so-called Heyd-Scuseria-Ernzerhof (HSE06) that we employ for investigating the electronic band structures, and Bethe-Salpeter equation (BSE) based calculations for the optical properties (dielectric functions) of the materials are discussed. In general, the inclusion of excitonic effects treated within the BSE framework provides results in better agreement with the experimental absorption spectra. This chapter also describes the basics of effective mass (EM) calculation and its relevance to the detailed study of the energy levels in solar devices.

The research carried out in this study has resulted in seven research articles. Three of the articles deal with the novel bulk materials with intermediate band gap and four with the low cost, non-silicon, direct band gap materials. In chapter 5, we give a brief introduction to intermediate band solar cells. Multi-band gap materials offer the possibility of increasing the efficiency of solar cells beyond the limit of traditional single band gap solar-cell materials. Intermediate-band (IB) materials are characterised by the splitting of the main band gaps into two or more sub-band gaps by narrow IBs and have been the focus of recent studies. It is shown that balance-limiting efficiencies of 63.2% can be achieved for IB solar cells, whereas 41% for single-band gap solar cells could be achieved at a concentration of 46 050 suns at earth and sun temperatures of 300 and 6000 K, respectively [20].

Chapter 5 discusses the types of intermediate band solar cells; there are quantum dots IB and bulk IB solar cells. In our search for novel intermediate band gap materials for PV applications, we carried out a comprehensive electronic structure study on 2100 different compounds. Because of the very high computational cost, we mainly focused on the electronic band structure, the density of states and effective mass calculations for 17 acceptable IB materials using generalized gradient approximation (GGA) [21]. The optimal band gap is of

importance in selecting the materials for solar cell applications. Publication I [22] listed in Chapter 7 presents the computational modelling on these novel bulk IB materials.

Although the GGA approximation is time efficient to investigate the electronic structure of a material, it underestimates the band gap. After the initial scanning of the bulk materials, we went for an accurate analysis of the electronic band structure of these materials by employing the HSE06 method. Our in-depth analysis of these seventeen intermediate band gap materials in Publication I revealed that four materials, namely, $Au_2Cs_2I_6$, Ag_2GeBaS_4, Ag_2ZnSnS_4, and $AgCuPO_4$ had a total band gap of less than 4 eV. Publication II listed in chapter 8 presents hybrid electronic and optical properties of these four IB compounds. We verified the applicability of these four materials for photovoltaic applications by studying the optical properties, structural and the mechanical stability analysis of the materials. Our numerical results show that these four materials are promising novel candidates for intermediate band gap solar cells.

Recently, organic-inorganic perovskites have made a lot of success in the recent past as a PV material, and the efficiency of perovskite solar cells have reached a record of 22.1% [23] in 2017. The perovskite material used in these solar cells are mostly methylammonium lead trihalide ($CH_3NH_3PbX_3$, where X : Cl, I, Br). The research community has been focusing on issues like stabilizing the structure in humidity and replacing the toxic lead with other ions. Our study of 2100 compounds led us to an interesting perovskite material Cs_2SnI_6 that had an intermediate band. Although the total band gap of this material is 4.98 eV, since it has an intermediate band, according to Green [6], cells representing VB to IB and IB to CB transitions can be regarded as two cells in series, and the VB to CB transition can be represented as a parallel cell. This unique feature of the intermediate band and the perovskite structure make this material an interesting candidate for PV applications. The detailed analysis of Cs_2SnI_6 is presented in Publication III [24] in chapter 8.

Chapter 6 non-conventional (so-called non-silicon) solar cells are discussed. Silicon solar cells are currently the dominating technology for photovoltaic devices. More than 80% of the solar cell modules installation worldwide are based on either mono or multi-crystalline silicon [7]. However, researchers are making considerable efforts in developing solar cells based on alternative materials (non-silicon materials). This is due to several reasons including the fact that silicon has an indirect band gap of 1.1 eV, resulting in low absorption coefficients. An optimum band gap of 1.4 eV results in an efficiency of 32% for an ideal solar cell [14].

Factors like high cost in material and production and the flexibility issue tends the research community to search alternative materials that have direct band gaps and better absorption properties compared to Silicon. Novel materials considered for PV applications include copper zinc tin sulphide (CZTS), ternary, binary and multinary compounds with a direct band gap, enabling high absorption properties. The desired features of these non-silicon materials are high photon conversion efficiency and low production cost. In another comprehensive study, we analyse electronic band structures of 1000 non-silicon based materials extensively in search for optimum band gaps and high absorption coefficients. We carry out less-accurate, but time efficient GGA based analysis in order to identify candidates that have a band gap between 0.5 eV and 1.1 eV. We performed band gap calculations on a database of 1000 non-silicon materials and identified 27 compounds with band gap values in the required range. We carried out the more accurate, but time-consuming HSE06 method for the analysis of the electronic structure of these 27 candidates. Among these 27 candidates, only four compounds namely $TlBiS_2$, Ba_3BiN, Ag_2BaS_2, and ZrSO revealed to exhibit direct band gap that is highly desirable for photovoltaic applications. We present the complete study in Publication IV [25] that is listed in chapter 10.

Our detailed study showed that the two compounds, namely, $TlBiS_2$ and Ba_3BiN have high absorption coefficients in the visible region. This led to our in-depth analysis of $TlBiS_2$ in Publication V [26] presented in chapter 11. $TlBiS_2$ has strong absorption coefficient with an optimum band gap that can result in high efficiency for the photovoltaic process.

There is a lot of research interest in the family of so-called dichalcogenide, ternary compounds with general formula III-III-VI_2 (where III=Al, Ga, In, Tl; VI=Se, Te, S) in a variety of fields, including solar energy field. Dichalcogenide-$TlGaTe_2$ is an interesting material to be considered, but only a limited number of work is done on this material theoretically. $TlGaTe_2$ is considered as an indirect band gap material, but our accurate analysis of the electronic structure of the material reveals that it possesses both a direct and an indirect band gap. The material has to be defined as direct band gap material since the difference in the photon energy between the k-points is 20 meV. Our finding is further confirmed by the analysis of optical properties of the material, and these results will highlight for the very first time $TlGaTe_2$ as a strong candidate for PV applications. The study is presented in Publication VI in chapter 12.

Our search for a new novel stabilized materials led us to study a material combining two different perovskites, $CsPbI_3$ and $CsSnI_3$ for PV applications. Our results show that through

band gap engineering, we can obtain higher absorption and efficiencies for non-silicon solar cells based on perovskites. Publication VII [27] presents the electronic and optical properties of $CsSn_xPb(1-x)I_3$ (x=0,0.5,1) [27] and is listed in chapter 13.

Chapter 2

Theoretical Methodology

2.1 Many body problems

The state of matter depends on the behaviour of the almost massless electrons which revolve around the heavier nuclei of atoms under normal conditions. Describing the motion of the electrons around a nucleus, was one of the big questions in physics at the beginning of the 20th century. Many researchers contributed to the solution of this problem, among them Schrödinger, Dirac, Heisenberg, and Bohr made large contributions to the progress of a theory they named quantum Mechanics. Today, quantum Mechanics has become the fundamental tool employed by solid state theorists. When modelling a certain material, we require to the interplay between of a very large number of particles, in most macroscopic cases of the order of many moles, $i.e$ 10^{23} electrons. This means that in order to model a realistic system some approximations and several simplifications have to be taken. In this work, our emphasis is restricted to bulk materials. This means that possible surface effects are excluded and that we considered the bulk to be an infinite crystal. To study the properties of a given quantum system, the so-called Schrödinger Equation has to be solved. The time-independent Schrödinger equation has the form [28],

$$H\psi = E\psi \tag{2.1}$$

where H is the Hamiltonian operator, E is the energy and ψ is the wave function. This equation can be solved analytically only in a few simple cases, including the case of a hydrogen atom (one nucleus and one electron). However, for a solid, the system is described by the many-electron wave function $\psi(\mathrm{r}_1,\mathrm{r}_2,\ldots\mathrm{r}_N)$, where r_i denotes the position and spin of particle i. In a solid, typically, we are dealing with 10^{23} particles and which make the problem very complicated. The Hamiltonian for the whole bulk system has been described as follows.

$$H = -\frac{\hbar}{2}\sum_{k}\frac{\nabla^2}{2M_k} + \frac{1}{2}\sum_{k\neq l}\frac{Z_k Z_l e^2}{|R_k - R_l|} - \frac{\hbar^2}{2m}\sum_{i}\nabla_i^2 + \frac{1}{2}\sum_{i\neq j}\frac{e^2}{|r_i - r_j|} - \sum_{i,k}\frac{Z_k e^2}{|r_i - R_k|} \tag{2.2}$$

In this Hamiltonian, $\hbar$ is the Planck constant h divided by 2π, m and r_k denotes the electron mass and coordinates, M_k and R_k nuclear masses and coordinate. Z is the charge of the constituent nuclei. The indiced i and j number the electrons and k and l the nuclei. The first term in Eq. (2.2) is the kinetic energy term for the nuclei, the second term is the Coulomb energy term between the nuclei (V_{NN}), the third term is the kinetic energy term for the electrons, the forth term is the interaction between the electrons (V_{ee}) and the last term is the coulombic interaction between the electrons and the nuclei and could be regarded as an external potential, (V_{ext}) acting upon the electrons. Since the nuclei are much heavier, and therefore slower than the electrons, we can make the so-called "Born-Oppenheimer approximation" and regard the nuclei as stationary. The nuclei positions can therefore be considered a fixed parameter while solving the electronic problem and Eq.(2.2)will be solved for the electrons around these stationary nuclei. This allows us to remove the first term in the Eq.(2.2). The second term is only a constant (since the nuclear positions are known) and is not considered until we calculate the total energy. Now, the Hamiltonian of the electronic problem can be expressed as

$$H_{el} = -\sum_i \nabla_i^2 + \sum_{i \neq j} \frac{1}{|r_i - r_j|} - \sum_{i,k} \frac{2Z_k}{|r_i - R_k|} \tag{2.3}$$

Here we have also introduced Rydberg atomic units, i.e., $e^2 = 2$, $\hbar = 1$, and $m = \frac{1}{2}$.

2.1.1 The Hartree approximation

In order to simplify the Eq.(2.2), we have introduced the Hartree approximation which we can solve easily. In Eq.(2.2), the potential which certain electrons feel depends upon all the other electron's positions. However, this potential can be obtained by an average single-particle potential

$$V_d(r_i) = e^2 \sum_{j \neq i} n_j \frac{|\psi_j(r_j)|^2}{|r_i - r_j|} \tag{2.4}$$

where n_j are the orbital occupation numbers and $\psi_j(\mathbf{r}_j)$ is a singleparticle wave-equation, *i.e.* a solution to the one-particle wave-equation,

$$[-\frac{\hbar^2}{2m}\nabla^2 + V_{ext} + V_d(r_i)]\psi_i(r_i) = \varepsilon_i\psi_i(r_i) \tag{2.5}$$

with this simplification the set of equations now become separable. However, the equations are still non-linear and have to be solved self-consistently by iteration.

The two electrons cannot be in the same quantum state according to the Pauli exclusive principle. However, the wave function in Hartree theory

$$\Psi(r_1\sigma_1, r_2\sigma_2, \ldots, r_N\sigma_N) = \prod_i^N \psi_i(r_i, \sigma_i) \tag{2.6}$$

Eq. (2.6) is not antisymmetric under the interchange of electron coordinates and accordingly does not follow the Pauli principle. Furthermore, the Hartree approximation fails to represent how the configuration of the $N-1$ electrons affectes the remaining electrons. This problem has been rectified by Hartree-Fock theory.

2.1.2 Hartree-Fock approximation

We assert that a solution to $H\Psi = E\Psi$ is given by any state Ψ that makes the following quantity stationary:

$$E = \frac{\langle\Psi\,|\mathrm{H}|\Psi\rangle}{\langle\Psi\,|\Psi\rangle} \tag{2.7}$$

From the ground-state wave function Ψ, the normalized expectation value of energy is minimized according to the variational principle [29].

A better explanation is to take over from the wave function in Eq.(2.6) by a Slater determinant of one-electron wave functions

$$\Psi(r_1\sigma_1, r_2\sigma_2, \ldots, r_N\sigma_N) = \frac{1}{\sqrt{N!}}\begin{vmatrix} \Psi_1(r_1\sigma_1) & \Psi_1(r_2\sigma_2) & \ldots & \Psi_1(r_N\sigma_N) \\ \Psi_2(r_2\sigma_2) & \Psi_2(r_2\sigma_2) & \ldots & \Psi_2(r_N\sigma_N) \\ \vdots & \vdots & \ddots & \vdots \\ \Psi_N(r_N\sigma_N) & \Psi_N(r_N\sigma_N) & \ldots & \Psi_N(r_N\sigma_N) \end{vmatrix} \tag{2.8}$$

This is a linear combination of products of the form given by of Eq. (2.6) moreover, all other products achievable from the permutation of the $\mathbf{r}_i\sigma_i$ amoung themselves. The Hartree-Fock equation which follows from an energy-minimization is given by:

$$[-\frac{\hbar^2}{2m}\nabla^2 + V_{ext} + V_d(r_i)]\psi_i(r_i) - \sum_j \int d' \frac{e^2}{|r-r'|}\psi_j^*(r')\psi_i(r')\psi_j(r)\delta_{s_i s_j} = \varepsilon_i \psi_i(r_i) \quad (2.9)$$

The last term on the left side due to exchange originates from the wave function (Slater determinant). This term only operates between electrons having the same spin; this is called the exchange term. In addition to this, there should also be a correlation interaction between electrons, which is not admitted here. Therefore, the correlation energy can be explained as the difference between the exact energy and the Hartree-Fock energy. Another more competent approach to treat the electrons in a solid will be introduced in the following sections.

2.1.2 Density functional theory

One of the most fruitful modern theories for scheming the properties of matter, the author was awarded the Nobel prize in 1998, is the Density Functional Theory (DFT) [30]. In DFT the primary variable is the electron charge density $n(\mathbf{r})$. The Theory was initially formulated by the theorems by Hohenberg and Kohn, but has since grown and is now one of the main theoretical tools for understanding the properties of matter. The idea to use the electron density as the basic variable when describing the properties of matter did not originate with Hohenberg and Kohn. Thomas-Fermi theory (Fermi 1928) proposes a scheme based on $n(\mathbf{r})$ but assumes uncorrelated motion of the electrons, this theory was latter improved by Dirac (1930) to include exchange by a term derived from the exchange energy in a homogeneous system. The exchange potential in a system of variable density can be approximated by a term $[n(\mathbf{r})]^{\frac{1}{3}}$, $n(\mathbf{r})$ being the local density. This $[n(\mathbf{r})]^{\frac{1}{3}}$ dependence is a consequence of the "exchange hole" or "Fermi hole". This hole is the region near an electron which is avoided by electrons of the same spin. Modern DFT approximates the full non-local exchange with a term based on the local density, hence called the *Local Density Approximation* (LDA). The LDA is widespread in solid state physics, but there are more modern approximations with which to treat the full non-local exchange such as the Generalized Gradient Approximation (GGA), where the term is more complex based on contributions also from the gradients of the local density or higher orders of derivatives such as the Laplacians, the being known as meta-GGAs [31]. The main motivation of these approximations (LDA, GGA, meta-GGA, LDA+U etc.) is that they allow us to solve Schrödinger type equations with local effective potentials.

One can speculate why DFT is so successful, one of the main reason that DFT and local approximations to the exchange term endeavour can be that in solid and another explanation to the benefit is that the approximations built in the LDA and GGAs to the non-local exchange are quite good.

2.1.2 Single-particle equations

For the physics of many-electron systems, we are now in the position where we can define the main principle of density functional theory, which is based on two fundamental theorems introduced by Hohenberg and Kohn [32], and later extended by Kohn and Sham [33].

Theorem 1

The ground state expectation value of any observable, including the total energy, is a unique functional of the exact ground state density n(r).

Theorem 2

The exact ground state density minimizes the total energy functional E[n]. The total energy functional that needs to be minimized in order to find the true ground-state is [33]:

$$E[n] = T_0[n] + \int dr^3 n(r)[V_{ext} + \Phi(r)] + E_{XC}[n], \tag{2.10}$$

where $T_0[n]$ is the kinetic energy of a non-interacting electron system with density $n(r)$, V_{ext} is the potential from the nuclei, $\Phi(r)$ is the Coulomb potential from the electron and $E_{XC}$is the exchange-correlation energy. We can thus look at this as if we have an effective potential, which must enter in the one-particle Schrödinger equations. Important to note here is that E_{XC} requires approximations in the practical implementation of the Kohn-Sham scheme.

$$V_{eff}(r) = V_{ext} + \Phi(r) + \frac{\delta E_{XC}[n]}{\delta n(r)} \tag{2.11}$$

As an effect, the calculation of the energy in terms of charge density is reduced to the self-consistent solution of a system of coupled, non-linear, one-particle Schrödinger equations.

$$\left[-\frac{1}{2}\nabla^2 + V_{ext}(\mathbf{r}) + \int \frac{\rho(\mathbf{r}')}{|\mathbf{r}-\mathbf{r}'|} d\mathbf{r}' + \frac{\delta E_{xc}[\rho]}{\delta\rho(\mathbf{r})}\right]\phi_i(\mathbf{r}) = \varepsilon_i\phi_i(\mathbf{r}) \tag{2.12}$$

This is so called Khon-Sham (KS) wave functions, $\phi_i$are single-particle eigenfunctions that are meaningful only for determining charge density. For more general

systems the spin is also included in the formulation above in a manner that is, at least conceptually, quite simple. The charge density $n(r)$ is replaced as the variable by the density matrix $\rho_{\alpha\beta}(r)$ defined by:

$$\rho_{\alpha\beta}(r) = \langle\Psi|\psi_{\beta}^{\dagger}(r)\psi_{\alpha}^{\dagger}(r)|\Psi\rangle \tag{2.13}$$

where

$$\sum_{\alpha} \int dr\rho_{\alpha\alpha} = N \tag{2.14}$$

and N is the number of electrons. All ground state properties are now functional of the energy E , which is needed to be stationary with respect to variations in $\rho_{\alpha\beta}$ and the density matrix $\rho_{\alpha\beta}$. The potentials are also allowed to be spin dependent so

$$V_{ext} \rightarrow V_{ext}^{\alpha\beta} \tag{2.15}$$

and

$$V_{XC}^{\alpha\beta} = \frac{\delta E_{XC}}{\delta_{\rho\alpha\beta}}. \tag{2.16}$$

This is called Local Spin Density Approximation (LSDA).

2.1.2 Exchange-correlation energy and the electron-hole

The exchange-correlation functional term in the Eq (2.10) is some way approximated in the current theoretical framework. Since the electrons interact with each other: “the probability of finding another electron at **r** ′ reduces by an electron at **r** ", and every electron is surrounded by a hole in the electron density of equal and opposite charge [34]. In LDA (LSDA) the exchange-correlation energy can be written as

$$E_{XC}^{LDA} = \int drn(r)\varepsilon_{XC}[n_{\uparrow}(r), n_{\downarrow}(r)], \tag{2.17}$$

where ε_{XC} is the exchange-correlaton energy per particle in a homogeneous spin-polarized electron gas. We can also write an exact term for the exchange-correlation energy using exchange correlation hole [34]:

$$E_{XC}\frac{1}{2}\int d(r)n(r)\int dr'\frac{1}{|r-r'}n_{XC}(r, r'-r), \tag{2.18}$$

where $n_{XC}(r, r' - r)$ is the exchange correlation hole and obeys the sum rule (charge = -1):

$$\int dr' n_{XC}(r, r' - r) = -1. \tag{2.19}$$

It can now be displayed that making a variable substitution $R = r' - r$, E_{XC} can be written as :

$$E_{XC} \frac{1}{2} \int d(r) n(r) \int_0^\infty dR R^2 \frac{1}{R} \int d\Omega_{XC}(r, R), \tag{2.20}$$

this implies the exchange depends only on the spherical average of n_{XC}. Here in lies the answer to why the LDA approximation works so well: even if LDA doesn't gives the right form for the exchange-correlation hole it does give a spherical average which is very close to the real one [34].

2.1.2 Limits of Density Functional Theory

There are fundamental limits to what a theoretical exact density functional, in combination with the Kohn-Sham approach can predict in terms of ground-state properties. For instance, the true Fermi and exact KS eigenvalue surfaces are generally not identical for both interacting and inhomogeneous systems [35]. It is at present an open question whether the DFT+KS approach is in principle valid for interacting systems with inhomogeneous density. DFT only burdens the electronic ground-state structure, and underestimate the band gap, in semiconductors, comes out incorrect by several factors. A famous error is also found in transition metal oxides that are predicted to be metallic when they are in fact insulators. Other traditional short-coming of DFT have later been attributed to the failure of the specific exchange-correlation functions used, for example, the failure to anticipate the ground-state structure of Fe (being bcc) has been found to be rectified when using a GGA instead of LDA. In practice, it is a complicated matter to single out the exact reason for a failure of a certain type of calculation, since there are so many approximations involved. It is substantial to be known that there are limitations to the propriety of DFT (the exchange-correlation functions used), one should perhaps not to be too despondent, and alternatively view these processes as an experimental computational set-up and simply attempt to push the limits of the theory, of course always looking to validate ones findings in experiment.

Chapter 3

The computational methods

At this is the stage we enter into the real problem. Solving the equations given from Density Functional Theory (DFT) is not as straight-forward as may be presumed. Many choices on various level of approximation and technical details have to be made along the way. Like in many other modern computational research disciplines, this means solving the equations using large computer clusters and massive computational power. In this chapter, we will briefly explain some of the mechanics of solving the single-particle equations in a crystal and outline the difference between the methods that have been used in this thesis to solve the equations. In the previous chapter, we have obtained an effective one-electron equation which can be solved in a self-consistent way,

$$[-\nabla^2 + V_{eff}(r)]\psi_i(r) = \varepsilon\psi_i(r) \tag{3.1}$$

from this equation we can find, the electron charge density $n(r)$ since:

$$n(r) = \sum_{j=1}^{N} |\psi_j|^2 \tag{3.2}$$

Because of both Φ and V $_{XC}$ depend on $n(r)$we can calculate a new V $_{eff}n(r)$ using the local density approximation, GGA, etc, for the exchange-correlation and the Poisson equation for the electrostatic contribution:

$$\nabla^2\Phi(r)_i = -4\pi \sum_{j=1,j\neq i} |\psi_j|^2. \tag{3.3}$$

We repeat/reiterate this process until self-consistency (the difference between V $_{eff}$ in the *m* and *m-1* iterations is almost the same – the difference is only in the chosen convergence criterion) is reached. When self-consistency has been reached we calculate the total energy of the system of electrons and nuclei using the total energy expression of the functional (Eq. (2.10)).

3.1 Periodicity and symmetry of the crystal

It would be difficult to solve the equations if we had to calculate them for all the electrons in the material. For an infinite crystal, the potential is periodic, i.e., invariant under lattice translation T, solving the equations in some shortened part of the system will solve the entire system since this solution will necessarily repeat themselves on the lattice of the crystal. For a monoatomic solid we have

$$V(r+T) = V(r) \tag{3.4}$$

where T is defined as

$$T = m_1 a_1 + m_2 a_2 + m_3 a_3. \tag{3.5}$$

The vectors $\{a_i\}$ are the real-space Bravais lattice vectors that span the crystal cell and $\{\mathrm{m}_i\}$ are integers. According to the Bloch's theorem, the eigenstates can be chosen to take the form of a plane wave times a function with the periodicity of the Bravais latice;

$$\psi_k(r+T) = e^{ik.T}\psi_k(r) \tag{3.6}$$

where k is the Block wave vector. The phase factor will be unit a for some electronic states.

Now, the one-electron function can be distinguished by the Bloch vector **k**. As an effect, Eq. (3.1) can be rewritten as

$$H_{eff}(r)\psi_n(k;r) = \varepsilon_n(k)\psi_n(k;r), \tag{3.7}$$

where the index i in Eq. (3.1) has been substituted by the quantum number n, and the band index. The one-electron wave function ψ_n and the corresponding eigenvalues, ε_n are now be characterized by the Bloch wave vector **k**.

This happens when the wave-vector corresponds to a $reciprocal$ lattice vector defined by

$$g = 2\pi(n_1 b_1 + n_2 b_2 + n_3 b_3) \tag{3.8}$$

the n_i are integers and b_i are the basis vectors of the reciprocal lattice, $i.e$

$$(a_i . b_j) = \delta_{ij} \tag{3.9}$$

for k = g

$$e^{ik.T} = e^{ig.T} = e^{2\pi i m_i n_i} = 1. \tag{3.10}$$

From this one can understand that the periodicity in real space also introduces a periodicity in reciprocal k-space and that an electron state with wave vector $k' = k + g$ will also satisfy the Block condition. When we consider the electronic structure of a solid it is thus not necessary to consider all the vectors. We have to consider only the wave vectors contained inside the region of reciprocal space known as *Brillouin Zone* (BZ). In addition to the translation symmetry, the crystal is also symmetric under rotations, this meaning that there are symmetries which transform one wave vector into another wave vector which reduced our problem further. The smallest possible zone which defines a complete set of wave vectors is called the *irreducible* part of the BZ. For example, in a cubic lattice, the irreducible part of the BZ is only 1/48 of the full BZ which is the only part we need to solve the electronic structure problem.

Following the energy principle (minimize the total energy), and the Pauli exclusion principle, the eigenstates with eigenvalues $\varepsilon_i\ (k)$ are filled starting from the lowest eigenvalue and up. The energy value of the highest filled eigenstate is called Fermi energy (E_F). The Fermi energy is defined by

$$N = \int_{-\infty}^{E_F} D(\varepsilon) d\varepsilon, \tag{3.11}$$

where N denotes the number of valence electrons and, D(E) is the density of the states (DOS),

$$D(E) = \frac{2}{8\pi^3} \int_{s(\varepsilon)} \frac{dS}{|\nabla \varepsilon(K)|} \tag{3.12}$$

This integration is carried out all over a surface of constant energy, S(E), in the first BZ. The one-electron states most appropriate for physical properties are those with energies around the Fermi level. These one-electron states are substantial for the stability of the crystal structure, susceptibility, transport properties etc.

3.2 Electronic structure methods

In order to solve Eq. (3.7), we need to expand by other known wave-functions into a certain basis set. To solve the problem, we need to resort to one of the many available electronic structure methods.

The choice of basis-functions is essential for the efficiency of the computational method, and the first step is to find suitable basis-set in the implementation of a DFT.

The first set of methods obey the Bloch condition explicitly. That is, in the expansion

$$\psi(r) = \sum_n c_n \phi_n(r) \tag{3.13}$$

the basis functions are fixed and the coefficients c_n are chosen to minimize the energy. One disadvantage of this method is that the wave functions are fixed. This often leads to great difficulty in obtaining a sufficiently converged a basis set.

In the second set of methods, the wave functions are varied. This is performed by introducing energy dependent wave functions $\phi_n(\varepsilon, r)$. The wave functions are energy dependent and have the form of

$$\psi(\varepsilon, r) = \sum_n c_n \phi_n(\varepsilon, r), \tag{3.14}$$

However, the Bloch conditions are automatically fulfilled. The solutions in one unit cell are chosen to fit smoothly to those of the neighbour cells, thus fulfilling the Bloch condition "indirectly". As the wave function can be modified with the problem at hand, these techniques converge very fast in the number of required basis functions. In APW and KKR, the price for doing so is the additional parameter ε. At every **k**-point of the band structures must be solved for a large number of ε. Solutions only exist for those ε that are actual eigenvalues. While these methods are accurate, they are also time/consuming. The solution to this problem is to linearize the energy dependent orbitals basis done in LAPW, LMTO, and ASW. They are expanded as a Taylor expansion in ε so that the orbitals themselves are energy independent, although the expansion retains the energy dependence. The variational equation (Eq.(3.7)) thus has to be solved only once for each k-point. These methods are extremely rapid and only slightly less accurate than the other non-linear methods.

3.3 The LMTO method

During the last decades, the linear-muffin-tin-orbital (LMTO) [36] method has become very popular for the calculation of the electronic structure of crystalline systems. The LMTO method associates the following advantages are: (a) it uses a minimal basis, which gives high efficiency and creates calculations possible for large unit cell, (b) it treats all elements in the same way, so that d and f metals, as well as atoms with a large number of core states, can be considered, (c) it is very accurate, due to the augmentation procedure which gives the wave function the correct shape near the nuclei, (d) it uses atom-centered basis functions of well-defined angular momentum, which makes the calculated properties transparent [37].

3.2.1 Muffin-tin orbitals

The crystal is divided into an *interstitial* region outside the spheres and non-overlapping *muffin-tin* spheres surrounding the atomic sites. Inside the muffin-tin sphere, the potential is defined to be spherically symmetric while in the interstitial region of the potential V_{MTZ} is taken to be constant or slowly varying. Because the potential in the interstitial is constant, we can shift the energy scale so as to set it to zero. In the following case, we have considered a crystal with only one atom per primitive cell. Within a single muffin-tin well we define the potential

$$V_{MT}(r) = \begin{cases} V(r) - V_{MTZ} & , \quad |r| < S_{MT} \\ 0 & , \quad |r| > S_{MT} \end{cases} \tag{3.15}$$

Here $V(r)$ is the spherically symmetric part of the crystal potential. The radii of the muffin-tin spheres are chosen so that they do not touch each other. In following, S_{MT} is expressed by S.

Now we try to solve the Schödinger equation for muffin-tin potential,

$$[-\nabla^2 + V_{MT}]\psi(\varepsilon, r) = (\varepsilon - V_{MTZ})\psi_n(r) \tag{3.16}$$

We define the kinetic energy κ^2 in the interstitial region by

$$\kappa^2 = (\varepsilon - V_{MTZ}) \tag{3.17}$$

For an electron moving in the potential well entrenched in the flat potential V_{MTZ} from an isolated muffin-tin, the spherical symmetry can extend throughout all space and the wave functions are

$$\psi_L(\varepsilon, r) = i^l Y_l^m(\hat{r})\psi_l(\varepsilon, r) \tag{3.18}$$

where we use the convention that $r = |r|$ and $\hat{r}$ is the direction of r. A phase factor i^l is included.

To get basis functions which are nearly independent of energy, reasonably localized, and normalisable for all values of κ^2, Anderson [38]accomplished these by muffin-tin orbitlas. A spherical Bessel function that cancels the divergent part of $\psi_l(\varepsilon, k, r)$ and simultaneously reduces the energy and potential dependence of the tails, we have the muffin-tin orbitals in form of

$$\chi_{lm}(\varepsilon, r) = i^l Y_l^m(\hat{r}) \begin{cases} \psi_l(\varepsilon, r) + P_l(\varepsilon)\frac{(r/S)^l}{2(2l+1)} & , \quad |r| < S \\ (r/S)^{-l-1} & , \quad |r| > S \end{cases} \tag{3.19}$$

where $\psi_l(\varepsilon, r)$ is a solution of the radial Schrödinger equation inside the atomic sphere. The potential function

$$P_l(\varepsilon) = 2(2l+1)\frac{D_l(\varepsilon)+l+1}{D_l(\varepsilon)-l} \tag{3.20}$$

moreover, the normalization of $\psi_l(\varepsilon, r)$ is determined by satisfying differentiability and continuity of the basis function on the sphere boundary. Here the $D_l(\varepsilon)$ is the logarithmic derivative of the wave function. The tail of the basis function, $i.e.$ the part outside the muffin-tin sphere can in general, be written as Neumann function. But in Eq. (3.17) the kinetic energy of this tail, known as k^2, is chosen to be zero. Therefore, the Neumann function has a simple form like this.

3.2.2 The LMTO-ASA method

In the atomic sphere approximation, LMTO-ASA, the muffin-tin spheres are overlapping in such a way that the total volume of a muffin-tin sphere is the same as the atomic volume. This means that the muffin-tin radius S is equal to the Wigner-Seitz radius S_{WS} where the total volume per atom is given by $V = (4\pi/3)S_{WS}^3$. In the ASA, the potential is also assumed to be spherically symmetric inside each muffin-tin sphere and the kinetic energy of the basis functions defined in the interstitial is restricted to be constant, actually zero in the calculation.

In order to construct a linear method, the energy-dependent terms in the muffin-tin spheres of the Eq. (3.19) are replaced by the energy independent function Φ. The function is defined as a combination of radial functions and their energy derivative

$$\Phi(D,r) = \phi_l(r) + \omega(D)\dot{\phi}_l(r), \tag{3.21}$$

where $\omega(D)$ is a function of the logarithmic derivative and $\omega(D)$ should make the energy dependent orbitals $\chi_{lm}(\varepsilon,r)$ defined in the Eq. (3.19) continuous and differentiable at the sphere boundary S. The boundary condition determines $D = -l-1$. The so obtained energy independent orbital can now be written as

$$\chi_{lm}(\varepsilon,r) = i^l Y_l^m(\hat{r}) \begin{cases} \Phi_l(D,r) & , \quad |r| < S \\ (r/S)^{-l-1} & , \quad |r| > S \end{cases} \tag{3.22}$$

3.4 Full potential LMTO method

The FP-LMTO calculations are fully relativistic, all electrons, without shape approximation to the charge density or potential. The crystal is divided into an interstitial region outside the spheres and a non-overlapping muffin-tin sphere. The wave function is then expressed differently in the two types of regions. The basis functions and inside a muffin-tin sphere are as in the LMTO-ASA method. They are Bloch sum of linear muffin-tin orbitals and are expanded by structure constant, $\phi_\nu(r)$ and $\dot{\phi}_\nu(r)$. However, the kinetic energy is not, as in the ASA approximation, restricted to the zero in the interstitial region. For simplicity, here we only consider a monoatomic solid and suppress the atomic site index. The κ dependent linear muffin-tin orbitals can now be written as

$$\psi_{klm}(k,r) = \chi_{klm}(r) + \sum_{lm} J_{klm}(r) S_{klm}, l'm'(r), \tag{3.23}$$

where

$$\chi_{lm}(r) = i^l Y_l^m(\hat{r}) \begin{cases} -ilh_l(\kappa S)\frac{\Phi(D_h,r)}{\Phi(D_h,S)} & , \quad |r| < S \\ -ikh_l(\kappa r) & , \quad |r| > S \end{cases} \tag{3.24}$$

and

$$J_{klm}(r) = i^l Y_l^m(\hat{r}) \begin{cases} J_l(\kappa S)(\kappa S)\frac{\Phi(D_j,r)}{\Phi(D_j,S)} & , \quad |r| < S \\ J_l(\kappa r) & , \quad |r| > S \end{cases} \tag{3.25}$$

Inside the muffin-tin at τ, we can also expand the electron densities and potential in spherical harmonics times a radial function,

$$n_\tau(r)|_\tau = \sum_h n_\tau(h; r_\tau) D_h(\hat{r}_\tau), \tag{3.26}$$

$$V_\tau(r)|_\tau = \sum_h V_\tau(h; r_\tau) D_h(\hat{r}_\tau), \tag{3.27}$$

where D_h are linear combinations of spherical harmonics, $Y_l^m(\hat{\boldsymbol{r}})$. D_h are chosen here because we need an invariant representation of the local point group of the atomic site contained in the muffin-tin. The expansion coefficients $n_\tau(h; r_\tau)$ and $V_\tau(h; r_\tau)$ are numerical functions given on a radial mesh.

In the interstitial region, the basis function, charge densities and potential are represented as Fourier series,

$$\psi(k; r)|_I = \sum_G e^{i(k+G).r} \psi(k+G), \tag{3.28}$$

$$n_I(r)|_I = \sum_G n_G e^{i(k+G).r}, \tag{3.29}$$

$$V_I(r)|_I = \sum_G VG e^{i((k+G)r}, \tag{3.30}$$

where G is reciprocal lattice vectors spanning the Fourier space.

3.3.1 The basis set

Envelope function is the basis function in the interstitial region. By choosing appropriate envelope functions, such as plane waves, Gaussians, and spherical waves (Hankel functions), we can generate various electronic structure methods (LAPW, LCGO, LMTO, etc.). The LMTO envelope function is represented as below,

$$K_{lm}(\kappa; r) = -\kappa^{l+1} i^l Y_l^m(\hat{r}) \begin{cases} (\kappa, r) & , \quad \kappa^2 \leq 0 \\ n_l(\kappa, r) & , \quad \kappa^2 > 0 \end{cases} \tag{3.31}$$

where n_l is a spherical Neumann function and h_l^+ is a spherical Hankel function of the first kind. The envelope function is a singular Hankel or Neumann functions with regards to the sign of the kinetic energy. This introduces a κ dependence for the basis functions inside the muffin-tin sphere through the matching conditions at the sphere boundary. This is not a

problem. Using the variational method, the ground state still has several basic functions with the same quantum numbers, n, l, and m, but different κ^2. This is called the double basis.

The basis set can always contain different bases corresponding to the atomic quantum number l but with different principle quantum numbers n. A basis constructed in this way form a fully hybridizing basis set, not a set of separate energy panels.

To illustrate the way the basis set is constructed, we take fcc Ce [39] (we used the similar configuration for our study in the Publications) as an example. The ground state configuration is $4f^1\ 5d^1 6s^2$. Thus we include the $6s$, $6p$, $5d$, $4f$ as valence states. To reduce the core leakage at the sphere boundary, we also treat the core states $5s$ and $5p$ as semi-core states. By this kind of construction, the basis set become more complete.

3.3.2 The LMTO matrix

We now propose an appropriate notation for the basis functions:

$$|\chi_i(k)\rangle = |\phi_i(k)\rangle, \tag{3.32}$$

where $|\phi\rangle$ is the basis function inside the muffin-tin spheres and $|\psi_i(k)\rangle$ denotes the basis functions, outside the spheres, tails.

We construct a wave function $\Psi_{kn}(k)$ by a linear combination of the LMTO basis functions, χ_i. Hence the linear combination can be written as

$$|\Psi\chi\rangle = \sum_i A_i|\chi_i\rangle \tag{3.33}$$

The Hamiltonian operator is

$$\widehat{H} = H_0 + V_{nmt} + V_I \tag{3.34}$$

where H_0 is the Hamiltonian operator containing the kinetic operator and the spherical part of the muffin-tin potential, V_{nmt} represents the non-spherical part of the muffin-tin potential, and V_I is the interstitial potential. Then by using the variational principle for the one-electron Hamiltonian, the LMTO secular matrix follow as

$$\sum_j [\langle chi_i(k)|H_0 + V_{mnt} + V_I\chi_j(k)\rangle - \varepsilon(k)\langle\chi_i(k)|\chi_j(k)\rangle]A_j = 0 \tag{3.35}$$

We can reduce it to

$$\sum_j [H_{ij}^0 + H_{ij}^1 - \varepsilon(k)O_{ij}]A_j = 0 \tag{3.36}$$

where

$$H_{ij}^0 = \langle \phi_i(k)|H_0|\phi_j(k)\rangle \tag{3.37}$$

$$O_{ij} = \langle \phi_i(k)|\phi_j(k)\rangle + \langle \psi_i(k)|psi_j(k)\rangle \tag{3.38}$$

$$H_{ij}^1 = \langle \phi_i(k)|V_{nmt}|\phi_j(k)\rangle + \frac{1}{2}(K_i^2 + K_j^2))\psi_i(k)|\psi_j(k)\rangle + \langle \psi_i(k)|V_I|\psi_j(k)\rangle \tag{3.39}$$

where $|\psi_j(k)\rangle$is an eigenfunction to ∇^2 with eigen value κ_j^2. H_{ij}^0 is the spherical muffin-tin part of the Hamiltonian matrix. O_{ij} is the overlap between the orbitals inside the sphere as well as in the interstitial. H_{ij}^1 contains the corrections to the Hamiltonian matrix coming from the muffin-tin and interstitial region. The first term in Eq. (3.39) is the non-spherical potential matrix. The next term is the expectation value of the kinetic energy operator in the interstitial region. The last term is the interstitial potential matrix.

3.3.3 Total energy

The total energy for the whole crystal can be expressed as [40]

$$E_{tot} = T_{val} + T_{cor} + E_c + E_{xc} \tag{3.40}$$

where T_{val} and T_{cor} are the kinetic energy for the valence and core electrons, E_c is electrostatic energy including electron-electron, electron-nucleus, and nucleus-nucleus energy, and E_{xc} is the exchange energy term. The kinetic energy is usually expressed as the expectation value of the kinetic operator $-\nabla^2$. By using the eigenvalue equation, the expectation value can be expressed as the sum over one electron energies minus the effective potential energy. The core eigenvalues $\varepsilon_{i\tau}$ are obtained as an exact solution to the Dirac equation with the spherical part of the muffin-tin potential.

$$E_{tot} = \sum_{kn}^{occ} w_{nk}\varepsilon_{kn} + \sum_{\mu\tau} f_{i\tau}\varepsilon_i\tau + \int_{Vc} nr\left[\frac{1}{2}V_c(r) - V_{in}(r)\right]dSr - \frac{1}{2}\sum_j Z_{\tau j}V_c(\tau_j;0) + \int_{V_c} n(r)\varepsilon_{\mathrm{xc}}(n(r))dr, \tag{3.41}$$

where the integral is over the unit cell [38]. The sum j is over the core states. The density $n(r)$ is the total charge density, valence as well as core electrons. V_{in} is the input potential obtained from LDA. Madelung term $V_c(\tau; 0)$ is the Coulomb potential at the nucleus less the Z/r self contribution and $\varepsilon_{\mathrm{xc}}$ is the excahnge-correlation energy.

3.5 Projected Augmented Wave Method

Blöchl [41] developed the projected augmented wave method (PAW) by combining the ideas from pseudopotentials and linear augmented-plane-wave (LAPW) methods. PAW method is an all-electron electronic structure method. It describes the wave functions by a superposition of different terms: expansions into atomic and pseudo-atomic orbitals at each atom and the plane wave part, the so-called pseudo wave function.

On the one hand, the plane wave part has the flexibility to describe the bonding and tail region of the wave functions, but if it is used alone, it requires prohibitive large basis sets to explain accurately all the oscillations of the wave function near the nuclei. Otherwise, the expansions into atomic orbitals can explain accurately the nodal structure of the wave function near the nucleus but lack the variational degrees of freedom for the tail regions and bonding. The PAW method connects the virtues of both numerical representations in one well-defined basis set.

To avoid the dual efforts by performing two electronic structure calculations, both plane waves and atomic orbitals, the PAW method does not determine the coefficients of the atomic orbitals variationally. Instead, they are unique functions of the plane wave coefficients. The total energy and most other observable quantities can be broken into three almost independent contributions: one from the plane wave part and a pair of expansions into atomic orbitals on each atom. The contributions from the atomic orbitals can be broken down furthermore into contributions from each atom so that strictly no overlap between atomic orbitals on different sites need to be computed.

In principle, if plane wave and atomic orbital expansions are complete, then the PAW method can reclaim literally the density-functional total energy. This supports us with a systematic way to enhance the basis set errors. The present implementation uses the frozen core approximation, which provides wave functions and correct densities, and thus permits us to find other parameters of the system. The limitations of the plane wave basis set to periodic systems

(crystals) can easily be overcome by making the unit cell sufficiently large and decoupling the long-range interactions. Thus, this method can be used to study solids, surfaces and molecules within the same approach.

3.4.1 Wave function

Firstly, we will introduce a transformation matrix τ. There are two Hilbert space, one called all electron (AE) Hilbert, and other called pseudo (PS) Hilbert. We need to map the AE valence wave functions onto to the PS wave functions.

Every PS wave function can be expanded into PS partial waves

$$|\tilde{\Psi}\rangle = \sum_i |\tilde{\phi}_i\rangle c_i \tag{3.42}$$

The equivalent AE wave function is of the form

$$|\Psi\rangle = \tau|\tilde{\Psi}\rangle = \sum_i |\phi_i\rangle c_i \tag{3.43}$$

From the above two equations, we derive

$$|\Psi\rangle = |\tilde{\Psi}\rangle - \sum_i |\tilde{\phi}_i\rangle c_i + \sum_i |\phi_i\rangle c_i \tag{3.44}$$

because we need the transformation τ to be linear, the coefficients must be linear functions of the PS wave functions. Therefore the coefficients are scalar products of PS wave function with projector functions $\langle\tilde{p}_i|$, $\langle\tilde{p}_i|\tilde{\Psi}\rangle$. The projector functions must fulfill the condition

$$\sum_i |\tilde{\phi}_i\rangle\langle\tilde{p}_i| = 1 \tag{3.45}$$

within the augmentation region Ω_R, which implies that

$$\langle\tilde{p}_i|\tilde{\phi}_j\rangle = \delta_{ij}. \tag{3.46}$$

Finally, the transformation matrix can be derived from Eq. (3.43) and Eq. (3.44) with the definition $c_i = \langle\tilde{p}_i|\tilde{\Psi}\rangle$

$$\tau = 1 + \sum_i (|\phi_i\rangle - |\tilde{\phi}_i\rangle)\langle\tilde{p}_i|. \tag{3.47}$$

Using this transformation matrix, the AE valence wave functions can be derived from PS wave function by

$$|\Psi\rangle = |\widetilde{\Psi}\rangle + \sum_i \left(|\phi_i\rangle - |\tilde{\phi}_i\rangle\right)\langle\tilde{p}_i|\widetilde{\Psi}\rangle \tag{3.48}$$

The core states wave functions $|\Psi\rangle^c$ are decomposed in a way similar to the valence wave functions. They are decomposed into three contributions:

$$|\Psi\rangle^c = |\widetilde{\Psi}\rangle^c + |\phi\rangle^c - |\tilde{\phi}\rangle^c \tag{3.49}$$

Here $|\widetilde{\Psi}\rangle^c$ is a PS core wave function, $|\phi\rangle^c$ is AE core potential wave and lastly $|\tilde{\phi}\rangle^c$ is the PS core partial wave. Compared to the valence wave functions no projector functions are needed to be defined for the core states, and the coefficients of the one-centre expansion are always unity.

3.4.2 Charge density

The charge density at point r in space is composed of three terms:

$$n(r) = \tilde{n}(r) + n'(r) - \tilde{n}'(r) \tag{3.50}$$

The soft pseudo charge density ñ(**r** is the expectation value of real-space projection operator **| r⟩⟨ r|** on the pseudo-wave-functions.

$$\tilde{n}(r) = \sum_n f_n\langle\widetilde{\Psi}_n|r\rangle + \langle r|\widetilde{\Psi}\rangle \tag{3.51}$$

The onsite charge densities n^1 and ñ ^{1} are treated on a radial support grid. They are given as :

$$n'(r) = \sum_n f_n\langle\widetilde{\Psi}_n|\tilde{p}_i\rangle\langle\phi_i|r\rangle\langle\tilde{p}_j|\widetilde{\Psi}_n\rangle = \rho_{ij}\langle\phi_i|r\rangle\langle r|\phi_j\rangle \tag{3.52}$$

here ρ_{ij} is the occupancies of each augmentation channel (i, j) and they are calculated from the pseudo-wave-functions applying the projector function: $\rho_{ij} = \sum_n f_n\langle\widetilde{\Psi}_n|\tilde{p}_i\rangle\langle\tilde{p}_j|\widetilde{\Psi}_n\rangle$. Similarly for

$$\tilde{n}'(r) = \sum_n f_n\langle\widetilde{\Psi}_n|\tilde{p}_i\rangle\langle\tilde{\phi}_i|r\rangle\langle\tilde{p}_j|\widetilde{\Psi}_n\rangle = \rho_{ij}\langle\tilde{\phi}_i|r\rangle\langle r|\tilde{\phi}_j\rangle \tag{3.53}$$

We will target the frozen core case, $\tilde{n}$, $\tilde{n}'$ and n' are restricted to the valence quantities. Besides that, we introduce four quantities what will be used to describe the core charge density:

n_c, $\tilde{n}_c$, n_{Zc}, $\tilde{n}_{Zc}$. n_c denote the charge density of the frozen core all-electron wave function in the reference atom. The partial core density ñ is introduced to calculate nonlinear core corrections. n_{Zc} is defined as the sum of the point charge of nuclei n_z and frozen core AE charge density n_c: $n_{Zc} = n_z + n_c$,

At final, the pseudized core density is a charge distribution that is equivalent to n_{Zc} outside the core radius and have the same moment as the n_{Zc} inside the core region.

$$\int_{\Omega r} n_{Zc}(r)d^3r = \int_{\Omega r} \tilde{n}_{Zc}(r)d^3r \tag{3.54}$$

The total charge density n_T [42]is decomposed into three terms:

$$n_T = n + n_{Zc} = (\tilde{n} + \hat{n} + \tilde{n}_{Zc}) + (n' + n_{Zc}) - (\tilde{n}^1 + \hat{n} + \tilde{n}_{Zc}) = \tilde{n}_T + n'_T - \tilde{n}'_T \tag{3.55}$$

A compensation charge n̂ is added to the soft charge densities $\tilde{n} + \tilde{n}_{Zc}$ and $\tilde{n}' + \tilde{n}_{Zc}$ to reproduced the correct multipole moments of the AE charge density $n' + n_{Zc}$ that is located in each augmentation region. Because n_{Zc} and have exactly the same monopole $-Z_{ion}$ (charge of an electron is +1), the compensation charge must be chosen so that $\tilde{n}' + \hat{n}$ has the same moments as the AE valence charge density n' within each augmentation sphere.

3.4.3 Total energy

The final expression can also be split into three terms for the total energy:

$$E(r) = \tilde{E}(r) + E^1(r) - \tilde{E}(r). \tag{3.56}$$

where $\tilde{E}(r)$, $E^1(r)$, $\tilde{E}(r)$ are given by

$$\tilde{E}(r) = \sum_n f_n \langle \tilde{\Psi}_n | -\frac{1}{2}\Delta | \tilde{\Psi}_n \rangle + E_{xc}[\tilde{n} + \hat{n} + \tilde{n}_c] + E_H[\tilde{n}\hat{n}] + \int v_H[\tilde{n}_{Zc}][\tilde{n}(r) + \hat{n}(r)]dr + U(R, Z_{ion} \tag{3.57}$$

$U(R, Z_{ion})$ is the electrostatic energy of point charges Z_{ion} in an uniform electrostatic background,

$$E'(r) = \sum_{ij} \rho_{ij} \langle \phi_i | -\frac{1}{2}\Delta | \phi_j \rangle + \overline{E_{xc}[n^1 + n_c]} + \overline{E_H[n']} + \int v_H[\tilde{n}Z_c]n'(r)dr \tag{3.58}$$

Here $\int$ v $_H$[ñZ $_c$]n ^{1}(**r**)d **r** is the electrostatic interaction between core and valence electrons and E_H is electrostatic energy

$$E_H[n] = \frac{1}{2}(n)(n) = \frac{1}{2}\int dr \int dr' \frac{n(r)n(rı)}{|r-rı|} \tag{3.59}$$

$$\tilde{E}^1(r) = \sum_{ij} \rho_{ij} \langle \tilde{\phi}_i \left| -\frac{1}{2}\Delta \right| \tilde{\phi}_j \rangle + \overline{E_{xc}[\tilde{n}' + \hat{n} + \tilde{n}_c]} + \overline{E_H[\tilde{n}' + \hat{n}]} + \int v_H[\tilde{n}Z_c][\tilde{n}'(r) + \hat{n}(r)]dr \tag{3.60}$$

The overline means that the corresponding terms must be evaluated on the radial grid with each augmentation region.

3.6 Ultrasoft pseudopotential

It is unaffordable to treat first-row elements, transition metals, and rare-earth elements by standard Norm-conserving Pseudopotentials (NC-PP). Therefore, various attempts have been made to create the so-called soft potentials, and Vanderbilt [43] ultrasoft pseudopotentials (US-PP) has been proved to be the most successful one among them. There is a number of improvements in the US-PP method: 1) nonlinear core corrections were included in the US-PP. 2) Lower cut-off energy, namely reduced number of plane waves, was required in US-PP than NC-PP. This enables us to perform molecular dynamics simulations for systems containing first-row elements and transition metals.

Because $\tilde{E}$ is exactly the same in the PAW method and US-PP method, we only need to consider the linearization of E^1 and $\tilde{E}^1$. We obtain E^1 to the first order by linearization of the E^1 in the PAW total energy functional around atomic reference occupancies ρ_{ij}

$$E' \approx C + \sum_{ij} \rho_{ij} \langle \phi_i | -\frac{1}{2}\Delta + v^a_{eff} | \phi_j \rangle \tag{3.61}$$

with $v^a_{eff} = v_H[n'_a + n_{Zc}] + V_{xc}[\tilde{n}_a{}' + n_c]$ and C is a constant. A similar linearization can also be done for $\tilde{E}'$

$$E^1 \approx \tilde{C} + \sum_{ij} [\rho_{ij} \langle \tilde{\phi}_i | -\frac{1}{2}\Delta + \tilde{v}^a_{eff} | \tilde{\phi}_j \rangle + \int \hat{Q}^L_{ij}(r)\tilde{v}^a_{eff}(r)dr] \tag{3.62}$$

with

$$\tilde{v}_{eff}^{a} = v_H[(\tilde{n}_a{}' + \hat{n}_a + \tilde{n}_{Zc})] + v_{xc}[(\tilde{n}_a{}' + \hat{n}_a + \tilde{n}_{Zc})] \quad (3.63)$$

$\hat{Q}_{ij}^{L}(r)$ is a pseudized augmentation charge in the US-PP approaches. Given $\hat{Q}_{ij}^{L}(r)$ = $Q_{ij}^{L}(r) = \phi_i^*(r)\phi_j(r) - \tilde{\phi}_i^*(r)\tilde{\phi}_j(r)$,

$$E_1 - \tilde{E}_1 = \sum_{ij} \rho_{ij}(\langle\phi_i| -\tfrac{1}{2}\Delta|\phi_j\rangle - \langle\tilde{\phi}_i| -\tfrac{1}{2}\Delta|\tilde{\phi}_j\rangle). \quad (3.64)$$

Now, we compare the PAW functional with the US-PP functional. In the PAW method, if the sum of the compensation charge and pseudo charge density, $\tilde{n}'+\hat{n}$, is corresponding to the onsite AE charge density n', and $\tilde{n}_{Zc} = n_{Zc}$, $\tilde{n}_c = n_c$, we can derive the same E_1 - $\tilde{E}_1$ from Eq. (3.58) and Eq. (3.60). In this limiting case, the PAW method is equivalent to the US-PP method.

3.7 PAW and US-PP

The general rule in Vienna *ab initio* simulation package (VASP) [44]is to use PAW potential wherever possible; the PAW potentials are specially generated for improving the accuracy for magnetic materials, alkali and alkali earth elements, $3d$ transition metals, lanthanides and actinides. For these materials, the treatment of semicores states as valence states are desirable. The PAW method is as efficient as the FLAPW method, it is easy to unfreeze of low lying core states, only one partial wave (and project) for the semicore states is included.

Difference between PAW and US-PP are only related to the pseudization of the augmentation charges. The discrepancies of both methods can be removed by choosing a very accurate pseudized augmentation function. However, augmentation charges must be denoted on a regular grid with the US-PP approach. Therefore, hard and accurate pseudized augmentation charges are expensive regarding computer time and memory. The PAW method avoids these problems (computer time and memory) by introducing a radial support grid. The rapidly varying functions can be elegantly and efficiently treated on radial support grids.

The PAW potentials are marginally harder than US-PP, and they retain similar hardness across the periodic table. Vice versa, the US-PP Potential become progressively softer when moving down in the periodic table. For multi-species compounds with very different covalent radii mixed, the PAW potentials are superior, except for one component system, the US-PP might be slightly faster at the price of reduced precision. Most PAW potential was optimised to work at a cut-off of 250-300 eV, which is only slightly higher than in the US-PP.

Chapter 4

Photovoltaic Properties

4.1 Electronic Properties

Since the efficiency of a solar cell is highly dependent on the band gap of the material, calculating the band structure using first-principle methods based on hybrid functional presents itself as a promising technique for designing a material suitable for the photovoltaic applications. In this section, we discuss the importance of hybrid functional for the accurate band gap calculation [45] [46].

We discussed the limitation of density functional theory in chapter 2 and 3. The use of the Hartree-Fock method leads to significantly underestimating the atomization energies, whereas local exchange and correlation functional overestimates these quantities. Therefore, it is expected that a hybrid treatment, combining both approaches in a suitable way, might yield to more accurate atomization energies, vibrational frequencies, and bond length.

4.1.1 Hybrid functional

It is also possible to advance some theoretical arguments based on the adiabatic connection formula in favour of using a hybrid functional for the exchange-correlation energy. A more refined method for improving the band gap value is to incorporate a certain amount of the Hartree-Fock (exact) exchange to the standard DFT exchange. This is a so-called hybrid functional. Becke *et al.,* firstly introduced the hybrid functional Becke three-parameter Perdew Wang 91 (B3PW91) and its successor Becke three-parameter Lee-Yang-Parr (B3LYP) in 1993 [47-49]. The ratio between contributions to the exchange functional (exact or GGA) is determined by fitting to experimental atomization energies. In this work, we have utilized HSE06 (within the Heyd, Scuseria and Ernzerhof functional), a hybrid functional constructed following a similar approach, although the fraction of exact and density functional approximation exchange are calculated by the conceptual model (Perdew *et al.,*) [50].

Following the work of Becke, the adiabatic connection formula (i.e. the rigorous *ab initio* formula describing the exchange-correlation energy within the Kohn-Sham theory) is presented here as the starting point for the theory of hybrid functionals [47, 48].

$$E_{xc} = \int_0^1 d\lambda E_{xc,\lambda} \tag{4.1}$$

where E_{xc} is the exchange-correlation energy, λ parametrizes the strength of the inter-electronic coupling.

$$|E_x = < \Psi_0 | V_{ee} | \Psi_0 > - \frac{e^2}{2} \int d^3r \int d^3r' \frac{\delta(\mathbf{r})\delta(\mathbf{r}')}{|\mathbf{r}-\mathbf{r}'|} \tag{4.2}$$

The lambda-dependent exchange-correlation term would be

$$E_{x,\lambda} = < \Psi_\lambda | V_{ee} | \Psi_\lambda > - \frac{e^2}{2} \int d^3r \int d^3r' \frac{\delta(\mathbf{r})\delta(\mathbf{r}')}{|\mathbf{r}-\mathbf{r}'|} \tag{4.3}$$

The Khon-Sham non-interacting system is recovered at λ=0. A model for the coupling constant dependence proposed by Perdew *et al.,* [50]

$$E_{xc,\lambda}^{hyb}(n) = E_{xc,\lambda}^{DFA} + (E_x - E_x^{DFA})(1-\lambda)^{n-1} \tag{4.4}$$

where $E^{hyb}x, \lambda = 0$ decreases to include the exact exchange and $E_c^{DFA} = E_{xc}^{DFA} - E_x{}^{DFA}$ and $n \geq 0$ is an integer, which controls how rapidly the correction to the density functional approximations vanishes. The optimal *n* is the lowest order of the perturbation providing a realistic description of the shape or λ-dependence of the exact $E_{xc,\lambda}$argued by Perdew *et al.* It can be written as,

$$E_{xc,\lambda} \approx e^2(c_0 + c_1\lambda + \cdots + c_{n-1}\lambda^{n-1}) \tag{4.5}$$

Perdew *et al.,* found that n=4 delivered good agreement amongst a dataset of molecules between E_{xc}^{hyb} and E_x^{DFA} both in the value, slope and second derivative. Thus, the hybrid exchange-correlation is written as (for n=4 and 0<lambda<1)

$$E_{xc}^{hyb} = \int_0^1 d\lambda E_{xc,\lambda}^{hyb} = E_{xc,\lambda}^{DFA} + \frac{1}{4}(E_x - E_x^{DFA}) \tag{4.6}$$

Since the exact exchange decays very slowly, PBE0 calculation is very challenging in terms of computations [51]. Because of the existence of this problem in PBE0 band structure calculations, Marsman *et al.,* [52] suggested that the hybrid functional could be decomposed into a short-range and a long-range part. A density functional approximation could then replace the long-range contribution of the exact exchange $E_x^{DFA,lr,\mu}$, the finalized equation was

obtained by Heyd, Scuseria and Ernzerhof [53] [54], who introduced the hybrid functional HSE defined as,

$$E_{xc}^{HSE} = \frac{1}{4}E_x^{sr,\mu} + \frac{3}{4}E_x^{DFA,sr,\mu} + E_x^{DFA,lr,\mu} + E_c^{DFA} \tag{4.7}$$

where E_c^{DFA} is the density functional approximation correlation energy, $E_x^{sr,\mu}$ is the short range exact exchange energy and μ is the partition into short-range and long-range parts, which is related to the characteristic distance. In practice, the short and long reange parts are separated by a decomposition of the Coloumb kernel by means of error functions,

$$\frac{1}{r} = \frac{erfc(\mu r)}{r} + \frac{erf(\mu r)}{r} \tag{4.8}$$

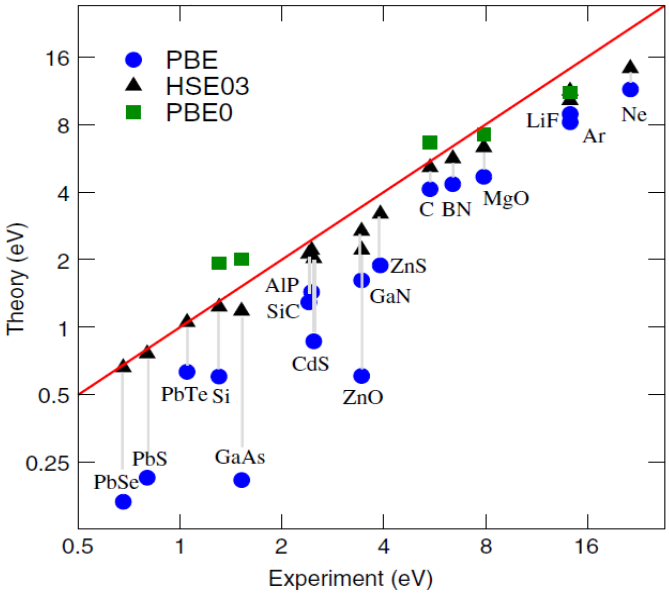

Figure 4.1. Comparison of PBE, HSE03 and PBE0 band gaps. The figure is taken from [52]

From Figure 4.1, we report the comparison of PBE, HSE03 and PBE0 band gaps. The HSE03 screened hybrid functional predicts results in better agreement with experiments for the electronic band gap. More recently, the HSE06 have been extensively applied to calculate the atomization energy, band gaps, lattice parameters and bulk moduli. The difference between HSE03 [53] and HSE06 [55] is the mixing parameter of the hybrid functional.

The electronic band structure of silicon using GGA and HSE06 method presented in Figure 4.2. We noted that the GGA band gap of silicon is 0.55 eV, which is an underestimation of the experimental band gap. However, the HSE06 band gap value of silicon is 1.15 eV, which is good agreement with the experimental value [56].

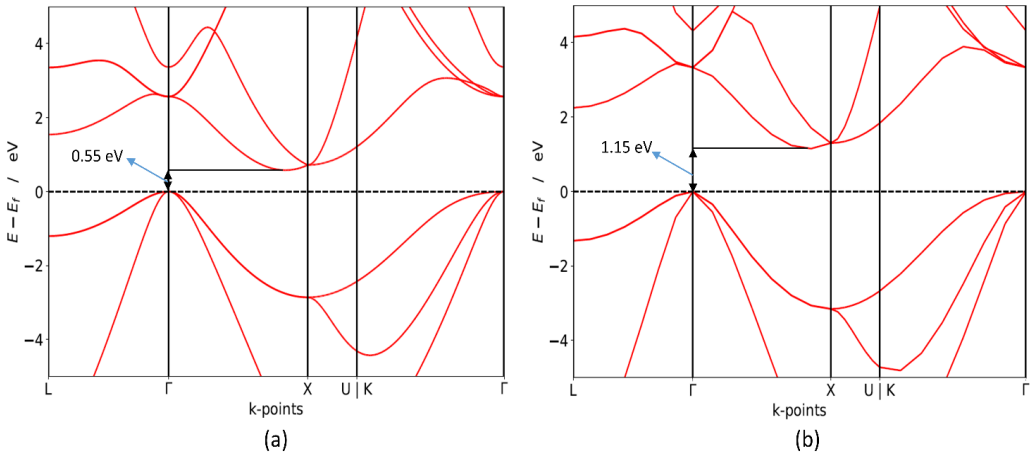

Figure 4.2. Calculated electronic band structure for Silicon using (a) GGA (b) HSE06

4.2 Optical Properties

The optical response of a compound has a major impact on its properties for photovoltaic applications. The optical dielectric function $\varepsilon(\omega)= \varepsilon_1(\omega)+i\varepsilon_2(\omega)$ is the fundamental quantity describing the optical properties. It is defined as the linear response of the system to electromagnetic radiation, and it describes the propagation of radiation in a medium. Here, $\varepsilon(\omega)$ is connected with the interaction between photons and electrons. Its imaginary part $\varepsilon_2(\omega)$ can be derived from the inter-band optical transitions by summing over the unoccupied states using the equation[57, 58],

$$\varepsilon_2^{(\alpha\beta)}(\omega) = \frac{4\pi^2 e^2}{\Omega} \lim_{q\to 0} \sum_{\boldsymbol{k},v,c} 2\, w_k \delta(\epsilon_{c\boldsymbol{k}} - \epsilon_{v\boldsymbol{k}} - \omega) \times \langle u_{c\boldsymbol{k}+e_\alpha q} \mid u_{v\boldsymbol{k}} \rangle \langle u_{c\boldsymbol{k}+e_\beta q} \mid u_{v\boldsymbol{k}} \rangle^* \quad (4.9)$$

where the indices α, β are the Cartesian components, Ω is the volume of the primitive cell, q denotes the Bloch vector of the incident wave, *c* and *v* are the conduction and valence band states respectively, **k** is the Bloch wave vector, w_k denotes the **k**-point weight, δ is a Dirac delta function, u_{ck} is the cell periodic part of the orbital at **k**-point k, ϵ_{ck} refers to the energy of conduction band and ϵ_{vk}refers to the energy of valence band. The real part $\varepsilon_1(\omega)$ of the dielectric function can be derived from $\varepsilon_2(\omega)$ using the Kramer-Kronig relationship[57, 58]

$$\varepsilon_1^{(\alpha\beta)} = 1 + \frac{2}{\pi} \mathrm{P} \int_0^{\infty} \frac{\varepsilon_{\alpha\beta}^2(\omega')\,\omega'}{\omega'^2 - \omega^2 + i\eta}\, d\omega' \tag{4.10}$$

where P indicates the principal value, η is the complex shift. All the frequency dependent linear optical properties such as the absorption coefficients $\alpha(\omega)$ can be calculated from $\varepsilon_1(\omega)$ and $\varepsilon_2(\omega)$.

$$\alpha(\omega) = \frac{\sqrt{2\omega}}{c} \left[(\varepsilon_1^2(\omega) + \varepsilon_2^2(\omega))^{\frac{1}{2}} - \varepsilon_1(\omega)\right] \tag{4.11}$$

In general, the inclusion of excitonic effects treated within the Bethe-Salpeter equation (BSE) framework is in better agreement with the experimental absorption spectra [59-61]. The calculated dielectric functions can be further improved by averaging over multiple grids using BSE.

4.2.1 The Bethe-Salpeter equation

Within the GW approach, the propagation of an electron or hole is explained by the one-particle Green's function. A higher order of Green's function permits to calculate the distribution of two or more particles. As in the case of optical absorption, electron energy loss, or inelastic X-ray scattering (neutral excitations), one has to deal with the interaction between the electron and the hole which is introduced in the material after an excitation. These electron-hole pairs are called excitons. Taking into account these interactions, it leads to the Bethe-Salpeter equation. Salpeter and Bethe derived the equation of motion for two-particle Green's function for bound state problems in 1951 [62, 63] and it is later extended to excitons by Sham *et al.* Afterwards, it is used to study the optical spectra of diamond and silicon. Afterward, it is used to study the optical spectra of diamond and silicon [64] [65]. In 1961, an exact formula was proposed by Baym and Kadanoff [66], and Strinati proposed to determine the excitons based on BSE, the GW method and Baym-Kadanoff theory [67]. Strinati's approach was used in 1995 by Onida *et al.,* to study the excitons on the sodium tetramer [68]. In recent years,

driven by the improvement of computational resources and theoretical methodology, the GW approximation and BSE have been applied to investigate the optical absorption spectra [69]. From Figure 4.3, we observed that schematic diagram of DFT, GW and BSE calculations. The DFT band gap calculation is an underestimation of the fundamental band gap, GW improves the calculated value of the fundamental gap, and BSE presents the exciton binding energies to obtain the optical band gap.

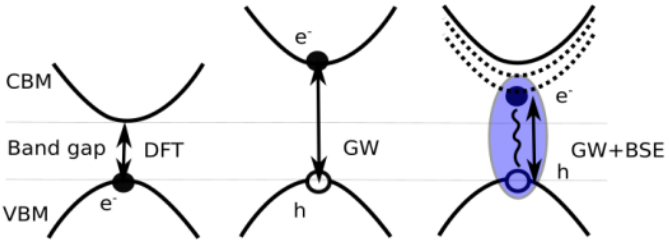

Figure 4.3. Schematic diagram of DFT, GW and BSE calculation

In order to couple the electrons and holes, the Green function has to be converted into an electron-hole Green function. These Green function G and the screened Coulomb interaction W are used to calculate the quasi-particle energies. The electron-hole interaction can then be included by adding the vertex corrections to get improved dielectric functions by solving the four-point BSE equation. The main aim of BSE is to find the value for the macroscopic dielectric function $\varepsilon(\omega)= \varepsilon_1(\omega)+i\varepsilon_2(\omega)$, which is directly linked to some measurable quantity. If we only examine the resonant part of the excitonic Hamiltonian, the macroscopic dielectric function can be written as,

$$\varepsilon_M(\omega) = 1 - \lim_{\mathbf{q}\to 0} v_0(\mathbf{q}) \sum_\lambda \frac{\left|\sum_{(n_1,n_2)} \langle n_1|e^{-i\mathbf{q}\cdot\mathbf{r}}|n_2\rangle A_\lambda^{(n_1 n_2)}\right|^2}{E_\lambda^{exc} - \omega - i\eta} \tag{4.12}$$

where $A_\lambda^{(n_1 n_2)}$ and E_λ^{exc} are the eigenvectors and eigenvalues of the two-particle Hamiltonian

$$H^{2p,reso}_{(n_1 n_2)(n_3 n_4)} A_\lambda^{(n_3 n_4)} = E_\lambda^{exc} A_\lambda^{(n_1 n_2)} \tag{4.13}$$

In the system, we calculate everything in the frequency domain, transition basis and reciprocal space. Thus, the excitonic Hamiltonian can be written as,

$$H^{reso}_{(vck)(v'c'k')} = (E_{c\mathbf{k}} - E_{v\mathbf{k}})\delta_{vv'}\delta_{cc'}\delta_{\mathbf{k}\mathbf{k}'} + 2v_{vc\mathbf{k}}^{v'\mathbf{k}'} - W_{vc\mathbf{k}}^{v'c'\mathbf{k}'} \tag{4.14}$$

where the indices *v, c, k* are an index of the valence band, index of the conduction band and k-vector, respectively. The spin has been summed up. The Hamiltonian is a collection of three parts and the diagonal part contains the quasi-particle energies,

$$H^{diag}_{(vck)(vck)} = (E_{ck} - E_{vk})\delta_{vv'}\delta_{cc'}\delta_{kk'} \tag{4.15}$$

The electron-hole exchange Hamiltonian can be written as,

$$H^{exch}_{(vck)(v'c'k')} = 2\frac{4\pi}{\Omega}\sum_{\mathbf{G}\neq 0}\frac{1}{|\mathbf{G}|^2}\langle c\mathbf{k}|e^{i\mathbf{G}\cdot\mathbf{r}}|v\mathbf{k}\rangle\langle v'\mathbf{k}'|e^{-i\mathbf{G}\cdot\mathbf{r}}|c'\mathbf{k}'\rangle \tag{4.16}$$

Finally, the screened electron-hole interaction part is given by,

$$H^{scr}_{(vck)(v'c'k')} = -\frac{4\pi}{\Omega}\sum_{\mathbf{GG}'}\frac{\varepsilon^{-1}_{\mathbf{GG}'}(\mathbf{q})}{|\mathbf{q}+\mathbf{G}|^2}\langle c\mathbf{k}|e^{i(\mathbf{q}+\mathbf{G})\cdot\mathbf{r}}|c'\mathbf{k}'\rangle\langle v'\mathbf{k}'|e^{-i(\mathbf{q}+\mathbf{G})\mathbf{r}}|v\mathbf{k}\rangle\delta_{\mathbf{q},\mathbf{k}-\mathbf{k}'} \tag{4.17}$$

In principle, the ingredients of BSE calculation include two-particle correlation and provide a better explanation of the absorption spectra. BSE calculations are performed following these steps: (i) find the ground state energies and states. (ii) calculate the quasi-particle energies using the GW approximation, S and (iii) construct the four-point BSE Kernel and diagonalise the BSE Hamiltonian. For comparison, we plotted the experimental and BSE calculated optical absorption coefficient of silicon in Figure 4.4. It can be seen that similar absorption coefficient of silicon for both the experiment [70] and the theoretical calculation[71].

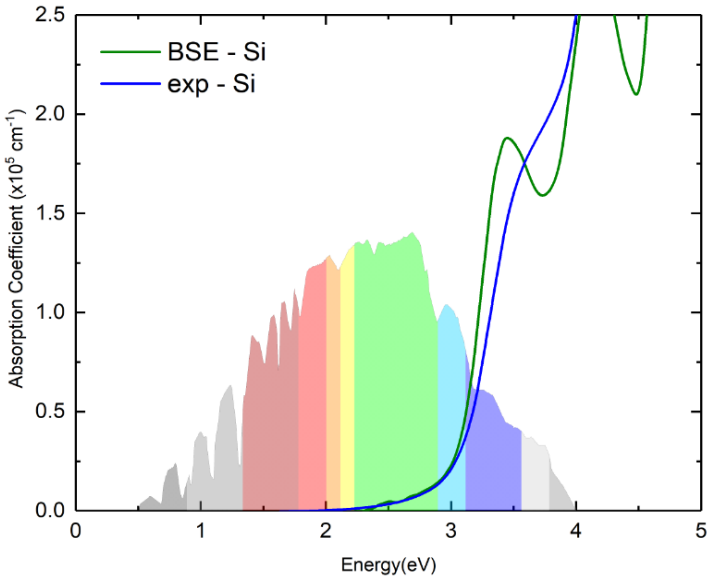

Figure 4.4. The calculated absorption coefficient for Silicon. Source: experimental data from [70], calculated data from [71]

4.3 Effective Mass calculation

The calculation of the effective mass is important for a detailed study of the energy levels in solar devices. The conductivity effective masses of electrons and holes describe the mobility, electrical resistivity, and free-carrier optical response of photovoltaic applications [72]. To investigate the electron/hole conduction properties of photovoltaic materials, we have computed the electron/hole effective mass (EM) at the VB/CB. For an excellent IB, a low effective mass corresponds to the high mobility of the electrons/holes at the VB/CB and consequently high conductivity. For the EM calculation, we have employed the effective mass calculator (EMC) [73]. EMC implements the calculation of the effective masses at the bands extreme using a finite difference method (FDM) (not a band-fitting method). The following equations are implemented in the effective mass calculator. The mobility within the Drude model is given by,

$$\mu = \frac{q\tau}{m^*} \tag{4.18}$$

where q is the charge, τ is the relaxation time of a charge carrier and m^* is the EM of the charge carrier. Effective masses are derived from a materials band structure. The effective mass tensor is a determination of the band curvature near valence band maximum (VBM) and conduction band minimum(CBM) in different directions. Under an external electric field, the effective mass (m*) of charge carriers or effective mass tensor is defined as,

$$\left(\frac{1}{m^*}\right)_{ij} = \frac{1}{\hbar^2}\frac{\partial^2 E_n(\vec{k})}{\partial k_i k_j}, i, j = x, y, z \tag{4.19}$$

where indices *i* and *j* indicate reciprocal constituents and $E_n(k)$ is the dispersion relation for the *n*-th band. A paraboloid can express the dispersion relation at the VBM or CBM for the covalently bonded group semiconductors.

$$E_n(\vec{k}) = \alpha_1 k_x^2 + \alpha_2 k_y^2 + \alpha_3 k_z^2 \tag{4.20}$$

Hence, constituents of the effective mass of charge carriers are just the inverse coefficients in front of the quadratic form.

$$m_{xx}^* = \frac{\hbar}{2\alpha_1}; m_{yy}^* = \frac{\hbar}{2\alpha_2}; m_{zz}^* = \frac{\hbar}{2\alpha_3} \tag{4.21}$$

It is not always possible to fit the band into a quadratic polynomial for organic semiconductors. Therefore, the effective masses calculated using this finite difference method are in good agreement with experimentally obtained values for both group III-IV and organic semiconductors. In this case, derivatives can bcomputed numerically, using finite difference method. The explicit form of the right-side symmetric tensor in (2) is:

$$\frac{\partial^2 E}{\partial k^2} = \begin{pmatrix} \frac{\partial^2 E}{\partial k_x^2} & \frac{\partial^2 E}{\partial k_x \partial k_y} & \frac{\partial^2 E}{\partial k_x \partial k_z} \\ \frac{\partial^2 E}{\partial k_x \partial k_y} & \frac{\partial^2 E}{\partial k_y^2} & \frac{\partial^2 E}{\partial k_y \partial k_z} \\ \frac{\partial^2 E}{\partial k_x \partial k_z} & \frac{\partial^2 E}{\partial k_y \partial k_z} & \frac{\partial^2 E}{\partial k_z^2} \end{pmatrix} \tag{4.22}$$

where second and mixed derivatives are calculated on the five-point stencil (*h* is step size), with an error of the order of *O(h4)* [2]:

$$\frac{\partial^2 f}{\partial x^2} \approx \frac{1}{12h^2}\begin{pmatrix} -(f_{-2}+f_2)+ \\ 16(f_{-1}+f_1)+ \\ -30(f) \end{pmatrix} \tag{4.23}$$

$$\frac{\partial^2 f}{\partial x\,\partial y} \approx \frac{1}{600h^2}\begin{pmatrix} -63\left(f_{1,-2}+f_{2,-1}+f_{-2,1}+f_{-1,2}\right)+ \\ 63\left(f_{-1,-2}+f_{-2,-1}+f_{1,2}+f_{2,1}\right)+ \\ 44\left(f_{2,-2}+f_{-2,2}-f_{-2,-2}-f_{2,2}\right)+ \\ 74\left(f_{-1,-1}+f_{1,1}-f_{1,-1}-f_{-1,1}\right) \end{pmatrix} \tag{4.24}$$

Following equations 4.19 and 4.22-4.24, the effective mass components are the inverse of the eigenvalues of equation 4.19 and the principal directions correspond to the eigenvectors. Since the EMC calculation obtained excellent agreement with previous results [74] (for example GaAs and InP)

Table 4.1 Comparison of the EMC with previous results

		GaAs		InP	
Band	Description	Kresse	EMC	Kresse	EMC
4	electron	0.030	0.029	0.054	0.054
3	heavy hole	0.320	0.318	0.435	0.371
2	light hole	0.036	0.035	0.073	0.074
1	split-off hole	0.108	0.109	0.139	0.139

In this chapter, we discussed efficient methods to model photovoltaic properties. We used the hybrid functional (HSE06) for the electronic structure calculation. Since this hybrid functional is in good agreement with experimental values, we have used the HSE06 method for all papers except Publication I. In the case of optical properties, we have used BSE method to explore the dielectric functions. We have used the BSE method for the non-silicon solar cells papers. We have used the effective mass calculator for all papers except Publication II.

Chapter 5

Intermediate Band solar cells

5.7 Introduction

The possibility of increasing the efficiency of photovoltaic solar cells through absorption of photons in a material without impurity has a relatively long history. Starting with the photovoltaic solar cell with an impurity in 1960, where the sequential absorption of the photon is suggested to proceed through defect levels. This concept gained renewed interest with the proposal of the intermediate band solar cell (IBSC) in the mid-1990s. The compelling difference between the impurity band and the IB concept is that forming an IB should, in principle, reduce the non-radiative transition rate that is likely to dominate when carriers are localised onto isolated impurities. However, the principal challenge to establish an IB within a semiconductor material that supports strong optical transitions with relatively low non-radiative recombination in comparison to the rate of photo-generation by solar photons has remained. This requirement places some fundamental constraints on the nature of the IB that are discussed from a theoretical standpoint in this chapter.

Multi-band gap materials offer the possibility of raising the efficiency of solar cells beyond the limit of traditional single band gap materials. Intermediate band (IB) materials are characterised by the splitting of the main band gaps into two or more sub-band gaps by narrow intermediate bands and have been the focus of several recent studies [75] [76]. In the intermediate band solar cell, an IB material is sandwiched between two ordinary *p*-type and *n*-type semiconductors, and deed as discriminating contacts to the valence band (VB) and conduction band (CB), respectively. In IB materials, an electron is promoted from the VB to CB through the intermediate band. Upon absorption of sub-band gap energy photons, the electrons transit from VB to CB, and later from IB to CB. It will add up to the electrons transition from VB to CB through conventional VB to CB photon absorption [75] [76]. By adopting hypothesis of Shockley and Queisser [14], it was shown in 1997 [20] that a balance-limiting efficiencies of 63,1% for IB solar cells and 41% for single-gap solar cells could be achieved at a concentration of 46,050 suns at earth temperatures of 300 K and sun temperatures of 6,000 K.

The IB should be partially filled, to permit the comparable rates for the low sub-bandgap energy photons absorption processes and should not overlap with either the VB or the CB to avoid fast transitions through thermalization [77]. We can consider the IB solar cells as a combination of three cells. Cells representing VB to IB and IB to CB transition can be regarded as two cells in series, and the VB to CB transition can represent a parallel cell. The cell will have a high tolerance to changes in the solar spectrum [78].

In the mid-twentieth century, the researchers [79-82] suggested the concept of creating intermediate levels in the middle of a forbidden gap to increase the maximum photocurrent by doping the semiconductor with a large concentration of impurities. At an early stage, it was believed that these IBs would cause non-radiative recombination. It has been later shown that the non-radiative recombination can be suppressed by using a sufficiently high concentration of dopants [82-85].

5.2 Types of IBSC

Two major approaches are considered in fabricating the intermediate band solar cells, namely, quantum dot IBs (QDIB) and bulk IB solar cells. By using quantum dots with different shape and sizes, the intermediate band levels can be tuned. The first QDIB was produced in 2004 based on the InAs/GaAs QD material with an efficiency of 15.3%. Energy levels of the confined states in a quantum dot can be used as IB in QDIBs. However, there are many challenges with QDIBs as quantum dots are very small and do not absorb a significant amount of light. With an increasing number of QDs, the cell structure can be damaged, and strain will cause severe damages. At room temperature, Shockley-Read-Hall recombination is a dominant mechanism that causes low efficiency in QD-IB solar cells due to deeper impurities. Several research groups have produced QD-IB solar cells [86-94], and efficiencies over 18% are reported by Blokin *et al* [92].

The second type of IB solar cells is based on bulk materials. IB was detected through photo reflectance measurements in some bulk materials, and this formation was credited to band anticrossing and heavily mismatched alloys [95]. The first of these bulk materials, ZnMnTeO, was developed by Walukiewicz and co-workers [95]. Later, numerous quantum-accurate calculations have been performed on VInS bulk material, characterised by an IB containing the Fermi levels. Philips and co-workers developed bulk IB solar cells using ZnTe doped with an oxygen atom and obtained higher efficiencies and short circuit current than QD-IB solar cells

[96, 97]. The band gap properties of bulk materials are widely studied, and the technologies are well verified by researchers [77, 98-105]. However, the search for intermediate band gap materials continues, in order to model high efficient intermediate band solar cells. In Figure 5.1, the band diagram of an IB solar cell showing the band gap Eg is band gap between the top of the valence band and bottom of the conduction band. E_{vi} is the energy gap between the top of the valence band to bottom of an intermediate band, E_{ci} is the energy gap between the top of the intermediate band to bottom of the conduction band, and ΔE_i- is the width of the intermediate band. In Figure 5.1 the electronic transitions of (V, I), (I, I), (I, C) and (V, C) is schematically depicted.

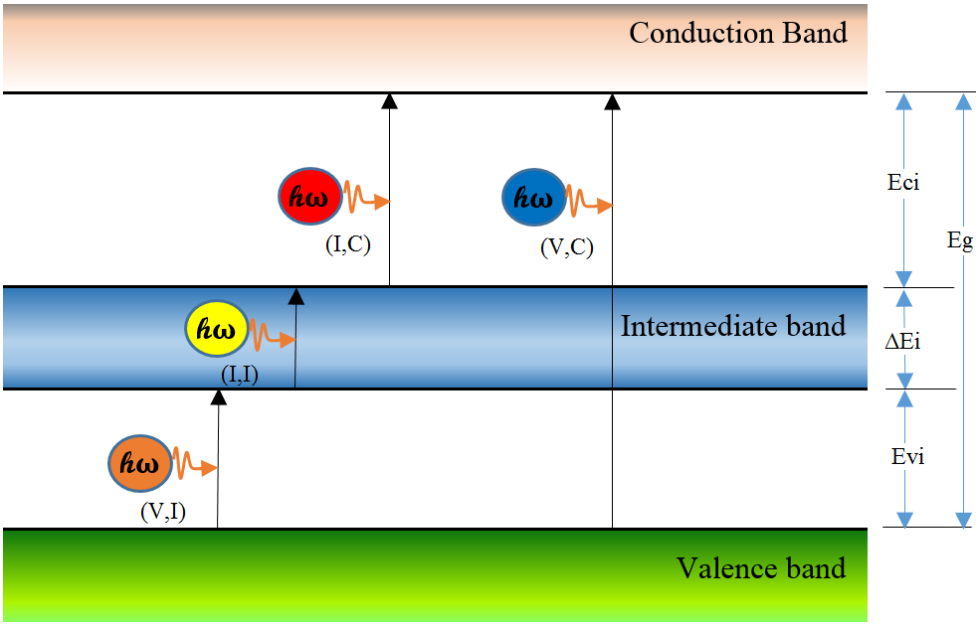

Figure 5.1. Band diagram of bulk IB Solar Cell

5.3 Publications related to Intermediate band solar cells

The main aim of the study is to identify potential candidates for photovoltaic purpose using advanced atomistic modelling techniques based on Density functional theory. The theoretical investigations have been of a cross-disciplinary nature and the research has addressed the photovoltaic properties of a selection of novel semiconductors. The theoretical studies presented in this thesis span over a number of topics and systems. A brief outline of the

research conducted is here presented, in a logical order, to provide the readers with some basic understanding of the motivation behind the study, the data analysis and the outcome of the investigation. We have carried out a comprehensive study of the electronic band structures of 2100 bulk compounds using first-principle DFT calculations (Publication I) [22]. From the first screening, we observed 312 compounds having an intermediate band with the maximum of the valence band at the Fermi level. Among these, 282 compounds were selected for further analysis and 30 compounds were found as heavy elements. After carrying out detailed analysis, we found out that only 17 compounds among the starting 282 would be acceptable semiconductor materials for photovoltaic applications. The rest were found to be perfect insulators, with band gap values larger than 3.51eV. These compounds could be potentially used as photovoltaic materials based on the detailed studies of band structure, the DOS and effective mass calculations. Our effective mass calculations show that these compounds have high electron/hole conduction properties, which make them suitable for PV applications. Although we have studied a large number of compounds (2100 entries from the ICSD database), our investigation cannot be considered exhaustive by any means, as novel materials are continuously discovered and classified, and the resulting data is uploaded onto a variety of databases.

In Publication II, we have carried out a comprehensive study of the structural, mechanical, and optical properties of $Au_2Cs_2I_6$, Ag_2GeBaS_4, Ag_2ZnSnS_4 and $AgCuPO_4$ by employing the range-separated hybrid functional, Heyd–Scuseria–Ernzerhof (HSE06). Our results revealed that HSE06 is capable of providing a more accurate description of the electronic band structure compared to the GGA+U approach, previously employed for the investigation of these materials. The calculation of the density of states of vibrational modes (phonons) revealed that $Au_2Cs_2I_6$, Ag_2GeBaS_4, and Ag_2ZnSnS_4 compounds are dynamically stable, as no imaginary frequency was observed. The zero-point energy for all the dynamically stable compounds is calculated. The mechanical properties such as Young's modulus, the bulk modulus, the shear modulus and the Poisson's ratio are calculated from the values of the elastic constants. Our elastic constant calculations illustrate that all four compounds are mechanically stable. The calculated G/B values are lower than 0.5 for these compounds, confirming the ductile nature of these materials. Numerical results for the static and the dynamic dielectric functions are provided using GGA and HSE06 methods. As expected, GGA overestimates the static dielectric constant. Interestingly, we also observe additional absorption peaks appear in the optical spectra of these four IBs compounds, accompanied by a broadened light absorption energy range and high absorption intensity. Our detailed studies of the electronic and optical

properties identify these materials as excellent potential candidates for photovoltaic application, especially for the development of third-generation intermediate band solar cells.

In Publication III [24], first-principle calculations employing the hybrid HSE06 method are undertaken to compute the electronic structures, effective mass and optical properties of the Cs_2SnI_6 compound. The calculated electronic structures and absorption coefficient confirmed that Cs_2SnI_6 contains an intermediate band. Furthermore, we calculated the phonons frequencies and the elastic constants, confirming Cs_2SnI_6 as dynamically and mechanically stable.

Chapter 6

Non-Silicon solar cells

6.1 Introduction

The solar energy reaching the earth amounts approximately to ten thousand times the primary energy usage by the world population. Solar photovoltaic cells are among the most important technologies for clean energy production. It is predicted that in the future the power from solar photovoltaic modules will reach the terawatt level [106]. Photovoltaic (PV) technology is currently dominated by silicon solar cells. If we look at the worldwide scenario more than 80% of the installed PV modules are mainly mono or multi-crystalline silicon-based [106]. However, researchers are making considerable efforts in developing solar cells based on alternative materials, the fact that silicon is an indirect band gap material that leads to low absorption coefficient. Novel materials considered for PV applications include copper zinc tin sulfide (CZTS), ternary, binary and multinary compounds with a direct band gap, enabling high absorption properties. High photon conversion efficiency and low production cost are the other desired features of these alternative materials. There is also considerable interest in the research community to find ways to develop solar cells that can have efficiencies greater than the Shockley-Queisser limit of 32% [14].

The development of non-silicon materials is a very active field, and several significant signs of progress have been recently made [106]. In the future, non-silicon materials will be most likely produced using thin film technologies, with a resulting device thickness of the order of 2 μm. Despite the crucial role played by these compounds for the next generation of energy materials, the current knowledge of the optical and electronic properties of these compounds is inadequate. Non-silicon materials such as organic semiconductors may become the main candidates for future photovoltaic devices even though they have low stability [107]. To be a promising solar cell material, a semiconductor should have a direct band gap with an appropriate band gap value resulting in efficient absorption of the solar spectrum.

Furthermore, it can be used in junction formation appropriate for guiding the electrical processes involved in energy conversion [108]. Variety of basic materials, GaAs, InP, CdTe, $CuInSe_2$ to name a few and large band gap materials such as ZnO, CdS, ZnCdS used as window

layers in creating heterojunctions have been studied extensively [108]. Reducing production cost is one of the focused areas in selecting materials for PV technologies. Compared to mono-crystalline Silicon solar cells, the production cost for poly-crystalline Silicon solar cells is lower, but the efficiency is lower [109]. According to Mitchell [110], materials that require only a few micrometer thicknesses to absorb the solar spectrum and photo-carriers effectively are created close to the electrical junction. One way to minimize the materials usage is to choose direct band gap materials over indirect band gap since direct band gap solar cells could be made substantially thinner [111]. Due to the low absorption, polycrystalline silicon solar cells structures must have a thickness in the range of 200μm that makes the overall cost higher.

6.2 Photoconversion Limits

The efficiency of solar cells device is limited to several losses. 1) The loss of low-energy photon is due to the absorption threshold related to the band gap of materials produce the loss of low-energy photons. 2) The thermalization losses are due to excited electrons by photons larger than the optical band gap. 3) The radiative and nonradiative recombination of photoexcited carriers occurs in the solar cell device. 4) There are some reflection losses of the incident photons. The first three losses are fundamental to the photoconversion process and cannot be skipped, thereby leading to the so-called detailed balance limit by Shockley-Queisser.

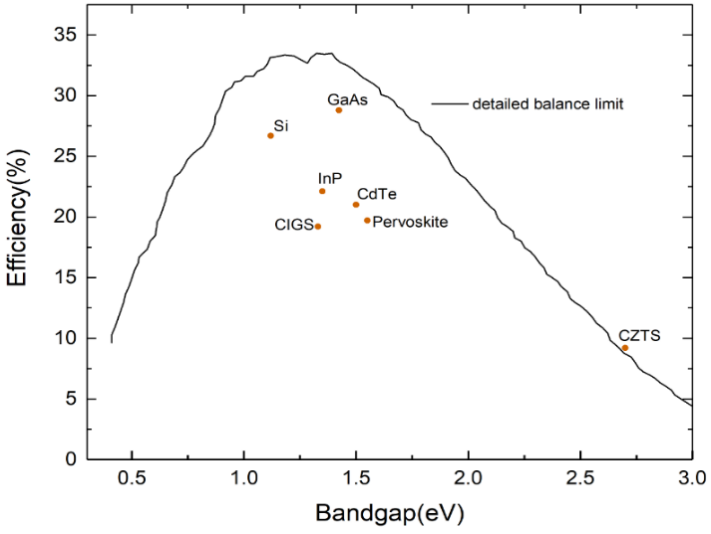

Figure 6.1. Theoretically achievable efficiencies versus band gap of solar cells. Values are taken from [110, 112, 113]

6.3 Material Issue

In principle, a vast variety of semiconductor materials may be used as functional layers or absorbers in photovoltaic solar cells. However, to maximize the solar conversion efficiency, the material should have stability, abundance and environmental aspects [106]. The material must exhibit stability in various aspects. The defect formation and diffusion of components have to be self-stabilising besides heterostructures under all operating conditions and chemical stability of layers. Metastable changes can arise from the light-induced changes in the charge density [114]. Hence, these effects have to be considered when photovoltaic materials and devices are evaluated.

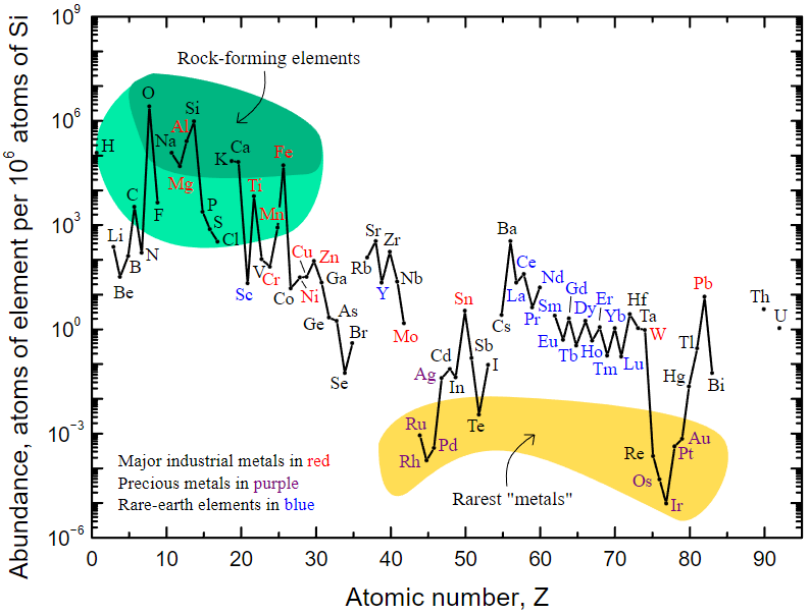

Figure 6.2. The abundance of the chemical elements in Earth's upper continental crust versus atomic number. The figure is taken from [115]

Next, the photovoltaic material always depends on the availability of material [115]. The extraction of elements from the Earth's crust is difficult because it depends on some factors. Additionally, the production rate of some elements is currently extracted only as by-products within the mining operation of other elements. For a direct comparison of the availability of

elements to be used in photoconversion, the abundance of the elements in the Earth's upper continental crust as a function of atomic number is shown in Figure 6.2. As a general trend, the abundance of the materials decreases exponentially with increasing atomic number of the elements. The final material issue is the environmental aspects; several factors have to be considered. Regarding toxicity, certain elements like Cd are toxic, which is accumulate in organisms and the food chain. The compound used in solar cells, such as CdTe, are stable and contained encapsulation, even after fires [116]. The solar cells production on the terawatt scale will involve material handling and material flow on a healthy, very large scale and environmental concerns. It will become a major issue for any photovoltaic technology. Therefore, as a principal goal for photovoltaic technology, material usage in PV modules and production processes should be reduced as far as possible.

6.4 Publications related to non-silicon solar cells

The main aim of the study is to identify potential candidates for photovoltaic purpose using advanced density-functional tools. The theoretical investigations have been of a cross-disciplinary nature and the research has addressed the photovoltaic properties of selective novel non-silicon semiconductors. The theoretical studies presented in this thesis spans over a number of topics and systems. A brief outline of the research conducted is presented in a logical order to the readers to understand how and why the studies were made in the order that is found. This study is to propose non-silicon based direct band gap materials with efficient photovoltaic properties.

In Publication IV, the most effective and accurate computational methods for modelling atomistic systems, density functional theory (DFT) has been widely applied in this work to extensively analyze the electronic band structure of thousand non-silicon based materials in order to identify candidates that have a band gap between 0.5 eV and 1.1 eV. Among these thousand non-silicon compounds, we considered twenty-seven of them with GGA band gap values in the range of 0.5–1.1 eV. Among these twenty-seven compounds, we identified fourteen compounds as direct band gap semiconductors and thirteen as indirect band gap semiconductors. We carried out a study on both the electronic and optical properties of twenty-seven semiconductors (both direct and indirect). Our study of the optical properties of semiconductor materials showed that four direct band gaps among the twenty-seven materials had higher absorption coefficients in the visible region. We have presented a set of first-

principle calculations employing the hybrid functional HSE06, utilized to compute the electronic structures, effective masses of the four chosen materials, namely, $TlBiS_2$, Ba_3BiN, Ag_2BaS_2 and ZrSO. The BSE method was employed to calculate the optical properties. Our study provided rational insights into the electronic structure and optical properties of these four non-silicon materials. These four materials exhibit a direct band gap in the range of 1.10 eV to 2.60 eV. Interestingly, $TlBiS_2$, Ba_3BiN and Ag_2BaS_2 have shown to exhibit a larger absorption coefficient than silicon in the visible region. The phonon calculations revealed that $TlBiS_2$, Ba_3BiN, Ag_2BaS_2 and ZrSO are dynamically stable, as no imaginary frequencies were observed. Our elastic constant calculations illustrate that the compounds are mechanically stable. The calculated G/B values are greater than 0.5, confirming the brittle nature of these materials. Our detailed studies of electronic, structural stability, mechanical stability and optical properties of these four materials reveal them as potential candidates for photovoltaic application, especially for the development of non-silicon multi-junction solar cells.

In Publication V [26], the first-principle calculations employing the hybrid HSE06 and BSE method were utilized to compute the electronic structures, effective masses and optical properties of the $TlBiS_2$ compound. The calculated HSE06 electronic structures without and with SOC effect confirmed that the $TlBiS_2$ exhibits a direct band gap, with a value of 1.10 eV and 0.67 eV respectively, at the Γ **k**-point. The calculated HSE06 electronic structures without and with SOC effect confirmed that the $TlBiS_2$ exhibits a direct band gap, with a value of 1.42 eV and 1.16 eV respectively, at the F **k**-point. Thus, the absorption peaks exhibited a high absorption intensity in the visible region. For the very first time, absorption spectra of $TlBiS_2$ based on BSE without and with SOC effects calculation is reported in this paper. It is shown that $TlBiS_2$ is more efficient absorption material than silicon. Our detailed studies of electronic and optical properties of the ternary chalcogenide material reveal that $TlBiS_2$ is a potential candidate for photovoltaic application, especially for the development of multi-junction solar cells.

In Publication VI [25], In summary, we investigated the electronic band structure and optical properties of $TlGaTe_2$ with accurate first-principle calculations. The calculated HSE06 electronic structures confirmed that the $TlGaTe_2$ exhibits an indirect band gap, with a value of 1.109 eV, at the Z_1 **k**-point. However, $TlGaTe_2$ also exhibits a direct band gap, with a value of 1.129 eV, at the Z **k**-point. This is further confirmed by the first absorption peak at a photon energy of 1.13 eV. Hence, we proved that the only 20 meV difference of direct and

indirect band gap exhibits effective absorption coefficient. Thus, the small energy difference between the direct and indirect band gaps has led to claims that the fundamental gap is direct. For the first time, the absorption spectra of $TlGaTe_2$ is reported here and, by using BSE calculation, shown to be more efficient than silicon. $TlGaTe_2$ has gained interest because of its optical absorption peaks attended high absorption intensity in the visible region.

Moreover, the phonon calculations revealed that $TlGaTe_2$ is dynamically stable, as no imaginary frequency was observed. Our elastic constant calculations illustrate that the $TlGaTe_2$ is mechanically stable. We simulated and compared Raman spectra and infrared spectra with previous results. Our detailed studies of electronic and optical properties of the ternary dichalcogenide material revealed that $TlGaTe_2$ is a potential candidate for photovoltaic application.

In Publication VII [27], we demonstrated that $CsSnI_3$ could be stabilized in four different polymorphs, three of which contain a direct band gap ideal for photovoltaic applications. By adding Pb to the perovskite to create $CsSn_{0.5}Pb_{0.5}I_3$, we found that although this the new perovskite has an indirect band gap, it could work as a direct band gap material due to the lower electron-hole distance in the Z-D **k**-points region. In general, we found that by combining $CsSnI_3$ and $CsPbI_3$ we got a new compound with different electronic and optical structure in addition to different chemical bonding. Based on this it could be viable to combine various compounds in an attempt to end up with an optimal compound for photovoltaic applications.

Bibliography

[1]. Bennett P. Earth, the incredible recycling machine: Thomson Learning; 1993.

[2]. Agency IE. CO_2 Emissions from Fuel Combustion 20172017.

[3]. Energy transition outlook 2017 : a global and regional forecast of the energy transition to 2050. Høvik: DNV GL; 2017.

[4]. Becquerel E. On Electric Effects under the Influence of Solar Radiation. Compt Rend. 1839;9:561.

[5]. Sze SM, Ng KK. Physics of semiconductor devices: John wiley & sons; 2006.

[6]. Ohl RS. Light-sensitive electric device. Google Patents; 1946.

[7]. Benzer S. Excess-defect germanium contacts. Physical Review. 1947;72(12):1267.

[8]. Chapin DM, Fuller C, Pearson G. A new silicon p-n junction photocell for converting solar radiation into electrical power. Journal of Applied Physics. 1954;25(5):676-7.

[9]. Reynolds D, Leies G, Antes L, Marburger R. Photovoltaic effect in cadmium sulfide. Physical Review. 1954;96(2):533.

[10]. Chodos A. April 25, 1954: Bell Labs Demonstrates the First Practical Silicon Solar Cell. APS News-This month in Physics history. 2009.

[11]. Green MA. Third generation photovoltaics: Ultra-high conversion efficiency at low cost. Progress in Photovoltaics: Research and Applications. 2001;9(2):123-35.

[12]. Green MA. Third generation photovoltaics: advanced solar electricity generation. Spriinger-Verlag, Berlin. 2003:4.

[13]. Green MA, Emery K, Hishikawa Y, Warta W, Dunlop ED. Solar cell efficiency tables (version 46). Progress in Photovoltaics: Research and Applications. 2015;23(7):805-12.

[14]. Shockley W, Queisser HJ. Detailed balance limit of efficiency of p-n junction solar cells. Journal of applied physics. 1961;32(3):510-9.

[15]. Barnham K, Mazzer M, Clive B. Resolving the energy crisis: nuclear or photovoltaics? Nature materials. 2006;5(3):161.

[16]. Sampaio PGV, González MOA. Photovoltaic solar energy: Conceptual framework. Renewable and Sustainable Energy Reviews. 2017;74:590-601.

[17]. Green MA. Third generation photovoltaics: solar cells for 2020 and beyond. Physica E: Low-dimensional Systems and Nanostructures. 2002;14(1-2):65-70.

[18]. Nelson J. The physics of solar cells. Series on Properties of Semiconductor Materials. Imperial College Press London, UK; 2003.

[19]. Landsberg PT. Recombination in semiconductors: Cambridge University Press; 2003.

[20]. Luque A, Martí A. Increasing the efficiency of ideal solar cells by photon induced transitions at intermediate levels. Physical Review Letters. 1997;78(26):5014.

[21]. Liechtenstein A, Anisimov V, Zaanen J. Density-functional theory and strong interactions: Orbital ordering in Mott-Hubbard insulators. Physical Review B. 1995;52(8):R5467.

[22]. Rasukkannu M, Velauthapillai D, Vajeeston P. Computational modeling of novel bulk materials for the intermediate-band solar cells. ACS Omega. 2017;2(4):1454-62.

[23]. Yang WS, Park B-W, Jung EH, Jeon NJ, Kim YC, Lee DU, et al. Iodide management in formamidinium-lead-halide–based perovskite layers for efficient solar cells. Science. 2017;356(6345):1376-9.

[24]. Rasukkannu M, Velauthapillai D, Vajeeston P. A first-principle study of the electronic, mechanical and optical properties of inorganic perovskite Cs_2SnI_6 for intermediate-band solar cells. Materials Letters. 2018;218:233-6.

[25]. Rasukkannu M, Velauthapillai D, Bianchini F, Vajeeston P. Properties of Novel Non-Silicon Materials for Photovoltaic Applications: A First-Principle Insight. Materials. 2018;11(10):2006.

[26]. Rasukkannu M, Velauthapillai D, Ponniah V. A promising high-efficiency photovoltaic alternative non-silicon material: A first-principle investigation. Scripta Materialia. 2018;156:134-7.

[27]. Eidsvåg H, Rasukkannu M, Vajeeston P, Velauthapillai D. Bandgap engineering in $CsSn_xPb_{(1-x)}I_3$ and their influence on light absorption. Materials Letters. 2018;218:253-6.

[28]. Wilson KG. The renormalization group: Critical phenomena and the Kondo problem. Reviews of modern physics. 1975;47(4):773.

[29]. Ashcroft NW, Mermin ND. Solid state physics (saunders college, philadelphia, 1976). Google Scholar. 2010:461.

[30]. Kohn W. Nobel Lecture: Electronic structure of matter—wave functions and density functionals. Reviews of Modern Physics. 1999;71(5):1253.

[31]. Kurth S, Perdew JP, Blaha P. Molecular and solid-state tests of density functional approximations: LSD, GGAs, and meta-GGAs. International journal of quantum chemistry. 1999;75(4-5):889-909.

[32]. Hohenberg P, Kohn W. Inhomogeneous electron gas. Physical review. 1964;136(3B):B864.

[33]. Kohn W. W. Kohn and LJ Sham, Phys. Rev. 140, A1133 (1965). Phys Rev. 1965;140:A1133.

[34]. Gunnarsson O. O. Gunnarsson and RO Jones, Rev. Mod. Phys. 61, 689 (1989). Rev Mod Phys. 1989;61:689.

[35]. Mearns D. Inequivalence of the physical and Kohn-Sham Fermi surfaces. Physical Review B. 1988;38(9):5906.

[36]. Skriver H. The LMTO Method, Springer-Verlag. New York. 1984.

[37]. Methfessel M. M. Methfessel, Phys. Rev. B 38, 1537 (1988). Phys Rev B. 1988;38:1537.

[38]. Andersen OK. Linear methods in band theory. Physical Review B. 1975;12(8):3060.

[39]. Johansson B. The α-γ transition in cerium is a Mott transition. Philosophical Magazine. 1974;30(3):469-82.

[40]. Trygg J. First principles studies of magnetic and structural properties of metallic systems. 1996.

[41]. Blöchl P. PE Blöchl, Phys. Rev. B 50, 17953 (1994). Phys Rev B. 1994;50:17953.

[42]. Kresse G. G. Kresse and D. Joubert, Phys. Rev. B 59, 1758 (1999). Phys Rev B. 1999;59:1758.

[43]. Laasonen K. K. Laasonen, A. Pasquarello, R. Car, C. Lee, and D. Vanderbilt, Phys. Rev. B 47, 10 142 (1993). Phys Rev B. 1993;47:10.

[44]. Kresse G, Hafner J. Ab initio molecular dynamics for liquid metals. Physical Review B. 1993;47(1):558.

[45]. Deák P, Aradi B, Frauenheim T, Janzén E, Gali A. Accurate defect levels obtained from the HSE06 range-separated hybrid functional. Physical Review B. 2010;81(15):153203.

[46]. Kuisma M, Ojanen J, Enkovaara J, Rantala T. Kohn-Sham potential with discontinuity for band gap materials. Physical review B. 2010;82(11):115106.

[47]. Becke AD. Density-functional thermochemistry. III. The role of exact exchange. The Journal of chemical physics. 1993;98(7):5648-52.

[48]. Becke AD. A new mixing of Hartree–Fock and local density-functional theories. The Journal of chemical physics. 1993;98(2):1372-7.

[49]. Stephens P, Devlin F, Chabalowski C, Frisch MJ. Ab initio calculation of vibrational absorption and circular dichroism spectra using density functional force fields. The Journal of Physical Chemistry. 1994;98(45):11623-7.

[50]. Perdew J. JP Perdew, M. Ernzerhof, and K. Burke, J. Chem. Phys. 105, 9982 (1996). J Chem Phys. 1996;105:9982.

[51]. Ernzerhof M, Scuseria GE. Assessment of the Perdew–Burke–Ernzerhof exchange-correlation functional. The Journal of chemical physics. 1999;110(11):5029-36.

[52]. Marsman M. M. Marsman, J. Paier, A. Stroppa, and G. Kresse, J. Phys.: Condens. Matter 20, 064201 (2008). J Phys: Condens Matter. 2008;20:064201.

[53]. Heyd J, Scuseria GE, Ernzerhof M. Hybrid functionals based on a screened Coulomb potential. The Journal of chemical physics. 2003;118(18):8207-15.

[54]. Heyd J, Scuseria GE. Efficient hybrid density functional calculations in solids: Assessment of the Heyd–Scuseria–Ernzerhof screened Coulomb hybrid functional. The Journal of chemical physics. 2004;121(3):1187-92.

[55]. Krukau AV, Vydrov OA, Izmaylov AF, Scuseria GE. Influence of the exchange screening parameter on the performance of screened hybrid functionals. The Journal of chemical physics. 2006;125(22):224106.

[56]. Precker JW, da Silva MA. Experimental estimation of the band gap in silicon and germanium from the temperature–voltage curve of diode thermometers. American Journal of Physics. 2002;70(11):1150-3.

[57]. Gajdoš M, Hummer K, Kresse G, Furthmüller J, Bechstedt F. Linear optical properties in the projector-augmented wave methodology. Physical Review B. 2006;73(4):045112.

[58]. Yang L-M, Vajeeston P, Ravindran P, Fjellvåg H, Tilset M. Revisiting isoreticular MOFs of alkaline earth metals: a comprehensive study on phase stability, electronic structure, chemical bonding, and optical properties of A–IRMOF-1 (A= Be, Mg, Ca, Sr, Ba). Physical Chemistry Chemical Physics. 2011;13(21):10191-203.

[59]. Albrecht S, Reining L, Del Sole R, Onida G. Ab initio calculation of excitonic effects in the optical spectra of semiconductors. Physical review letters. 1998;80(20):4510.

[60]. Bokdam M, Sander T, Stroppa A, Picozzi S, Sarma D, Franchini C, et al. Role of polar phonons in the photo excited state of metal halide perovskites. Scientific reports. 2016;6:28618.

[61]. Rohlfing M, Louie SG. Electron-hole excitations in semiconductors and insulators. Physical review letters. 1998;81(11):2312.

[62]. Salpeter E. EE Salpeter and HA Bethe, Phys. Rev. 84, 1232 (1951). Phys Rev. 1951;84:1232.

[63]. Gell-Mann M, Low F. Bound states in quantum field theory. Physical Review. 1951;84(2):350.

[64]. Sham L, Rice T. Many-particle derivation of the effective-mass equation for the Wannier exciton. Physical Review. 1966;144(2):708.

[65]. Hanke W, Sham L. Many-particle effects in the optical excitations of a semiconductor. Physical Review Letters. 1979;43(5):387.

[66]. Baym G, Kadanoff LP. Conservation laws and correlation functions. Physical Review. 1961;124(2):287.

[67]. Strinati G. Dynamical shift and broadening of core excitons in semiconductors. Physical Review Letters. 1982;49(20):1519.

[68]. Onida G, Reining L, Godby R, Del Sole R, Andreoni W. Ab initio calculations of the quasiparticle and absorption spectra of clusters: the sodium tetramer. Physical review letters. 1995;75(5):818.

[69]. Leng X, Jin F, Wei M, Ma Y. Wiley Interdiscip. Rev.: Comput. Mol. Sci. 6, 532–550 (2016).

[70]. Aspnes DE, Studna A. Dielectric functions and optical parameters of Si, Ge, GaP, GaAs, GaSb, InP, InAs, and InSb from 1.5 to 6.0 ev. Physical review B. 1983;27(2):985.

[71]. Paier J, Marsman M, Kresse G. Dielectric properties and excitons for extended systems from hybrid functionals. Physical Review B. 2008;78(12):121201.

[72]. Van Zeghbroeck B. Principles of semiconductor devices. Colarado University. 2004.

[73]. Fonari A, Sutton C. Effective Mass Calculator for Semiconductors. 2015.

[74]. Kim Y-S, Marsman M, Kresse G, Tran F, Blaha P. Towards efficient band structure and effective mass calculations for III-V direct band-gap semiconductors. Physical Review B. 2010;82(20):205212.

[75]. Luque A, Martí A, Stanley C. Understanding intermediate-band solar cells. Nature Photonics. 2012;6(3):146.

[76]. Luque A, Marti A. A metallic intermediate band high efficiency solar cell. Progress in Photovoltaics: Research and Applications. 2001;9(2):73-86.

[77]. Palacios P, Aguilera I, Sánchez K, Conesa J, Wahnón P. Transition-metal-substituted indium thiospinels as novel intermediate-band materials: prediction and understanding of their electronic properties. Physical Review Letters. 2008;101(4):046403.

[78]. Green MA. Multiple band and impurity photovoltaic solar cells: General theory and comparison to tandem cells. Progress in Photovoltaics: Research and Applications. 2001;9(2):137-44.

[79]. Shockley W, Read Jr W. Statistics of the recombinations of holes and electrons. Physical review. 1952;87(5):835.

[80]. Hall RN. Electron-hole recombination in germanium. Physical review. 1952;87(2):387.

[81]. Lang D, Henry C. Nonradiative recombination at deep levels in GaAs and GaP by lattice-relaxation multiphonon emission. Physical Review Letters. 1975;35(22):1525.

[82]. Wolf M. Limitations and possibilities for improvement of photovoltaic solar energy converters: Part I: Considerations for earth's surface operation. Proceedings of the IRE. 1960;48(7):1246-63.

[83]. Ekins-Daukes N, Honsberg C, Yamaguchi M, editors. Signature of intermediate band materials from luminescence measurements. Photovoltaic Specialists Conference, 2005 Conference Record of the Thirty-first IEEE; 2005: IEEE.

[84]. Strandberg R, Reenaas TW. Photofilling of intermediate bands. Journal of applied physics. 2009;105(12):124512.

[85]. Levy MY, Honsberg C. Solar cell with an intermediate band of finite width. Physical Review B. 2008;78(16):165122.

[86]. Hubbard S, Cress C, Bailey C, Raffaelle R, Bailey S, Wilt D. Effect of strain compensation on quantum dot enhanced GaAs solar cells. Applied Physics Letters. 2008;92(12):123512.

[87]. Oshima R, Takata A, Okada Y. Strain-compensated InAs/GaNAs quantum dots for use in high-efficiency solar cells. Applied Physics Letters. 2008;93(8):083111.

[88]. Kechiantz A, Sun K, Kechiyants H, Kocharyan L. Self-ordered Ge/Si quantum dot intermediate band photovoltaic solar cells. Int Sci J Alt Energ Ecol. 2005;12:85-7.

[89]. Laghumavarapu R, El-Emawy M, Nuntawong N, Moscho A, Lester L, Huffaker D. Improved device performance of In As⁄ Ga As quantum dot solar cells with GaP strain compensation layers. Applied Physics Letters. 2007;91(24):243115.

[90]. Popescu V, Bester G, Hanna MC, Norman AG, Zunger A. Theoretical and experimental examination of the intermediate-band concept for strain-balanced (In, Ga) As/Ga (As, P) quantum dot solar cells. Physical review B. 2008;78(20):205321.

[91]. Bailey CG, Forbes DV, Raffaelle RP, Hubbard SM. Near 1 V open circuit voltage InAs/GaAs quantum dot solar cells. Applied Physics Letters. 2011;98(16):163105.

[92]. Blokhin S, Sakharov A, Nadtochy A, Pauysov A, Maximov M, Ledentsov N, et al. AlGaAs/GaAs photovoltaic cells with an array of InGaAs QDs. Semiconductors. 2009;43(4):514-8.

[93]. Guimard D, Morihara R, Bordel D, Tanabe K, Wakayama Y, Nishioka M, et al. Fabrication of InAs/GaAs quantum dot solar cells with enhanced photocurrent and without degradation of open circuit voltage. Applied Physics Letters. 2010;96(20):203507.

[94]. Zhou D, Sharma G, Thomassen S, Reenaas T, Fimland B. Optimization towards high density quantum dots for intermediate band solar cells grown by molecular beam epitaxy. Applied Physics Letters. 2010;96(6):061913.

[95]. Walukiewicz W, Shan W, Yu K, Ager III J, Haller E, Miotkowski I, et al. Interaction of localized electronic states with the conduction band: Band anticrossing in II-VI semiconductor ternaries. Physical Review Letters. 2000;85(7):1552.

[96]. Wang W, Lin AS, Phillips JD. Intermediate-band photovoltaic solar cell based on ZnTe: O. Applied Physics Letters. 2009;95(1):011103.

[97]. Wang W, Lin AS, Phillips JD, Metzger WK. Generation and recombination rates at ZnTe: O intermediate band states. Applied Physics Letters. 2009;95(26):261107.

[98]. Antolín E, Martí A, Olea J, Pastor D, González-Díaz G, Mártil I, et al. Lifetime recovery in ultrahighly titanium-doped silicon for the implementation of an intermediate band material. Applied Physics Letters. 2009;94(4):042115.

[99]. Wahnón P, Tablero C. Ab initio electronic structure calculations for metallic intermediate band formation in photovoltaic materials. Physical Review B. 2002;65(16):165115.

[100]. Ling C, Zhou LQ, Banerjee D, Jia H. Band structures of ZnTe: O alloys with isolated oxygen and with clustered oxygen impurities. Journal of Alloys and Compounds. 2014;584:289-94.

[101]. Strandberg R. Evaluation of a selection of intermediate band materials based on their absorption coefficients. IEEE Journal of Photovoltaics. 2013;3(3):997-1003.

[102]. Aguilera I, Palacios P, Sánchez K, Wahnón P. Theoretical optoelectronic analysis of $MgIn_2S_4$ and $CdIn_2S_4$ thiospinels: effect of transition-metal substitution in intermediate-band formation. Physical Review B. 2010;81(7):075206.

[103]. Kong-Ping W, Shu-Lin G, Jian-Dong Y, Kun T, Shun-Ming Z, Meng-Ran Z, et al. Theoretical optoelectronic analysis of intermediate-band photovoltaic material based on ZnY1− xOx (Y= S, Se, Te) semiconductors by first-principles calculations. Chinese Physics B. 2013;22(10):107103.

[104]. Palacios P, Wahnón P, Pizzinato S, Conesa JC. Energetics of formation of $TiGa_3As_4$ and $TiGa_3P_4$ intermediate band materials. The Journal of chemical physics. 2006;124(1):014711.

[105]. Sánchez K, Aguilera I, Palacios P, Wahnón P. Assessment through first-principles calculations of an intermediate-band photovoltaic material based on Ti-implanted

silicon: Interstitial versus substitutional origin. Physical Review B. 2009;79(16):165203.

[106]. Unold T, Schock H-W. Nonconventional (non-silicon-based) photovoltaic materials. Annual Review of Materials Research. 2011;41:297-321.

[107]. Goetzberger A, Hebling C, Schock H-W. Photovoltaic materials, history, status and outlook. Materials Science and Engineering: R: Reports. 2003;40(1):1-46.

[108]. Bube RH. Materials for photovoltaics. Annual Review of Materials Science. 1990;20(1):19-50.

[109]. Birkmire RW, Eser E. Polycrystalline thin film solar cells: present status and future potential. Annual Review of Materials Science. 1997;27(1):625-53.

[110]. Mitchell KW. Status of new thin-film photovoltaic technologies. Annual Review of Materials Science. 1982;12(1):401-13.

[111]. Boer K, Rothwarf A. Materials for solar photovoltaic energy conversion. Annual Review of Materials Science. 1976;6(1):303-33.

[112]. Green MA, Emery K, Hishikawa Y, Warta W. Solar cell efficiency tables (version 36). Progress in photovoltaics: research and applications. 2010;18(5):346.

[113]. Merdes S, Mainz R, Klaer J, Meeder A, Rodriguez-Alvarez H, Schock H, et al. 12.6% efficient CdS/Cu (In, Ga)S_2-based solar cell with an open circuit voltage of 879 mV prepared by a rapid thermal process. Solar Energy Materials and Solar Cells. 2011;95(3):864-9.

[114]. Guillemoles JF, Rau U, Kronik L, Schock HW, Cahen D. Cu (In, Ga)Se_2 solar cells: device stability based on chemical flexibility. Advanced Materials. 1999;11(11):957-61.

[115]. Lide D. CRC Handbook of Chemistry and Physics. Section 14, Geophysics, Astronomy, and Acoustics; Abundance of Elements in the Earth's Crust and in the Sea. Boca Raton, Florida: CRC Press; 2005.

[116]. Fthenakis V, Fuhrmann M, Heiser J, Lanzirotti A, Fitts J, Wang W. Emissions and encapsulation of cadmium in CdTe PV modules during fires. Progress in Photovoltaics: Research and Applications. 2005;13(8):713-23.

Chapter 7

Publication I

Computational Modeling of Novel bulk materials for the Intermediate Band Solar cells

Murugesan Rasukkannu[1], Dhayalan Velauthapillai[1], Ponniah Vajeeston[2]

[1]*Western Norway University of Applied Sciences, Department of Computing, Mathematics and Physics, Inndalsveien 28, Box 5063, Bergen, Norway*

[2]*Center for Materials Science and Nanotechnology, Department of Chemistry, University of Oslo, Box 1033 Blindern N-0315, Oslo, Norway*

Published in

American chemical society (ACS) Omega

Vol. 2 (4) **2017**, Page 1454-1462

ACS OMEGA

Article

http://pubs.acs.org/journal/acsodf

Computational Modeling of Novel Bulk Materials for the Intermediate-Band Solar Cells

Murugesan Rasukkannu,*[,†] Dhayalan Velauthapillai,[†] and Ponniah Vajeeston[‡]

[†]Department of Computing, Mathematics and Physics, Western Norway University of Applied Sciences, Inndalsveien 28, 5063 Bergen, Norway

[‡]Department of Chemistry, Center for Materials Science and Nanotechnology, University of Oslo, P.O. Box 1033, Blindern, N-0315 Oslo, Norway

Supporting Information

ABSTRACT: Research communities have been studying materials with intermediate bands (IBs) in the middle of the band gap to produce efficient solar cells. Cells based on these materials could reach theoretical efficiencies up to 63.2%. In this comprehensive study, we investigate by means of accurate first-principle calculation the electronic band structure of 2100 novel compounds (bulk materials) to discover whether the IB is present in these materials. Our calculations are based on the density functional theory, using the generalized-gradient approximation for exchange and correlation terms and focusing on the band structure, the density of states, and the electron effective masses of the structures in the database. The IB structures are obtained by adding metallic or semimetallic atoms in the bulk material. By means of these calculations, we have clearly identified a number of compounds that may having high potential to be used as photovoltaic materials. We present here the numerical results for 17 novel IB materials, which could theoretically prove to be suitable for photovoltaic applications.

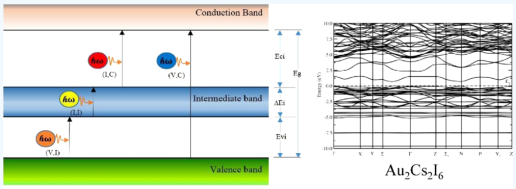

Research communities have been studying materials with intermediate bands in the middle of the bandgap to achieve efficient solar cells. Cells based on these materials could reach theoretical efficiencies up to 63.2%.

INTRODUCTION

Multi-band gap materials offer the possibility of increasing the efficiency of solar cells beyond the limit of traditional single-band gap solar-cell materials. Intermediate-band (IB) materials are characterized by the splitting of the main band gaps into two or more sub-band gaps by narrow IBs and have been the focus of recent studies.[1,2] In IB solar cells, an IB material is sandwiched between two ordinary p-type and n-type semiconductors and deed as discriminating contacts to the valence band (VB) and the conduction band (CB), respectively. In IB materials, an electron is promoted from the VB to the CB through the IB. Upon absorption of sub-band gap-energy photons, the electrons transit from VB to CB and later from IB to CB. It will add up to the transition of electrons from VB to CB through conventional VB-to-CB photon absorption.[1,2] By adopting a hypothesis similar to that of Shockley and Queisser,[3] it was shown in 1997[4] that balance-limiting efficiencies of 63.2% for IB solar cells and 41% for single-band gap solar cells can be achieved at a concentration of 46 050 suns at earth and sun temperatures of 300 and 6000 K, respectively.

The IB should be partially filled to permit the comparable rates for the low sub-band gap-energy photon absorption processes and should not overlap with either the VB or the CB to avoid fast transitions through thermalizations.[5] We can consider the IB solar cells as a combination of three cells. Cells representing VB-to-IB and IB-to-CB transitions can be regarded as two cells in series, and the VB-to-CB transition can represent a parallel cell. The cell will have a high tolerance to changes in the solar spectrum.[6]

In the mid-20th century, researchers[7−10] suggested the concept of creating intermediate levels in the middle of a forbidden band gap to increase the maximum photocurrent by doping the semiconductor with a large concentration of impurities. At an early stage, it was believed that these IBs would cause nonradiative recombination. It has been later shown that the nonradiative recombination can be suppressed by using a sufficiently high concentration of dopants.[10−13]

Two major approaches are considered in fabricating IB solar cells, namely, quantum-dot IBs (QDIBs) and bulk IB solar cells. By using quantum dots with different shapes and sizes, the IB levels can be tuned. The first QDIB was produced in 2004 on the basis of the InAs/GaAs QD material with an efficiency of 15.3%. Energy levels of the confined states in a quantum dot can be used as IB in QDIBs. However, there are many challenges with QDIBs as quantum dots are very small and do not absorb a significant amount of light. With an increasing number of QDs, the cell structure can be damaged, and strain will cause severe damages. At room temperature, the Shockley−Read−Hall recombination is a dominant mechanism that leads to low efficiency in QDIB solar cells due to deeper impurities.

Received: December 21, 2016
Accepted: March 31, 2017
Published: April 13, 2017

DOI: 10.1021/acsomega.6b00534
ACS Omega 2017, 2, 1454−1462

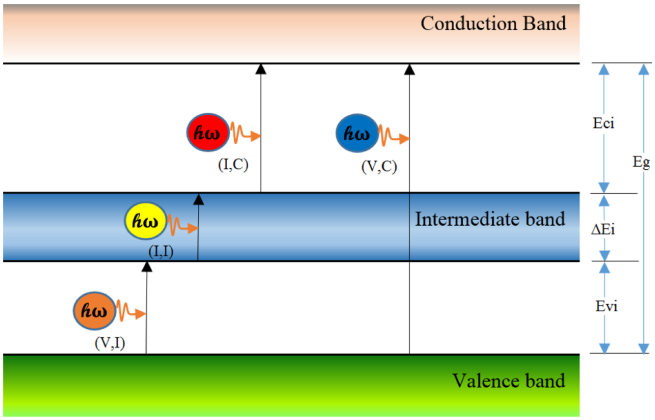

Figure 1. Band diagram of bulk IB solar cell; E_{vi}—energy gap between the top of the VB and the bottom of an IB, E_{ci}—energy gap between the top of the IB and the bottom of the CB, ΔE_i—width of the IB, E_g—total band gap between the top of the VB and the bottom of the CB. The electronic transitions (V, I), (I, I), (I, C), and (V, C) are also explained.

Table 1. Calculated Selected Narrow-Band Gap Semiconductors with IBs and Band Gap Type

serial no.	chemical formula	Pearson symbol	space group number	band gap (E_{vi})	band gap (E_{ci})	width of IB (ΔE_i)	total band gap (E_g)	band gap type
1.	K_6C_{60}	cI132	204	0.61	0.28	0.39	1.28	ID
2.	$Au_2Cs_2I_6$	tI20	139	0.64	1.01	0.7	2.35	ID
3.	Ag_2GeBaS_4	tI16	121	0.90	0.35	1.16	2.41	ID

Table 2. Wide-Band Gap 1 Semiconductors with IB Ranging from 2.62 to 3.15 eV

serial no.	chemical formula	Pearson symbol	space group number	band gap (E_{vi})	band gap (E_{ci})	width of IB (ΔE_i)	total band gap (E_g)	band gap type
1.	$CuAgPO_4$	oP56	61	1.27	0.61	0.74	2.62	DB
2.	Ag_2ZnSnS_4	tI16	121	0.47	0.57	1.66	2.70	DB
3.	$Au_2Cs_2Br_6$	tI20	139	0.67	1.23	0.81	2.71	DB
4.	Ag_3AsS_4	oP16	31	0.73	1.04	1.00	2.77	DB
5.	Ag_2KSbS_4	tI16	121	0.81	1.08	0.94	2.93	ID
6.	Na_3Se_4Sb	cI16	217	1.02	1.24	0.71	2.97	DB
7.	AgK_2SbS_4	oP32	118	1.52	1.03	0.47	2.97	DB
8.	$AsRb_3Se_4$	oP32	62	1.32	0.98	0.97	3.15	DB

Several research groups have produced QDIB solar cells,[14−22] and efficiencies over 18% have been reported by Blokhin et al.[20]

The second type of IB solar cells is based on bulk materials. The IB was detected through photoreflectance measurements in some bulk materials, and this formation was attributed to band anticrossing and heavily mismatched alloys.[23] The first of these bulk materials, ZnMnTeO, was developed by Walukiewicz and co-workers.[23] Later, numerous quantum-accurate calculations have been performed on VInS bulk material, characterized by an IB containing Fermi levels. Phillips and coworkers developed bulk IB solar cells using ZnTe doped with an oxygen atom and obtained higher efficiencies and short-circuit current than QDIB solar cells.[24,25] The band gap properties of bulk materials are widely studied, and the technologies are well verified by researchers.[5,26−33] However, the search for intermediate-band gap materials continues, to model high-efficiency IB solar cells. Figure 1 shows the band diagram of an IB solar cell with E_g, the total band gap between the top of the VB and the bottom of the CB. In the figure, E_{vi} is the energy gap between the top of the VB to the bottom of an IB, E_{ci} is the energy gap between the top of the IB to the bottom of the CB, and ΔE_i is the width of the IB. Furthermore, the electronic transitions of (V, I), (I, I), (I, C), and (V, C) are schematically depicted in the figure.

In the present work, we study 2100 structures with the aim of identifying ideal candidates for solar-cell materials. We employ density functional theory (DFT) calculations to verify the presence of an IB, isolated in the band gap of the semiconductor compounds of bulk material compounds with different substitutional impurities forming ternary alloys. The calculated band gap values are used to identify the most suitable compounds for solar-cell applications. We also present density of states (DOS) and effective mass calculations for the selected IB materials.

RESULTS AND DISCUSSION

The main focus of the present work is to find the potential IB materials from the selected 2100 compounds. Because of the very high computational cost, we mainly focused on the electronic structure, the DOS and effective mass calculations. The hybrid electronic structure and optical properties of the selected IB compounds are under investigation, and the results will be published in a forthcoming work. We employ the DFT method to elucidate the band structure arrangement of 2100

DOI: 10.1021/acsomega.6b00534
ACS Omega 2017, 2, 1454−1462

bulk materials, vital for the interaction of IB and could be potent solar cells with sufficient band gap. The DFT approaches to reveal the significant and computational features of the bulk materials and these features can be used as virtual screenings of band structures of the 2100 compounds to identify the novel IB compounds. From the first screening, we observed 312 compounds having an IB with the maximum of the VB at the Fermi level. Among these, 282 compounds were selected for further analysis and 30 compounds were found as heavy elements. After carrying out a detailed analysis, we found out that only 17 compounds among the starting 282 would be acceptable semiconductor materials for photovoltaic applications. The rest were found to be perfect insulators, with band gap values larger than 3.51 eV.[34] The electronic properties of these 17 compounds are presented in Tables 1−3. It is well known that the band gap (E_g) values of solids obtained from usual DFT calculations are systematically underestimated due to discontinuity in the exchange-correlation potential. Thus, the calculated E_g values are typically 30−50% smaller than those measured experimentally.[35] It is recognized that the theoretically calculated E_g for semiconductors and insulators are strongly dependent on the approximations used, particularly on the exchange and correlation terms of the potential. In the present work, because of the large number compounds involved in the screening process, we have used only generalized-gradient approximation. However, the overall structure is not going to change except the band gap value irrespective of the approximation.

Table 3. Calculated Effective Masses of Narrow-Band Gap Compounds; Light Holes (m^*_{lh}), Heavy Holes (m^*_{hh}), and Electrons (m^*_e)

serial no.	plane directions	compound	$m^*_{lh}\cdot m_e$	$m^*_{hh}\cdot m_e$	$m^*_e\cdot m_e$
1.	110	K_6C_{60}	0.092	0.164	0.216
2.	110	$Au_2Cs_2I_6$	0.096	0.265	0.095
3.	110	Ag_2GeBaS_4	0.059	0.114	0.021

We have chosen to divide the 17 compounds with IBs into three groups depending on the magnitude of their band gap values. The first group of three compounds is named as narrow-band gap semiconductors, which is characterized by band gaps varying from 1.2 to 2.5 eV. The second group of eight compounds is named wide-band gap 1 semiconductors, which includes materials with band gaps varying from 2.6 to 3.15 eV. Finally, the third group is named as wide-band gap 2 semiconductors. In this case, the band gap values vary from 3.15 to 3.5 eV. The band structures of these compounds are presented in Figures 2a−c, 3a−d, 4a−d, and 5a−f, and we calculate the total band gaps, band gaps E_{vi}, E_{ci}, and the widths of the IB (ΔE_i) bands for all of the compounds. The electronic structure properties of these compounds are presented in Tables 1, 2, and S1.

As presented in Table 1, narrow-band gap semiconductors K_6C_{60} (alkali fullerides), $Au_2Cs_2I_6$, and Ag_2GeBaS_4 had total indirect band gaps of 1.28, 2.35, and 2.41 eV, respectively.

From Figure 2a, the calculated values for K_6C_{60} are: The total indirect band gap is 1.28 eV, band gaps E_{vi} and E_{ci} are 0.61 and 0.28 eV, respectively, and the width of the IB is 0.39 eV. The band gap of 1.28 eV makes an optimal compound for the PV applications as their light responses are in the infrared region. Also, the IB will help the material to absorb additional photons with lower energy. It should be noted that K_6C_{60} is already known as a semiconductor and the nature of the band structure is not well explained about the IB. However, they explained that the electronic structure of crystalline K_6C_{60} is indirect band gap of 0.48 eV.[36] The DOS around the VB maximum is very similar to that of the isolated C_{60} molecule, and the K atoms are almost completely ionized.[36]

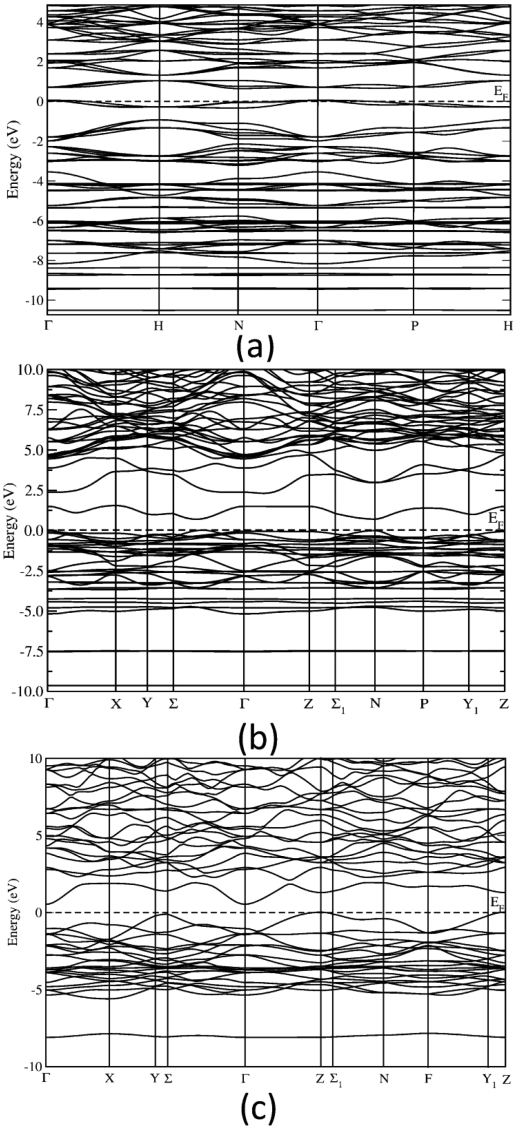

Figure 2. Calculated electronic band structures of (a) K_6C_{60}, (b) $Au_2Cs_2I_6$, (c) and Ag_2GeBaS_4. The Fermi level is set to zero.

Similarly, from Figure 2b, the calculated values for $Au_2Cs_2I_6$ are as follows: The total indirect band gap is 2.35 eV, band gaps E_{vi} and E_{ci} are 0.64 and 1.01 eV, respectively, and the width of the IB, ΔE_i is 0.70 eV. The band gap of 2.35 eV for $Au_2Cs_2I_6$ shows that the material has its response to light in the visible

DOI: 10.1021/acsomega.6b00534
ACS Omega 2017, 2, 1454−1462

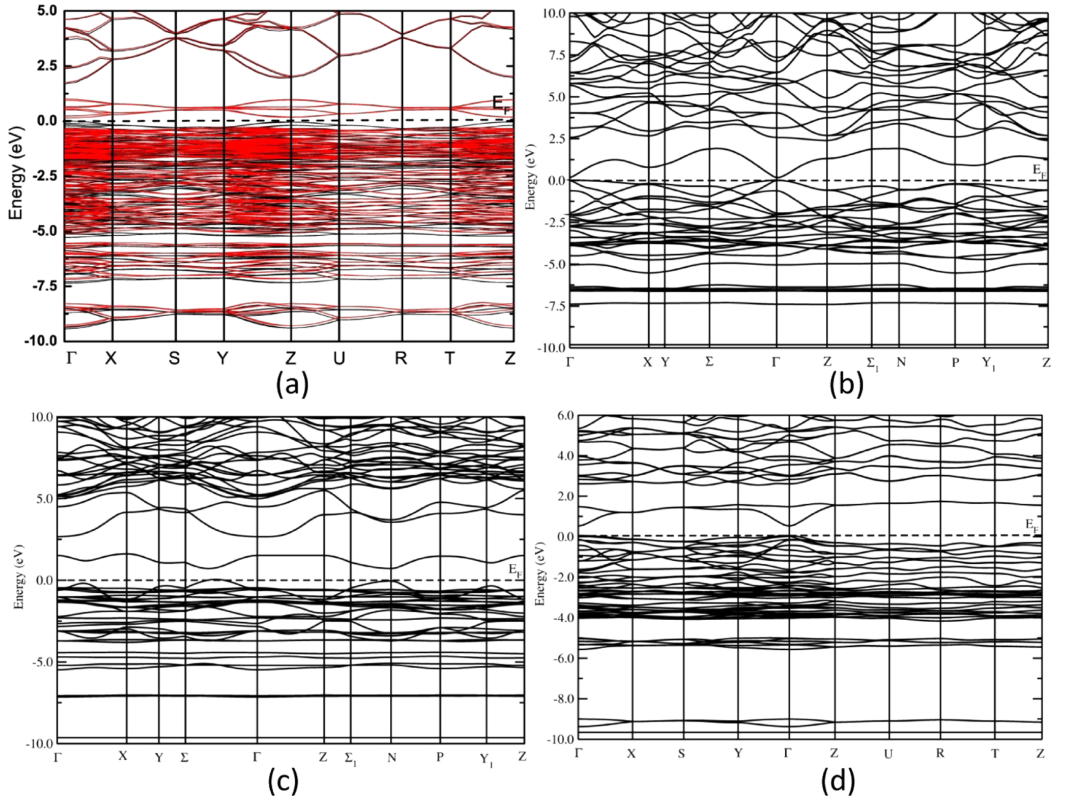

Figure 3. Calculated electronic band structures of (a) $CuAgPO_4$ (up and down spin bands; up—black, down—red), (b) Ag_2ZnSnS_4, (c) $Au_2Cs_2Br_6$, and (d) Ag_3AsS_4. The Fermi level is set to zero.

region. For $Au_2Cs_2I_6$, the IB region has the optimal thickness to balance the absorption rate and recombination rate.[37] In Figure 2b, $Au_2Cs_2I_6$ has a broad band dispersion of IB, enough to produce an optical depth for subgap light, ensuring the compound to absorb subgap light so that it can be considered as a potential PV material.[37]

From Figure 2c, the calculated values for Ag_2GeBaS_4 are: The total indirect band gap is 2.41 eV, band gaps E_{vi} and E_{ci} are 0.90 and 0.35 eV, respectively, and the width of the IB is 1.16 eV. The band gap of 2.35 eV for Ag_2GeBaS_4 shows that the material has its response to light in the visible region. Here, we observe that the width of the IB, ΔE_i, in Ag_2GeBaS_4 is much higher than E_{ci} and E_{vi}. Because of the broadness of the IB, photons can also be absorbed by the electrons from lower-energy states of the IB to excite to higher-energy states of IB. When the IB broadens, the absorption of photons for the transition of electrons from the VB to lower-energy states of IB as well as from the higher-energy states of IB to CB will be reduced. These effects will lead to lower efficiencies of the solar cell based on Ag_2GeBaS_4. It has been shown that the efficiency limit for an IB solar cell is reduced from higher to lower efficiencies if the width is infinitesimally significant.[38] It is important to note that all of these three materials, K_6C_{60}, $Au_2Cs_2I_6$, and Ag_2GeBaS_4, present indirect band gaps.

As presented in Table 2, the wide-band gap semiconductors $CuAgPO_4$, Ag_2ZnSnS_4, $Au_2Cs_2Br_6$, Ag_3AsS_4, Ag_2KSbS_4, Na_3Se_4Sb, AgK_2SbS_4, and $AsRb_3Se_4$ had the total band gaps of 2.62, 2.70, 2.71, 2.77, 2.93, 2.97, 2.97, and 3.15 eV, respectively. Figures 3a–d and 4a–d show the calculated band structures of $CuAgPO_4$, Ag_2ZnSnS_4, $Au_2Cs_2Br_6$, Ag_3AsS_4, Ag_2KSbS_4, Na_3Se_4Sb, AgK_2SbS_4, and $AsRb_3Se_4$ with IB, respectively. The calculated values of E_{vi}, E_{ci}, and ΔE_i, and the total band gaps are presented in Table 2. The band gap type of the above eight compounds is direct band gap except for Ag_2KSbS_4 (indirect band gap). From Figure 2c, the calculated values for Ag_2ZnSnS_4 are: The total direct band gap is 2.70 eV, band gaps E_{vi} and E_{ci} are 0.47 and 0.57 eV, respectively, and the width of the IB is 1.66 eV. The band gap of 2.70 eV for Ag_2ZnSnS_4 shows that the material has its response to light in the visible region. Here, we observe that the width of the IB, ΔE_i, in Ag_2ZnSnS_4 is much higher than E_{ci} and E_{vi}. The increase in the IB width leads to a decrease in efficiency; however, it is still significantly higher than that of a single-band gap solar cell.[39] The band gaps associated with optimum efficiencies are constant for all IB solar cells when the IB width exceeds 2 eV.[39] Because of the display of the small amount of data, we added the remaining six compounds in the Supporting Information.

In general, the electrochemical potentials of the electrons in the different bands are close to the edges of the bands. The

DOI: 10.1021/acsomega.6b00534
ACS Omega 2017, 2, 1454−1462

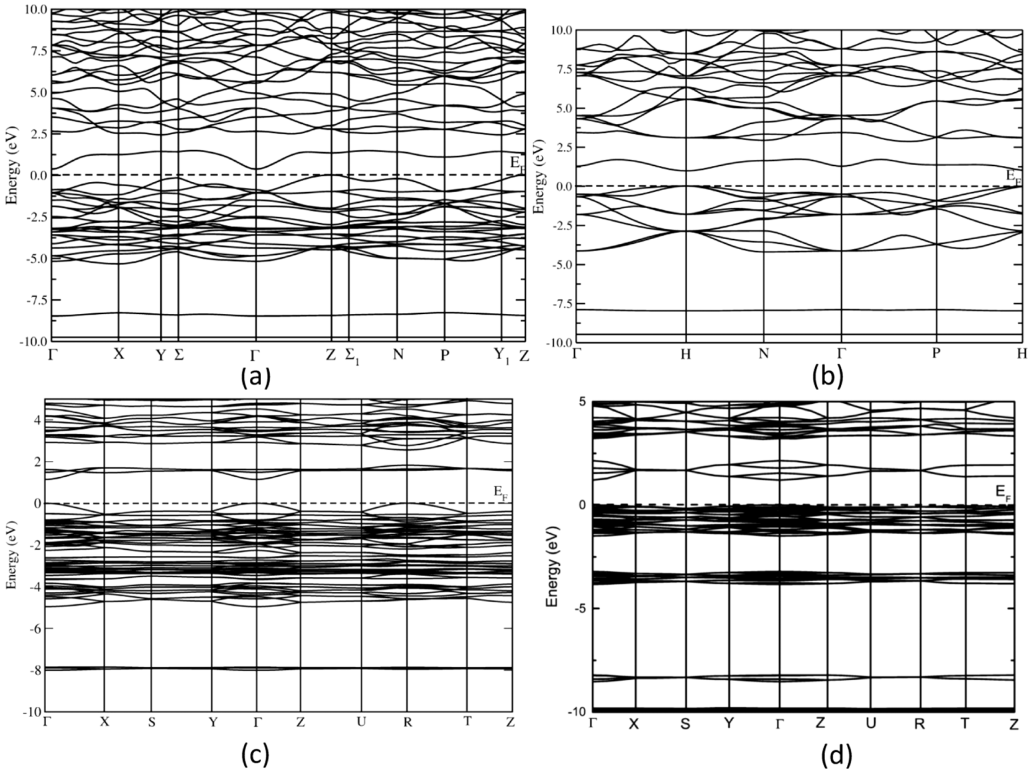

Figure 4. Calculated electronic band structures of (a) Ag_2KSbS_4, (b) Na_3Se_4Sb, (c) AgK_2SbS_4, and (d) $AsRb_3Se_4$. The Fermi level is set to zero.

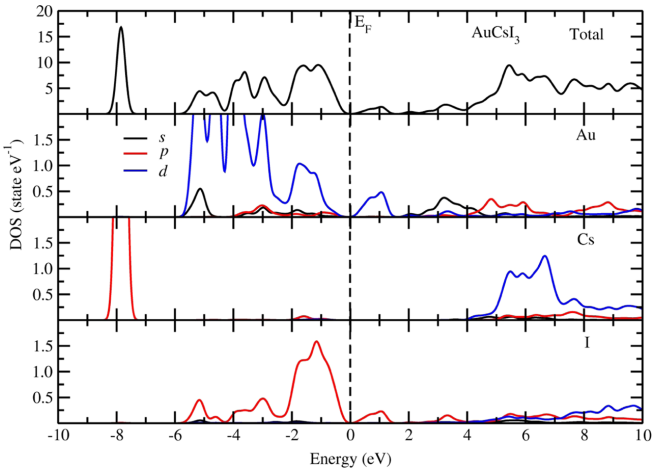

Figure 5. Total and site-projected DOS of $Au_2Cs_2I_6$. The Fermi level is set to zero and marked by a vertical dotted line.

open-circuit voltage of any solar cell is the difference between the CB minimum at the electrode in contact with the n-type side and the VB maximum at the electrode in contact with the p-type side. Thus, the maximum photovoltage of IB solar cells on the materials presented in Tables 1 and S1 is limited to 2.41 and 3.51 eV, respectively. Ag_2GeBaS_4 is still capable of absorbing energy photons above 0.28 eV in Table 1 and Ag_6SiSO_8 of 0.47 eV in Table 2. IB solar cells can deliver a maximum photovoltage by absorbing two sub-band gap

DOI: 10.1021/acsomega.6b00534
ACS Omega 2017, 2, 1454−1462

photons to produce one high-energy electron; the laws of thermodynamics would be violated if this were not the case.[1]

All of the 17 semiconductor compounds presented in this work have properties that make them suitable for PV applications; we show here the DOS analysis for three compounds, namely, $Au_2Cs_2I_6$, Ag_2GeBaS_4, and Ag_2ZnSnS_4. The band gaps of 1.28 and 2.41 eV, respectively, make $Au_2Cs_2I_6$ and Ag_2GeBaS_4 optimal PV materials. Solar cells based on Ag_2ZnSnS_4 materials are interesting as a high efficiency gain for these types of cells has been recently observed.[40] There are also reports on the possibilities to integrate Ag_2ZnSnS_4 in the Cu-based solar cells as an additional absorption layer.[40] The total DOS of $Au_2Cs_2I_6$ in Figure 5 shows that the IB is formed in the energy region between 0.64 and 1.34 eV. The IB composed of I 2p are described by the projected density of states (PDOS), as shown in Figure 5. Figure 6 shows that the IB is formed in the

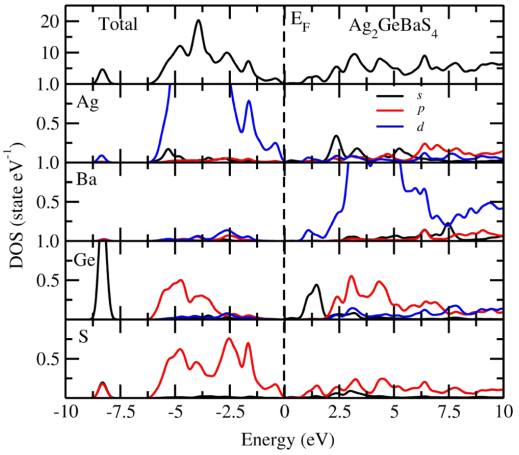

Figure 6. Total and site PDOS of Ag_2GeBaS_4. The Fermi level is set to zero and marked by a vertical dotted line.

energy region between 0.90 and 2.06 eV of the total DOS of Ag_2GeBaS_4. We have also plotted the PDOS at the IB mainly composed of the S 2p band and the Ge 4s band as well as the smaller mixing of the Ba 4d band. For Ag_2ZnSnS_4, the IB is formed in the energy region between 0.47 and 2.13 eV, and the electron density, as shown in Figure 7 better describes the states. The PDOS of Ag_2ZnSnS_4 at the IB mainly composed of the Sn 5s band and the S 2p band is shown in Figure 7. The Ag_2ZnSnS_4 has an energy gap of 2.62 eV. We found the excellent IB peaks between CB and VB in the three materials, namely, $Au_2Cs_2I_6$, Ag_2GeBaS_4, and Ag_2ZnSnS_4. We observed that the p and s states play a vital role in the band structure for the applicability of semiconductor for PV applications.

In Figures 5−7, broadening of IB indicates a highly parabolic dispersion relationship that induces lower values for the DOS.[41] From Tables 3 and 4, the electron effective masses of $Au_2Cs_2I_6$, Ag_2GeBaS_4, and Ag_2ZnSnS_4 are $0.095m_e$, $0.021m_e$, and $0.025m_e$, respectively. Lower values for the electron effective mass are as expected because the effective mass is directly related to the values of DOS. In addition, the IB region has the optimal thickness to balance the absorption rate and the recombination rate.[37] We may expect the effective IBSC to have IB thickness enough to ensure these materials to absorb sufficient subgap

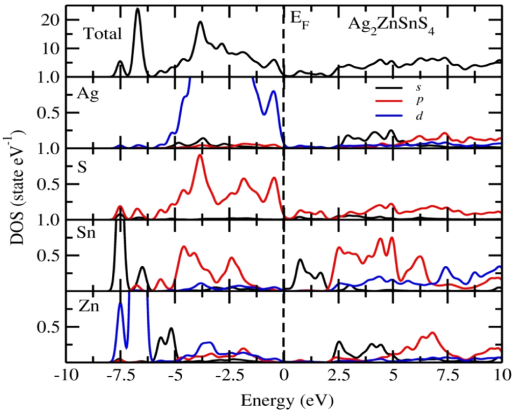

Figure 7. Total and site PDOS of Ag_2ZnSnS_4. The Fermi level is set to zero and marked by a vertical dotted line.

Table 4. Effective Mass of Wide-Band Gap IB Compounds

serial no.	plane directions	compound	$m^*_{lh}\cdot m_e$	$m^*_{hh}\cdot m_e$	$m^*_e\cdot m_e$
1.	100	$CuAgPO_4$	3.875	4.969	14.229
2.	110	Ag_2ZnSnS_4	0.033	0.237	0.025
3.	110	$Au_2Cs_2Br_6$	0.870	1.810	0.806
4.	100	Ag_3AsS_4	0.200	0.234	0.012
5.	110	Ag_2KSbS_4	0.125	0.526	0.034
6.	110	Na_3Se_4Sb	0.377	0.381	0.085
7.	100	AgK_2SbS_4	1.524	12.025	1.007
8.	100	$AsRb_3Se_4$	6.213	84.330	2.595
9.	100	$AsCs_3Se_4$	8.213	24.794	3.561
10.	110	Al_2HgSe_4	0.070	0.255	0.021
11.	110	$PdPbF_4$	0.391	0.592	0.094
12.	100	$C_2Te_2F_4$	3.293	5.165	7.659
13.	100	$AlMoVO_7$	1.680	2.756	1.959
14.	110	Ag_6SiSO_8	0.145	2.634	0.053

light. We conclude that the conversion efficiency of bulk IBSC strongly depends not only on the band gap but also on the position and thickness of IB and DOS.[37,41]

EFFECTIVE MASS CALCULATION

The calculation of the effective mass is important for a detailed study of energy levels in solar devices. The conductivity effective masses of electrons and holes affect the mobility, electrical resistivity, and free-carrier optical response of photovoltaic applications.[42] To investigate the electron/hole conduction properties of the identified IB materials, we have computed the electron/hole effective mass at the VB/CB. For an excellent IB, a low effective mass corresponds to a high mobility of the electrons/holes at the VB/CB and consequently high conductivity. For the EM calculation, we have employed the effective mass calculator (EMC).[43] EMC implements the calculation of the effective masses at the bands extreme using the finite difference method (FDM) (not the band-fitting method). The effective mass (m^*) of charge carriers is defined as[43]

$$\left(\frac{1}{m^*}\right)_{ij} = \frac{1}{\hbar^2}\frac{\partial^2 E_n(\vec{k})}{\partial k_i k_j}, \quad i, j = x, y, z \tag{1}$$

DOI: 10.1021/acsomega.6b00534
ACS Omega 2017, 2, 1454−1462

where x, y, and z are the directions in the reciprocal Cartesian space ($2\pi/A$), $E_n(k)$ is the dispersion relation for the nth electronic band, and indices i and j denote reciprocal components. The explicit form of the symmetric tensor in the right-hand side of eq 1 is[43]

$$\frac{d^2E}{dk^2} = \begin{pmatrix} \frac{d^2E}{dk_x^2} & \frac{d^2E}{dk_x\,dk_y} & \frac{d^2E}{dk_x\,dk_z} \\ \frac{d^2E}{dk_x\,dk_y} & \frac{d^2E}{dk_y^2} & \frac{d^2E}{dk_y\,dk_z} \\ \frac{d^2E}{dk_x\,dk_z} & \frac{d^2E}{dk_y\,dk_z} & \frac{d^2E}{dk_z^2} \end{pmatrix} \quad (2)$$

The effective mass components are the inverse of the eigenvalues of eq 2, and the principal directions correspond to the eigenvectors.[43]

To better understand the effective mass of semiconductors, it is not possible to fit the band to the quadratic polynomial. In this case, the results from the parabolic fitting can be reproduced with the FDM.[43] The FDM employed to solve the effective mass approximation equations because the spurious solutions can be included in the formalism, and the FDM can be solved by the hard equation having a high degree of polynomial.[44] This approach is quite reliable, and it was successfully applied for several classes of materials in the literature.[43] We present the effective masses of 14 compounds in Tables 3 and 4. The effective mass of an electron was computed from the minimum of the CB; the effective mass of the heavy hole was computed from the maximum of the first VB curvature, whereas the second VB curvature was used for the light hole. In the case of materials presented in Tables 3 and 4, the PBE functional predicts the effective masses of the light hole, heavy hole, and electron, which are parabolic-fitted values with a step size of 0.05 (1/bohr). The three narrow-band gap compounds, K_6C_{60}, $Au_2Cs_2I_6$, and Ag_2GeBaS_4, have low effective masses, as presented in Table 3.

The thirteen wide-band gap compounds in Table 4 have effective masses of electron lower than those of light holes and heavy holes except for $CuAgPO_4$. The effective masses of electron of photovoltaic materials silicon (Si), germanium (Ge), and gallium arsenide (GaAs) are $0.26m_e$, $0.067m_e$, and $0.12m_e$, respectively.[45,46] The above three photovoltaic materials are single-band gap materials. It is well known that the band gaps of Si, Ge, and GaAs are 1.12, 0.66, and 1.424 eV, respectively. The maximum energy conversion of silicon and GaAs solar cells can reach 30% efficiency.[48] We can use germanium as the doping material in silicon solar cells because of its low band gap. We noticed that the effective masses of the electron for the silicon and GaAs are low.[45] From our results, we observed that the effective masses of electron for K_6C_{60}, $Au_2Cs_2I_6$, and Ag_2GeBaS_4 are $0.216m_e$, $0.095m_e$, and $0.021m_e$, respectively.

From Table 4, we noted that the effective masses of electron for Ag_2ZnSnS_4, $Au_2Cs_2Br_6$, Ag_3AsS_4, Ag_2KSbS_4, Na_3Se_4Sb, Al_2HgSe_4, $PdPbF_4$, Ag_6SiSO_8 are $0.025m_e$, $0.806m_e$, $0.012m_e$, $0.034m_e$, $0.085m_e$, $0.021m_e$, $0.094m_e$, and $0.053m_e$, respectively. Hence, the effective masses of electron of our narrow-band gap and wide-band gap materials are approximately equal to those of the photovoltaic materials. From Table 4, the effective mass of an electron is $0.025m_e$ for Ag_2ZnSnS_4 in [110] plane direction. We observed from Jing et al. that the effective mass of an electron is $0.16m_e$ for Ag_2ZnSnS_4 in [100] plane direction.[42] Hence, we found a lower effective mass in [110] direction than in [100] direction. These effective masses are better described by the band structures of the most curved parabolic band, as shown in Figures 3−5. Because of the effective masses for the presented materials, in this article, the electron mobility from VB to CB will be higher and the recombination effect will be lower.

CONCLUSIONS

We have carried out a comprehensive study of the electronic band structures of 2100 new bulk compounds using first-principle calculations with the DFT. Among these compounds, we have found that only 17 compounds have IBs. These compounds could be potentially used as photovoltaic materials based on the detailed studies of band structure, the DOS and effective mass calculations. Our effective mass calculations show that these compounds have high electron/hole conduction properties, which make them suitable for PV applications. Although we have studied 2100 new compounds from the ICSD database, our study clearly demonstrates the possibility of having more IB materials from the list of currently known compounds from the database. Thus, we are in the process of investigating more IB-compounds and results of the detailed analysis will be published in a forthcoming article.

COMPUTATIONAL DETAILS

Total energies have been calculated by the projected augmented plane-wave (PAW) implementation of the Vienna ab initio simulation package.[47] Ground-state geometries were determined by minimizing stresses and the Hellman−Feynman forces using the conjugate-gradient algorithm with a force convergence threshold if 10^{-3} eV Å^{-1}. Brillouin-zone integration was performed using the Monkhorst−Pack k-meshes with a Gaussian broadening of 0.1 eV. A 600 eV kinetic energy cutoff was used for the plane-wave expansion. All of these calculations usually set to use approximately the same density of k-points in the reciprocal space for all structures. Because a large variety of structures was considered in this study, both metallic and insulating, we ensured that the k-points mesh was dense enough to determine the total energy with meV/atom accuracy. All structures containing transition elements are treated using the spin-polarized approach. In some cases, the starting magnetization vanished as self-consistency was reached. For all of these computations, the starting structures were directly taken from the ICSD database and input parameters, and file generation was done automatically by locally developed code "Tool". For the calculation of band structure, the k-point files were generated again with the help of locally developed code "KPATH". The information about the high symmetric points of the k-vector in the Brillouin zone was taken from the Bilbao Crystallographic Server.[48−50] All of the calculated electronic structures of the studied systems are documented in the DFTBD database. For the transition metals, we have used exchange-correlation functional with the Hubbard parameter correction (GGA+U), following the rotationally invariant form. The full details about the computed U and J values are presented in the DFTBD database website.[51−54]

DOI: 10.1021/acsomega.6b00534
ACS Omega 2017, 2, 1454−1462

■ ASSOCIATED CONTENT

Supporting Information

The Supporting Information is available free of charge on the ACS Publications website at DOI: 10.1021/acsomega.6b00534.

Tables, list of computed compounds and figures (PDF)

■ AUTHOR INFORMATION

Corresponding Author

*E-mail: rmu@hvl.no.

ORCID

Murugesan Rasukkannu: 0000-0002-2167-3242

Notes

The authors declare no competing financial interest.

■ ACKNOWLEDGMENTS

The authors gratefully acknowledge the Bergen University College for financially supporting M.R. P.V. and D.V. acknowledge the NOTUR computing facilities of project. numbers NN2867K and NN2875K, which have been used to conduct the calculations presented in this article, and further acknowledge Dr.Vishnu for fruitful discussions.

■ REFERENCES

(1) Luque, A.; Marti, A.; Stanley, C. Understanding Intermediate-Band Solar Cells. *Nat. Photonics* **2012**, *6*, 146−152.

(2) Luque, A.; Marti, A. A metallic intermediate band high efficiency solar cell. *Prog. Photovoltaics* **2001**, *9*, 73−86.

(3) Shockley, W.; Queisser, H. J. Detailed balance limit of efficiency of p-n junction solar cells. *J. Appl. Phys.* **1961**, *32*, 510−519.

(4) Luque, A.; Martí, A. Increasing the efficiency of ideal solar cells by photon induced transitions at intermediate levels. *Phys. Rev. Lett.* **1997**, *78*, 5014.

(5) Palacios, P.; Aguilera, I.; Sánchez, K.; Conesa, J.; Wahnón, P. Transition-metal-substituted indium thiospinels as novel intermediate-band materials: prediction and understanding of their electronic properties. *Phys. Rev. Lett.* **2008**, *101*, No. 046403.

(6) Green, M. A. Multiple band and impurity photovoltaic solar cells: general theory and comparison to tandem cells. *Prog. Photovoltaics* **2001**, *9*, 137−144.

(7) Shockley, W.; Read, W., Jr. Statistics of the recombinations of holes and electrons. *Phys. Rev.* **1952**, *87*, 835−842.

(8) Hall, R. N. Electron-hole recombination in germanium. *Phys. Rev.* **1952**, *87*, 387.

(9) Lang, D.; Henry, C. Nonradiative recombination at deep levels in GaAs and GaP by Lattice-Relaxation Multiphonon Emission. *Phys. Rev. Lett.* **1975**, *35*, 1525.

(10) Wolf, M. Limitations and possibilities for improvement of photovoltaic solar energy converters: part I: considerations for earth's surface operation. *Proc. IRE* **1960**, *48*, 1246−1263.

(11) Ekins-Daukes, N.; Honsberg, C.; Yamaguchi, M. In *Signature of Intermediate Band Materials from Luminescence Measurements*, Proceedings of the 31st IEEE Photovoltaic Specialists Conference, 2005; IEEE, 2005; pp 49−54.

(12) Strandberg, R.; Reenaas, T. W. Photofilling of intermediate bands. *J. Appl. Phys.* **2009**, *105*, No. 124512.

(13) Levy, M. Y.; Honsberg, C. Solar cell with an intermediate band of finite width. *Phys. Rev. B* **2008**, *78*, No. 165122.

(14) Hubbard, S.; Cress, C.; Bailey, C.; Raffaelle, R.; Bailey, S.; Wilt, D. Effect of strain compensation on quantum dot enhanced GaAs solar cells. *Appl. Phys. Lett.* **2008**, *92*, No. 123512.

(15) Oshima, R.; Takata, A.; Okada, Y. Strain-compensated InAs/GaNAs quantum dots for use in high-efficiency solar cells. *Appl. Phys. Lett.* **2008**, *93*, No. 083111.

(16) Kechiantz, A.; Sun, K.; Kechiyants, H.; Kocharyan, L. Self-ordered Ge/Si quantum dot intermediate band photovoltaic solar cells. *ISJAEE* **2005**, *12*, 85−87.

(17) Laghumavarapu, R.; El-Emawy, M.; Nuntawong, N.; Moscho, A.; Lester, L.; Huffaker, D. Improved device performance of InAs/GaAs quantum dot solar cells with GaP strain compensation layers. *Appl. Phys. Lett.* **2007**, *91*, 243115.

(18) Popescu, V.; Bester, G.; Hanna, M. C.; Norman, A. G.; Zunger, A. Theoretical and experimental examination of the intermediate-band concept for strain-balanced (In, Ga) As/Ga (As, P) quantum dot solar cells. *Phys. Rev. B* **2008**, *78*, No. 205321.

(19) Bailey, C. G.; Forbes, D. V.; Raffaelle, R. P.; Hubbard, S. M. Near 1 V open circuit voltage InAs/GaAs quantum dot solar cells. *Appl. Phys. Lett.* **2011**, *98*, No. 163105.

(20) Blokhin, S.; Sakharov, A.; Nadtochy, A.; Pauysov, A.; Maximov, M.; Ledentsov, N.; Kovsh, A.; Mikhrin, S.; Lantratov, V.; Mintairov, S.; et al. AlGaAs/GaAs photovoltaic cells with an array of InGaAs QDs. *Semiconductors* **2009**, *43*, 514−518.

(21) Guimard, D.; Morihara, R.; Bordel, D.; Tanabe, K.; Wakayama, Y.; Nishioka, M.; Arakawa, Y. Fabrication of InAs/GaAs quantum dot solar cells with enhanced photocurrent and without degradation of open circuit voltage. *Appl. Phys. Lett.* **2010**, *96*, No. 203507.

(22) Zhou, D.; Sharma, G.; Thomassen, S.; Reenaas, T.; Fimland, B. Optimization towards high density quantum dots for intermediate band solar cells grown by molecular beam epitaxy. *Appl. Phys. Lett.* **2010**, *96*, No. 061913.

(23) Walukiewicz, W.; Shan, W.; Yu, K.; Ager, J., III; Haller, E.; Miotkowski, I.; Seong, M.; Alawadhi, H.; Ramdas, A. Interaction of localized electronic states with the conduction band: Band anticrossing in II−VI semiconductor ternaries. *Phys. Rev. Lett.* **2000**, *85*, 1552.

(24) Wang, W.; Lin, A. S.; Phillips, J. D. Intermediate-band photovoltaic solar cell based on ZnTe: O. *Appl. Phys. Lett.* **2009**, *95*, No. 011103.

(25) Wang, W.; Lin, A. S.; Phillips, J. D.; Metzger, W. K. Generation and recombination rates at ZnTe: O intermediate band states. *Appl. Phys. Lett.* **2009**, *95*, No. 261107.

(26) Antolín, E.; Martí, A.; Olea, J.; Pastor, D.; González-Díaz, G.; Mártil, I.; Luque, A. Lifetime recovery in ultrahighly titanium-doped silicon for the implementation of an intermediate band material. *Appl. Phys. Lett.* **2009**, *94*, No. 042115.

(27) Wahnón, P.; Tablero, C. Ab initio electronic structure calculations for metallic intermediate band formation in photovoltaic materials. *Phys. Rev. B* **2002**, *65*, No. 165115.

(28) Ling, C.; Zhou, L. Q.; Banerjee, D.; Jia, H. Band structures of ZnTe: O alloys with isolated oxygen and with clustered oxygen impurities. *J. Alloys Compd.* **2014**, *584*, 289−294.

(29) Strandberg, R. Evaluation of a selection of intermediate band materials based on their absorption coefficients. *IEEE J. Photovoltaics* **2013**, *3*, 997−1003.

(30) Aguilera, I.; Palacios, P.; Sánchez, K.; Wahnón, P. Theoretical optoelectronic analysis of $MgIn_2S_4$ and $CdIn_2S_4$ thiospinels: effect of transition-metal substitution in intermediate-band formation. *Phys. Rev. B* **2010**, *81*, No. 075206.

(31) Kong-Ping, W.; Shu-Lin, G.; Jian-Dong, Y.; Kun, T.; Shun-Ming, Z.; Meng-Ran, Z.; You-Rui, H.; Rong, Z.; You-Dou, Z. Theoretical optoelectronic analysis of intermediate-band photovoltaic material based on ZnY1 − xOx (Y = S, Se, Te) semiconductors by first-principles calculations. *Chin. Phys. B* **2013**, *22*, No. 107103.

(32) Palacios, P.; Wahnón, P.; Pizzinato, S.; Conesa, J. C. Energetics of formation of $TiGa_3As_4$ and $TiGa_3P_4$ intermediate band materials. *J. Chem. Phys.* **2006**, *124*, No. 014711.

(33) Sánchez, K.; Aguilera, I.; Palacios, P.; Wahnón, P. Assessment through first-principles calculations of an intermediate-band photovoltaic material based on Ti-implanted silicon: Interstitial versus substitutional origin. *Phys. Rev. B* **2009**, *79*, No. 165203.

(34) Huang, F.-W.; Sheu, J.-K.; Lee, M.-L.; Tu, S.-J.; Lai, W.-C.; Tsai, W.-C.; Chang, W.-H. Linear photon up-conversion of 450 meV in InGaN/GaN multiple quantum wells via Mn-doped GaN intermediate band photodetection. *Opt. Express* **2011**, *19*, A1211−A1218.

(35) Lundqvist, S.; March, N. H. *Theory of the Inhomogeneous Electron Gas*; Springer US, 1983; pp 309−389.
(36) Erwin, S. C.; Pederson, M. R. Electronic structure of crystalline K_6C_{60}. *Phys. Rev. Lett.* **1991**, *67*, 1610.
(37) Sullivan, J. T.; Simmons, C. B.; Buonassisi, T.; Krich, J. J. Targeted search for effective intermediate band solar cell materials. *IEEE J. Photovoltaics* **2015**, *5*, 212−218.
(38) Levy, M. Y.; Honsberg, C. Solar cell with an intermediate band of finite width. *Phys. Rev. B* **2008**, *78*, No. 165122.
(39) Levy, M. Y.; Honsberg, C. Intraband absorption in solar cells with an intermediate band. *J. Appl. Phys.* **2008**, *104*, No. 113103.
(40) Jing, T.; Dai, Y.; Ma, X.; Wei, W.; Huang, B. Electronic Structure and Photocatalytic Water-Splitting Properties of $Ag_2ZnSn(S1-x\ Se\ x)_4$. *J. Phys. Chem. C* **2015**, *119*, 27900−27908.
(41) Okada, Y.; Ekins-Daukes, N.; Kita, T.; Tamaki, R.; Yoshida, M.; Pusch, A.; Hess, O.; Phillips, C.; Farrell, D.; Yoshida, K.; et al. Intermediate band solar cells: Recent progress and future directions. *Appl. Phys. Rev.* **2015**, *2*, No. 021302.
(42) Riffe, D. M. Temperature dependence of silicon carrier effective masses with application to femtosecond reflectivity measurements. *J. Opt. Soc. Am. B* **2002**, *19*, 1092−1100.
(43) Fonari, A.; Sutton, C. Validation of the Effective Masses Calculated Using Finite Difference Method on a Five-Point Stencil for Inorganic and Organic Semiconductors. 2013, arXiv:condensed matter/1302.4996. arXiv.org e-Print archive. https://arxiv.org/abs/1302.4996.
(44) Cartoixa, X.; Ting, D.-Y.; McGill, T. Numerical spurious solutions in the effective mass approximation. *J. Appl. Phys.* **2003**, *93*, 3974−3981.
(45) Van Zeghbroeck, B. *Principles of Semiconductor Devices*; Colarado University, 2004.
(46) Green, M. A.; Emery, K.; Hishikawa, Y.; Warta, W.; Dunlop, E. D. Solar cell efficiency Tables (Version 45). *Prog. Photovoltaics* **2015**, *23*, 1−9.
(47) Kresse, G.; Furthmüller, J. Efficient iterative schemes for ab initio total-energy calculations using a plane-wave basis set. *Phys. Rev. B* **1996**, *54*, 11169−11186.
(48) Aroyo, M.; Perez-Mato, J.; Orobengoa, D.; Tasci, E.; De La Flor, G.; Kirov, A. Crystallography online: Bilbao crystallographic server. *Bulg. Chem. Commun.* **2011**, *43*, 183−197.
(49) Aroyo, M. I.; Perez-Mato, J. M.; Capillas, C.; Kroumova, E.; Ivantchev, S.; Madariaga, G.; Kirov, A.; Wondratschek, H. Bilbao Crystallographic Server: I. Databases and crystallographic computing programs. *Z. Kristallogr. - Cryst. Mater.* **2006**, *221*, 15−27.
(50) Aroyo, M. I.; Kirov, A.; Capillas, C.; Perez-Mato, J.; Wondratschek, H. Bilbao Crystallographic Server. II. Representations of crystallographic point groups and space groups. *Acta Crystallogr., Sect. A: Found. Crystallogr.* **2006**, *62*, 115−128.
(51) Dudarev, S.; Botton, G.; Savrasov, S. Y.; Szotek, Z.; Temmerman, W.; Sutton, A. Electronic Structure and Elastic Properties of Strongly Correlated Metal Oxides from First Principles: LSDA + U, SIC-LSDA and EELS Study of UO_2 and NiO. *Phys. Status Solidi A* **1998**, *166*, 429−443.
(52) Kresse, G.; Furthmüller, J. Efficiency of ab-initio total energy calculations for metals and semiconductors using a plane-wave basis set. *Comput. Mater. Sci.* **1996**, *6*, 15−50.
(53) Liechtenstein, A.; Anisimov, V.; Zaanen, J. Density-functional theory and strong interactions: Orbital ordering in Mott-Hubbard insulators. *Phys. Rev. B: Condens. Matter Mater. Phys.* **1995**, *52*, No. R5467.
(54) Perdew, J. P.; Burke, K.; Ernzerhof, M. Generalized gradient approximation made simple. *Phys. Rev. Lett.* **1996**, *77*, 3865.

DOI: 10.1021/acsomega.6b00534
ACS Omega 2017, 2, 1454−1462

Computational Modeling of Novel bulk materials for the Intermediate Band Solar cells

Murugesan Rasukkannu*[1], Dhayalan Velauthapillai[1], Ponniah Vajeeston[2]

[1]*Western Norway University of Applied Sciences, Department of Computing, Mathematics and Physics, Inndalsveien 28, Box 5063, Bergen, Norway*

[2]*Center for Materials Science and Nanotechnology, Department of Chemistry, University of Oslo, Box 1033 Blindern N-0315, Oslo, Norway*

Supporting information, tables, list of computed compounds and figures

The wide-bandgap semiconductors $AsCs_3Se_4$, Al_2HgSe_4, $C_2Te_2F_4$, $PdPbF_4$, $AlMoVO_7$ and Ag_6SiSO_8 have the total bandgap vary from 3.26 to 3.51 eV (see Table S1). Figure S1(a-f) shows the calculated band structure with IB of $AsCs_3Se_4$, Al_2HgSe_4, $C_2Te_2F_4$, $PdPbF_4$, $AlMoVO_7$ and Ag_6SiSO_8 respectively. The calculated values of E_{vi}, E_{ci}, ΔE_i and the total bandgaps are presented in . The bandgap types of over six compounds are the direct bandgap except for the indirect bandgap of $C_2Te_2F_4$ and $PdPbF_4$. From figure S5b, the calculated values for Al_2HgSe_4 are: total direct bandgap is 3.28 eV, whereas the bandgap E_{vi} is 1.41 eV. The transition between IB to CB is fast because the bandgap E_{ci} is 0.04 eV. However, the width of IB is 1.83 eV, ΔE_i in Al_2HgSe_4, which is much higher than E_{ci} and E_{vi}.

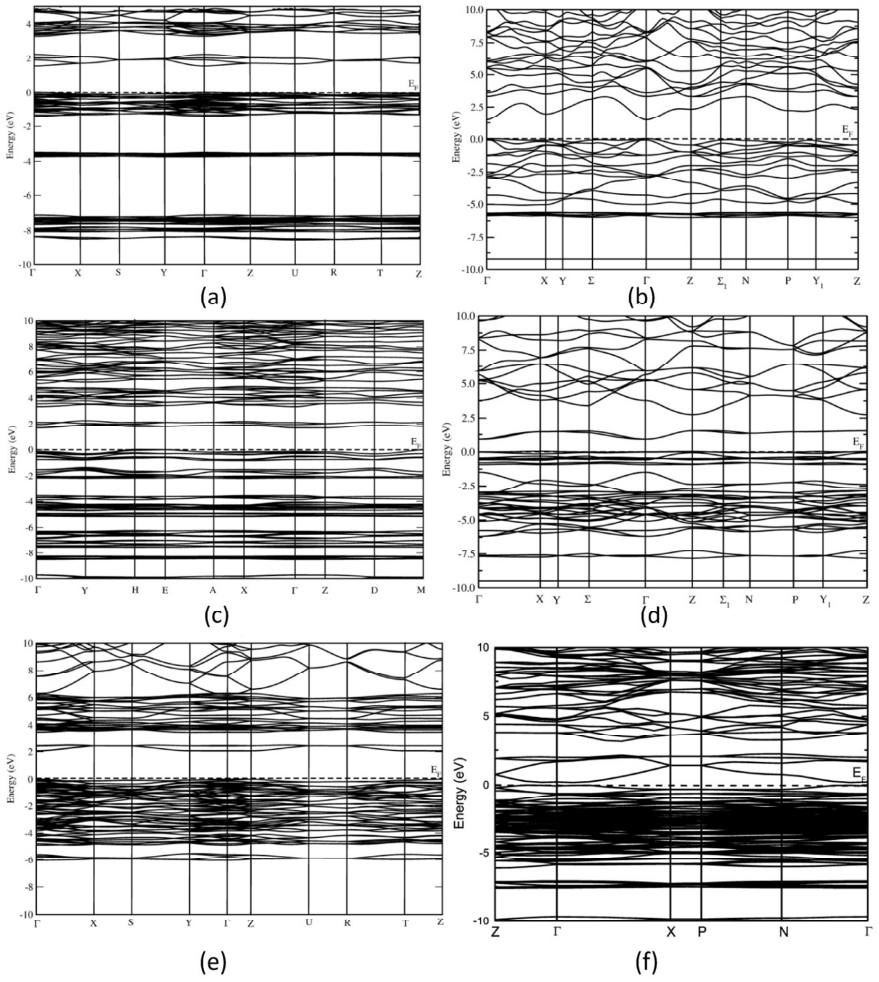

Figure S1. Calculated electronic band structure of (a) $AsCs_3Se_4$, (b) Al_2HgSe_4, (c) $C_2Te_2F_4$ and (d) $PdPbF_4$. (e) $AlMoVO_7$ and (f) Ag_6SiSO_8. The Fermi level is set to zero.

Table S1. Wide-bandgap 2 semiconductors with intermediate band ranging from 3.15 eV to 3.51 eV

Serial no.	Chemical Formula	Pearson symbol	Space group number	Bandgap (E_{vi})	Bandgap (E_{ci})	Width of IB ΔE_i	Total Bandgap (Eg)	Bandgap type
1.	$AsCs_3Se_4$	oP32	62	1.49	1.04	0.73	3.26	DB
2.	Al_2HgSe_4	tI14	121	1.41	0.04	1.83	3.28	DB
3.	$C_2Te_2F_4$	mP32	4	1.67	1.08	0.58	3.33	ID
4.	$PdPbF_4$	tI24	140	1.92	0.8	0.61	3.33	ID
5.	$AlMoVO_7$	oP40	62	2.31	0.72	0.46	3.49	DB
6.	Ag_6SiSO_8	tI64	141	0.16	0.71	2.64	3.51	DB

Ground state structure of Ag_2ZnSnS_4:

In literature two types of tetragonal structures I-4 (kesterite-type; space group 82) and I-42m (stannite-type; space group 121) are described for Ag_2ZnSnS_4. Both of these two modifications are having similar atomic arrangement (see Figure S2) and are highlighted by square box in Figure S. Our total energy calculation predicted that kesterite-type structure is energetically favourable for Ag_2ZnSnS_4 compound (see Figure S3). This finding is consistence with the recent experimental findings by Gong *et al*. **[1]** The calculated structural parameters and atomic positions are well fitted with the experimental findings. The involved energy difference between the two structures is 0.14 eV/f.u.

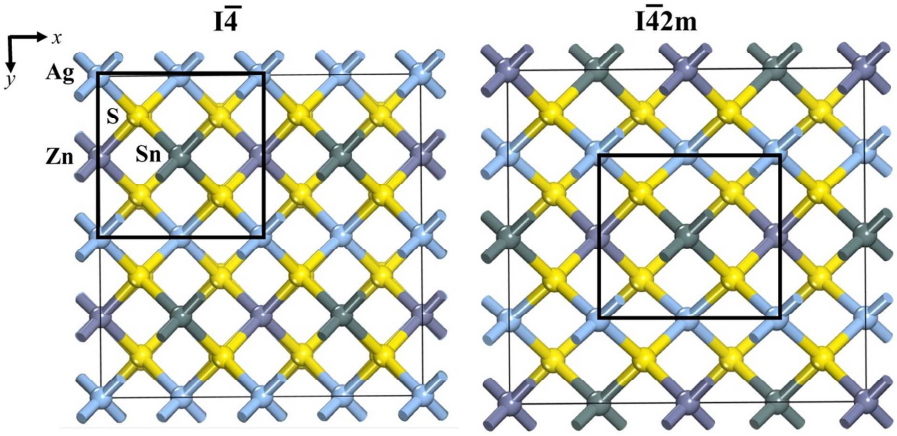

Figure S2 *Crystal structures of tetragonal Ag_2ZnSnS_4 in I-4and I-42m structure viewed along [001]. Both of these two modifications are having similar atomic arrangement and are highlighted by square box. The atomic label for the different kinds of atoms is given in the illustration.*

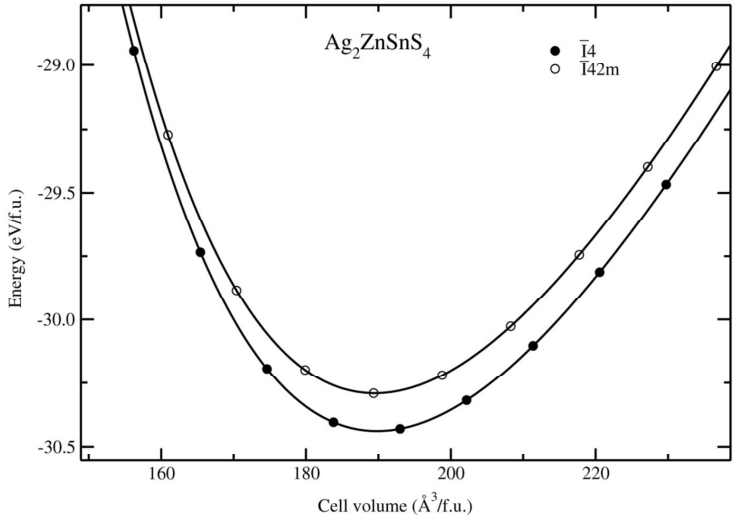

Figure S3 *Calculated unit cell volume vs. total energy (per formula unit; f.u.) curves for Ag_2ZnSnS_4 in I-4and I-42m structure arrangements; structure types are labelled on the illustration.*

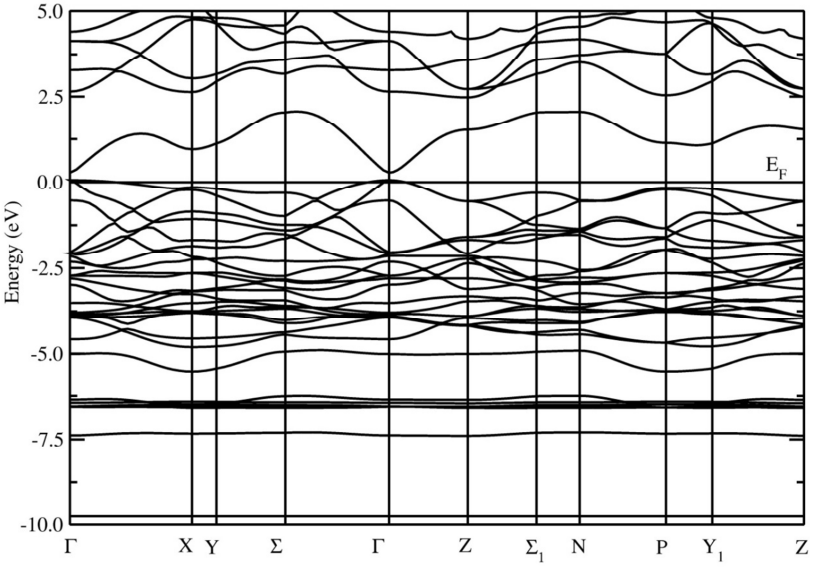

Figure S4 *Band structure of tetragonal Ag_2ZnSnS_4 in I-4 space group. The Fermi level is set to zero.*

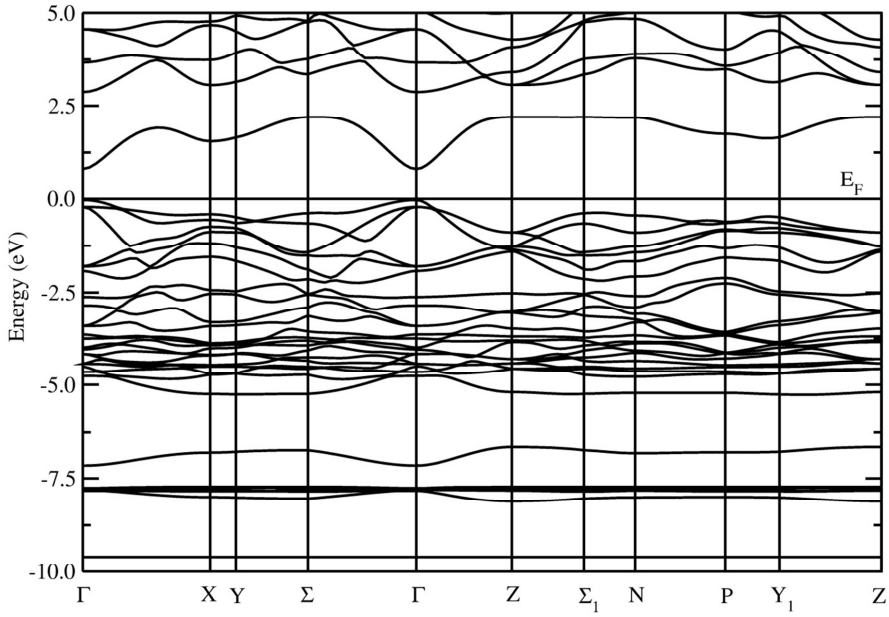

Figure S5 *Band structure of tetragonal Ag_2ZnSnS_4 in I-42m space group. The Fermi level is set to zero.*

We observed 312 compounds having an intermediate band with the maximum of the valence band at the Fermi level. Among these, 282 compounds (listed below) were selected for further analysis and 30 compounds were found as heavy elements. After carrying out detailed analysis, we found out that only 17 compounds among the starting 282 would be acceptable semiconductor materials for photovoltaic applications. The rest were found to be perfect insulators, with bandgap values larger than 3.51eV

Table S2 List of Compounds with Intermediate band considered in this study are listed bellow. The chemical formula, pearson symbol, space group number, E_{vi}- Energy gap between top of the valence band to bottom of an intermediate band, E_{ci}- Energy gap between top of the intermediate band to bottom of the conduction band, Ei1-Ei2- gap between two IBs, ΔE_{i1} and ΔE_{i2}- bandwidth of the intermediate bands , Eg-total bandgap between top of the valence band and bottom of the conduction band, ID-indirect bandgap type, DB-direct bandgap type are listed

Serial no.	Chemical Formula	Pearson symbol	Space group number	Bandgap (E_{vi})	Bandgap (E_{ci})	Multibands gap (Ei1-Ei2)	Width of IBss ΔEi1, ΔEi2	Total Bandgap (Eg)	Band gap type
1.	$AgAsSe_2$	hR4	166	0.13	0.02	-	3.66	3.81	ID
2.	$AgClO_4$	tI12	121	3.60	0.57	0.13	2.59, 2.28	9.17	ID
3.	$AgPXe_2F_{10}$	tI56	140	2.48	0.72	2.39	0.99, 1.12	7.7	DB
4.	AgF_2	oP12	61	1.03	1.15	-	1.43	3.61	DB
5.	AgF_3	hP24	178	1.24	4.13	-	0.77	6.14	DB
6.	$AgKF_4$	tI24	140	2.13	4.12	-	0.19	6.44	DB
7.	$AgNaF_4$	tI24	140	1.78	4.01	-	0.36	6.15	DB
8.	$AgIO_4$	tI24	88	0.77	1.27	1.59	2.13, 3.26	9.02	ID
9.	$AgTcO_4$	tI24	88	2.34	0.35	0.8	0.98, 3.45	7.92	ID
10.	Ag_2GeBaS_4	tI16	121	0.90	0.35	-	1.16	2.41	ID
11.	Ag_2HgI_4	tI14	121	1.43	1.31	-	0.89	3.63	DB
12.	Ag_2KSbS_4	tI16	121	0.81	1.08	-	0.94	2.93	ID
13.	Ag_2ZnSnS_4	tI16	121	0.47	0.57	-	1.66	2.70	DB
14.	Ag_4TeSO_4	cP40	198	1.06	0.44	-	2.17	3.67	DB
15.	Ag_6SiSO_8	tI64	141	0.16	0.71	-	2.64	3.51	DB
16.	$AlAsO_4$	tI12	121	4.22	1.82	-	1.92	7.96	DB
17.	$AlH_{12}N_3O_{15}$	cI248	206	3.38	1.22	-	0.58	5.18	DB

18.	Al_2HgS_4	tI14	121	2.0	0.03	-	1.64	3.64	ID
Serial no.	Chemical Formula	Pearson symbol	Space group number	Bandgap (E_{vi})	Bandgap (E_{ci})	Multibands gap (Ei1-Ei2)	Width of IBs ΔEi1, ΔEi2	Total Bandgap (Eg)	Band gap type
19.	$AsBiO_4$	tI24	88	2.81	0.6	-	4.08	7.49	ID
20.	Al_2HgSe_4	tI14	121	1.41	0.04	-	1.83	3.28	DB
21.	$AsBO_4$	tI12	82	4.25	1.72	-	1.48	7.45	ID
22.	$AsCsF_4$	mP12	4	4.62	0.39	-	1.04	6.05	DB
23.	$AsCsF_6$	hR8	148	5.11	3.49	-	0.67	9.27	DB
24.	$AsCuF_7$	oI36	74	2.18	2.06	1.01	0.85, 1.17	7.27	DB
25.	$AsDyO_4$	tI24	141	3.61	0.65	-	2.04	6.30	DB
26.	AsF_3	oP16	33	5.15	0.28	-	2.79	8.22	ID
27.	AsF_5	hP12	194	4.55	3.82	-	0.88	9.25	DB
28.	AsF_6I_5	mS48	15	1.39	2.11	1.22	0.59, 0.27	5.58	DB
29.	$AsInF_6$	hR8	148	3.33	2.25	1.53	0.65, 1.26	9.02	ID
30.	$AsK1F_6$	hR8	166	4.76	3.63	-	0.90	9.29	DB
31.	$AsRbF_6$	hR8	166	4.94	3.60	-	0.75	9.29	DB
32.	$AsTlF_6$	hR8	148	4.56	1.55	-	0.64	6.75	ID
33.	$AsKrF_7$	mP36	14	2.44	3.79	2.32	0.17, 0.48	9.20	DB
34.	AsH_6NO_4	tI48	122	4.12	1.16	-	1.9	7.18	ID
35.	$AsHoO_4$	tI24	141	3.60	0.73	-	2.04	6.37	DB
36.	$AsLuO_4$	tI24	141	3.50	0.89	-	2.06	6.45	DB
37.	$AsTbO_4$	tI24	141	3.64	0.63	-	2.04	6.31	DB
38.	$AsYO_4$	Ti24	141	3.65	0.54	-	1.93	6.12	DB
39.	$As2Cl_4F_6$	tP24	85	2.84	2.34	2.35	0.22, 0.75	8.50	ID

Serial no.	Chemical Formula	Pearson symbol	Space group number	Bandgap (E_{vi})	Bandgap (E_{ci})	Multibands gap (Ei1-Ei2)	Width of IBs ΔEi1, ΔEi2	Total Bandgap (Eg)	Band gap type
40.	$As_4C_4F_{12}$	tP40	137	3.31	0.43	-	2.84	6.58	DB
41.	$As_3Mg_4NaO_{12}$	tI80	122	3.19	1.13	-	2.60	6.92	DB
42.	$As2KF_7$	mP40	14	4.78	0.28	-	2.92	7.98	DB
43.	$AuLiF_4$	mP24	15	2.59	0.41	2.41	0.37, 2.84	8.62	DB
44.	$AuLiF_4$	mS24	15	2.60	0.45	2.36	0.43, 2.9	8.74	ID
45.	$AuKF_6$	hR8	166	2.20	4.43	-	0.39	7.02	ID
46.	$AuTlF_6$	tP64	92	1.80	0.41	1.17	3.4, 1.94	8.72	ID
47.	Au_2BaO_4	tI28	88	1.69	0.11	-	1.77	3.57	ID
48.	$Au_2Cs_2Br_6$	tI20	139	0.67	1.23	-	0.81	2.71	DB
49.	Au_2CaF_{12}	tP15	99	1.72	4.31	-	0.84	6.87	DB
50.	Au_2CaO_4	tI28	88	1.81	0.18	-	1.65	3.64	ID
51.	Au_2CdF_{12}	mS60	12	2.0	2.72	-	0.36	5.08	DB
52.	Au_2CdF_8	tP22	127	2.33	1.2	-	0.72	4.25	DB
53.	$Au_2Cs_2Cl_6$	tI20	xx	0.93	1.72	-	0.73	3.38	DB
54.	Au_2CsF_7	mS40	15	2.29	2.07	0.38	0.21, 0.12	5.07	DB
55.	$Au_2Cs_2I_6$	tI20	139	0.64	1.01	-	0.7	2.35	ID
56.	Au_2HgF_8	tP22	127	2.1	0.21	1.21	2.88, 2.25	8.65	DB
57.	Au_2MgF_8	mP22	14	2.45	0.79	2.26	0.5, 2.94	8.94	DB
58.	Au_2NiF_8	mP22	14	2.24	0.41	1.58	0.63, 3.57	8.43	DB
59.	Au_2ZnF_8	mP22	14	2.24	0.02	1.85	0.65, 3.25	8.01	DB
60.	Au_3LaF_{12}	hR32	167	2.55	0.39	2.59	0.22, 1.95	7.70	ID
61.	$BClF_6$	mP32	14	3.32	4.37	-	0.65,	8.34	DB

Serial no.	Chemical Formula	Pearson symbol	Space group number	Bandgap (E_{vi})	Bandgap (E_{ci})	Multibands gap (Ei1-Ei2)	Width of IBs ΔEi1, ΔEi2	Total Bandgap (Eg)	Band gap type
62.	BSF_7	oP36	62	4.94	1.22	1.75	0.34, 0.43	8.68	DB
63.	$BN1F_8$	oP40	57	2.91	3.34	1.4	0.18, 0.16	7.99	DB
64.	B_2F_4	mP12	14	4.9	2.01	-	0.09	7.00	DB
65.	$Co_4B_6O_{13}$	cI46	217	3.72	0.89	-	2.25	6.86	ID
66.	$Zn_4B_6O_{13}$	cI46	217	4.04	1.97	-	1.12	7.13	ID
67.	BiF_5	tI12	87	1.98	3.73	-	1.38	7.09	ID
68.	BrF_3	oS16	36	2.17	3.08	0.8	0.49, 0.7	7.24	ID
69.	BrF_5	oS24	63	3.47	3.35	1.36	0.39, 0.49	9.06	ID
70.	$Ca_2U_6K_8O_{24}$	cI40	229	2.95	0.37	-	1.90	5.22	ID
71.	$Ca_3Te_2Zn_3O_{12}$	cI160	230	2.46	1.74	-	1.68	5.88	ID
72.	$CdPdF_6$	aP8	148	2.27	1.72	2.26	0.52, 1.91	8.69	ID
73.	$CdPtF_6$	hR8	148	2.74	0.95	0.68	0.66, 2.33	7.36	DB
74.	$CdSnF_6$	hR8	148	3.59	0.76	0.95	2.01, 1.93	9.24	ID
75.	$CdTiF_6$	hR8	148	4.92	0.98	0.79	0.24, 2.55	9.48	ID
76.	Cd_4OF_6	tP22	137	2.09	0.36	-	5.28	7.73	DB
77.	$Cd_4P_6N_{12}S$	cI46	217	3.08	0.42	-	0.87	4.37	ID
78.	$CeZrF_7$	mP18	4	4.24	1.05	-	0.28	5.57	ID
79.	SnClF	oP12	62	3.47	1.58	-	3.09	8.14	DB
80.	ClF	mP8	14	2.13	3.87	-	1.07	7.07	DB
81.	ClF_3	oP16	62	2.59	2.77	1.58	0.3, 0.73	7.97	ID
82.	$SbClF_8$	aP20	2	3.17	3.46	0.97	0.81, 0.72	9.13	ID
83.	$Hg_3 Se_2Cl_2$	cI28	199	1.75	0.65	-	1.92	4.32	ID

Serial no.	Chemical Formula	Pearson symbol	Space group number	Bandgap (E_{vi})	Bandgap (E_{ci})	Multibands gap (Ei1-Ei2)	Width of IBs ΔEi1, ΔEi2	Total Bandgap (Eg)	Band gap type
84.	$Hg_3Te_2Cl_2$	cI28	199	1.90	0.41	-	1.6	3.91	DB
85.	Li_2ZnCl_4	cF56	227	4.56	0.58	-	1.73	6.87	DB
86.	CoF_3	hR8	167	1.49	2.44	-	3.10	7.03	ID
87.	$CrNbF_6$	tI16	139	1.34	0.19	-	1.26	2.79	DB
88.	$CsCuF_4$	tI24	140	1.82	4.60	-	0.11	6.53	ID
89.	$CsHgF_3$	cP5	221	0.75	1.00	-	4.61	6.36	DB
90.	Cs_2HgF_4	tI14	139	2.05	0.88	-	2.56	5.49	ID
91.	$Cs2GeF_6$	cF36	225	6.01	1.64	-	1.08	8.73	DB
92.	$Cs_3Tl\ F_6$	tI20	139	3.34	1.78	-	0.78	5.90	ID
93.	CuF_2	mP6	14	1.75	0.98	-	1.38	4.11	DB
94.	HOF	oP12	19	3.23	2.91	-	0.66	6.80	ID
95.	PbIF	tP6	129	2.17	0.53	-	3.45	6.15	DB
96.	NOF	oP12	19	3.21	3.06	1.78	0.24, 0.64	8.93	ID
97.	TcO_3F	mP20	14	2.48	1.06	1.74	1.09, 1.55	7.92	ID
98.	HNF_2	oP16	29	4.41	0.88	-	1.62	6.91	DB
99.	PHF_2	oP16	19	3.83	0.36	0.73	2.43, 1.64	8.99	ID
100.	HgF_2	cF12	225	0.98	3.21	-	4.08	8.27	DB
101.	KrF_2	tP6	136	2.79	4.13	-	0.59	7.51	ID
102.	KrF_2	tI6	139	2.89	4.08	-	0.80	7.77	ID
103.	Pb_2OF_2	tP20	105	0.89	0.36	-	6.3	7.55	ID
104.	$SeOF_2$	oP16	29	4.15	0.88	0.99	1.63, 1.00	8.65	DB
Serial no.	Chemical Formula	Pearson symbol	Space group	Bandgap (E_{vi})	Bandgap	Multibands gap	Width of IBs	Total Bandgap	Band gap type

			number		(E_{ci})	(Ei1-Ei2)	ΔEi1, ΔEi2	(Eg)	
105.	XeF_2	tI6	139	2.74	3.60	-	0.88	7.22	ID
106.	FeF_3	cF64	227	2.80	1.34	-	2.26	6.40	ID
107.	FeF_3	hR8	167	2.71	1.14	-	2.44	6.29	DB
108.	FeF_3	hR32	167	2.77	1.19	-	2.40	6.36	DB
109.	IF_3	oP16	62	1.78	2.10	0.39	1.36, 1.58	7.21	ID
110.	NiF_3	hR8	167	1.24	2.54	2.84	0.62, 0.17	7.41	ID
111.	RhF_3	hP12	150	1.30	1.61	0.16	1.00, 1.56	5.63	ID
112.	$N_2H_8F_4$	hR14	166	5.27	1.27	-	0.53	7.07	ID
113.	HfF_4	mS60	15	5.39	0.31	-	1.50	7.20	ID
114.	K_2PdF_4	mS14	12	3.09	1.48	-	0.19	4.76	ID
115.	$NaSbF_4$	mP24	14	4.34	0.33	-	2.40	7.07	ID
116.	Na_2PdF_4	mP14	14	2.67	1.46	-	0.13	4.26	ID
117.	$TcOF_4$	hP36	176	1.97	1.49	1.35	0.59, 1.44	6.84	DB
118.	PdF_4	oF40	109	1.05	4.67	-	1.28	7.00	ID
119.	SnF_4	tI10	139	2.74	1.47	-	3.77	7.98	ID
120.	VF_4	mP10	14	1.92	1.74	-	3.61	7.27	DB
121.	XeF_4	mP10	14	2.81	4.10	0.04	0.57, 0.26	7.78	DB
122.	$KTeF_5$	oP28	57	5.24	1.14	-	1.20	7.58	DB
123.	$NaTeF_5$	oP28	62	5.25	1.21	-	1.36	7.82	ID
124.	Sn_2OF_5	mS32	12	1.56	1.10	0.25	1.51, 1.32	5.74	ID
125.	$PdRb_3F_5$	tP18	127	2.87	1.51	-	0.05	4.43	ID
126.	$SbSrF_5$	oP28	57	4.77	0.70	-	2.02	7.49	ID
Serial no.	Chemical Formula	Pearson symbol	Space group	Bandgap (E_{vi})	Bandgap	Multibands gap	Width of IBs	Total Bandgap	Band gap type

			number		(E_{ci})	(Ei1-Ei2)	ΔEi1, ΔEi2	(Eg)	
127.	Rb_2GeF_6	hP9	164	5.77	2.30	-	1.10	9.17	ID
128.	Rb_2GeF_6	cF36	225	5.94	1.96	-	1.22	9.12	DB
129.	$KNbF_6$	tP16	116	5.60	2.22	-	0.12	7.94	ID
130.	$LiNbF_6$	hR8	148	5.48	2.60	-	0.21	8.29	DB
131.	Li_2TiF_6	tP18	136	4.88	1.58	1.54	0.16, 0.31	8.47	DB
132.	MoF_6	oP28	62	4.06	1.06	3.84	0.11, 0.16	9.23	DB
133.	MoF_6	cI14	229	4.10	0.49	3.78	0.12, 0.38		ID
134.	$P_3N_3F_6$	oP48	62	5.69	0.24	-	1.51	7.44	DB
135.	$NiSrF_6$	hR8	166	1.65	5.88	-	0.44	7.97	DB
136.	Sn_2F_6	cF32	221	2.26	0.54	1.01	2.06, 1.20	7.07	ID
137.	TeF_6	oP28	62	4.37	4.58	-	0.54	9.49	DB
138.	WF_6	oP28	62	5.04	3.79	-	0.14	8.97	DB
139.	Xe_2F_6	mP16	14	2.56	3.97	0.51	0.22, 0.29	7.55	ID
140.	K_2NbF_7	mP40	62	4.93	0.68	1.48	0.10, 0.13	7.32	DB
141.	K_2PaF_7	mS40	15	3.99	2.84	-	0.64	7.47	ID
142.	K_2TaF_7	oP40	62	5.68	1.05	-	0.17	6.90	DB
143.	$NiRb_3F_7$	tP22	127	0.78	4.91	-	0.15	5.84	ID
144.	Pb_2RhF_7	mP40	14	2.85	1.06	1.27	0.38, 3.01	8.57	DB
145.	$TiRb_3F_7$	tP22	127	3.52	1.80	-	0.04	5.36	DB
146.	$SbXeF_7$	mP36	14	2.79	3.44	1.69	0.27, 0.56	8.75	DB
147.	$SnTlF_7$	mP36	14	1.63	1.93	-	3.69	7.25	DB
148.	$SrTaF_7$	mP18	11	5.66	0.21	1.46	0.19, 0.25	7.77	ID
Serial no.	Chemical Formula	Pearson symbol	Space group	Bandgap (E_{vi})	Bandgap	Multibands gap	Width of IBs	Total Bandgap	Band gap type

			number		(E_{ci})	(Ei1-Ei2)	ΔEi1, ΔEi2	(Eg)	
149.	$Pb_5I_2F_8$	hR15	160	2.90	0.87	-	3.53	7.30	ID
150.	K_3TaF_8	hP24	186	3.98	0.09	1.48	0.06, 0.30	5.91	DB
151.	Sn_3F_8	mP22	14	2.70	0.83	0.85	0.95, 3.06	8.39	DB
152.	$NbSeF_9$	hR44	146	5.53	1.99	0.68	0.62, 0.09	8.91	DB
153.	$Na_3Ga_3Te_2O_{12}$	cI160	230	1.91	0.97	-	2.00	4.88	DB
154.	Hg_3TeO_6	CI160	230	0.59	0.39	-	3.90	4.88	DB
155.	LiO_3I	tP40	86	3.59	0.68	-	3.11	7.38	DB
156.	LiO_3I	hP10	173	3.65	2.04	-	2.53	8.22	ID
157.	K_3SbS_4	cI16	217	2.14	1.58	-	0.39	4.11	ID
158.	Li_2WO_4	tI12	141	4.12	1.43	-	0.97	6.52	DB
159.	Li_3NbO_4	cI64	197	4.03	1.65	-	1.17	6.85	DB
160.	$Li_3Nd_3W_2O_{12}$	cI160	230	3.28	0.22	-	0.96	4.46	DB
161.	Li_3TaO_4	mS64	15	4.66	0.69	-	1.18	6.53	ID
162.	Li_3VO_4	oP16	31	4.02	0.59	0.49	0.20, 0.80	6.10	ID
163.	$Li_6Zr_2O_7$	mS60	15	3.92	0.50	-	2.40	6.82	DB
164.	Li_7TaO_6	aP14	146	4.56	0.25	-	0.64	5.45	ID
165.	$Zn_8P_{12}N_{24}O_2$	cI46	217	3.44	0.57	-	0.25	4.26	ID
166.	Na_3SbS_4	cI16	217	1.92	1.27	-	0.42	3.61	ID
167.	Na_3SbSe_4	cI16	217	1.02	1.24	-	0.71	2.97	DB
168.	$ZnSr_2WO_6$	cF40	225	3.05	1.31	-	1.01	5.37	ID
169.	$AgBiSe_2$	hR4	166	0.44	0.08	-	3.36	3.88	ID
170.	$AgBiTe_2$	hR4	166	0.17	0.09	-	3.27	3.53	ID
Serial no.	Chemical Formula	Pearson symbol	Space group	Bandgap (E_{vi})	Bandgap	Multibands gap	Width of IBs	Total Bandgap	Band gap type

			number		(E_{ci})	(Ei1-Ei2)	ΔEi1, ΔEi2	(Eg)	
171.	$AgCN_3O_2$	oP28	57	3.18	0.61	-	0.46	4.25	DB
172.	$AgCuPO_4$	oP56	61	1.27	0.61	-	0.74	2.62	DB
173.	AgK_2SbS_4	oP32	118	1.52	1.03	-	0.47	2.97	DB
174.	AgN_3O_4	oP64	61	2.67	1.19	1.04	0.28, 2.18	7.36	DB
175.	AgP_4TaO_{13}	oP76	19	3.41	0.70	-	0.49	4.60	DB
176.	Ag_3AsS_4	oP16	31	0.73	1.04	-	1.00	2.77	DB
177.	$AlAsH_4O_6$	oP96	61	3.66	1.2	-	2.19	7.05	DB
178.	$AlCl_4NS_2$	oP32	62	2.14	0.13	2.88	0.10, 0.4	5.65	DB
179.	$AlCsSiO_4$	oP28	36	1.21	2.07	-	1.39	4.54	DB
180.	$AlMoVO_7$	oP40	62	2.31	0.72	-	0.46	3.49	DB
181.	$Al_2Ca_2Sn_2O_9$	oP60	60	2.45	0.78	-	2.91	6.14	DB
182.	$Al_5NaTi_2O_{12}$	oP40	55	3.13	0.54	-	1.27	4.94	DB
183.	$AsCl_3$	oP16	19	4.04	1.97	-	0.84	6.85	ID
184.	AsCoSe	oP24	61	0.46	0.30	-	4.43	5.19	ID
185.	$AsCs_3Se_4$	oP32	62	1.49	1.04	-	0.73	3.26	DB
186.	$AsZn_2HO_5$	oP36	58	2.65	1.01	-	2.71	6.37	ID
187.	$AsLiZnH_2O_5$	oP40	33	3.41	0.83	-	2.22	6.46	DB
188.	$AsNaH_4O_5$	oP44	19	3.87	1.33	-	1.92	7.12	ID
189.	$AsNH_6O_4$	oP48	19	3.41	1.00	-	1.71	6.12	DB
190.	$AsLiMgO_4$	oP28	62	3.46	1.28	-	2.00	6.74	DB
191.	$AsLiNiO_4$	oP28	62	2.79	1.03	-	2.35	6.17	DB
192.	$AsLi_2NaO_4$	oP16	31	3.92	1.51	-	1.82	7.25	ID
Serial no.	Chemical Formula	Pearson symbol	Space group	Bandgap (E_{vi})	Bandgap	Multibands gap	Width of IBs	Total Bandgap	Band gap type

			number		(E_{ci})	(Ei1-Ei2)	ΔEi1, ΔEi2	(Eg)	
193.	$AsRbSnO_5$	oP64	33	1.83	0.72	-	3.94	6.49	DB
194.	$AsSbO_5$	oP28	19	1.77	1.00	-	4.22	6.99	DB
195.	$AsRb_3Se_4$	oP32	62	1.32	0.98	-	0.97	3.15	DB
196.	$As_2MgXe_2F_{16}$	oP42	55	2.98	3.27	0.93	0.44, 0.6	8.22	DB
197.	As_2O_5	oP28	92	1.46	1.17	-	6.65	9.28	DB
198.	Au $K1C_4$ N_4H_2O	oP52	19	4.29	1.17	0.3	0.05, 0.36	5.87	DB
199.	$BaTe_2F_{10}$	mS52	15	4.90	1.93		1.15	7.98	ID
200.	$BaZr_2F_{10}$	mS52	15	5.75	0.37		1.47	7.59	ID
201.	$BaSb_2F_{12}$	aP15	1	4.07	2.65	1.06	0	7.78	DB
202.	$BaSbF_5$	oP28	57	4.73	0.22		1.84	6.79	ID
203.	$BaGeF_6$	hR8	166	5.55	3.11		0	8.66	DB
204.	$BaNiF_6$	hR8	166	1.72	6.01		0.37	8.09	DB
205.	$BaPbF_6$	hR8	166	2.86	5.02		0	7.88	DB
206.	$BaSnF_6$	hR8	148	4.98	3.52		0	8.50	DB
207.	$BaTeF_6$	oF128	43	4.79	1.67		1.26	7.72	ID
208.	$BaTiF_6$	hR8	166	4.80	0.94	1.6	0.14, 0.33	7.81	ID
209.	$BaZrF_6$	mP32	14	6.32	0.41	0.274	0.53, 0.146	7.68	DB
210.	$BaZrF_6$	oS32	67	6.26	0.35	-	0.64	7.25	ID
211.	$BaTm_2F_8$	mS22	12	1.98	5.36		0	7.34	ID
212.	Ba_2PdF_6	oS36	64	2.84	2.04	-	4.88	9.76	ID
213.	Ba_2ZrF_8	oP44	62	5.95	1.1	-	0	7.05	DB
214.	Ba_2SrTeO_6	hR10	225	3.16	1.96	-	5.12	10.24	ID
Serial no.	Chemical Formula	Pearson symbol	Space group	Bandgap (E_{vi})	Bandgap	Multibands gap	Width of IBs	Total Bandgap	Band gap type

			number		(E_{ci})	(Ei1-Ei2)	ΔEi1, ΔEi2	(Eg)	
215.	$Ba_3In_2F_{12}$	tP34	127	4.70	0.9	0.52	1.1, 0.28	7.50	DB
216.	$BiClF_8$	aP20	2	2.22	4.12	0.82	0.36, 0.83	8.35	DB
217.	$BiCsF_6$	hR8	148	2.92	5.5	-	0	5.5	DB
218.	$BiKF_6$	tP16	116	2.90	5.2	-	0.35	8.45	DB
219.	$BiLiF_6$	hR8	148	2.75	6.14	-	0	8.89	DB
220.	$BiNaF_6$	hR8	148	2.89	5.74	-	0	8.63	ID
221.	$BiRbF_6$	hR8	148	2.79	5.61	-	0	8.40	DB
222.	$BiKrF_7$	mP36	14	2.438	5.11	0.38	0.212, 0.41	8.55	DB
223.	$BiNa_3O_3$	cI56	217	2.89	0.37	0.65	1.3, 1.58	6.79	DB
224.	$Bi_{24}Pb_2O_{40}$	cI66	197	1.52	1.4	0.73	5.63	9.28	ID
225.	$Bi_4Si_3O_{12}$	cI76	220	3.93	1.59	-	2.1	7.62	DB
226.	$CsBrF_6$	hR8	148	4.03	3.34	-	0.31	7.68	DB
227.	PbBrF	tP6	129	2.72	0.33		3.82	6.75	DB
228.	Sn_3BrF_5	mP36	14	3.21	0.3	-	3.96	7.47	DB
229.	$CsBr_2F$	tP4	123	1.77	1.34	-	1.41	4.52	DB
230.	$GeBr_2F_{10}$	mP26	14	2.85	2.73	1.85	0.8,0.19	8.42	ID
231.	Hg_3Te2Br_2	cI28	199	1.73	0.47	-	1.48	3.68	DB
232.	CBr_3F	oP20	62	3.27	0.23	1.13	0.37, 0.92	5.92	DB
233.	$C_{12}SeF_{10}$	mP46	4	2.78	0.54	-	1.74	5.06	DB
234.	$C_{12}Ru_4Se_4O_{12}$	cI64	217	2.19	1.32	0.93	0, 1.33	5.77	ID
235.	$CClF_3$	oS20	36	6.55	0.7	-	0.47	7.72	ID
236.	CCl_2F_2	oF40	43	4.73	0.57	-	0.66	5.96	DB
Serial no.	Chemical Formula	Pearson symbol	Space group	Bandgap (E_{vi})	Bandgap	Multibands gap	Width of IBs	Total Bandgap	Band gap type

			number		(E_{ci})	(Ei1-Ei2)	ΔEi1, ΔEi2	(Eg)	
237.	CCl_3F	oP40	61	4.91	0.26	0.76	0.33, 0.62	6.88	DB
238.	CF_3I	oS40	64	3.71	1.78	-	0.37	5.86	ID
239.	ClF_7	mP36	14	4.65	2.41	-	1.22	8.28	DB
240.	$C_2O_3F_2$	oP56	19	5.27	0.68	-	0.47	6.42	DB
241.	$C_2Te_2F_4$	mP32	4	1.67	1.08	-	0.58	3.33	ID
242.	$C_2Te_2F_6$	mP40	14	2.41	1.01	0.22	0.35, 0.83	4.82	DB
243.	K_6C_{60}	cI132		0.61	0.28	-	0.39	1.28	ID
244.	$CaPdF_6$	hR8	148	2.62	4.51	-	0.24	7.37	ID
245.	$CaPtF_6$	hR8	148	3.17	2.77	-	0.25	6.19	ID
246.	$CaSnF_6$	hR8	148	4.85	4.07	-	0	8.92	DB
247.	$AgAsF_7$	P36	62	1.46	1.35	1.83	0.92,1.27	6.83	DB
248.	$AgSbF_6$	cI64	206	3.37	1.29	0.94	1.92, 1.45	8.97	DB
249.	$AgTiF_6$	aP8	2	1.46	0.89	2.64	0.52, 0.20	5.73	DB
250.	$AsNaF_6$	cF32	225	4.93	3.42	-	0.87	9.22	DB
251.	As_2MnF_{12}	tI60	141	4.01	1.4974	-	1.2119	6.7258	DB
252.	$AuTh_2F_{11}$	tI56	139	2.59	0.24	3.00	0, 1.67	7.51	DB
253.	PbF_4	tI10	139	1.86	3.31	-	3.15	8.32	ID
254.	$AuKF_4$	tI24	140	2.88	2.24	-	0.2614	5.39	DB
255.	$AuNaF_4$	tI24	140	2.61	2.03	-	0.401	5.05	DB
256.	$AuRbF_4$	tI24	140	2.96	2.227	-	0.23	5.42	DB
257.	Au_2BaF_{12}	cP60	224	1.79	1.03	3.12	0.7, 0.5	7.14	DB
Serial no.	Chemical Formula	Pearson symbol	Space group number	Bandgap (E_{vi})	Bandgap (E_{ci})	Multibands gap (Ei1-Ei2)	Width of IBs ΔEi1, ΔEi2	Total Bandgap (Eg)	Band gap type

258.	Au_2BaF_8	tI44	82	2.96	0.41	2.29	0.25, 2.38	8.29	ID
259.	$BaPdF_4$	tI24	140	2.56	1.74	-	0.39	4.69	ID
260.	$BaTaF_7$	cP72	205	5.79	1.49	-	0.21	7.49	DB
261.	$BiKF_4$	cF96	225	3.25	0.45	-	3.30	6.55	DB
262.	$BiKF_6$	cI64	206	2.90	5.07	-	0.58	8.55	ID
263.	$BrKF_4$	tI24	140	3.12	2.52	-	0.85	6.49	ID
264.	$BrRbF_4$	tI24	140	3.31	1.92	-	0.85	6.08	DB
265.	$Cs_2Br_2F_2$	tI12	139	2.52	2.05	-	0.26	4.83	ID
266.	$CaPdF_4$	tI24	140	2.22	1.89	-	0.49	4.60	DB
267.	$CaPbF_6$	cF32	225	3.41	4.63	-	0.64	8.68	DB
268.	$CaSnF_6$	cF32	225	4.82	3.28	-	0.8	8.9	DB
269.	$TaCl_4F$	tI48	82	3.21	0.49	1.72	0.58, 0.54	6.54	ID
270.	Cs_3TlF_6	tI20	139	3.32	1.73	-	0.8	5.85	ID
271.	KYb_3F_{10}	cF112	225	0.96	0.39	6.27	0.07, 0.81	8.5	DB
272.	KSb_4F_{13}	tI36	82	4.66	0.9	-	2.91	8.47	ID
273.	Rb_2HgF_4	tI14	139	1.96	0.37	-	2.81	5.14	DB
274.	$PbPdF_4$	tI24	140	1.92	0.8	-	0.61	3.33	ID
275.	$PdSrF_4$	tI24	140	2.37	1.8	-	0.43	4.60	DB
276.	Rb_2GeF_6	cF36	225	5.92	1.96	-	1.20	9.08	DB
277.	K_2NiF_6	cF36	225	2.22	5.2	-	0.33	7.75	ID
278.	$NaSbF_6$	cP32	225	4.86	3.38	-	0.9	9.14	DB
279.	$NiRb_2F_6$	cF36	225	2.29	4.90	-	0.24	7.43	ID
Serial no.	Chemical Formula	Pearson symbol	Space group number	Bandgap (E_{vi})	Bandgap (E_{ci})	Multibands gap (Ei1-Ei2)	Width of IBs ΔEi1, ΔEi2	Total Bandgap (Eg)	Band gap type

280.	$PdRb_2F_6$	cF36	225	2.84	3.69	-	0.29	6.82	DB
281.	Rb_3TlF_6	tI20	139	3.16	1.63	-	0.97	5.76	ID
282.	Pb_2F_6	tP16	116	1.96	1.10	2.40	1.23, 1.89	8.58	DB

Reference

1. Gong, W.; Tabata, T.; Takei, K.; Morihama, M.; Maeda, T.; Wada, T. Crystallographic and Optical Properties of $(Cu, Ag)_2ZnSnS_4$ and $(Cu, Ag)_2ZnSnSe_4$ Solid Solutions. Phys. Status Solidi C **2015**, 12, 700−703.

Chapter 8

Publication II

Hybrid density functional study of $Au_2Cs_2I_6$, Ag_2GeBaS_4, Ag_2ZnSnS_4 and $AgCuPO_4$ for the Intermediate band solar cells

Murugesan Rasukkannu[1], Dhayalan Velauthapillai[1], Ponniah Vajeeston[2]

[1]*Western Norway University of Applied Sciences, Department of Computing, Mathematics and Physics, Inndalsveien 28, Box 5063, Bergen, Norway*

[2]*Center for Materials Science and Nanotechnology, Department of Chemistry, University of Oslo, Box 1033 Blindern N-0315, Oslo, Norway*

Submitted to

Applied Energy Materials

(ACS)

Hybrid density functional study of $Au_2Cs_2I_6$, Ag_2GeBaS_4, Ag_2ZnSnS_4 and $AgCuPO_4$ for the Intermediate band solar cells.

Murugesan Rasukkannu*[1], Ponniah Vajeeston[2], Dhayalan Velauthapillai[1]

[1]*Western Norway University of Applied Sciences, Department of Computing, Mathematics and Physics, Inndalsveien 28, Box 5063, Bergen, Norway*

[2]*Center for Materials Science and Nanotechnology, Department of Chemistry, University of Oslo, Box 1033 Blindern N-0315, Oslo, Norway*

Abstract

We present a comprehensive study on structural, electronic, mechanical and optical properties of four promising candidates namely $Au_2Cs_2I_6$, Ag_2GeBaS_4, Ag_2ZnSnS_4, and $AgCuPO_4$ for the intermediate band (IB) solar cells. We employ the hybrid functional of Heyd -Scuseria -Erhzerhof (HSE06) within the density functional theory framework. Calculations reveal that IBs are present in all proposed compounds at unoccupied states in the range 0.34-2.19 eV from the Fermi level. Additional absorption peaks are present in the optical spectra of these compounds, characterised by a broadened energy range and high intensity for light absorption. The structural and mechanical stability of these four materials are also systematically investigated. Our findings, reported in this work, may provide a substantial breakthrough on the understanding of these materials, thus help the design of more efficient intermediate band solar cell.

Keywords: HSE06, intermediate bands, bulk solar cell materials, PV materials, hybrid density functional

---

* Electronic address: rmu@hvl.no, vdh@hvl.no, ponniah.vajeeston@kjemi.uio.no,

1. Introduction

Multi-bandgap materials offer the prospect of increasing the efficiency of standard solar cells that are based on-single bandgap materials. Intermediate band (IB) materials are identified by their energy bands where the main bandgap are split into two or more sub-bandgaps [1-2]. The IB material is inserted between the two ordinary *p*-type and *n*-type semiconductors and acts as contacts between the conduction band (CB) and valence band (VB).

In IB materials, an electron is excited from the VB to CB through IB. The electrons transit from the VB to the IB, and later from the IB to the CB by the absorption of sub-bandgap energy photons. It will add up together to the current of conventional photons absorbed through VB to CB transition [1-2]. Based on Shockley and Queisser [3], Luque *et al.,*[4] showed that the balance-limiting efficiencies of 63.2% for IB solar cells and 41% for single-gap solar cells could be achieved at a concentration of 46,050 suns at earth temperatures of 300 K and sun temperatures of 6,000 K.

IB solar cells can be considered as a combination of three cells, where VB to IB and IB to CB transitions can be regarded as two cells in series and the VB to CB transition can be regarded a parallel cell. The IB should not overlap with either the VB or the CB to get rid of fast transitions and should be partially filled to allow the comparable rates for the low sub-bandgap energy photons absorption processes [5]. The IB solar cell will have a high tolerance to changes in the solar spectrum [6]. Further increasing the number of IBs will increase the efficiency to nearly 80% [7-8]. Both theoretical and experimental reports have verified that IB materials could efficiently increase the optical absorption [9-12].

IBs can be formed through appropriate doping of bulk host semiconductors [13]. In a previous work [14], we carried out a comprehensive study on the electronic band structures of 2100 new bulk compounds to identify promising candidates for IB solar cells. For the initial screening of IB compounds, we employed GGA+U approximation, which is demands less computing resource compared to other more accurate methods. Based on these calculations, we found only 17 compounds to have IBs among the 2100 bulk materials. We reported the band structure, the density of states and the electron effective masses of these compounds in [14].

In this work, we employ a a more accurate method, namely, a screened–exchange hybrid density functional Heyd-Scuseria-Ernzerhof (HSE06) for the density functional calculation of the band structure and the density of states to identify the best candidates among the 17 compounds reported in [14] basd on GGA+U aproximation. The band structure of these materials showed a more substantial bandgap compared to the previous DFT results within the GGA+U scheme. Optimal bandgap is of importance in selecting the materials for solar cell applications. Although higher bandgaps give a high open-circuit voltage, but it gives less short-circuit current affecting the efficiency of the cell. Considering this fact, we analysed 17 indirect bandgap materials and found out that only four materials, namely, $Au_2Cs_2I_6$, Ag_2GeBaS_4, Ag_2ZnSnS_4, and $AgCuPO_4$ had a total bandgap less than 4 eV.

Here we report in-depth analysis of $Au_2Cs_2I_6$, Ag_2GeBaS_4, Ag_2ZnSnS_4, and $AgCuPO_4$ by employing a more accurate and computer rosource demanding HSE06 method. The calculated density of states for these four compounds helps to understand the origin of IB further and to identify the higher density of IB states. For one of the four materials, namely Ag_2ZnSnS_4 experimental results were reported by [15], and we carry out a comparison of numerical results based on HSE06 with these results. To our knowledge, there are still no experimental results reported for either $Au_2Cs_2I_6$, Ag_2GeBaS_4 or $AgCuPO_4$. In this article, we verify the applicability of these four materials in photovoltaic applications by studying the optical properties, structural and the mechanical stability of the materials.

2. Computational details

Total energies of compounds $Au_2Cs_2I_6$, Ag_2GeBaS_4, Ag_2ZnSnS_4, and $AgCuPO_4$ have been calculated using the projected augmented plane-wave (PAW) implementation of the Vienna *ab initio* simulation package (VASP) [16].

The Perdew–Burke–Ernzerhof (PBE) functional is used to treat exchange and correlation within the GGA approach [17]. For the transition metals, we have used exchange-correlation functional with the Hubbard parameter correction (GGA+*U*), following the rotationally invariant form [18-20]. The full details of the computed *U* and *J* values are presented in the DFTBD database website [21]. These GGA+U calculations are used for the structural optimisation of the considered compounds, as the relaxation using HSE06 is time-consuming and has no significant effect on the structural properties. Ground-state geometries are calculated by minimizing the stress tensor and the Hellman-Feynman forces using the conjugate-gradient algorithm with a force convergence threshold of 10^{-3}eV $Å^{-1}$. The hybrid nonlocal exchange-correlation functional of Heyd–Scuseria–Ernzerhof (HSE06) is used to calculate the electronic structure and the optical properties. In the HSE06 method, the screened parameter is set to 0.2 A^{-1}, and 30% of the screened Hartree-Fock (HF) exchange is mixed with the PBE exchange functional [22]. The cut-off energy for the plane-wave basis set is set to 600 eV, and we use a 6 x 6 x 6 Γ-centered Monkhorst-pack k-point mesh for Brillouin zone integration. This setting is used in both PBE and HSE06 calculations.

The PAW methodology is used for the calculation of the macroscopic dielectric matrix including local field effects in density functional approximation [23]. For the optical calculation, we used GGA and HSE06 for calculating the static dielectric constant. Moreover, we used HSE06 for calculating the dynamic dielectric functions. The optical properties such as the

optical spectra and the absorption of these compounds are evaluated using the calculated dynamic dielectric functions. The static dielectric constants are calculated using density functional perturbation theory with local field effects approaches in GGA [23] and HSE06 [24]. A 12 x 12 x 12 Γ-centered Monkhorst-pack k-point mesh is used for these calculations of optical properties. To get a more accurate peak position and intensities in optical spectra, the optical calculation counts the contribution from 400 electronic bands. For all of these computations, the initial structures are directly taken from the ICSD database [25]. The input parameters and file generation are done automatically using locally developed code. For the calculation of band structure, the *k*-point files are generated again with the help of locally developed code. The information about the high symmetric points of the *k*-vector in the Brillouin zone was taken from the Bilbao Crystallographic Server [26-28].

A frozen phonon calculation was performed on suitable supercells of the relaxed structures, generated using the phonopy program [29]. This software is also used to obtain the phonon dispersion curve and the phonon density of states from the converged calculations [30]. The atomic displacement of 0.0075 Å was used, with symmetry considerations to obtain the force constants for the phonon calculations. The displacements in opposite directions along all possible axes were incorporated in the calculations to improve the precision. The force calculations were made using the VASP code (with GGA+*U* correction), and the resulting data were imported into the Phonopy program. The dynamical matrices were calculated from the force constants, and phonon DOS curves were computed using the Monkhorst-Pack scheme [31].

3. Results and Discussion

3.1 Structural properties

$AgCuPO_4$:

There are two structural forms of $AgCuPO_4$ (i.e., the high-temperature form, β-$AgCuPO_4$ and the low-temperature form, α-$AgCuPO_4$) and an irreversible phase transition from the α- to the β-form takes place at 848 K [32]. The structure consists of $Cu_2P_2O_8$ layers parallel to the (100) plane which are separated by silver double layers. The local environment of Cu^{2+} is a distorted square pyramid with four Cu to basal O atom (Cu-Oba) distances in the range of 1.88-2.03 Å and a Cu to apical O atom (Cu-Oap) distance of 2.58 Å (Fig. 1a,

Table *1*). The average of the four Cu-Oba distances is 1.96 Å, which is close to the ionic radii sum 14. The bond valence sum 15 for Cu is calculated to be 1.98, in good agreement with the +2 oxidation state expected for Cu. Every two CuO_5 distorted square pyramids share one common basal edge to form a Cu_2O_8 dimer (Fig. *1*a) with a Cu-Cu distance of 3.05 Å and the Cu-O-Cu bridging angle of 101.1°. The Cu_2O_8 dimers are corner-shared with PO_4 tetrahedral to form $Cu_2P_2O_8$ layers parallel to the (100) plane. Every two nearest-neighbor Cu atoms are connected either by two Cu-O-Cu bridges, as in the Cu_2O_8 dimers, or by one Cu-O-Cu bridge. The silver atom is surrounded by five oxygen atoms with Ag-O distances ranging between 2.32 and 2.66 Å. The local environment of Ag^+ is a distorted trigonal bipyramid, which is axially compressed along the pseudo-3-fold rotational axis with the average Ag to axial O distance of 2.38 Å and an average Ag to equatorial O distance of 2.56 Å.

Ag_2GeBaS_4:

The Ag_2GeBaS_4 is crystalizing in a tetragonal structure with the space group I-42m (Fig. *1*b). Among the four compounds considered in this study, Ag_2GeBaS_4 is the less studied in the literature. Only one structure is reported [33], and the physical and chemical properties of this phase are unknown. Ag_2BaGeS_4 is one of the homologous tin compound corresponding tetrahedron construct-like construction type with Ba in anti-prismatic, Ge in tetrahedral and Ag in strongly deformed tetrahedral coordination sphere. A particularly striking feature of the structure is the four equidistant distances of Ag-S in 2.60Å in the much-flattened AgS_4-tetrahedra. This type of the structure feature is sporadic in sulfidic Ag compounds.

$Au_2Cs_2I_6$:

The $Au_2Cs_2I_6$ compound adopts a distorted perovskite structure (Fig. 1c). Although simple charge counting arguments might indicate a single gold valence Au^{II}, and hence a metallic state, the materials are in fact found to be non-metallic, comprising two distinct Au sites with different formal valences Au^{I} and Au^{III}, and form linear AuI_2^- and square AuI_4^- molecules. These two kinds of molecules align alternately in the tetragonal lattice. However, hydrostatic pressure can induce a coupled first-order structural and valence transition at 5.5 GPa, spurring considerable recent interest in the associated changes in the electronic behaviour [34-35]. The $Au_2Cs_2I_6$ structure comprises of a distorted perovskite structure in which linearly coordinated AuI_2 and square-planar coordinated AuI_4 complexes alternate through the crystal lattice. As previously suggested [34], the coordination is typical of Au^{I} and Au^{III} formal valences

respectively. The ratios of short-to-long Au–I bonds (Au- I)/(Au-I_2) and (Au_2 -I_2) is slightly closer to unity 0.7631 and 0.8017 respectively.

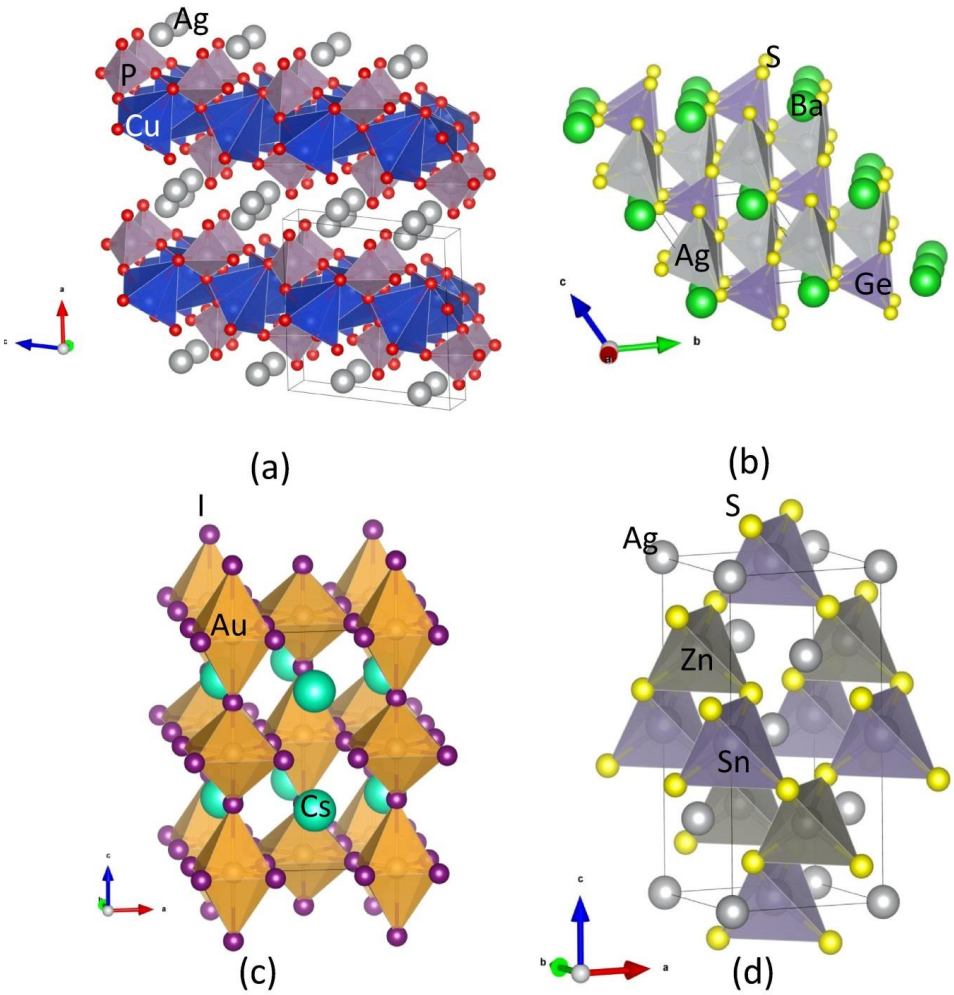

Fig. 1. Crystal structures for (a) $AgCuPO_4$; (b) Ag_2GeBaS_4; (c) $Au_2Cs_2I_6$; and (d) Ag_2ZnSnS_4 (in *I*-4; kesterite-type). The legends for the different kinds of atoms shown in the illustration.

Ag_2ZnSnS_4:

In literature, two types of tetragonal structures I-4 (kesterite-type; space group 82) and I-42m (stannite-type; space group 121) are described for Ag_2ZnSnS_4. Both modifications present a similar atomic arrangement [14]. Our total energy calculation predicted that kesterite-type structure is energetically favorable for Ag_2ZnSnS_4 compound [14] (Fig. 1d). Both structures, the kesterite type, and the stannite type consist of a *ccp* array of anions, with cations occupying

one-half of the tetrahedral voids. Thus, the structures are closely related but assigned to different space groups due to different distributions of the cations. The kesterite type structure characterized by alternating cation layers of AgSn and AgZn. Thus one Ag occupies the 2*a* (0, 0, 0) position with zinc and the remaining Ag ordered at 2*c* (0, 1/2, 1/4) and 2*d* (0, 1/2, 3/4) resulting in the space group *I*-4. On the other hand, in the stannite type structure ZnSn layers alternate with Ag layers. The structure is consistent with the symmetry of the space group *I*-42*m*, with the divalent cation located at the origin (2*a*) and the monovalent cation at the 4*d* position (0,1/2,1/4). Sn is located at the 2*b* site (0, 0, 1/2) in both structures. The anion lies on the (1 1 0) mirror plane at 8*i* (*x*,*x*,*z*) for the stannite type and 8*g* (*x*,*y*,*z*) for the kesterite type structure.

Table 1. Calculated structural parameters and atomic positions of $AgCuPO_4$, Ag_2GeBaS_4, $Au_2Cs_2I_6$, and Ag_2ZnSnS_4.

Phase	Lattice parameter				*Atomic positions*
	a	*b*	*c*	*β(deg)*	
$AgCuPO_4$- P21/c; 14	8.010(7.8365[a])	5.6438(5.6269[a])	7.6480 (7.4938[a])	98.15(99.07[a])	[a]Ag(4e): 0.9287, 0.1093, 0.1909 [a]Cu(4e): 0.5834, 0.1205, 0.8533 [a]P(4e): 0.2754, 0.1150, 0.4925 [a]O1(4e): 0.3150, -0.0490, 0.6480, [a]O2(4e): 0.2760, -0.0130, 0.3120 [a]O3(4e): 0.0990, 0.2370, 0.4920 [a]O4(4e): 0.4280, 0.3050, 0.5200
Ag_2BaGeS_4- *I-42m 121*	6.9327 (6.8280[b])		8.1705(8.0170[b])	90	[b]Ba(2a): 0,0,0 [b]Ag(4d): 0,1/2, 1/4 [b]Ge(2b): 0,0,1/2 [b]S(8i): 0.1883, 0.1883, 0.3440
$Au_2Cs_2I_6$- I4/mmm; 139	8.4089 (8.2847[c])		12.301(12.0845[c])	90	[c]Cs(4d): 0, ½, ¼ [c]Au1(2a): 0,0,0 [c]Au2(2b):1/2, ½, 0 [c]I1(8h):0.2258, 0.2285, 0 [c]I2(4e):1/2, ½, 0.2131
Ag_2ZnSnS_4- I-4*m; 121*	5.703(5.693[d])		11.350(11.342[d])	90	[d]Zn(2d): ½, 0, ¼ [d]Sn(2b): ½, ½, 0 [d]Ag(2c): 0, ½, ¼

					[d]Ag(2a): 0, 0, 0 [d]S(8g):0.249, 0.240, 0.128
Ag_2ZnSnS_4- I-42m	5.6503(5.7860[e])		11.4884(10.8290[e])	90	[e]Zn(2a): 0, 0, 0 [e]Sn(2b): ½, ½, 0 [e]Ag(4d): 0, ½, ¼ [e]S(8i):0.7560, 0.7560, 0.8700

[a]Reference [36]; [b]Reference [33]; [c]Reference [37]; [d]Reference [15]; [e]Reference [38].

3.2 Electronic properties

The bandgap of the photoactive semiconductors determines the upper bound on the short-circuit current and open-circuit voltage. A large-bandgap cell has a larger open-circuit voltage, and lower short-circuit current than a small-bandgap cell, it absorbs fewer solar photons than a small-bandgap cell. However, the detailed-balance limiting efficiency of an ideal solar cell of optimal bandgap E_g = 1.4 eV is 32% [3]. In real cells, thermalization loss occurs because of the solar resource used has a broad energy spectrum, and it poorly matches the bandgap, resulting in lower efficiencies below the detailed-balance limit [3]. Since, the efficiency of solar cell is highly dependent on the bandgap of material, the use of electronic band structure presents itself as a promising opportunity for engineering the material for the photovoltaic application. The band structures of $Au_2Cs_2I_6$, Ag_2GeBaS_4, Ag_2ZnSnS_4 and $AgCuPO_4$ are presented in Fig. 2 and total and site projected density of states (PDOS) of $Au_2Cs_2I_6$ is presented in Fig. 3. The calculated values of the main bandgap and the sub-bandgap for the four compounds are reported in Table 2. As we explained in [14], all the four compounds have indirect bandgaps materials between VB and CB. However, Ag_2ZnSnS_4 and $AgCuPO_4$ have direct bandgap between VB and IB.

The HSE06 band structure of $Au_2Cs_2I_6$ exhibits a bandgap of 2.92 eV, significantly larger than the bandgap calculated with less accurate GGA+U method (2.35 eV) [14]. The direct bandgap between the top of the VB and the bottom of the IB (E_{vi}) is 0.89 eV, and the energy gap between the top of the IB and the CB (E_{ci}) is 1.13eV. The width of the IB (ΔE_i) is 0.90 eV. The intermediate band minimum corresponds to the Cs-5*p* and the Au-6*s* states, the valence band maximum to the Au-5*p* and the Cs-6*s* state, and the conduction band minimum to the Au-6s and Cs-6*s* states, as shown in Fig. 2a and Fig. 3. The dispersion of IB of $Au_2Cs_2I_6$ is high (as shown in Fig. 2a) and it is of the great significance for high electron mobility. For $Au_2Cs_2I_6$, the

IB located at 0.89 eV, it is mainly derived from the Cs-5p state, and little contribution from Au-6s state presented in Fig. 3.

The band structure of Ag_2GeBaS_4 is presented in Fig. 2b and the total indirect bandgap at the Γ point is 3.33 eV (2.41 eV using GGA+U [14]), whereas bandgap E_{vi} is 2.08 eV and E_{ci} is 0.34eV. From Fig. 2b and supporting information from Fig.S1, the intermediate band minimum is mainly derived from the Ge-4*s* and Ag-5*s* with little contribution from state Ba -6*s* states. The S-3*p* states contribute to the VB maximum, and the CB is derived from the Ag-5*s* and the Ge-4*s* states. The dispersion of Ag_2GeBaS_4 IB is very high at Γ -point (as shown in Fig. 2b), resulting in high electron mobility.

The band structure of Ag_2ZnSnS_4 shows a direct bandgap at the Γ point of 3.34 eV (2.70 eV using GGA+U [14]), whereas bandgap E_{vi} is 1.15eV, E_{ci} is 0.34eV, and 1.85eV IB width, as shown in Fig. 2c. From Fig. 2c and supporting information Fig.S2, we observe that the IB minimum corresponds to the Sn-5*s* states, the VB maximum to the S-3*p* state and the CB minimum to the Sn-4*d* state. The dispersion of Ag_2ZnSnS_4 IB is very high at Γ -point as shown in Fig. 2c, resulting in Ag_2ZnSnS_4 in high electron mobility. Our total energy calculation predicted that the kesterite-type structure is energetically favorable for Ag_2ZnSnS_4 phase. We found the IB at 1.15 eV for the kesterite-type structure. According to Gong *et al.,* the energy gap between VB and CB is 2.01 eV for Ag_2ZnSnS_4 kesterite-type [35]. From Fig. 2d, the HSE06 calculated values for $AgCuPO_4$ are as follows: the total direct bandgap is 2.96 eV, more significant than the previous GGA+U study (2.35 eV) [14], whereas bandgap E_{vi} is 0.33 eV, E_{ci} is 2.19 eV, and width of the IB is 0.44 eV. From Fig. 2d and supporting information Fig.S3, we directly observe that the IB minimum corresponds to the Ag-4*d* and the Cu-3*d* states. The VB maximum extracted from O-2*p*, Ag-4*d* and Cu-3*d* states and CB derived from Ag-5*s* and P-3*s* states. The dispersion of $AgCuPO_4$ is low when compared to other compounds, resulting in low electron mobility.

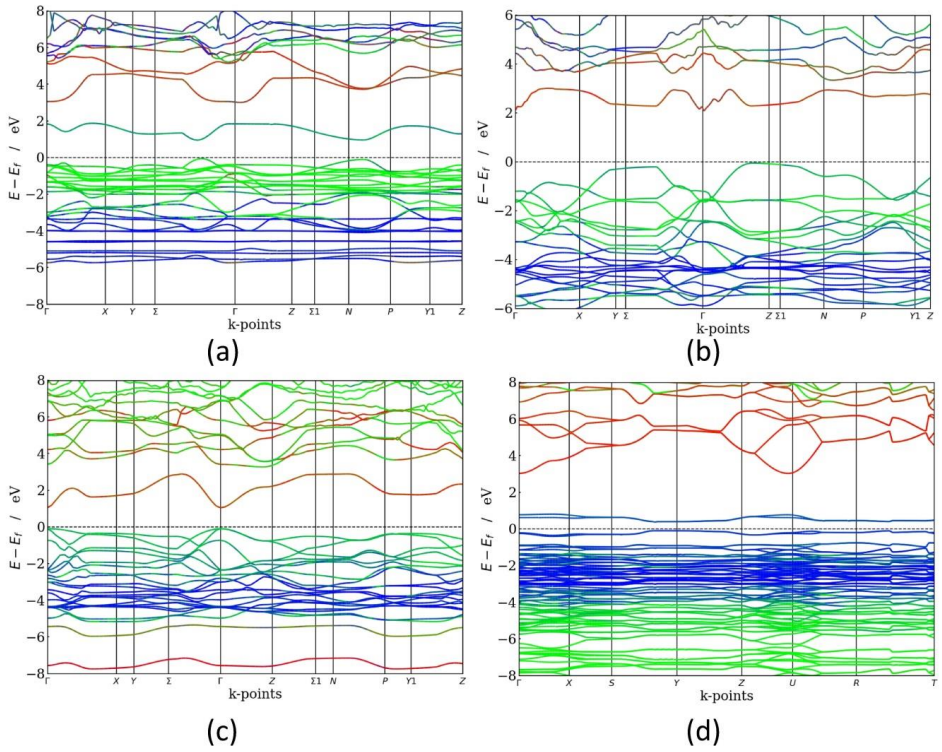

Fig. 2. Calculated electronic band structure of (a) $Au_2Cs_2I_6$, (b) Ag_2GeBaS_4, (c) Ag_2ZnSnS_4 and d) $AgCuPO_4$. Colour code: red line – *s* states, green line – *p* states, blue –*d* states). The Fermi level is set to zero

Table 2. Calculated HSE06 total bandgap (E_g; in eV), bandgap between the top of the VB and the bottom of the IB (E_{vi}; in eV), energy gap between the top of the IB and the bottom of the CB (E_{ci}; in eV) and the width of the IB (ΔE_i; in eV) are listed here for $Au_2Cs_2I_6$, Ag_2GeBaS_4, Ag_2ZnSnS_4, and $AgCuPO_4$.

Compounds	Bandgap (E_{vi})	Bandgap (E_{ci})	Width of IB (ΔE_i)	Total Bandgap (E_g)
$Au_2Cs_2I_6$	0.89	1.13	0.90	2.92
Ag_2GeBaS_4	2.08	0.34	0.91	3.33
Ag_2ZnSnS_4	1.15	0.34	1.85	3.34
$AgCuPO_4$	0.33	2.19	0.44	2.96

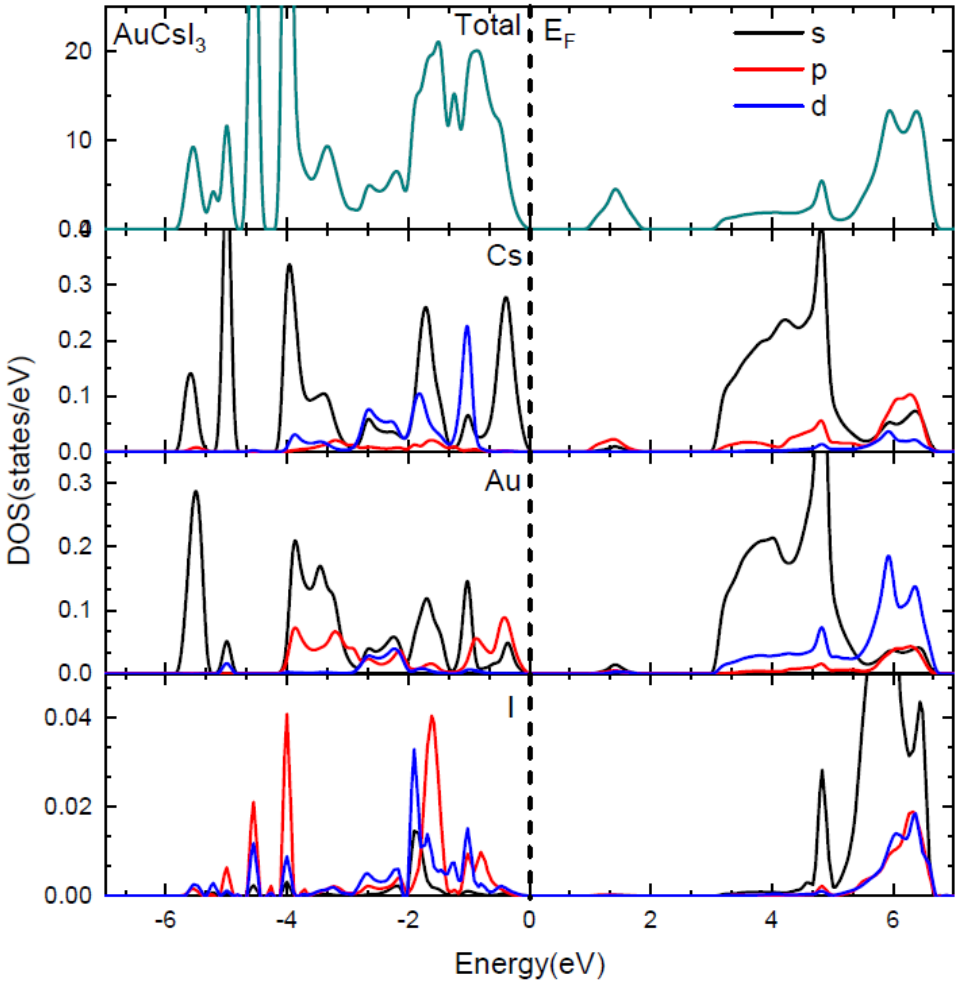

Fig. 3. Total and site projected density of states (PDOS) of $Au_2Cs_2I_6$. The Fermi level is set to zero and marked by a vertical dotted line.

3.3 Lattice dynamical stability

To identify the dynamical stability of the studied systems, the total phonon density of states is calculated at the equilibrium volumes for $Au_2Cs_2I_6$, Ag_2GeBaS_4, Ag_2ZnSnS_4 and $AgCuPO_4$. The results are presented in Fig. 4. For all these compounds, no imaginary frequencies were observed (with the only exception of $AgCuPO_4$), indicating that all the compounds are stable or at least dynamically stable at ambient conditions. In the $AgCuPO_4$, phase the ambient condition phonon soft modes are not disappearing even at the high pressure. In some selected cases, for example in Li_2FeSiO_4, the stable high-pressure phase has soft modes

at ambient condition, but they are disappearing at pressures above the phase transition point [39]. This finding indicates that this phase may not be dynamically stable even at high pressure, or the considered supercell size (2x1x2; 32 formula unit with a total number of atoms 224) might not be sufficient. The other possible reason is that this compound has an antiferromagnetic ordering in both low temperature and high-temperature modification [37, 40]. However, due to a large number of atoms involved in this theoretical simulation the magnetic ordering is not taken into account. Since $AgCuPO_4$ is least dynamically stable at ambient conditions, we present the projected phonon density of states for $Au_2Cs_2I_6$, Ag_2GeBaS_4, Ag_2ZnSnS_4 in Fig. 5. For $Au_2Cs_2I_6$ phase, the vibrational modes spread over the 0 to 60 THz range. The Au-I stretching modes are present between 53-61 THz and the lattice vibrational mode for the Au, Cs, and I are present in between 15-25, 2-10, and 2-20 THz, respectively.

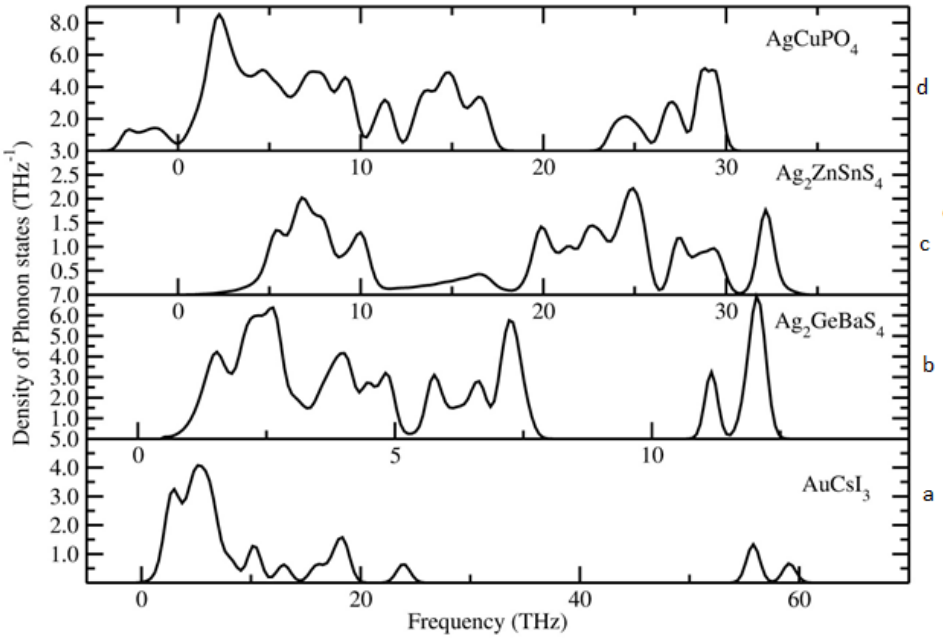

Fig. 4. Calculated total phonon density of states for a) $Au_2Cs_2I_6$, b) Ag_2ZnSnS_4, c) Ag_2GeBaS_4 and d) $AgCuPO_4$ phases.

For Ag_2GeBaS_4, the vibrational modes spread over 1 to 13 THz. The Ge-S stretching and bending modes are present at 11-13 THz and 6-8 THz, respectively. The lattice vibrational modes for Ag, Ge, Ba, S presented in between 1 to 5 THz. For Ag_2ZnSnS_4, the calculated vibrational modes spread over 2 to 35THz and the Ag-S, Sn-S stretching modes are present between 27 to 35 THz. In the phonon spectra, the combined bending and stretching modes of

Zn-S, Sn-S, and Ag-S presented in between the 18-25 THz region, and below 12 THz region the lattice translational modes of Ag, S, Sn, and Zn are presented. The calculated zero-point energy (ZPE) for the studied phases varies from 0.24 to 0.84 eV/f.u. (see Table *4*) and following the sequence $Ag_2GeBaS_4 < Ag_2ZnSnS_4 < Au_2Cs_2I_6 < AgCuPO_4$. However, the calculated ZPE for the all the dynamically stable compounds are very close to each other.

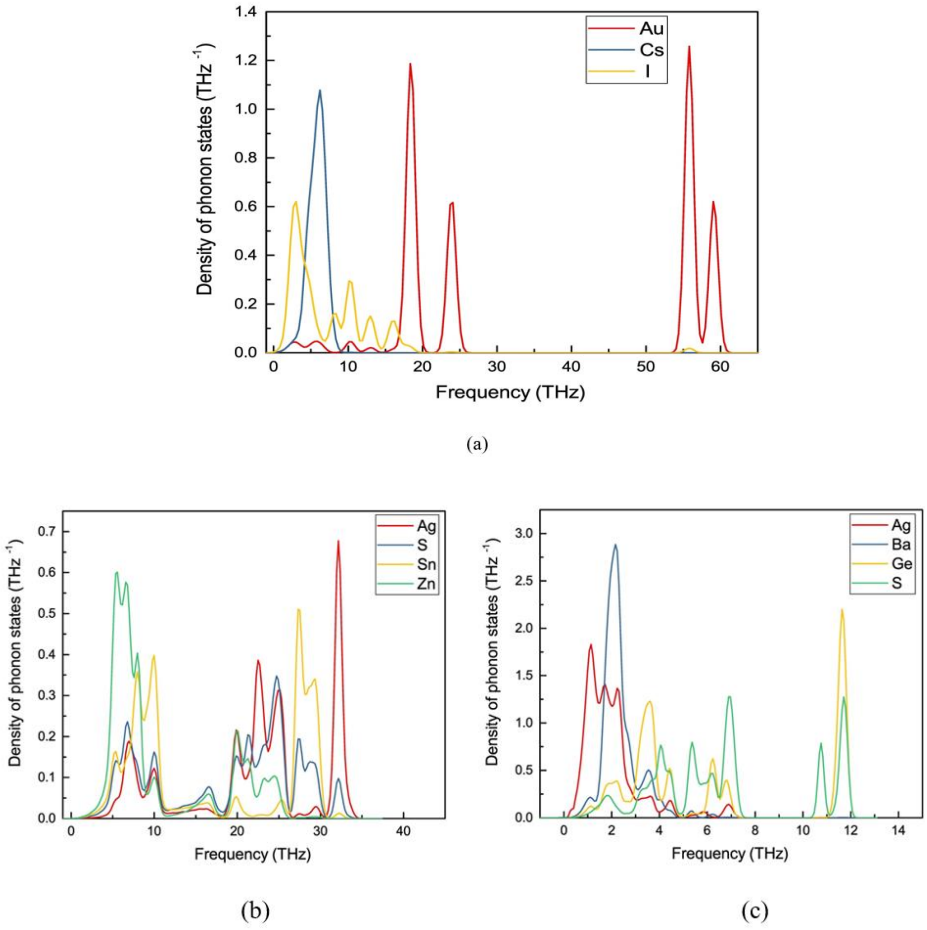

Fig. 5. Calculated site projected phonon density of states for (a) $Au_2Cs_2I_6$, (b) Ag_2ZnSnS_4, (c) Ag_2GeBaS_4 phases

3.4 Mechanical stability

Single crystal elastic constants and mechanical stability

To verify the mechanical stability of the considered phases, we have calculated the single-crystal elastic constants using the finite strain technique. The elastic constants of a

material describe its response to applied stress or conversely the stress required to maintain a given deformation. Both stress and strain have three tensile and three shear components, giving six components in total. The linear elastic constants form a 6 × 6 symmetric matrices, having 27 different components, such that $s_{ij} = C_{ij}\,\varepsilon_j$ (s_{ij} is stress tensor, C_{ij} is elastic constant, ε_j (j denotes 1,6 in Voigt index) is strain tensor, i index denotes 1 to 6) for small stresses σ and strains ε [41]. Any symmetry present in the structure may make some of these components equal, and others may be fixed to zero. Thus, a cubic crystal has only three different symmetry elements (C_{11}, C_{12}, and C_{44}), each of which represents three same elastic constants ($C_{11}=C_{22}=C_{33}$; $C_{12}=C_{23}=C_{31}$; $C_{44}=C_{55}=C_{66}$). In this present study monoclinic $AgCuPO_4$ has 13 independent elastic constants, and the other three compounds Ag_2GeBaS_4, $Au_2Cs_2I_6$ and Ag_2ZnSnS_4 have a tetragonal structure with type (I) that has six independent elastic constants. All the computed elastic constants are presented in

Table *3*.

The mechanical stability criteria for the monoclinic phase are given by [42]:

$$C_{11} > 0,\ C_{22} > 0,\ C_{33} > 0,\ C_{44} > 0, C_{55} > 0,\ C_{66} > 0, \tag{1}$$

$$[C_{11} + C_{22} + C_{33} + 2(C_{12} + C_{13} + C_{23})] > 0, \tag{2}$$

$$(C_{35}\cdot C_{55} - C^2_{35}) > 0,\ (C_{44}\cdot C_{66} - C^2_{46}) > 0,\ (C_{22} + C_{33} - 2C_{23}) > 0, \tag{3}$$

$$[C_{22}(C_{33}\cdot C_{55} - C^2_{35}) + 2C_{23}\cdot(C_{25}\cdot C_{35} - C^2_{23}\cdot C_{55} - C^2_{25}\cdot C_{33})\ ] > 0, \tag{4}$$

$$\{2[C_{15}\cdot C_{25}(C_{33}\cdot C_{12} - C_{13}\cdot C_{23}) + C_{15}\cdot C_{35}(C_{22}\cdot C_{13} - C_{12}\cdot C_{23}) + C_{25}\cdot C_{35}(C_{11}\cdot C_{23} - C_{12}\cdot C_{13})] - [C^2_{15}(C_{22}\cdot C_{33} - C^2_{23}) + C^2_{25}(C_{11}\cdot C_{33} - C^2_{13}) + C^2_{35}(C_{11}\cdot C_{22} - C^2_{12}) + C_{55}(C_{11}\cdot C_{22}\cdot C_{33} - C_{11}\cdot C^2_{23} - C_{22}\cdot C^2_{13} - C_{33}\cdot C^2_{12} + 2C_{12}\cdot C_{13}\cdot C_{23})]\} > 0, \tag{5}$$

The thirteen computed independent single crystalline elastic stiffness constants for monoclinic $AgCuPO_4$ at the equilibrium volume are shown in

Table *3*. In *P*21/n monoclinic polymorph, the most significant component is C_{22}, corresponding to the in-plane strain. The second largest component, C_{33} is just a few tens of GPa smaller than C_{22}. It is also evident that there is a significant degree of elastic anisotropy among the three principal directions due to $C_{11} \neq C_{22} \neq C_{33}$. All the five conditions given in

Equations (1-5) are simultaneously satisfied, and this indicates that $AgCuPO_4$ is a mechanically stable phase.

The mechanical stability criteria for the tetragonal (type I) phase [42] are given by:

$$C_{11}>|C_{12}| \quad (6)$$

$$2C^2_{13}<C_{33}(C_{11}+C_{12}) \quad (7)$$

$$C_{44}>0,\ C_{66}>0 \quad (8)$$

All the six calculated independent single crystalline elastic stiffness constants for tetragonal Ag_2GeBaS_4, $Au_2Cs_2I_6$, Ag_2ZnSnS_4-I and Ag_2ZnSnS_4-II are given in

Table *3*. All the three conditions for mechanical stability given in Equations (6-8) are simultaneously satisfied for all these structures, and this finding clearly indicates that these tetragonal phases are mechanically stable. This outcome is consistent with the phonon calculations; we presented in section 3.3.

Like the elastic constant tensor, the bulk (B_v, B_R) and shear moduli (G_v, G_R) contain information related to the hardness of material under various types of deformation. Properties such as bulk moduli, shear moduli, Young's moduli and Poisson's ratios can be computed from the values of elastic constants, and the calculated values are tabulated in

Table 3. All these polymorphs present a very scattered Young's (varying from 9 to 63 GPa) and shear modulus (vary from 3.4 to 23 GPa). The compressibility value of these polymorphs suggests that these compounds are very soft materials. A parameter G/B introduced, in which B indicates the bulk modulus and G represent the shear modulus. The bulk (B_v, B_R) and shear moduli (G_v, G_R) are calculated from the Voigt–Reuss–Hill approximations [43-44]. Calculated values for Lame Constant, longitudinal (ν_L; in m/s), transverse (ν_T; in m/s), and average sound velocity ($\bar{\nu}$, in m/s) for all four compounds are listed in Table 3 for the sake of completeness. The high/low G/B value is associated with ductility/brittleness, and the critical value which separates ductile and brittle materials is higher than 0.5 [45]. The calculated G/B values of all these compounds are lower than 0.5, implying the ductile characteristics of materials.

Table 3. The calculated single-crystal elastic constants C_{ij} (in GPa), bulk modulus B (in GPa), shear modulus G (in GPa), Poisson's ratio (σ), Young's modulus E (in GPa), compressibility (GPa^{-1}), Ductility, Lame constant, longitudinal (ν_L; in m/s), transverse (ν_T; in m/s), and average sound velocity ($\bar{\nu}$, in m/s), and Debye temperature (θ_D) for $AgCuPO_4$, Ag_2GeBaS_4, $Au_2Cs_2I_6$, and Ag_2ZnSnS_4 phases. Subscript V indicates the Voigt bound, R indicates the Reuss bound and VRH indicates the Hill average.

Properties	Phase				
	$AgCuPO_4$	Ag_2GeBaS_4	$Au_2Cs_2I_6$	Ag_2ZnSnS_4	
	P21/n	***I-42m***	I4/mmm	***I-4***	***I-42m***
C_{ij}	C_{11} = 86	C_{11} = 74	C_{11} = 18	C_{11} = 67	C_{11} = 63
	C_{12} = 66	C_{12} = 48	C_{12} = 11	C_{12} = 44	C_{12} = 45
	C_{13} = 52	C_{13} = 33	C_{13} =3	C_{13} = 43	C_{13} = 44
	C_{16}=18	C_{33} = 47	C_{33} = 21	C_{33} = 63	C_{33} = 74
	C_{22} = 162	C_{44} = 22	C_{44} = 7	C_{44} = 28	C_{44} = 29
	C_{23} = 72	C_{55} = 18	C_{55} =1	C_{55} = 25	C_{55} = 27
	C_{26}=9				
	C_{33} = 110				
	C_{36}=23				
	C_{44} = 21				
	C_{45}=5				
	C_{55} = 18				
	C_{66} = 19				
B_V	82	47	*10*	51	52
B_R	52	43	*10*	51	52
B_{VRH}	67	44.5	*10*	51	52
G_V	27	17	*4.5*	20	21
G_R	20	16	*2.3*	17	17
G_{VRH}	23	16.7	*3.4*	18.3	18.5
E	63	45	*9*	49	50
Compressibility	0.02	0.02	*0.10*	0.02	0.02
Ductility	0.35	0.38	*0.34*	0.36	0.36
Lame Constant	51.4	33	*8*	39	39
σ	0.34	0.33	*0.35*	0.34	0.34
v_L	4366	3777	*1632*	4073	4086
	2129	1888	*792*	2007	2011

ν_t	2391	2118	*891*	2253	2258
$\bar{\nu}$	771	592	*150*	634	637
Θ_b					

3.5 Optical properties

The optical properties have a high impact on the solar cell materials. To investigate the optical behavior of $Au_2Cs_2I_6$, Ag_2GeBaS_4, Ag_2ZnSnS_4, and $AgCuPO_4$, we used the optical dielectric function $\varepsilon(\omega)= \varepsilon_1(\omega)+i\varepsilon_2(\omega)$. The optical dielectric function is the fundamental quantity of the optical properties. It is defined as the linear response of the system to electromagnetic radiation, which controls the propagation behavior of radiation in a medium. Here, $\varepsilon(\omega)$ is connected with the interaction of photons and electrons. The imaginary part $\varepsilon_2(\omega)$ of the dielectric function $\varepsilon(\omega)$ can be derived from the inter-band optical transitions by calculating summation over unoccupied states using the equation [23],

$$\varepsilon_2^{(\alpha\beta)}(\omega) = \frac{4\pi^2 e^2}{\Omega} \lim_{q\to 0} \sum_{k,v,c} 2\, w_k \delta(\epsilon_{ck} - \epsilon_{vk} - \omega) \times \langle u_{ck+e_\alpha q} \mid u_{vk} \rangle \langle u_{ck+e_\beta q} \mid u_{vk} \rangle^* \quad (9)$$

where the indices α, β are the Cartesian components, Ω is the volume of the primitive cell, q denotes Bloch vector of the incident wave, *c* and *v* are the conduction and valance band states respectively, k is the Bloch wave vector, w_k denotes the k-point weight, δ is Dirac delta function, u_{ck} is the cell periodic part of the orbital at k-point k, ϵ_{ck} refers to energy of conduction band and ϵ_{vk} refers to energy of valence band.

The real part $\varepsilon_1(\omega)$ of dielectric function can be derived from the $\varepsilon_2(\omega)$ by Kramer-Kronig relationship [23, 46],

$$\varepsilon_1^{(\alpha\beta)}(\omega) = 1 + \frac{2}{\pi} \mathrm{P} \int_0^\infty \frac{\varepsilon_{\alpha\beta}^2(\omega')\, \omega'}{\omega'^2 - \omega^2 + i\eta}\, d\omega' \quad (10)$$

where P indicates the principal value, η is the complex shift. All the frequency dependent linear optical properties such as absorption coefficients $\alpha(\omega)$, reflectivity $R(\omega)$ can be calculated from $\varepsilon_1(\omega)$ and $\varepsilon_2(\omega)$ [23, 46].

$$\alpha(\omega) = \frac{\sqrt{2\omega}}{c} \left[(\varepsilon_1^2(\omega) + \varepsilon_2^2(\omega))^{\frac{1}{2}} - \varepsilon_1(\omega)\right] \quad (11)$$

$$R(\omega) = \left|\frac{\sqrt{\varepsilon_1(\omega)+i\varepsilon_2(\omega)}-1}{\sqrt{\varepsilon_1(\omega)+i\varepsilon_2(\omega)}+1}\right| \quad (12)$$

The calculated imaginary part of the dielectric function and absorption coefficients of $Au_2Cs_2I_6$, Ag_2GeBaS_4, Ag_2ZnSnS_4, and $AgCuPO_4$ compounds are presented in Fig. 6 and Fig. 7. In general, hybrid functional produce better results than semi-local functional for the semiconductor or small gap insulator materials due to the separation of the exchange energy into a short-range nonlocal and orbital-dependent exchange term [24]. Numerical results of ε(ω) for the four compounds are calculated using the HSE06 method.

In Fig. 6, both real and imaginary part of the dielectric function of tetragonal phases $Au_2Cs_2I_6$ and Ag_2GeBaS_4 are plotted against photon energy. From directional dependency of $\varepsilon_1(\omega)$ and $\varepsilon_2(\omega)$, we clearly see the anisotropic characteristics of these two materials. In particular, sharp peaks that are present in *x* and *y*-direction are equal. However, these sharp peaks are less pronounced in the *z*-direction. We observe clearly that large anisotropy is present in the lower-energy region due to tetragonal distortion. The peaks at 0.84 and 1.12 eV for $\varepsilon_2(\omega)$ along *x* and *y*-directions confirm the earlier results presented for energy gap VB-IB and IB-CB in Fig. 2a. For photovoltaic purposes, it is of interest to study the transitions that contribute to each peak in the spectra and influence of the intermediate band on absorption. The electronic transition from Cs-6*s* to Cs-5*p* and Cs-5*p* to Cs-6*s* states in Fig. 3 clearly demonstrate this. From Fig. 6b, we observe that optical absorption for $Au_2Cs_2I_6$ begins at 0.3 eV, and it is mainly extending from infrared region to the ultraviolet region of the solar spectrum. Absorption starts to increase from the infrared region due to the formation of intermediate states in between VB and CB. The overall optical absorption intensity presents a high peak at 1.32 eV, attributed to the states Au-5*p* to Au-6*s* transition as shown in Fig. 3. The peak at 2.5 eV is attributed to the states from the 6*s* orbitals of the substitutional Cs as shown in Fig. 3. In Fig. 6b where the absorption coefficient is plotted against the energy for $Au_2Cs_2I_6$, we clearly see the peaks at 2.7 and 3.2 eV along the *z*-direction. Until 3.5 eV, the absorption coefficient of $Au_2Cs_2I_6$ in *x, y* directions is more pronounced, and from 3.5 eV the absorption coefficient in the *z*-direction is higher.

Optical reflectivity plays a vital role in the selection of efficient photovoltaic materials. We present results from our study in which first principle calculation is carried out employing

hybrid functional HSE06 to calculate the optical reflectivity of the materials of interest. In supporting information Fig. S4, we show reflectivity of $Au_2Cs_2I_6$ as a function of photon energy in all directions. As compared to other three compounds, anisotropy is more pronounced in $Au_2Cs_2I_6$. We notice that the reflectivity is 0.35 – 0.5 in the infrared region and the value drops in the high energy region along *x* and *y* directions. In the *z*-direction, we notice that the reflectivity is 0.185 in the infrared region and 0.165-0.24 in the visible region with some peaks. It is also noticed that the reflectivity of $Au_2Cs_2I_6$ is less in visible region, which indicates $Au_2Cs_2I_6$ can be a good candidate for photovoltaic applications.

We present $\varepsilon_1(\omega)$ and $\varepsilon_2(\omega)$ of the dielectric function and the absorption coefficients of Ag_2GeBaS_4 in Fig. 6(c, d). Despite the tetragonal phase, the dielectric function and absorption coefficient of Ag_2GeBaS_4 show that the anisotropy features in this material are less pronounced than other three compounds as shown in Fig. 6(c, d). For Ag_2GeBaS_4 along the *x*-direction, absorption peaks at 2.56 eV (resulting from the transition from the VB to the empty IB states) and 3.56 eV are attributed to the states S-3*p* to Ge-4*s* transition and S-3*p* to Ag-5*s* transition respectively are presented in the supporting information Fig. S1. However, this curve fails to show the IB to CB transition. We observe the absorption starts to increase after 2 eV and it is mostly extending to the visible region presented in Fig. 6d. We clearly notice that the peaks are present at 3 and 3.6 eV along the *z*-direction. From 0-6 eV, the absorption coefficient of Ag_2GeBaS_4 along *z*-direction is less pronounced than *x* and *y* directions. The appearance of absorption peaks in the visible region makes Ag_2GeBaS_4 a promising candidate for photovoltaic applications. We present reflectivity of Ag_2GeBaS_4 as a function of photon energy in *x*, *y* and *z* directions in the supporting information Fig.S5. We notice that the reflectivity is in the range of 0.165 to 0.24 in the infrared region and low-energy side of the visible region along the *z*-direction. At 3 eV, the reflectivity drops by small values and then the value increases in the high energy region along the *z*-direction. In *x* and *y*-direction, we notice that the reflectivity is around 0.22-0.32 in the infrared region and visible region. The reflectivity of Ag_2GeBaS_4 is little high in the visible region along *x, y* and *z* directions.

The real and imaginary parts of the dielectric function of tetragonal phase Ag_2ZnSnS_4 and monoclinic phase $AgCuPO_4$ have more optical anisotropic characteristics than other two compounds as shown in Fig. 7. The calculated real and imaginary parts of the dielectric function and absorption coefficients of Ag_2ZnSnS_4 are presented in Fig. 7(a, b). At 0-2 eV photon energy, the $\varepsilon_1(\omega)$, $\varepsilon_2(\omega)$ and absorption peaks for *z*-direction are more pronounced than *x* and *y*

directions(*x* and *y*-direction are same). From 3-3.8 eV photon energy, $\alpha(\omega)$ and $\varepsilon(\omega)$ along *x*-direction are more pronounced than *z*-direction. For Ag_2ZnSnS_4 along *x*-direction, absorption peaks seen at 1.08 eV (resulting in the electronic transition from the IB-CB) are attributed to the states Sn-5*s* to Sn-3*d* transition and the results are presented in the supporting information Fig.S2. Next absorption peaks are noticed at 1.45 eV (electronic transition from the occupied VB to the empty IB state) corresponding to states S-3*p* to Sn-5*s* transition. The absorption peak at 1.94 eV (resulting in electronic transition within IB) is due to the contribution from states S-3*p* to Zn-3*d* transition and 3.27 eV (VB to CB transition) for S-3*p* to Sn-4*d* transition as shown in the supporting information Fig.S2. We observed that the absorption peaks start to increase from the infrared region due to the intermediate state, and it is greatly extended to the visible region. The reflectivity of Ag_2ZnSnS_4 is high at 0.6 and 2 eV photon energy and very low at 3 eV photon energy for *z*-direction as shown in supporting information Fig.S6. However, the reflectivity is very low at 1.5 – 2 eV along *x* and *y* directions, which indicates this material, can be used for photovoltaic applications.

We present both $\varepsilon_1(\omega)$ and $\varepsilon_2(\omega)$ of the dielectric function and the absorption coefficients for $AgCuPO_4$ in Fig. 7(c, d). The calculated values for $\varepsilon_1(\omega)$ and $\varepsilon_2(\omega)$ of the dielectric function and absorption coefficients indicate that monoclinic $AgCuPO_4$ phase has more optical anisotropic characteristics than other compounds. After 2 eV photon energy, the absorption coefficient of $AgCuPO_4$ is quite similar to *y* and *z* directions. However, the $\alpha(\omega)$ along *x*-direction are more pronounced than *y* and *z* directions. From Fig. 7d, we observe that the absorption peaks at 0.57 eV, 1.2 eV, 3 eV and 4eV along *x*-direction. In supporting information Fig. S7, we show reflectivity of the $AgCuPO_4$ as a function of photon energy in all direction. We notice that the reflectivity 0.1 to 0.59 in the infrared region and the value drops in the visible region along *x*, *y* and *z* directions. This validates that $AgCuPO_4$ can be used in photovoltaic applications. Overall, from the numerical results for the dielectric function, absorption coefficient and reflectivity conclude that all four compounds exhibit three-level optical transitions. This will lead to enhanced light absorption in the extended visible region.

The static dielectric constant $\varepsilon_1(0)$ is given by the low energy limit of $\varepsilon_1(\omega)$ and are presented for all four compounds in Table 4. Here, we use both GGA and HSE06 to calculate the static dielectric constant and presented in Table 4. As expected [45], we observe that the static dielectric constant are overestimated when GGA is employed. This can be explained by the fact that the bandgap values are underestimated when GGA is employed. The bandgap

between VB and IB is smaller in $AgCuPO_4$, so the static dielectric constant is very high compared to other three compounds.

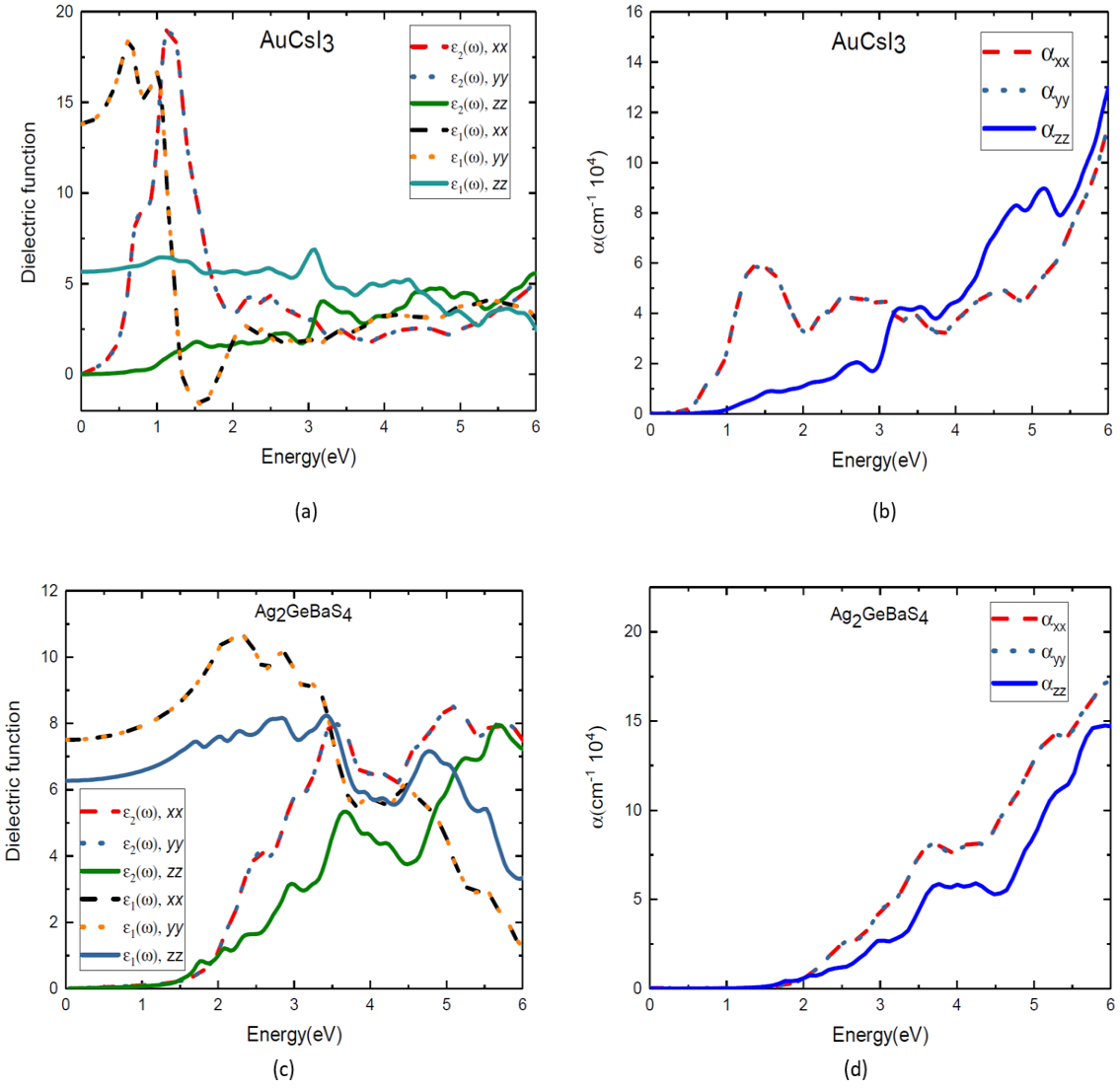

Fig. 6. Calculated dielectric function (a and c) and optical absorption coefficients (b and d) of $Au_2Cs_2I_6$ and Ag_2GeBaS_4, respectively along *x*, *y* and *z* directions.

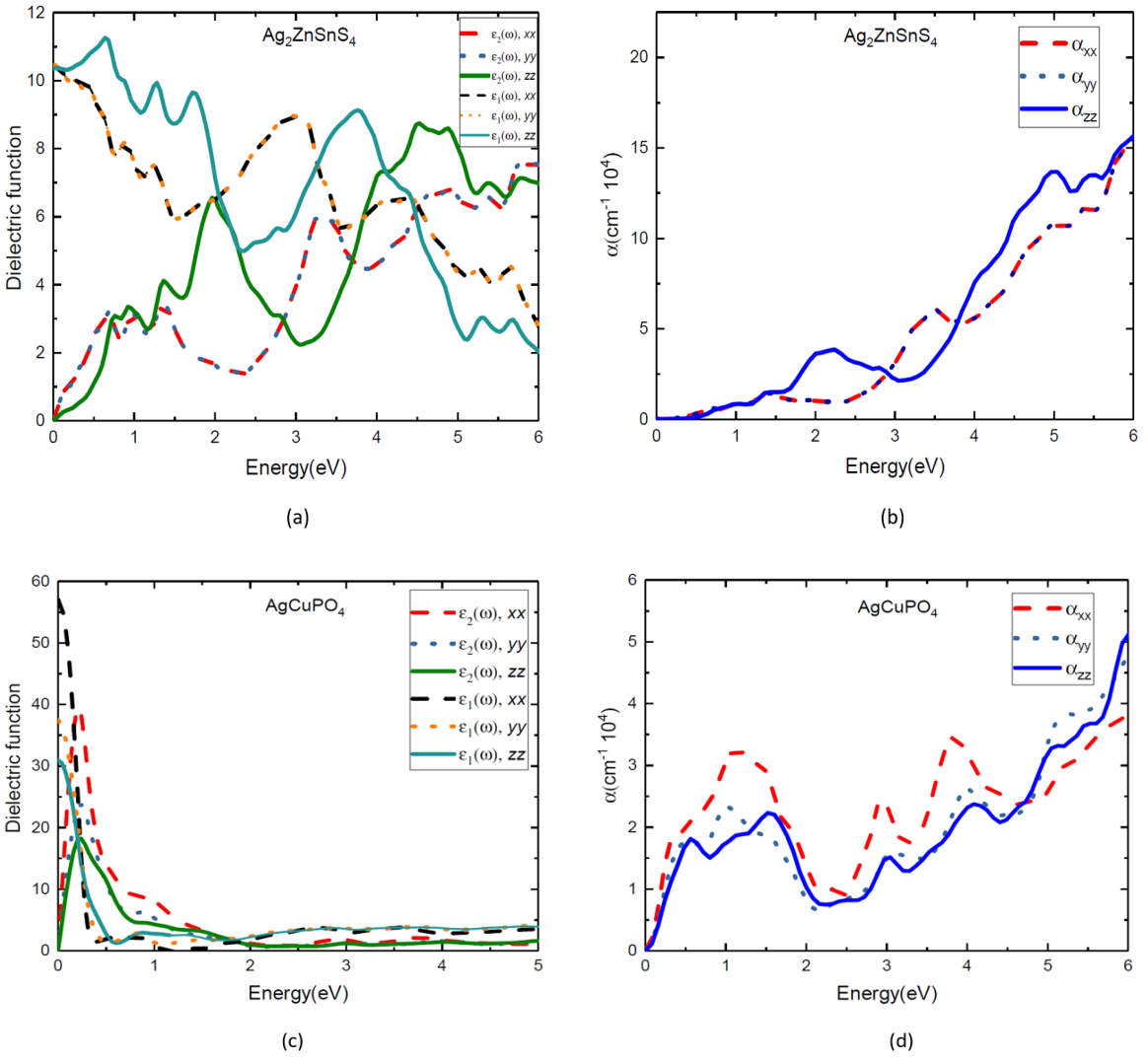

Fig. 7. Calculated dielectric function (a and c) and absorption coefficients (b and d) of $AgCuPO_4$ and Ag_2ZnSnS_4, respectively along *x*, *y* and *z* directions.

Table 4. Calculated static dielectric constants from optical studies for $Au_2Cs_2I_6$, Ag_2GeBaS_4, Ag_2ZnSnS_4 and $AgCuPO_4$. Supercell size used for the phonon study and the calculated zero-point energy (ZPE) for the studied compounds also listed below.

Compounds	GGA	HSE	Supercell size	ZPE
$Au_2Cs_2I_6$	14.04	11.09	3X3 X 3	0.3
Ag_2GeBaS_4	7.48	7.09	3 X 3 X 2	0.24

Ag_2ZnSnS_4	10.45	10.42	4 X 4 X 2	0.25
$AgCuPO_4$	64.86	41.84	2 X 1 X 2	0.84

Conclusions

In summary, we have carried out a comprehensive study of the structural, mechanical, and optical properties of $Au_2Cs_2I_6$, Ag_2GeBaS_4, Ag_2ZnSnS_4 and $AgCuPO_4$ by employing the range-separated hybrid functional, Heyd–Scuseria–Ernzerhof (HSE06). Our results revealed that HSE06 could give a more accurate description of the electronic band structure compared to GGA+U that was employed earlier on these materials. The phonon calculations revealed that $Au_2Cs_2I_6$, Ag_2GeBaS_4, and Ag_2ZnSnS_4 compounds are dynamically stable, as no imaginary frequency was observed. Zero-point energy for all the dynamically stable compounds are calculated. The mechanical properties such as Young's modulus, the bulk modulus, the shear modulus and the Poisson's ratio are calculated from the values of the elastic constants. Our elastic constant calculations illustrate that all four compounds are mechanically stable. The calculated G/B values are lesser than 0.5 for these compounds, and this confirms the ductile nature of the materials.

Numerical results for the static and the dynamic dielectric functions are provided using GGA and HSE06 methods. As expected, GGA overestimates the static dielectric constant. Interestingly, we also observe additional absorption peaks appear in the optical spectra of these four IBs compounds, accompanied by a broadened light absorption energy range and high absorption intensity. Our detailed studies of electronic and optical properties of these four materials reveal of them are potential candidates for photovoltaic application, especially for the development of third-generation intermediate band solar cells.

Acknowledgment

The authors gratefully acknowledge the Western Norway University of Applied Sciences for financially supporting the project and UNINETT Sigma2 for computing facilities of project numbers NN2867K and NN2875K, which have been used to conduct the calculations presented in this article, and MR gratefully acknowledge Dr. Frederico Bianchini for fruitful discussions.

Reference

(1) Luque, A.; Martí, A.; Stanley, C. Understanding intermediate-band solar cells. *Nature Photonics* **2012,** *6* (3), 146-152.

(2) Luque, A.; Marti, A. A metallic intermediate band high efficiency solar cell. *Progress in Photovoltaics: Research and Applications* **2001,** *9* (2), 73-86.
(3) Shockley, W.; Queisser, H. J. Detailed balance limit of efficiency of p-n junction solar cells. *Journal of applied physics* **1961,** *32* (3), 510-519.
(4) Luque, A.; Martí, A. Increasing the efficiency of ideal solar cells by photon induced transitions at intermediate levels. *Physical Review Letters* **1997,** *78* (26), 5014.
(5) Palacios, P.; Aguilera, I.; Sánchez, K.; Conesa, J.; Wahnón, P. Transition-metal-substituted indium thiospinels as novel intermediate-band materials: prediction and understanding of their electronic properties. *Physical review letters* **2008,** *101* (4), 046403.
(6) Green, M. A. Multiple band and impurity photovoltaic solar cells: general theory and comparison to tandem cells. *Progress in Photovoltaics: Research and Applications* **2001,** *9* (2), 137-144.
(7) Nozawa, T.; Arakawa, Y. Detailed balance limit of the efficiency of multilevel intermediate band solar cells. *Applied Physics Letters* **2011,** *98* (17), 171108.
(8) Okada, Y.; Ekins-Daukes, N.; Kita, T.; Tamaki, R.; Yoshida, M.; Pusch, A.; Hess, O.; Phillips, C.; Farrell, D.; Yoshida, K. Intermediate band solar cells: Recent progress and future directions. *Applied physics reviews* **2015,** *2* (2), 021302.
(9) Aguilera, I.; Palacios, P.; Wahnón, P. Optical properties of chalcopyrite-type intermediate transition metal band materials from first principles. *Thin Solid Films* **2008,** *516* (20), 7055-7059.
(10) Han, M.; Zhang, X.; Zeng, Z. The investigation of transition metal doped $CuGaS_2$ for promising intermediate band materials. *RSC Advances* **2014,** *4* (107), 62380-62386.
(11) Aguilera, I.; Palacios, P.; Wahnón, P. Enhancement of optical absorption in Ga-chalcopyrite-based intermediate-band materials for high efficiency solar cells. *Solar Energy Materials and Solar Cells* **2010,** *94* (11), 1903-1906.
(12) Chen, P.; Qin, M.; Chen, H.; Yang, C.; Wang, Y.; Huang, F. Cr incorporation in $CuGaS_2$ chalcopyrite: A new intermediate-band photovoltaic material with wide-spectrum solar absorption. *physica status solidi (a)* **2013,** *210* (6), 1098-1102.
(13) Han, M.; Zhang, X.; Zhang, Y.; Zeng, Z. The group VA element non-compensated n–p codoping in $CuGaS_2$ for intermediate band materials. *Solar Energy Materials and Solar Cells* **2016,** *144*, 664-670.
(14) Rasukkannu, M.; Velauthapillai, D.; Vajeeston, P. Computational Modeling of Novel Bulk Materials for the Intermediate-Band Solar Cells. *ACS Omega* **2017,** *2* (4), 1454-1462.

(15) Gong, W.; Tabata, T.; Takei, K.; Morihama, M.; Maeda, T.; Wada, T. Crystallographic and optical properties of (Cu, $Ag)_2ZnSnS_4$ and (Cu, $Ag)_2ZnSnSe_4$ solid solutions. *physica status solidi (c)* **2015,** *12* (6), 700-703.

(16) Kresse, G.; Furthmüller, J. Efficient iterative schemes for ab initio total-energy calculations using a plane-wave basis set. *Physical review B* **1996,** *54* (16), 11169.

(17) Perdew, J. P.; Burke, K.; Ernzerhof, M. Generalized gradient approximation made simple. *Physical review letters* **1996,** *77* (18), 3865.

(18) Dudarev, S.; Botton, G.; Savrasov, S. Y.; Szotek, Z.; Temmerman, W.; Sutton, A. Electronic Structure and Elastic Properties of Strongly Correlated Metal Oxides from First Principles: LSDA+ U, SIC-LSDA and EELS Study of UO_2 and NiO. *Physica status solidi (a)* **1998,** *166* (1), 429-443.

(19) Kresse, G.; Furthmüller, J. Efficiency of ab-initio total energy calculations for metals and semiconductors using a plane-wave basis set. *Computational materials science* **1996,** *6* (1), 15-50.

(20) Liechtenstein, A.; Anisimov, V.; Zaanen, J. Density-functional theory and strong interactions: Orbital ordering in Mott-Hubbard insulators. *Physical Review B* **1995,** *52* (8), R5467.

(21) Ponniah , V., Density Functional Theory Based Database (DFTBD). University of Oslo, Norway, 2013.

(22) Heyd, J.; Scuseria, G. E. Efficient hybrid density functional calculations in solids: assessment of the Heyd–Scuseria–Ernzerhof screened Coulomb hybrid functional. *The Journal of chemical physics* **2004,** *121* (3), 1187-1192.

(23) Gajdoš, M.; Hummer, K.; Kresse, G.; Furthmüller, J.; Bechstedt, F. Linear optical properties in the projector-augmented wave methodology. *Physical Review B* **2006,** *73* (4), 045112.

(24) Paier, J.; Marsman, M.; Kresse, G. Dielectric properties and excitons for extended systems from hybrid functionals. *Physical Review B* **2008,** *78* (12), 121201.

(25) Hellenbrandt, M. The inorganic crystal structure database (ICSD)—present and future. *Crystallography Reviews* **2004,** *10* (1), 17-22.

(26) Aroyo, M. I.; Perez-Mato, J. M.; Capillas, C.; Kroumova, E.; Ivantchev, S.; Madariaga, G.; Kirov, A.; Wondratschek, H. Bilbao Crystallographic Server: I. Databases and crystallographic computing programs. *Zeitschrift für Kristallographie-Crystalline Materials* **2006,** *221* (1), 15-27.

(27) Aroyo, M. I.; Kirov, A.; Capillas, C.; Perez-Mato, J.; Wondratschek, H. Bilbao Crystallographic Server. II. Representations of crystallographic point groups and space groups. *Acta Crystallographica Section A: Foundations of Crystallography* **2006,** *62* (2), 115-128.

(28) Aroyo, M. I.; Perez-Mato, J.; Orobengoa, D.; Tasci, E.; De La Flor, G.; Kirov, A. Crystallography online: Bilbao crystallographic server. *Bulg. Chem. Commun* **2011,** *43* (2), 183-97.

(29) Togo, A.; Tanaka, I. First principles phonon calculations in materials science. *Scripta Materialia* **2015,** *108*, 1-5.

(30) Togo, A.; Oba, F.; Tanaka, I. First-principles calculations of the ferroelastic transition between rutile-type and $CaCl_2$-type SiO_2 at high pressures. *Physical Review B* **2008,** *78* (13), 134106.

(31) Monkhorst, H. J.; Pack, J. D. Special points for Brillouin-zone integrations. *Physical review B* **1976,** *13* (12), 5188.

(32) Quarton, M.; Oumba, M. Proprietes de l'ion Cu^{2+} dans la structure de AgCuPO4-β. *Materials research bulletin* **1983,** *18* (8), 967-974.

(33) Teske, C. L. Darstellung und Kristallstruktur von Silber-Barium-Thiogermanat (IV). Ag_2BaGeS_4/Preparation and Crystal Structure of Silver-Barium-Thiogermanate (IV). Ag_2BaGeS_4. *Zeitschrift für Naturforschung B* **1979,** *34* (4), 544-547.

(34) Matsushita, N.; Kitagawa, H.; Kojima, N. A Three-Dimensional Iodo-Bridged Mixed-Valence Gold (I, III) Compound, $Cs_2Au^IAu^{III}_6$. *Acta Crystallographica Section C: Crystal Structure Communications* **1997,** *53* (6), 663-666.

(35) Liu, X.; Matsuda, K.; Moritomo, Y.; Nakamura, A.; Kojima, N. Electronic structure of the gold complexes $Cs_2Au_2X_6$ (X= I, Br, and Cl). *Physical Review B* **1999,** *59* (12), 7925.

(36) Ben Yahia, H.; Gaudin, E.; Darriet, J.; Dai, D.; Whangbo, M.-H. Comparison of the crystal structures and magnetic properties of the low-and high-temperature forms of AgCuPO4: Crystal structure determination, magnetic susceptibility measurements, and spin dimer analysis. *Inorganic chemistry* **2006,** *45* (14), 5501-5509.

(37) Riggs, S. C.; Shapiro, M.; Corredor, F.; Geballe, T.; Fisher, I.; McCandless, G. T.; Chan, J. Y. Single crystal growth by self-flux method of the mixed valence gold halides $Cs_2[Au^IX_2][Au^{III}X_4]$(X= Br, I). *Journal of Crystal Growth* **2012,** *355* (1), 13-16.

(38) Johan, Z.; Picot, P. La pirquitasite, Ag2ZnSnS4, un nouveau membre du groupe de la stannite. *Bull. Mineral* **1982,** *105*, 229-235.

(39) Vajeeston, P.; Fjellvåg, H. First-principles study of structural stability, dynamical and mechanical properties of Li_2FeSiO_4 polymorphs. *RSC Advances* **2017,** *7* (27), 16843-16853.

(40) Hase, M.; Matsuda, M.; Kakurai, K.; Ozawa, K.; Kitazawa, H.; Tsujii, N.; Dönni, A.; Kuroe, H. Inelastic neutron scattering study of the spin-gap cuprate β− $AgCuPO_4$. *Physical Review B* **2007,** *76* (13), 134403.

(41) Ashcroft, N. W.; Mermin, N. D. Solid State Physics (Holt, Rinehart and Winston, New York, 1976). *Google Scholar* **2005,** *403*.

(42) Nye, J. F. *Physical properties of crystals: their representation by tensors and matrices*, Oxford university press: 1985.

(43) Reuss, A. Berechnung der fließgrenze von mischkristallen auf grund der plastizitätsbedingung für einkristalle. *ZAMM-Journal of Applied Mathematics and Mechanics/Zeitschrift für Angewandte Mathematik und Mechanik* **1929,** *9* (1), 49-58.

(44) Hill, R. The elastic behaviour of a crystalline aggregate. *Proceedings of the Physical Society. Section A* **1952,** *65* (5), 349.

(45) Pugh, S. XCII. Relations between the elastic moduli and the plastic properties of polycrystalline pure metals. *The London, Edinburgh, and Dublin Philosophical Magazine and Journal of Science* **1954,** *45* (367), 823-843.

(46) Yang, L.-M.; Vajeeston, P.; Ravindran, P.; Fjellvåg, H.; Tilset, M. Revisiting isoreticular MOFs of alkaline earth metals: a comprehensive study on phase stability, electronic structure, chemical bonding, and optical properties of A–IRMOF-1 (A= Be, Mg, Ca, Sr, Ba). *Physical Chemistry Chemical Physics* **2011,** *13* (21), 10191-10203.

Supporting information for Article Titled: "Hybrid density functional study of $Au_2Cs_2I_6$, Ag_2GeBaS_4, Ag_2ZnSnS_4 and $AgCuPO_4$ for the Intermediate band solar cells"

Murugesan Rasukkannu*[1], Ponniah Vajeeston[2] , Dhayalan Velauthapillai[1],
[1]*Western Norway University of Applied Sciences, Department of Computing, Mathematics and Physics, Inndalsveien 28, Box 5063, Bergen, Norway*

[2]*Center for Materials Science and Nanotechnology, Department of Chemistry, University of Oslo, Box 1033 Blindern N-0315, Oslo, Norway*

Supplementary data includes tables, list of computed compounds and figures

From Fig. S1, Ag_2GeBaS_4 IB is mainly contributed from the S-3p and small extraction from Ag-5s and Ba-6s states at 0.9 eV. The calculated DOS and PDOS values of Ag_2ZnSnS_4 presented in Fig. S2, Ag-5s and Sn-5p states contribute the IB. From Fig.S3, we observed that the calculated DOS and PDOS of $AgCuPO_4$. The IB derived from Ag-4d and Cu-3d states.

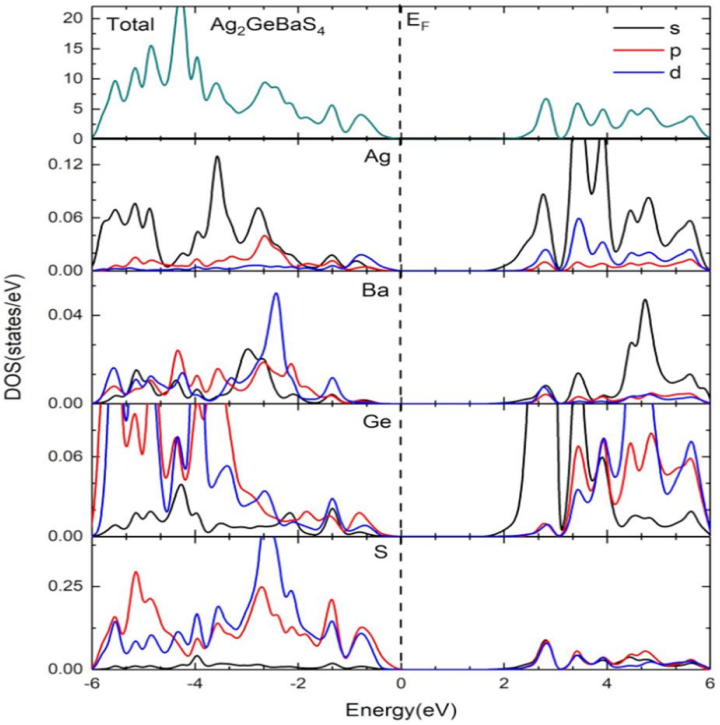

Fig. S1. Calculated total and site projected density of states of Ag_2GeBaS_4. The Fermi level is set to zero and marked by a vertical dotted line.

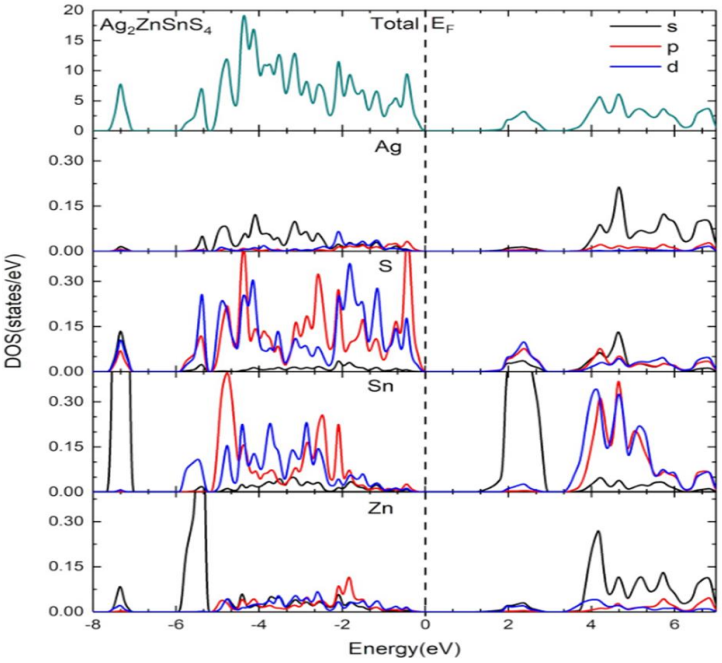

Fig. S2. Calculated total and site projected density of states of Ag_2ZnSnS_4. The Fermi level is set to zero and marked by a vertical dotted line.

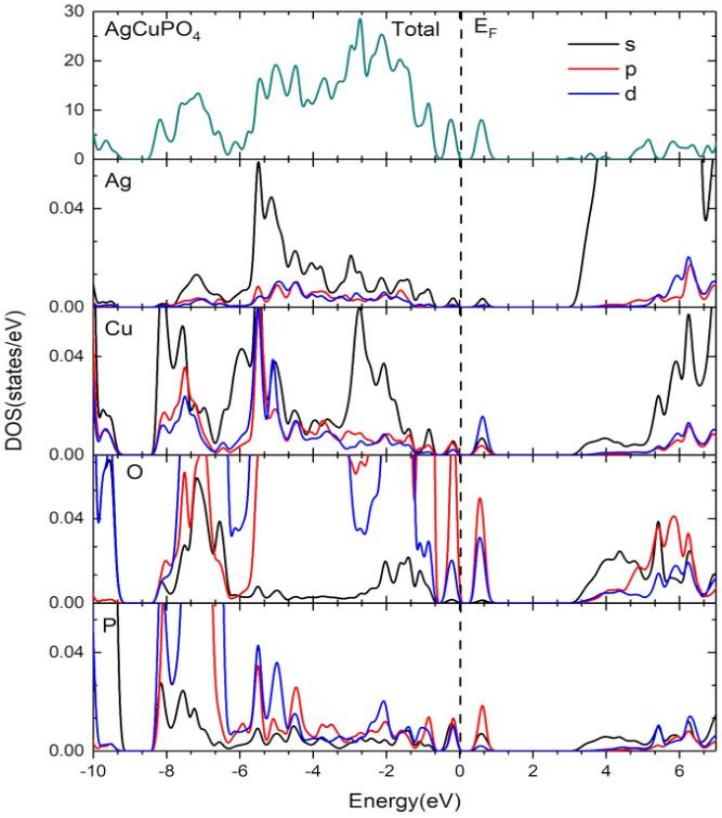

Fig. S3. Calculated total and site projected density of states of $AgCuPO_4$. The Fermi level is set to zero and marked by a vertical dotted line.

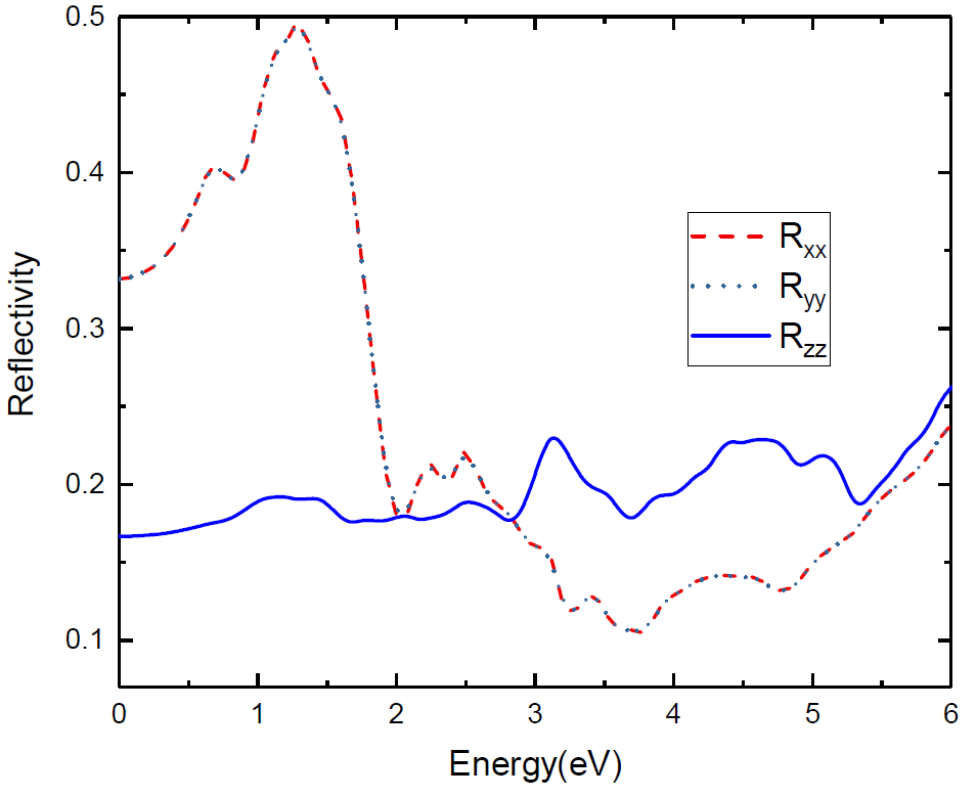

Fig. S4. Reflectivity of $Au_2Cs_2I_6$ along x, y and z directions.

In the quest of an efficient photovoltaic material, its optical reflectivity plays also vital role. We present results from our study in which first principle calculation is carried out employing hybrid functional HSE06 to calculate the optical reflectivity of the materials of interest. In Fig. S4, we show reflectivity of $Au_2Cs_2I_6$ as function of photon energy in all directions. As compared to other three compounds, anisotropy is more pronounced in $Au_2Cs_2I_6$. We notice that the reflectivity is 0.35 – 0.5 in the infrared region and the value drops in the high energy region along *x* and *y* directions. In the *z*-direction, we notice that the reflectivity is 0.185 in the infrared region and 0.165-0.24 in the visible region with some peaks. It is also noticed that the reflectivity of $Au_2Cs_2I_6$ is less in visible region, which indicates $Au_2Cs_2I_6$ can be used as photovoltaic applications.

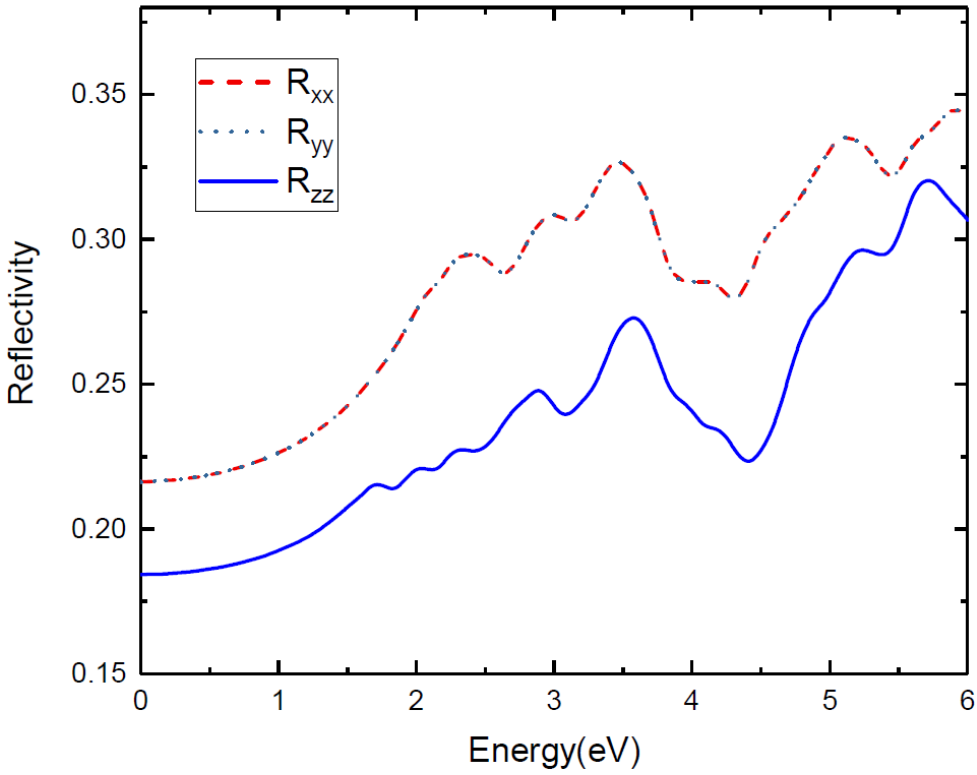

Fig. S5. Reflectivity of Ag_2GeBaS_4 along x, y and z directions.

We show reflectivity of Ag_2GeBaS_4 as function of photon energy in *x*, *y* and *z* directions in the Fig.S5. We notice that the reflectivity 0.165 – 0.24 present in the infrared region and low-energy of visible region along *z*-direction. At 3 eV, the reflectivity drops by small values and then the value increases in the high energy region along *z*-direction. In *x* and *y* direction, we notice that the reflectivity 0.22-0.32 present in the infrared region and visible region with some peaks. It is also noticed that the reflectivity of Ag_2GeBaS_4 is little high in visible region along *x, y* and *z* directions.

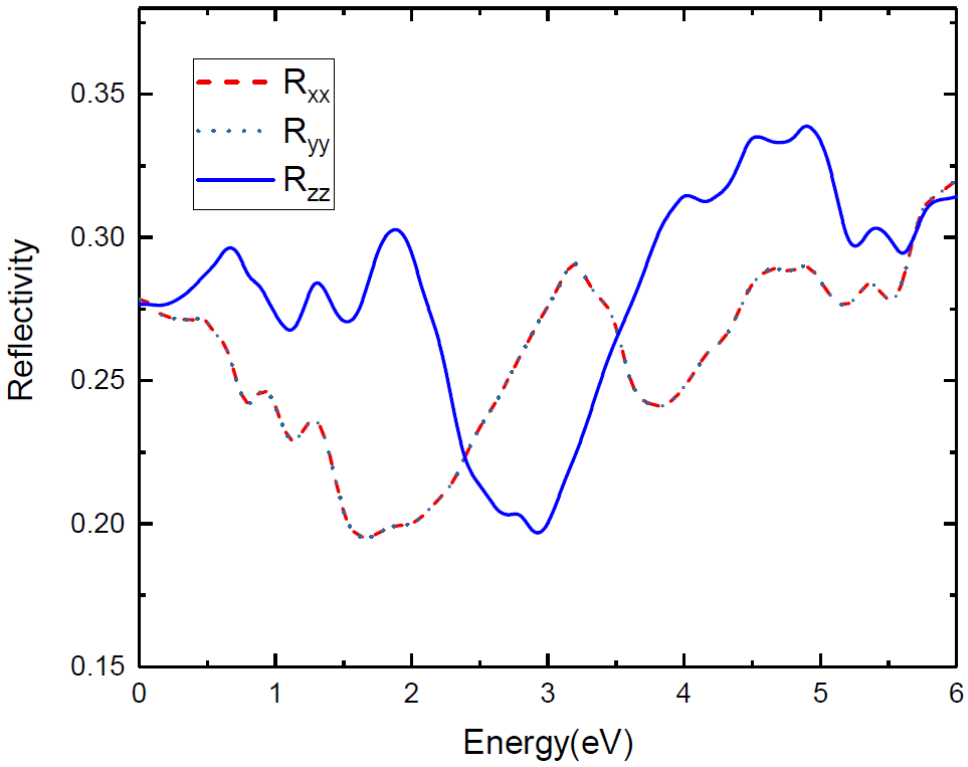

Fig. S6. Reflectivity of Ag_2ZnSnS_4 along x, y and z directions.

The reflectivity of Ag_2ZnSnS_4 is high at 0.6 and 2 eV photon energy and very low at 3 eV photon energy for *z*-direction as shown in Fig.S6. However, the reflectivity is very low at 1.5 – 2 eV along *x* and *y* directions, which indicates this material, can be used as photovoltaic applications.

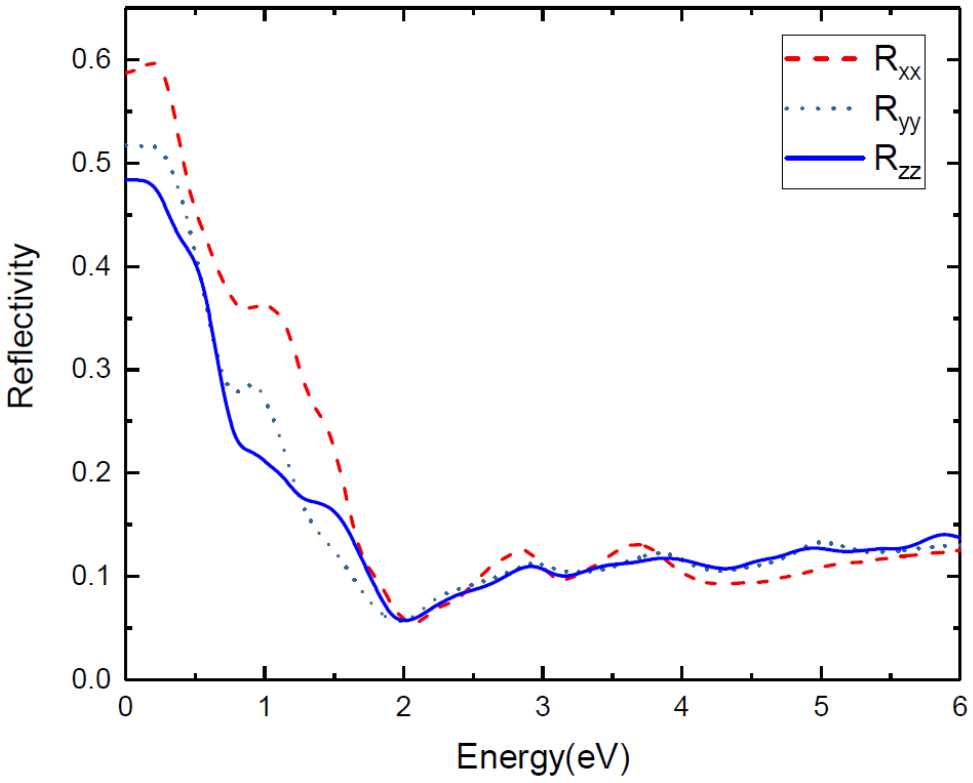

Fig. S7. Reflectivity of $AgCuPO_4$ along x, y and z directions.

In Fig. S7, we show reflectivity of the $AgCuPO_4$ as function of photon energy in all direction. We notice that the reflectivity 0.1–0.59 present in the infrared region and the value drops in the visible region along *x*, *y* and *z* directions. It is also noticed that the reflectivity of $AgCuPO_4$ is less in visible region in all directions, which indicates this material can be used as photovoltaic applications. From the imaginary part of the dielectric function, absorption coefficients and electronic band structures, we can conclude that all four compounds exhibit three-level optical transitions. This will lead to enhanced light absorption in the extended visible region.

Chapter 9

Publication III

A first-principle study of the electronic, mechanical and optical properties of inorganic perovskite Cs_2SnI_6 for intermediate-band solar cells

Murugesan Rasukkannu[1], Dhayalan Velauthapillai[1], Ponniah Vajeeston[2]

[1]*Western Norway University of Applied Sciences, Department of Computing, Mathematics and Physics, Inndalsveien 28, Box 5063, Bergen, Norway*

[2]*Center for Materials Science and Nanotechnology, Department of Chemistry, University of Oslo, Box 1033 Blindern N-0315, Oslo, Norway*

Published in

Materials Letters

(Elsevier)

*Vol. 2*18 **2018**, Page 233-236

Materials Letters 218 (2018) 233–236

Contents lists available at ScienceDirect

Materials Letters

journal homepage: www.elsevier.com/locate/mlblue

A first-principle study of the electronic, mechanical and optical properties of inorganic perovskite Cs_2SnI_6 for intermediate-band solar cells

Murugesan Rasukkannu [a], Dhayalan Velauthapillai [a], Ponniah Vajeeston [b,*]

[a] Western Norway University of Applied Sciences, Department of Computing, Mathematics and Physics, Inndalsveien 28, Box 5063, Bergen, Norway
[b] Center for Materials Science and Nanotechnology, Department of Chemistry, University of Oslo, Box 1033 Blindern N-0315, Oslo, Norway

ARTICLE INFO

Article history:
Received 15 January 2018
Received in revised form 6 February 2018
Accepted 7 February 2018
Available online 8 February 2018

Keywords:
HSE06
Cs_2SnI_6
Simulation and modelling
Solar energy materials
Perovskite
Optical materials and properties

ABSTRACT

The power conversion of perovskite solar cells has increased steadily and reached 22.1%, recently. This has led the researchers to study lead-free halide perovskite materials like Cs_2SnI_6 due to the toxic nature of lead used in the record-breaking organic-inorganic perovskite structures. Since the presence of an intermediate band in semiconductors leads to enhancement of efficiency of the solar cells, we have also investigated the electronic structure of Cs_2SnI_6, to find whether the intermediate band is likely to exist in the middle of the band gap. The computational results for the electronic band structure and density of states indicate that Cs_2SnI_6 contains an intermediate band (IB). Additional absorption peaks that appear in the optical spectra of this material presented in this paper explicitly confirm this. All these studies and the presence of an IB that we identified in Cs_2SnI_6 suggests that Cs_2SnI_6 may have high potential used as intermediate band solar cell material.

1. Introduction

The intermediate band solar cells (IBSCs) are designed to provide superior energy efficiency. Initially, IBSCs were suggested by Wolf [1]. Later, Luque and Marti revealed that IBSCs could achieve very high solar power efficiencies conversion [2]. The well-designed of the IBSC concept has encouraged researchers to search for novel materials with an intermediate band (IB) that would satisfy the requirements regarding photon absorption and charge collection. In general, IB materials are identified by the splitting of the bandgap into two or more sub-bandgaps [3]. In IB materials, an electron is excited from the valence band (VB) to the conduction band (CB) through IB. The electrons transit from VB to IB, later from IB to CB by the absorption of sub-bandgap energy photons. It will add up to the electrons transition from VB to CB by conventional VB to CB photon absorptions. Prominent examples of bulk intermediate bands are previously studied [4].

Recently, the power conversion of inorganic perovskite material Cs_2SnI_6 has received attention as an alternative to the Pb-based halide perovskite due to the toxicity of lead and poor chemical stability of Cs_2PbI_6. Cs_2SnI_6 has shown to feature enhanced stability and efficiency in ambient environments compared with lead-based perovskite materials [5]. In this present work, we study the electronic properties of halide perovskite material Cs_2SnI_6 with the aim of identifying IB candidate for solar cell materials by employing density functional theory (DFT). In this work, we employ a screened–exchange hybrid density functional Heyd-Scuseria-Ernzerhof (HSE06) within the density functional calculation of electronic structure and density of states for Cs_2SnI_6. Furthermore, we study its dynamical and mechanical stability. All the results obtained in this work indicate that Cs_2SnI_6 perovskite material is a suitable candidate for IBSC application.

2. Computational details

Calculations were carried out by employing Heyd–Scuseria–Ernzerhof (HSE06). The Perde–Burke–Ernzerhof (PBE) version of the generalized gradient approximation(GGA) based DFT methods using the projector augmented plane-wave (PAW) [6] implementation of the Vienna ab initio simulation package (VASP) [7]. The ionic coordinates are optimised with an energy convergence threshold of 10^{-6} eV per atom. The structural relaxations were undertaken until forces were 0.05 eV $Å^{-1}$. In the HSE06 method, the screened parameter is set to 0.2 A^{-1} and 30% of the screened Hartree-Fock(HF) exchange is mixed with the PBE exchange functional [8]. The cut-off energy for the plane-wave basis set is 600

* Corresponding author.
E-mail addresses: rmu@hvl.no (M. Rasukkannu), vdh@hvl.no (D. Velauthapillai), ponniah.vajeeston@kjemi.uio.no (P. Vajeeston).

https://doi.org/10.1016/j.matlet.2018.02.034
0167-577X/

eV, and we use a 12 × 12 × 12 Γ-centered Monkhorst-pack k-point mesh for sampling the Brillouin zone (BZ).

A frozen phonon calculation is used within the supercell approach, as implemented in the phonopy program, to obtain the phonon dispersion curve and phonon density of states [9]. The dynamical matrices were calculated from the force constants, and phonon DOS curves were computed using a Monkhorst-Pack scheme for BZ sampling. The PAW methodology is used for the calculation of macroscopic dielectric matrix including local field effects in density functional approximation [10].

3. Results and discussions

3.1. Structural properties

Cs_2SnI_6 stabilizes into the face-centered-cubic (fcc) with the space group Fm–3 m (the anti-fluorite structure) and the structure type of K_2PtCl_6. The lattice parameter of this crystal is a = 11.65 Å [10]. As shown in Fig. 1a, the unit cell is composed of eight Cs_2^+ cations at the tetragonal interstitials and four $[SnI_6]^{2-}$ octahedra at the corners and at the face centres. Alternatively, Cs_2SnI_6 can form a defective variant of the perovskite $CsSnI_3$ as can be observed by comparing Fig. 1a and 1b. Fig. 1b shows a 2 × 2 × 2 supercell of $CsSnI_3$ in which the $[SnI_6]^{2-}$ octahedra bond to each other by sharing corners. The Cs_2SnI_6 structure is obtained by removing half of the Sn atoms at each centre of the $[SnI_6]^{2-}$ octahedron at intervals (i.e., the edge centres and the body centre in Fig. 1b), and hence the corner-shared $[SnI_6]^{2-}$ octahedra in Fig. 1b become isolated in Cs_2SnI_6 (Fig. 1a). After the half of the Sn atoms are removed, the $[SnI_6]^{2-}$ octahedra shrink slightly, leading to the smaller intra-octahedral I═I bond lengths and the smaller Sn═I bond lengths [11] in Cs_2SnI_6 than that in $CsSnI_3$. According to the survey of perovskite-based compounds in the ICSD database [11], Cs_2SnI_6 is cubic(Fm-3 m) due to higher radius ratio and higher octahedral factor. It is important to note that the Cs_2SnI_6 is one of the stable compound than the $CsSnI_3$ phase.

3.2. Electronic structure and effective mass calculation

From the electronic structure (see Fig. 2a and Fig. 2b), we found that Cs_2SnI_6 could have an intermediate band even if a second band of the CB minimum extents to 4.98 eV from VB maximum. According to Green [12], cells representing VB to IB and IB to CB transitions can be regarded as two cells in series, and the VB to CB transition can represent a parallel cell. Therefore, we could use the VB to IB and IB to CB transitions for Cs_2SnI_6 and hence obtain a higher performance than a single bandgap solar cell. From Fig. 2a, the band structure of Cs_2SnI_6 exhibits a VB to IB transition as a direct bandgap at the Γ k-point of 1.48 eV (experimental band gap varies from 1.3 to 1.6 eV [13]). The indirect band gap between the top of the IB to bottom of CB is 2.13 eV and width of IB is 1.35 eV. From Fig. 2b, the intermediate band minimum is mainly derived from the Sn-5 *s* and I-5*p* states. The VB maximum contributed by I-5*p* states and the CB is derived from Sn-4*d* and I-5*p* states. The dispersion of Cs_2SnI_6 IB is very high at Γk-point (as shown in Fig. 2b).

The calculation of the effective mass (EM) is crucial for a detailed study of energy levels in solar devices. The conductivity of the effective masses of electrons and holes affect the mobility, electrical resistivity, and free-carrier optical response of photovoltaic applications [14]. For the EM calculation, we have employed the effective mass calculator (EMC) [14]. EMC implements the calculation of the effective masses at the bands extreme using finite difference method (not the band fitting method). Effective masses of Cs_2SnI_6 calculated by GGA and HSE06 are listed in Table 1. We noted that the EM of holes is found to be heavier than EM of electrons. This result can be understood from the fact that the VB is derived from unhybridized I-*p* state, which is less dispersed compared with the CB that is derived from antibonding I anions and Sn site cations. The EM of electron photovoltaic materials such as silicon (Si) and gallium arsenide (GaAs) are 0.26m_e and 0.12m_e [15] respectively. The calculated EM of electrons of the Cs_2SnI_6 is 0.152m_e (GGA calculation), the EM of the electron is low for Cs_2SnI_6 compare to Si. However, the difference between Si and Cs_2SnI_6 is 0.04m_e for HSE06 calculation. Still, this perovskite material can have high electron mobility due to more dispersed in IB and CB.

3.3. Optical properties

The optical property has a high influence on the solar cell materials. To investigate the optical behavior of Cs_2SnI_6, we have calculated the optical dielectric function $\varepsilon(\omega) = \varepsilon_1(\omega) + i\varepsilon_2(\omega)$. The absorption coefficients of Cs_2SnI_6 are presented in Fig. 3a. The peaks are observed are 1.48 eV, 3.7 eV and 5.7 eV. The corresponding electronic transition from VB to IB is at around 1.5 eV (direct band gap from the band structure), IB to CB is at around 3.7 eV. According to Wang *et al.* [16], Cs_2SnI_6 exhibits an absorption

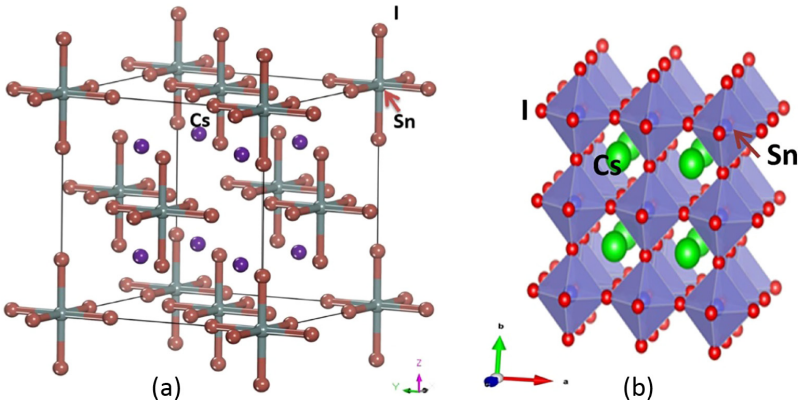

Fig. 1. Crystal structures for (a) Cs_2SnI_6, (b) $CsSnI_3$. The legends for the different kinds of atoms are given in the illustration.

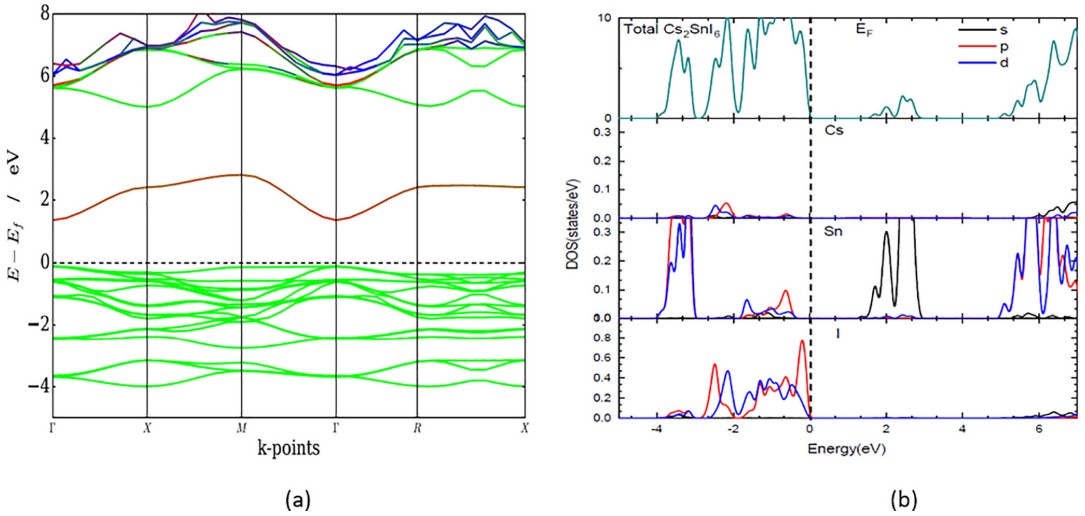

Fig. 2. Calculated electronic band structure of (a) Cs_2SnI_6. Colour code: red line – s states, green line – p states, blue – d states, (b) total and site projected density of states of Cs_2SnI_6. The Fermi level is set to zero. (For interpretation of the references to colour in this figure legend, the reader is referred to the web version of this article.)

Table 1
The calculated effective mass of Cs_2SnI_6, effective masses of light holes (m^*_{lh}), heavy holes (m^*_{hh}) and electrons (m^*_e).

Compound	Plane Directions	GGA			HSE06		
		m^*_{lh}·m_e	m^*_{hh}·m_e	m^*_e·m_e	m^*_{lh}·m_e	m^*_{hh}·m_e	m^*_e·m_e
Cs_2SnI_6	100	0.534	1.4173	0.152	0.643	1.491	0.306

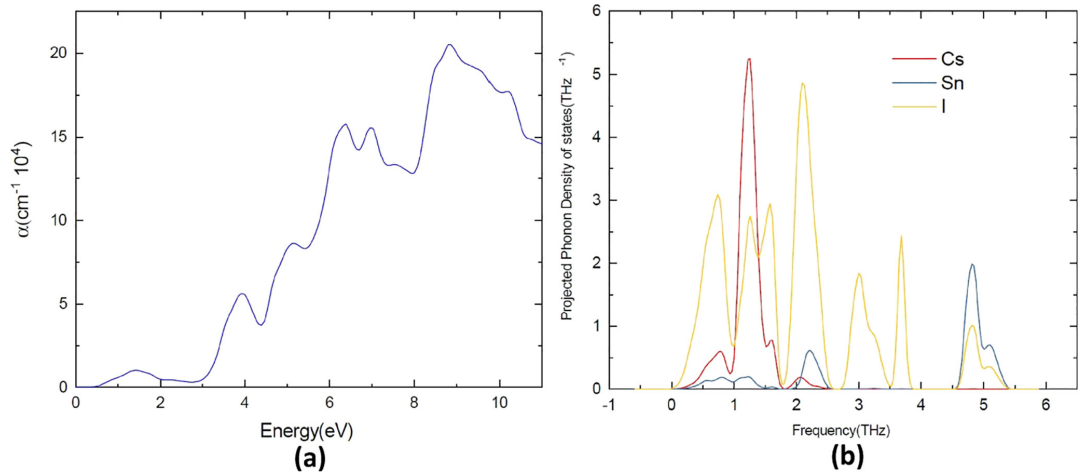

Fig. 3. (a) The calculated optical absorption coefficients of Cs_2SnI_6, (b) Calculated site projected phonon density of states of Cs_2SnI_6.

coefficient at a photon energy of 1.5 eV and Cs_2SnI_6 also exhibits a remarkable absorption peak at 1.48 eV, reported by Qiu et al. [17]. From Fig. 3b, the absorption peak is also observed at a photon energy of 1.48 eV and additional peaks are observed from 2 eV to 6 eV. We noted the VB to CB transition is at 5.7 eV, but it is well suited for solar cell application. According to the PDOS in Fig. 2b, the sub-bandgaps 1.4 eV attributed to the states Sn-5 *s* and I-5*p* states. We observed that the absorption starts to increase from the low energy region due to the formation of intermediate states in between VB and CB. Besides, the optical absorption begins at 0.5

eV, and it fails to show the IB to CB transition by the HSE06 method. Hence, the additional absorption peaks that appear in the optical spectra of this material presented in this study confirmed that Cs_2SnI_6 contains an IB.

3.4. Lattice dynamic stability and mechanical stability

The Cs_2SnI_6 site projected phonon density of states, calculated at the equilibrium volumes, is presented in Fig. 3b. From Fig. 3. (a) The calculated optical absorption coefficients of Cs2SnI6, (b) Calculated site projected phonon density of states of Cs2SnI6. The vibrational modes are spread over from 0 to 5.5 THz. The Cs-I stretching modes are present between 4.5 and 5.4 THz and the lattice vibrational modes for the Cs, Sn are present in the 1 to −1.8 THz range and in the 4.5 to −5.4 THz range respectively. To understand the mechanical stability of the Cs_2SnI_6 phase, we have calculated the single-crystal elastic constants using the finite strain technique. The elastic constants of a material characterise its response to applied stress or, conversely, the stress required to maintain a given deformation. The cubic crystal system has the simplest form of an elastic matrix, with only three independent constants: C_{11} = 17.7 GPa, C_{12} = 11.8 GPa, and C_{44} = 8.99. The three Born stability criteria for the cubic system are well known and satisfied for Cs_2SnI_6, $C_{11} - C_{12} > 0$, $C_{11} + 2C_{12} > 0$ and $C_{44} > 0$. Properties such as bulk-moduli(B) = 13.72 GPa, shear moduli(G) = 7.55 GPa, Young's moduli(E) = 19.14 GPa and Poisson's ratio(σ) = 0.27 can be calculated from the values of elastic constants. The calculated compressibility value = 0.07(GPa^{-1}) of this polymorph suggested that this compound is very soft material. The calculated G/B value of this compound is lower than 0.55, suggesting Cs_2SnI_6 is ductile characteristics.

Conclusion

In summary, first-principle calculations employing the hybrid HSE06 method have undertaken to compute the electronic structures, effective mass and optical properties of the Cs_2SnI_6 compound. The calculated electronic structures and absorption coefficient confirmed that Cs_2SnI_6 contains intermediate band. Furthermore, we calculated the lattice stability and mechanical stability that confirmed Cs_2SnI_6 is dynamically stable and mechanically stable respectively. Hence, this compound could be used as an efficient photovoltaic material.

Acknowledgments

The authors gratefully acknowledge the Bergen University College for financially supporting and NOTUR for computing facilities with the project numbers NN2867K and NN2875K, which have used to conduct the calculations presented in this article.

References

[1] M. Wolf, Limitations and possibilities for improvement of photovoltaic solar energy converters: Part I: considerations for earth's surface operation, Proc. IRE 48 (7) (1960) 1246–1263.
[2] A. Luque, A. Martí, Increasing the efficiency of ideal solar cells by photon induced transitions at intermediate levels, Phys. Rev. Lett. 78 (26) (1997) 5014.
[3] A. Luque, A. Martí, C. Stanley, Understanding intermediate-band solar cells, Nat. Photonics 6 (3) (2012) 146–152.
[4] M. Rasukkannu, D. Velauthapillai, P. Vajeeston, Computational modeling of novel bulk materials for the intermediate-band solar cells, ACS Omega 2 (4) (2017) 1454–1462.
[5] Y. Cai, W. Xie, H. Ding, Y. Chen, K. Thirumal, L.H. Wong, N. Mathews, S.G. Mhaisalkar, M. Sherburne, M. Asta, computational study of halide perovskite-derived A2bX6 inorganic compounds: chemical trends in electronic structure and structural stability, Chem. Mat. 29 (18) (2017) 7740–7749.
[6] P.E. Blöchl, Projector augmented-wave method, Phys Rev B 50 (24) (1994) 17953.
[7] G. Kresse, J. Furthmüller, Efficient iterative schemes for ab initio total-energy calculations using a plane-wave basis set, Phys Rev B 54 (16) (1996) 11169.
[8] J. Heyd, G.E. Scuseria, Efficient hybrid density functional calculations in solids: assessment of the Heyd–Scuseria–Ernzerhof screened Coulomb hybrid functional, J. Chem. Phys 121 (3) (2004) 1187–1192.
[9] A. Togo, F. Oba, I. Tanaka, First-principles calculations of the ferroelastic transition between rutile-type and $CaCl_2$-type SiO_2 at high pressures, Phys. Rev. B 78 (13) (2008) 134106.
[10] M. Gajdoš, K. Hummer, G. Kresse, J. Furthmüller, F. Bechstedt, Linear optical properties in the projector-augmented wave methodology, Phys. Rev. B 73 (4) (2006) 045112.
[11] W. Werker, Die Krystallstruktur des Rb_2SnJ_6 und Cs_2SnJ_6, Recl. Trav. Chim. Pays-Bas 58 (3) (1939) 257–258.
[12] M.A. Green, Multiple band and impurity photovoltaic solar cells: general theory and comparison to tandem cells, Prog. Photovoltaics Res. Appl. 9 (2) (2001) 137–144.
[13] B. Lee, C.C. Stoumpos, N. Zhou, F. Hao, C. Malliakas, C.-Y. Yeh, T.J. Marks, M.G. Kanatzidis, R.P. Chang, Air-stable molecular semiconducting iodosalts for solar cell applications: Cs_2SnI_6 as a hole conductor, J. Am. Chem. Soc 136 (43) (2014) 15379–15385.
[14] A. Fonari, C. Sutton, Validation of the effective masses calculated using finite difference method on a five-point stencil for inorganic and organic semiconductors, arXiv preprint arXiv:1302.4996 (2013).
[15] B. Van Zeghbroeck, Principles of Semiconductor Devices, Colarado University, 2004.
[16] G. Wang, D. Wang, X. Shi, Electronic structure and optical properties of Cs 2 AX 2' X 4 (A = Ge, Sn, Pb; X', X = Cl, Br, I), AIP Adv. 5 (12) (2015) 127224.
[17] X. Qiu, B. Cao, S. Yuan, X. Chen, Z. Qiu, Y. Jiang, Q. Ye, H. Wang, H. Zeng, J. Liu, From unstable CsSnI 3 to air-stable Cs 2 SnI 6: A lead-free perovskite solar cell light absorber with bandgap of 1.48 eV and high absorption coefficient, Sol. Energy Mater. Sol. Cells 159 (2017) 227–234.

Chapter 10

Publication IV

Properties of novel non-silicon materials for the photovoltaic applications: A first-principle insight

Murugesan Rasukkannu[1], Dhayalan Velauthapillai[1], Federico Bianchini[2], Ponniah Vajeeston[2]

[1]*Western Norway University of Applied Sciences, Department of Computing, Mathematics and Physics, Inndalsveien 28, Box 5063, Bergen, Norway*

[2]*Center for Materials Science and Nanotechnology, Department of Chemistry, University of Oslo, Box 1033 Blindern N-0315, Oslo, Norway*

Published in

Materials

(MDPI)

Vol. 11 **2018**, Page 2006

materials

MDPI

Article

Properties of Novel Non-Silicon Materials for Photovoltaic Applications: A First-Principle Insight

Murugesan Rasukkannu [1,*], Dhayalan Velauthapillai [1], Federico Bianchini [2] and Ponniah Vajeeston [2]

[1] Department of Computing, Mathematics and Physics, Western Norway University of Applied Sciences, Inndalsveien 28, 5063 Bergen, Norway; vdh@hvl.no

[2] Department of Chemistry, Center for Materials Science and Nanotechnology, University of Oslo, Box 1033, Blindern, N-0315 Oslo, Norway; federico.bianchini@smn.uio.no (F.B.); ponniah.vajeeston@kjemi.uio.no (P.V.)

* Correspondence: rmu@hvl.no; Tel.: +47-5558-7786

Received: 18 September 2018; Accepted: 11 October 2018; Published: 17 October 2018

Abstract: Due to the low absorption coefficients of crystalline silicon-based solar cells, researchers have focused on non-silicon semiconductors with direct band gaps for the development of novel photovoltaic devices. In this study, we use density functional theory to model the electronic structure of a large database of candidates to identify materials with ideal properties for photovoltaic applications. The first screening is operated at the GGA level to select only materials with a sufficiently small direct band gap. We extracted twenty-seven candidates from an initial population of thousands, exhibiting GGA band gap in the range 0.5–1 eV. More accurate calculations using a hybrid functional were performed on this subset. Based on this, we present a detailed first-principle investigation of the four optimal compounds, namely, $TlBiS_2$, Ba_3BiN, Ag_2BaS_2, and ZrSO. The direct band gap of these materials is between 1.1 and 2.26 eV. In the visible region, the absorption peaks that appear in the optical spectra for these compounds indicate high absorption intensity. Furthermore, we have investigated the structural and mechanical stability of these compounds and calculated electron effective masses. Based on in-depth analysis, we have identified $TlBiS_2$, Ba_3BiN, Ag_2BaS_2, and ZrSO as very promising candidates for photovoltaic applications.

Keywords: HSE06; non-silicon; non-conventional solar cells; PV materials; hybrid density function; BSE

1. Introduction

The solar energy reaching the earth amounts to approximately ten thousand times the primary energy usage by the world population. Solar photovoltaic cells are among the most important technologies for clean energy production. It is predicted that in future, the power from solar photovoltaic modules will reach the terawatt level [1]. Photovoltaic (PV) technology is currently dominated by silicon solar cells. If we look at the worldwide scenario, more than 80% of the installed PV modules are mainly mono or multi-crystalline silicon based [1]. However, researchers are making considerable efforts to develop solar cells based on alternative materials because silicon is an indirect band gap material with a low absorption coefficient. Novel materials considered for PV applications include copper zinc tin sulfide (CZTS), ternary, binary, and multinary compounds with a direct band gap, enabling high absorption properties. High photon conversion efficiency and low production cost are the other desired features of these alternative materials. There is also considerable interest in the research community to find ways to develop solar cells that have efficiencies greater than the Shockley-Queisser limit of 32% [2].

The development of non-silicon materials is a very active field, and several significant signs of progress have been made recently [1]. In the future, non-silicon materials will most likely be produced using thin film technologies, with a resulting device thickness in the order of 2 μm. Despite the crucial role played by these compounds for the next generation of energy materials, the current knowledge of the optical and electronic properties of these compounds is inadequate. Non-silicon materials such as organic semiconductors may become the main candidates for future photovoltaic devices, even though they have low stability [3]. To be a promising solar cell material, a semiconductor preferably have a direct band gap with an appropriate band gap value resulting in efficient absorption of the solar spectrum.

Furthermore, it can be used in a junction formation, which is appropriate for guiding the electrical processes involved in energy conversion [4]. A variety of basic materials, GaAs, InP, CdTe, $CuInSe_2$ to name a few, and large band gap materials such as ZnO, CdS, ZnCdS used as window layers in creating heterojunctions have been studied extensively [4]. Reducing production cost is one of the priorities in selecting materials for PV technologies. Compared to mono-crystalline Silicon solar cells, the production cost for poly-crystalline Silicon solar cells is lower, but the efficiency is lower [5]. According to Mitchell [6], materials that require only a few micrometers of thickness to absorb the solar spectrum and photo-carriers effectively are created close to the electrical junction. One way to minimize material usage is to choose direct band gap materials over indirect band gap materials, since direct band gap solar cells could be made substantially thinner [7]. Due to the low absorption, polycrystalline silicon solar cell structures must have a thickness in the range of 200 μm, which makes the overall cost higher. We have earlier reported several non-silicon intermediate band gap materials that can be used for solar cell applications [8,9]. Our main aim in this study is to propose non-silicon based direct band gap materials with highly efficient photoelectric properties such that material costs become lower.

As one of the most effective and accurate computational methods for modelling atomistic systems, density functional theory (DFT) has been widely applied in this work to extensively analyze the electronic band structure of thousand non-silicon based materials in order to identify candidates that have a band gap between 0.5 eV and 1.1 eV. The band structure calculation for these presented materials is based on the generalized gradient approximation (GGA) that underestimates the value of the band gap. However, this technique is efficient and time-effective in terms of computational resources, and it can be used for an initial screening of a large number of compounds. The initial structural parameters of thousand compounds were directly taken from the ICSD database [10], and then the GGA band gap for thousands of non-silicon compounds were calculated in our DFTB database [11]. These are multinary compounds including conductors, semiconductors, and insulators. Among these thousand non-silicon compounds, we considered twenty-seven of them with GGA band gap values in the range of 0.5–1.1 eV (Table S1 of Supplementary Materials). Among these twenty-seven compounds, we identified fourteen compounds as direct band gap semiconductors and thirteen as indirect band gap semiconductors. We carried out a study on both the electronic and optical properties of twenty-seven semiconductors (both direct and indirect). Our study of the optical properties of semiconductor materials showed that four direct band gaps among the twenty-seven materials had higher absorption coefficients in the visible region. Due to the space constraint, the optical properties of all the twenty-seven semiconductors are not presented in the supporting information.

We carry out a comprehensive study on these four materials, namely $TlBiS_2$, Ba_3BiN, Ag_2BaS_2, and ZrSO, and report accurate electronic structure results for these four compounds by employing a more accurate calculation based on the screened–exchange hybrid density functional Heyd-Scuseria-Ernzerhof (HSE06). HSE06 helps to identify the contributions of individual elements to the electronic structure of the compounds. We also study the structural and mechanical stability and the optical properties of these four materials to verify the applicability of these four materials for photovoltaic applications. In a recently published article, we focused on $TlBiS_2$, and have presented electronic band structure and optical spectra based on spin-orbit coupling (SOC) [12].

2. Computational Details

We employed DFT analysis using Vienna ab initio simulation package (VASP, 5.4.1. Feb. 16) with the projected augmented plane-wave (PAW) approach [13] to study the electronic structures of $TlBiS_2$, Ba_3BiN, Ag_2BaS_2, and ZrSO. The Perdew–Burke–Ernzerhof (PBE) functional is used to treat exchange and correlation within the GGA approach [14]. To obtain an improved description of the interaction between oxygen and the transition metal atoms, we used the Hubbard parameter correction (DFT+U), following the rotationally invariant form [15–17]. The full details about the computed *U* and *J* values are presented in the DFTBD database website [11]. These DFT+U calculations are used for the structural optimisation of the considered compounds, as the relaxation using HSE06 is time-consuming and has no significant effect on the structural properties. Ground-state geometries are calculated using the conjugate-gradient algorithm with a force convergence threshold of 10^{-3} eV $Å^{-1}$, and minimizing the stress tensor and the Hellman-Feynman forces. In order to achieve better and detailed band structures, we used the hybrid functional of Heyd–Scuseria–Ernzerhof (HSE06). For the standard HSE06 functional, the screened parameter was assigned to 0.2 A^{-1}, and the screened Hartree-Fock (HF) exchange was set to 30% mixing with the PBE exchange functional [18]. The cut-off energy for the plane-wave basis expansion was set to 600 eV, and for Brillouin zone integration we used a $6 \times 6 \times 6$ Γ-centered Monkhorst-pack **k**-point mesh. In both calculations (i.e., PBE and HSE06), this setting is used.

Solving the Casida's equation is one of the best approaches for determining the dielectric function [19]. We have summed the contributions over a number of $8 \times 8 \times 8$ **k**-points grids, shifted with respect to each other to reproduce$16 \times 16 \times 16$ Γ-centered **k**-points mesh, using a plane-wave cut-off of 410 eV for both GW and Bethe-Salpeter equation (BSE). To get a more accurate peak position and intensities in optical spectra, the optical calculation counts the contribution from 200 electronic bands. For all of these computations, the initial structural parameters were taken directly from the ICSD database [10]. The information about the high symmetric points of the *k*-vector in the Brillouin zone was taken from the Bilbao Crystallographic Server [20–22].

A frozen phonon calculation was performed on suitable supercells of the relaxed structures, generated using the phonopy program (1.9.2). This software is also used to obtain the phonon dispersion curve and the phonon density of states from the converged calculations [23,24]. The atomic displacement of 0.0075 is used, with symmetry considerations to obtain the force constants for the phonon calculations. The displacements in opposite directions along all the axes were incorporated into the calculations to improve the precision. The force calculations were performed using the VASP code (DFT+U level), and the resulting data were imported into PHONOPY. The dynamical matrices were derived from the force constants, and phonon DOS curves were computed using the Monkhorst-Pack scheme [25].

3. Results and Discussion

3.1. Structural Properties

$TlBiS_2$: $TlBiS_2$ has rhombohedral structures with space group D5 3d (R-3m, Space group No. 166), similar to Bi_2Te_3. There are four atoms, namely, 1-Tl, 1-Bi, and 2-S positioned in layers normal to the three-fold axis in the arrangement Tl-S-Bi-S, as shown in Figure 1a. Each Tl/Bi layer is placed between two S layers, which indicates a strong interlayer coupling so that the crystal structure is substantially three-dimensional. Tl, Bi, and S are placed at the (0, 0, 0), (0.5, 0.5, 0.5), and (±u, ±u, ±u) sites, respectively. This structure has inversion symmetry where both Bi and Tl represent inversion centers. The basic $TlBiS_2$ structure is a simple NaCl-type lattice. It is similar to ABQ_2-type compounds (*A*, *B* and *Q* are monovalent atom, trivalent atom and chalcogen respectively). The $TlBiS_2$ structure is rhombohedral along the cubic [111] direction and matching to the *c* axis of the primitive hexagonal arrangement. The sum of the ionic radii for a coordination number (CN) of 6 is 2.87 Å for Bi^{3+}/S^{2-} and 3.34 Å for Tl^{+}/S^{2-} [26]. The experimentally-determined and theoretically-derived bond length matches well for Bi-S, but for the Tl-S distance the value is about 5.3% smaller. Our calculated lattice parameters and the positional parameters all fitted well with the experimental findings (see Table S2) [26].

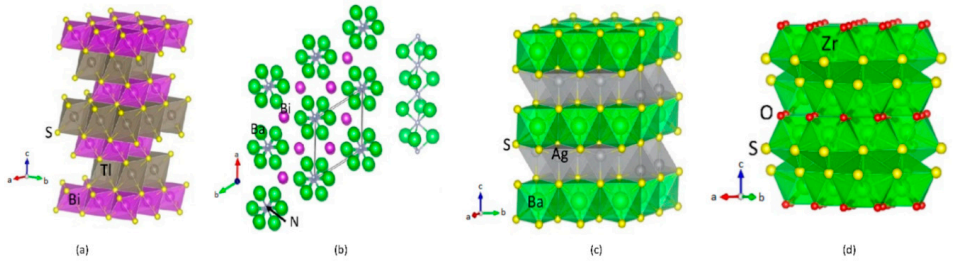

Figure 1. Crystal structures for (**a**) $TlBiS_2$; (**b**) Ba_3BiN; (**c**) Ag_2BaS_2; (**d**) Tetragonal-ZrSO. The illustration shows the legends for the different type of atoms.

Ba_3BiN: (Ba_3N)Bi crystallizes in a hexagonal anti-perovskite variant of the $BaNiO_3$ structure type (*P*63/*mmc*, space group No. 194, *Z* = 2). This phase consists of Ba_6N octahedral units sharing faces formed with three Ba ions according to a rod-like structure along [001] (see Figure 1b). The calculated Ba-N distance is 2.677 Å which compares well with those in sub-nitrides with nitrogen species in octahedral coordination [27,28]. Hexagonal perovskite crystal structures can only be expected for compounds containing alkaline-earth metal species with large radii. Hence, the resulting distance *d* (N-N) and the Coulomb repulsion between N^{3-} in face-sharing octahedra has to be formed. The resulting distance N-N is 3.3218 Å is sufficiently large.

Ag_2BaS_2: Ag_2BaS_2 crystallises in the trigonal $CaA1_2Si_2$-type structure, a = 4.386 (1) A, *c* = 7.194 (2) A, space group P3m1, *Z* = 1, where S and Ag atoms are arranged in the chemically ordered double-corrugated hexagonal layers and Ca atoms are intercalated between them [29], as shown in Figure 1c. These layers can, in turn, be described as being made up from two stacked AgS layers, with each layer being a two-dimensional infinite net of chair-like six-membered rings. Every atom in the Ag_2S_2 layer is four-coordinate, but the coordination environment is very different for Ag and S. Each Ag is surrounded by four S atoms, forming a distorted tetrahedron. The S is also four-coordinate in Ag, but the environment is most unusual, a flipped tetrahedron or umbrella shape.

ZrSO: ZrSO crystalizes in cubic ($P2_13$, space group No. 198) and tetragonal (P4/nmm, space group No. 129) form [30,31]. Tetragonal ZrSO crystallises in the PbFCl-type structure. The form of this phase has not yet been synthesized [31]. All preparations techniques proved that the tetragonal phase was always accompanied by considerable proportions of cubic ZrSO, and in some cases, even by ZrO_2. It seemed likely, therefore, that the tetragonal phase also contains oxygen [31]. According to our theoretical energy volume curve (see Figure S1), the cubic form is more stable than the tetragonal form and the energy difference between these two structures is very small (36 meV/f.u.). Moreover, it is clear from Figure S1 that the energy minima for these two structures are well separated, and the energy well is deep enough to stabilize the individual phases. We can thus conclude that this phase can be experimentally stabilized using a high-pressure technique.

There are four S and three O atoms surround each Zr atom in the cubic phase. The S atoms form a stretched tetrahedron with one Zr-S separation of 2.61 Å and three of 2.63 Å. The O atoms form an equilateral triangle centered at the Zr site, in such a way that there is an O atom in each of the stretched faces of the S atoms tetrahedron. At a distance of 2.13 Å from each oxygen atom, the Zr atom is slightly out of the plane of the oxygen triangle. The configuration may be regarded as a distorted octahedron consisting of three S atoms and three O atoms, with an extra sulfur atom above the center of the face of the octahedron driven by the oxygen atoms. From this point of view, the co-ordination of zirconium is quite similar to that observed in K_3ZrF_7. The separations of S-S and S-O are 3.59 and 2.96 Å, respectively. These separations are shorter than the sum of the radii (3.68 Å for S-S and 3–24 Å for S-O) owing to the sharing of edges between the coordination polyhedra [30].

3.2. Electronic Properties

In order to investigate the potential applicability of non-silicon semiconductors as a light-harvesting medium, the band gap of these materials is a crucial factor that needs to be further explored. Both short-circuit current and open-circuit voltage is regulated by the band gap of the photoactive semiconductors. Broader band gap leads to higher open-circuit voltage but fewer excited electrons, which results in lower short-circuit current. Narrower band gap leads to low open circuit voltage but more excited electrons, which result in larger short-circuit current. The ideal solar cell is theoretically shown to have a maximum of 32% efficiency with an optimal band gap E_g = 1.4 eV is [2]. In real cells, the solar spectrum is a broad energy spectrum and it does not match the band gap well where thermalisation loss occurs, which eventually results in efficiencies below the detailed-balance limit [2]. Band gap calculation using electronic band structures gives a promising opportunity to identify suitable PV materials. The calculated band structure of trigonal-$TlBiS_2$, hexagonal-Ba_3BiN, trigonal-Ag_2BaS_2 and tetragonal-ZrSO crystals along a high-symmetry path in the first Brillouin zone are presented in Figure 2. For electronic structure calculations, we employ hybrid functional (HSE06) and estimate the band gap values for these materials. The results of electronic structure calculations, listed in Table 1, span the in the range from 1.10 to 2.6 eV. The four compounds exhibit a direct band gap at the Γ **k**-point, as shown in Figure 2.

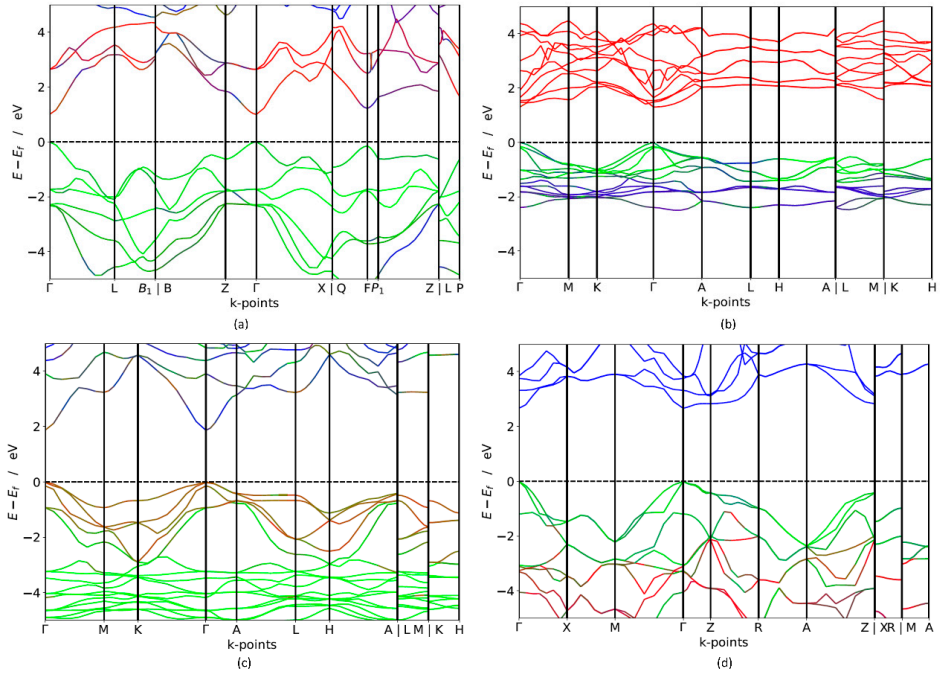

Figure 2. Calculated electronic band structure (using HSE06) of (**a**) $TlBiS_2$(Colour code: red line—Bi, green line—S, blue—Tl), (**b**) Ba_3BiN (Colour code: red line—Ba, green line—Bi, blue—N), (**c**) Ag_2BaS_2 (Colour code: red line—S, green line—Ag, blue—Ba) and (**d**) ZrSO (Colour code: red line—O, green line—S, blue—Zr). The Fermi level is set to zero.

The HSE06 band structure of $TlBiS_2$ is shown in Figure 2a. Both the valence band maximum (VBM) and the conduction band minimum (CBM) are well placed at the Γ **k**-point. This clearly shows that $TlBiS_2$ is a direct band gap semiconductor with valence bands derived from Bi-s, S-p, and Tl-s states, and conduction bands derived from S-s, Bi-p, and Bi-d states (Figure 3). The HSE06 band

gap is 1.1 eV for $TlBiS_2$, which is nearly equal to that of Silicon. Bahadur Singh et al., showed that $TlBiS_2$ has GGA band gap of 0.64 eV with direct band gap type at Γ **k**-point [32]. It is important to note that we employed a more accurate HSE06 method compared to the GGA calculation method used by Bahadur Singh et al. [32] and the difference is approximately 0.46 eV. This is as expected because it is well known that calculations using GGA underestimate the band gap value, while the HSE06 screened hybrid functional is very successful in precisely calculating the band gap value. Our calculation shows that we have a band gap of 1.42 eV at F **k**-point $TlBiS_2$ as shown in Figure 2a. This shows that $TlBiS_2$ well suited for PV applications as optimal band gap for the best performance is 1.4 eV as mentioned earlier [12].

Table 1. Calculated GGA and HSE06 band gap values, type of band gap for $TlBiS_2$, Ba_3BiN, Ag_2BaS_2, and ZrSO phases.

Compounds	GGA (eV)	HSE06 (eV)	Type of Band Gap
$TlBiS_2$	0.505	1.10	direct
Ba_3BiN	0.679	1.29	direct
Ag_2BaS_2	0.716	1.95	direct
ZrSO	0.891	2.60	direct

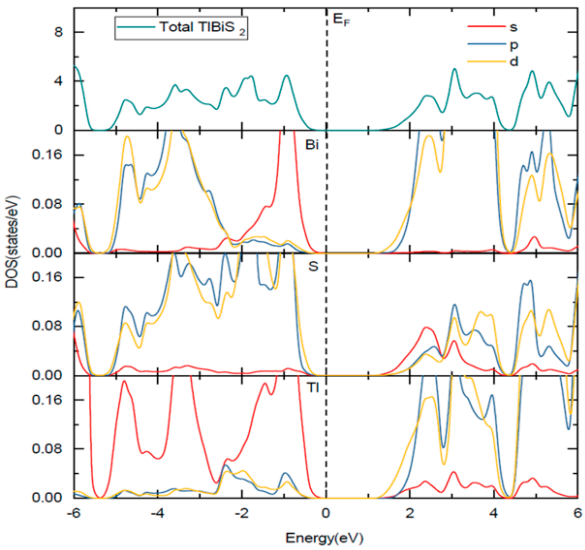

Figure 3. Total and site projected density of states of $TlBiS_2$. The Fermi level is set to zero. The Fermi level is set to zero and marked by a vertical dotted line.

In the case of Ba_3BiN, the VBM and CBM are located at Γ **k**-point. Thus, the calculated HSE06 band structure in Figure 2b shows that Ba_3BiN is a direct band gap semiconductor with a band gap of 1.29 eV. From the Figure S3 of Supplementary Materials, the valence band derived from Bi-p and hybridized Ni-d states and conduction bands are mainly composed of Bi-s and Ba-s states. According to Imran Ullah et al., Ba_3BiN is a direct band gap semiconductor with a band gap of 0.64 eV at Γ **k**-point [33]. The comparison between the present results using HSE06 with the previous results using GGA [33] reveals that the band gap of Ba_3BiN is previously underestimated by 0.79 eV. To the best of our knowledge, no HSE06 or experimental studies have been previously reported on Ba_3BiN. For Ag_2BaS_2, the calculated HSE06 band structure in Figure 2c shows that the VBM and CBM are located at the Γ **k**-point. Thus, Ag_2BaS_2 is a direct band gap semiconductor with a band gap of 1.95 eV. Note that our direct band gap value of 1.95 eV calculated with HSE06 closely matches the previous HSE06 band

gap value of 2.01 eV [34] calculated by Aditi Krishnapriyan et al. To the best of our knowledge, no experimental study has been previously reported on Ag_2BaS_2. From Figure 2b and the Figure S4 of Supplementary Materials, the valence band maximum is derived from S-p states and conduction band derived from Ag-s states. In the case of ZrSO, both the VBM and the CBM are located at Γ. Thus, ZrSO is a direct band gap semiconductor with valence bands derived from S-p states, and conduction bands derived from O-s states (Figure S5). The calculated HSE06 band gap between VBM and CBM is 2.60 eV. To the best of our knowledge, no HSE06 and experimental study have previously reported on ZrSO.

3.3. Effective Mass Calculation

We calculate the conductivity effective masses for all four materials; calculated values are listed in Table 2. To study of energy levels in solar devices, calculations of the effective mass (EM) play a crucial role. The conductivity effective masses of electrons and holes deal with the mobility, electrical resistivity, and free-carrier optical response in the semiconductor material used in PV applications. For EM calculation, we have used a finite difference method as implemented in the effective mass calculator (EMC) [35]. For $TlBiS_2$, Ba_3BiN, and Ag_2BaS_2, the EM of holes was found to be heavier than the EM of electrons. This result can be ascribed to the fact that the VBM is less dispersed than the CBM. Prominent PV materials Silicon (Si) and gallium arsenide (GaAs) have EMs of 0.26 m_e and 0.12 m_e [36] respectively for electrons. The calculated EM of electrons are 0.154 m_e, 0.092 m_e, and 0.149 m_e for $TlBiS_2$, Ba_3BiN, and Ag_2BaS_2 respectively. Compared to Si, for $TlBiS_2$, Ba_3BiN, and Ag_2BaS_2, the EM of the electron is lower. Hence, the electron mobility in these three compounds is better than that of silicon. However, in the case of ZrSO, the EM of the hole is lighter than the EM of electrons; this is due to CBM being less dispersed than VBM in ZrSO.

Table 2. The calculated effective mass of non-silicon compounds. m^*_{lh}, m^*_{hh} and m^*_e are the effective masses of light holes, heavy holes and electrons, respectively. m_e is the mass of the electron.

Serial No.	Plane Directions	Compound	$m^*_{lh} \times m_e$	$m^*_{hh} \times m_e$	$m^*_e \times m_e$
1.	110	$TlBiS_2$	0.182	0.224	0.154
2.	110	Ba_3BiN	0.016	0.165	0.092
3.	110	Ag_2BaS_2	0.150	0.728	0.149
4.	110	ZrSO	0.308	0.482	0.361

3.4. Lattice Dynamic Stability

Lattice dynamic calculations have also been performed on $TlBiS_2$, Ba_3BiN, Ag_2BaS_2, and ZrSO under ambient conditions. To validate the dynamical stability of these compounds, the total phonon density of states is calculated at the equilibrium volume. In Figure 4, we displayed their total phonon density of states. No imaginary frequencies were observed, revealing that $TlBiS_2$, Ba_3BiN, Ag_2BaS_2, and ZrSO are dynamically stable. We present the site projected phonon density of states for $TlBiS_2$, Ba_3BiN, Ag_2BaS_2, and ZrSO in Figure 5. The vibrational modes spread over the 2 to 50 THz range in the case of $TlBiS_2$ phase. In the low frequencies region, Tl is dominant over Bi and S. The lattice vibrational modes for the Tl, S, and Bi are present between 3–10, 5–21, and 18–50 THz, respectively. In the case of Ba_3BiN, the vibrational modes spread over 0 to 52 THz. The lattice vibrational modes for N, Bi, and Ba are present between 0–19, 2–20 and 3–51 THz, respectively. For Ag_2BaS_2, the vibrational modes spread over 0.3 to 7.5 THz. The Ag-S and Ba-S stretching modes are present between 1–3 THz. Other Ag-Ba, S-Ag, and S-Ba stretching modes are present between 5–6.5, 5–6.5 and 4.3–7 THz, respectively. The lattice vibrational modes for Ag, Ba, and S are present between 0.3–3.6, 0.3–3.6, and 4.3–7.5 THz, respectively.

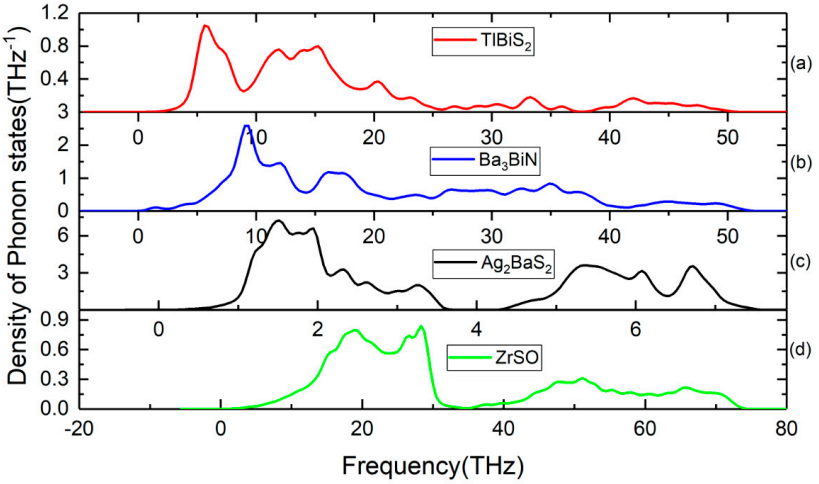

Figure 4. Calculated total phonon density of states for (**a**) $TlBiS_2$, (**b**) Ba_3BiN, (**c**) Ag_2BaS_2, and (**d**) ZrSO phases.

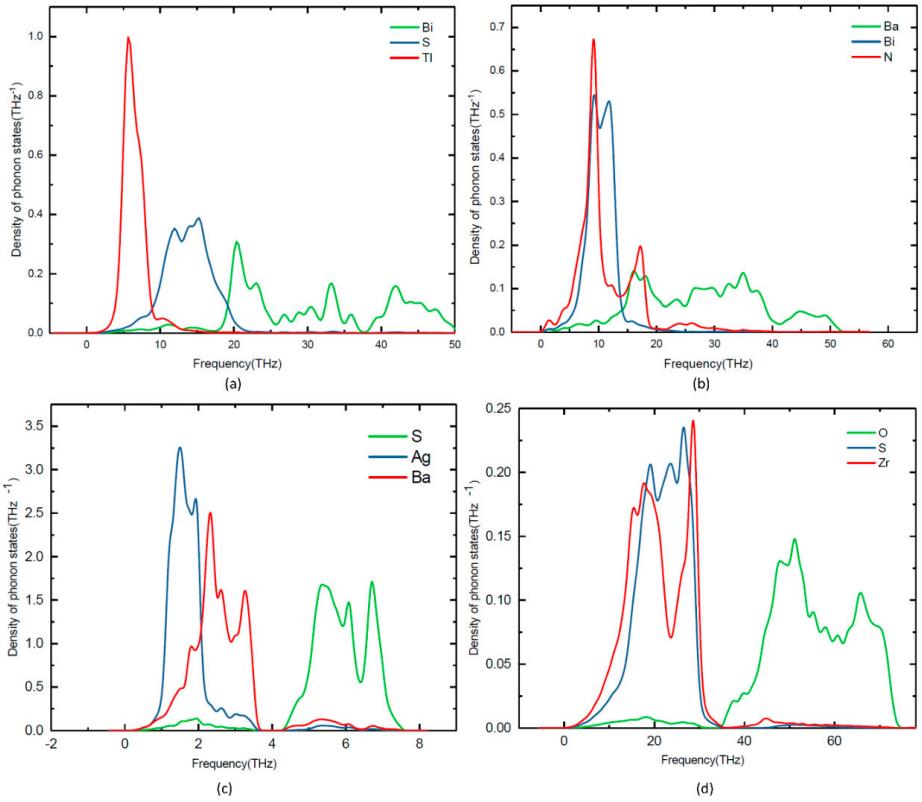

Figure 5. Calculated site projected phonon density of states for (**a**) $TlBiS_2$, (**b**) Ba_3BiN, (**c**) Ag_2BaS_2, (**d**) ZrSO.

In the case of ZrSO, the vibrational modes spread over 2 to 74 THz. The Zr-O and S-O stretching modes are present between 5–30 THz. Other O-Zr and O-S stretching modes are present at 40–65 and 47–60 THz, respectively. The lattice vibrational modes for Zr, S, and O are present between 2–35, 2–35, and 35–74 THz, respectively. The calculated zero-point energy (ZPE) for the $TlBiS_2$, Ba_3BiN, Ag_2BaS_2, and ZrSO phases varies from 0.10 to 1.3 eV/f.u. (see Table 3), and the following ZPE sequence are: Ag_2BaS_2 < $TlBiS_2$ < ZrSO < Ba_3BiN.

Table 3. Computational details for the phonon calculation (supercell size, number of atoms), calculated zero-point energy (ZPE) and information on dynamical stability based on phonon density of states for $TlBiS_2$, Ba_3BiN, Ag_2BaS_2, and ZrSO phases.

Compounds	Supercell Size	Number of Atoms	ZPE (eV)	Dynamical Stability
$TlBiS_2$	2 × 2 × 2	32	0.4045	stable
Ba_3BiN	2 × 2 × 2	80	1.3050	stable
Ag_2BaS_2	2 × 2 × 2	40	0.1093	stable
ZrSO	2 × 2 × 2	48	1.2100	stable

In addition to the dynamic stability, we employ the vibrational density of states to compute the specific heat capacity (C_v) of $TlBiS_2$, Ba_3BiN, Ag_2BaS_2, and ZrSO at constant volume and pressure. The C_v as a function of temperature presented in Figure 6 in the temperature range from 0 K to 1000 K. For $TlBiS_2$, the specific heat capacity increases rapidly below 500 K. The value of C_v is almost constant at 90 J/K/mol for above 500 K. In the case of Ba_3BiN, the C_v increases rapidly up to 1000 K. The specific heat capacity increases rapidly below 100 K for Ag_2BaS_2. The C_v is almost constant at 125 J/K/mol for above 100 K. For ZrSO, the C_v increases from 100 K to 1000 K. The following C_v sequence are: $TlBiS_2$ < ZrSO < Ag_2BaS_2 < Ba_3BiN.

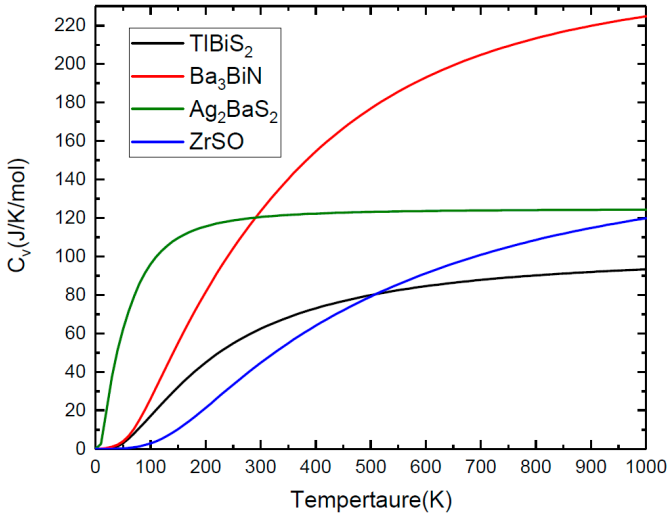

Figure 6. The heat capacity at constant volume as a function of temperature from zero up to 1000 K.

3.5. Mechanical Stability

The mechanical stability of a system is an essential condition to validate the existence of a compound in a given crystalline structure. The elastic constants are typically used to describe the mechanical properties of a system and to estimate its hardness. To validate the mechanical stability of $TlBiS_2$, Ba_3BiN, Ag_2BaS_2, and ZrSO, we calculated the single-crystal elastic constant tensor using the

finite strain technique. The elastic constants describe the ability of materials to deform, or conversely, the stress required to maintain a given deformation. Both stresses and strains have three tensile and three shear components. The linear elastic constants form a 6 × 6 symmetric matrices, with 27 independent components, so that (s_i only) $s_{ij} = C_{ij}\ \varepsilon_j$ (s_i is stress tensor, C_{ij} is elastic constant matrix, ε_j (j = 1, 6 in Voigt index) is the strain tensor, and i = 1, . . . , 6) for small stresses and strains [37].

The stiffness of a crystal against an externally applied strain can be determined from its elastic constants. Any symmetry present in the structure may make some of these components equal, while others may be fixed to zero. The calculated elastic constants of four non-silicon materials listed in Table 4. The elastic constant C_{44} is a crucial parameter, indirectly describing the indentation hardness of the materials. As shown in Table 4, all the examined compounds have a small C_{44} value, indicating these materials possess a relatively weak shear strength.

Table 4. The calculated single-crystal elastic constants C_{ij} (in GPa), bulk modulus B (in GPa), shear modulus G (in GPa), Poisson's ratio (σ), Young's modulus E (in GPa), compressibility (GPa^{-1}), Ductility for $TlBiS_2$, Ba_3BiN, Ag_2BaS_2 and ZrSO phases. Subscript V illustrates the Voigt bound, R indicates the Reuss bound and VRH indicates the Hill average.

Properties	$TlBiS_2$	Ba_3BiN	Ag_2BaS_2	ZrSO
C_{ij}	C_{11} = 63.47 C_{12} = 34.68 C_{13} = 27.49 C_{14} = 0.608 C_{33} = 88.90 C_{44} = 28.90	C_{11} = 56.604 C_{12} = 14.1 C_{13} = 7.947 C_{33} = 75.35 C_{44} = 21.20	C_{11} = 84.61 C_{12} = 31.538 C_{13} = 34.611 C_{14} = 0.0732 C_{33} = 89.994 C_{44} = 26.642 C_{66} = 14.590	C_{11} = 293.04 C_{12} = 133.66 C_{13} = 118.96 C_{33} = 303.06 C_{44} = 100.64 C_{66} = 91.94
B_V	44.85	27.762	51.59	181.407
B_R	44.46	27.5620	51.28	181.39
B_{VRH}	44.65	27.662	51.34	181.403
G_V	54.99	47.7264	53.45	194.92
G_R	21.08	5.70729	19.24	90.88
G_{VRH}	38.04	26.716	36.35	142.90
Ductility	0.852	0.96	0.708	0.7877
σ	0.168	0.1346	0.213	0.188
E	89	61	29	339
compressibility	0.022	0.04	0.02	0.0055

For trigonal structures, the mechanical stability criteria at zero pressure are as follows [38]:

$$C_{11} > |C_{12}|, C_{11} > 0, C_{33} > 0, C_{44} > 0 \quad (1)$$

$$[(C_{11} + C_{12})\, C_{33} - 2C^2_{13}] > 0 \quad (2)$$

$$[(C_{11} - C_{12})\, C_{44} - 2C^2_{14}] > 0 \quad (3)$$

In this study, trigonal $TlBiS_2$ and Ag_2BaS_2 have six independent elastic constants. All the three mechanical stability conditions given in Equations (1)–(3) are satisfied for the $TlBiS_2$ and Ag_2BaS_2 phases. Hence, this indicates that these two trigonal phase materials are mechanically stable.

For the hexagonal system, the Born stability criteria are [38]:

$$C_{44} > 0 \quad (4)$$

$$C_{11} - |C_{12}| > 0 \quad (5)$$

$$[(C_{11} + C_{12})\, C_{33} - 2C^2_{13}] > 0 \quad (6)$$

The hexagonal-Ba_3BiN has five independent elastic constants. All three conditions for the mechanical stability given in equations 4 to 6 are satisfied for this structure, and this finding indicates that hexagonal-Ba_3BiN phases are mechanically stable.

The mechanical stability criteria for the tetragonal phase are given by [38]:

$$C_{11} - C_{12} \tag{7}$$

$$2(C_{11} + C_{12}) + C_{33} + 4C_{13} \tag{8}$$

$$C_{44} > 0, C_{66} > 0 \tag{9}$$

$$C_{11} + C_{12} - 2C_{13} > 0 \tag{10}$$

ZrSO has a tetragonal structure, and thus, six independent elastic constants. All three conditions for mechanical stability given in Equations (7)–(10) are satisfied for this structure. Hence, the tetragonal-ZrSO phase is mechanically stable at ambient conditions. Equations (1)–(9) and Table 4 validated the mechanical stability criteria for the crystal under ambient conditions. This outcome is consistent with the phonon calculations presented in Section 3.4.

From the calculated elastic constants, the bulk (B_v, B_R) and shear moduli (G_v, G_R) are calculated from Voigt–Reuss–Hill approximations [39,40]. The bulk and shear moduli contain information related to the hardness of the material under various types of deformation. Generally, very hard materials hold very large bulk and shear moduli to support the volume decrease and to restrict deformation, respectively [41]. From Table 4, it can be identified that the listed $TlBiS_2$, Ba_3BiN, and Ag_2BaS_2 phases have a smaller bulk modulus than ZrSO (181.403 GPa). This indicates that ZrSO is more difficult to compress than the other three materials. Among these compounds, the bulk modulus sequence is: ZrSO > Ag_2BaS_2 > $TlBiS_2$ > Ba_3BiN. As we know, the shear modulus is more closely-connected to hardness than the bulk modulus. From Table 4, the shear modulus of ZrSO is higher than the other three compounds. Hence, the hardness of the tetragonal-ZrSO phase is higher than trigonal-$TlBiS_2$, hexagonal-Ba_3BiN, and trigonal-Ag_2BaS_2. Among these compounds, the shear modulus trend is ZrSO > $TlBiS_2$ > Ag_2BaS_2 > Ba_3BiN. Seemingly, the bulk and shear moduli of Ba_3BiN are smaller than other compounds. Thus, Ba_3BiN is easy to compress and is the softest of the examined materials.

The parameter G/B can be introduced, in which G indicates the shear modulus and B the bulk modulus. The low/high of G/B value is connected with the ductility or brittleness of the materials. The critical G/B value that separates the ductile and brittle materials is 0.5 [41]. If the G/B value of materials is smaller than 0.5, then those materials are ductile; otherwise they are brittle. From Table 4, the calculated G/B values of all four materials are greater than 0.5, indicating that these materials are ductile. Next, the value of Poisson's ratio is indicative of the degree of directionality of the covalent bonding. Among these compounds, the small Poisson's ratio (0.13) for hexagonal-Ba_3BiN indicates a high degree of covalent bonding. All these phases present a very scattered Young's (varying from 29 to 339 GPa). The compressibility value of these phases suggests that these compounds, with the exception of ZrSO, are very soft materials. The compressibility sequence is ZrSO < Ag_2BaS_2 < $TlBiS_2$ < Ba_3BiN.

3.6. Optical Properties

The optical behavior of a compound has a major impact on its properties for photovoltaic applications. Optical dielectric function $\varepsilon(\omega) = \varepsilon_1(\omega) + \iota\varepsilon_2(\omega)$ is the fundamental quantity that describes the optical properties of a material. It describes the response of a material to a radiated electromagnetic field and the propagation of the field inside the material. The dielectric function is dependent on the frequency of electromagnetic field, and it is connected to the interaction between photons and electrons. The absorption coefficient of the material is dependent on the imaginary part,

$\varepsilon_2(\omega)$, and it can be derived from the inter-band optical transitions by summing over the unoccupied states, using the equation [42,43],

$$\varepsilon_2^{(\alpha\beta)}(\omega) = \frac{4\pi^2 e^2}{\Omega} \lim_{q\to 0} \sum_{k,v,c} 2w_k \delta(\epsilon_{ck} - \epsilon_{vk} - \omega) \times \langle u_{ck+e_\alpha q} | u_{vk} \rangle \langle u_{ck+e_\beta q} | u_{vk} \rangle^* \tag{11}$$

where the indices α, β are the Cartesian components, Ω is the volume of the primitive cell, q denotes the Bloch vector of the incident wave, c and v are the conduction and valence band states respectively, k is the Bloch wave vector, w_k denotes the **k**-point weight, δ is a Dirac delta function, u_{ck} is the cell periodic part of the orbital at **k**-point k, ϵ_{ck} refers to the energy of the conduction band, and ϵ_{vk} refers to the energy of the valence band. The real part $\varepsilon_1(\omega)$ of the dielectric function can be derived from $\varepsilon_2(\omega)$ using the Kramer-Kronig relationship [42,43]

$$\varepsilon_1^{(\alpha\beta)} = 1 + \frac{2}{\pi} \mathrm{P} \int_0^\infty \frac{\varepsilon_{\alpha\beta}^2(\omega')\omega'}{\omega'^2 - \omega^2 + i\eta} d\omega' \tag{12}$$

where P indicates the principal value, η is the complex shift. All the frequency dependent linear optical properties, such as the absorption coefficients $\alpha(\omega)$, can be calculated from $\varepsilon_1(\omega)$ and $\varepsilon_2(\omega)$ [42,43].

$$\alpha(\omega) = \frac{\sqrt{2\omega}}{c} [\left(\varepsilon_1^2(\omega) + \varepsilon_2^2(\omega)\right)^{\frac{1}{2}} - \varepsilon_1(\omega)] \tag{13}$$

Experimental absorption spectra are in agreement with the inclusion of excitonic effects treated within the Bethe-Salpeter equation (BSE) in general [44–46]. By averaging multiple grids using BSE, the calculated the dielectric function of these four materials can be further improved. The calculated $\varepsilon_2(\omega)$ of the dielectric function and the absorption coefficients of $TlBiS_2$, Ba_3BiN, Ag_2BaS_2, and ZrSO are presented in Figures 7 and 8, respectively. From the directional dependency of $\varepsilon_1(\omega)$ and $\varepsilon_2(\omega)$, trigonal-$TlBiS_2$ is highly isotropic, whereas hexagonal-Ba_3BiN, trigonal-Ag_2BaS_2, and tetragonal-ZrSO are less anisotropic. We present the average of the real and imaginary parts of the dielectric function for the four examined compounds.

In Figure 7, we plotted both real and imaginary part of the dielectric function of (a) $TlBiS_2$, (b) Ba_3BiN, (c) Ag_2BaS_2, and (d) ZrSO is plotted against the photon energy. The optical absorption coefficients of all these materials were calculated using BSE and plotted in Figure 8. For a comparison, we have also plotted both the experimentally-verified [47] and the BSE-calculated [19] values for the optical absorption coefficient of silicon in the same Figure 8. Absorption in a material take place only when the incident photon has more energy than energy band gap of the material. Since $TlBiS_2$ is a direct band gap material with a band gap of 1.10 eV, we notice the absorption to occur when the energy of the photon is around 1.08 eV, as shown in Figure 8. It is clearly seen in Figure 8 that there are absorption peaks at 1.32 eV, 1.93 eV, 2.45 eV, and 3.6 eV. The absorption coefficient of $TlBiS_2$ has a maximum value when the photon energy is about 3.6 eV. For silicon, the absorption coefficient becomes appreciably different from zero after 2.5 eV, and it is still not very large up to 3 eV. This phenomenon can be attributed to the indirect band gap of silicon that leads to low absorption in the visible region. We observe that the absorption coefficient of $TlBiS_2$ is superior to silicon in the visible region. This is due to the direct band gap at Γ and F **k**-points that prevails in the $TlBiS_2$.

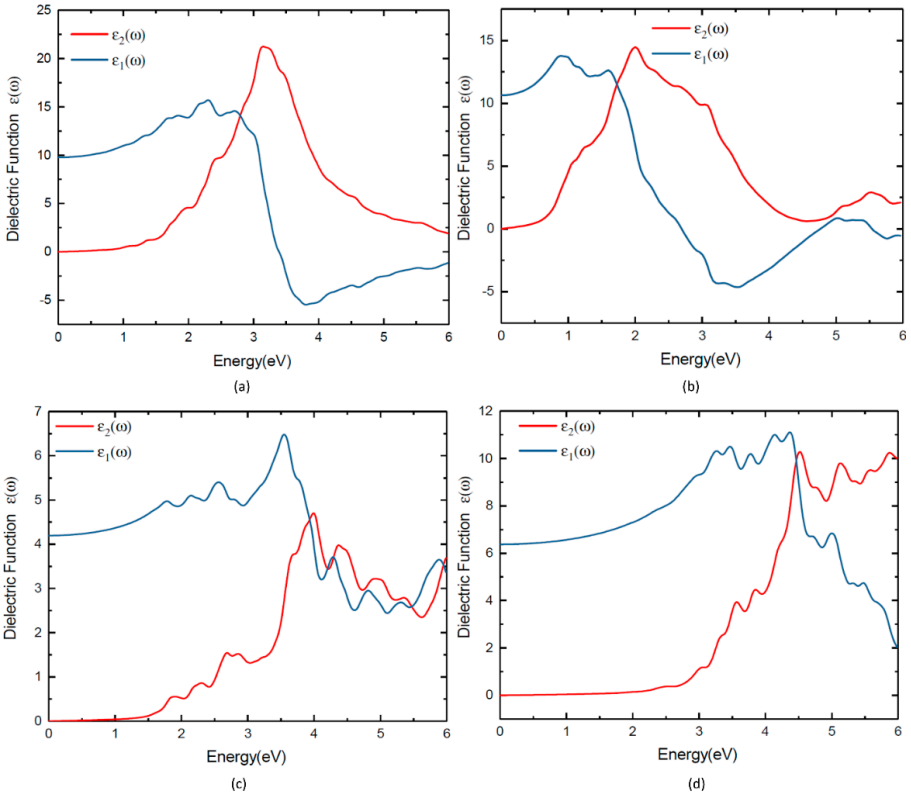

Figure 7. Dielectric function of (**a**) $TlBiS_2$, (**b**) Ba_3BiN, (**c**) Ag_2BaS_2 and (**d**) ZrSO.

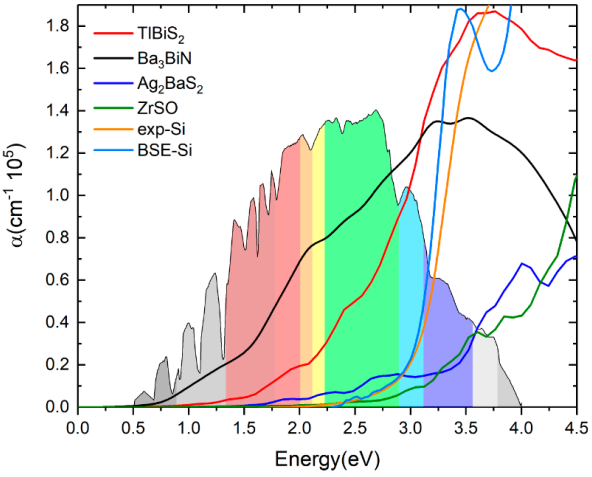

Figure 8. Optical absorption coefficients of $TlBiS_2$, Ba_3BiN, Ag_2BaS_2 and ZrSO. For comparison, we plotted the silicon optical absorption coefficient (color code: orange—experimental absorption coefficient of Si, navy blue—BSE calculation of Si).

In the case of hexagonal-Ba_3BiN, the dielectric function is calculated at the BSE level (Figure 7b). Due to the narrow band gap, Ba_3BiN can absorb photons mostly in the visible region. The HSE06 band gap is 1.29 eV, and it is direct. Therefore, Ba_3BiN exhibits an absorption which rapidly increases after 1.26 eV. It can be observed that the absorption peaks of Ba_3BiN are at 2.08 eV, 3.21 eV, and 3.5 eV (Figure 8). The absorption coefficient of Ba_3BiN reaches its maximum when the photon energy is about 3.5 eV. From Figure 8, it can be noted that the optical absorption of Ba_3BiN occurs in the visible region, with higher values compared to other materials considered. The reason behind the high optical absorption of Ba_3BiN is due to the direct band gap of 1.29 eV. From Figure 8, it can be observed that absorption peaks of Ag_2BaS_2 are at 1.94 eV, 2.24 eV, 2.7 eV, and 3.6 eV. Ag_2BaS_2 seems to have a lower absorption coefficient than $TlBiS_2$ and Ba_3BiN in the visible region. However, Ag_2BaS_2 exhibits better optical absorption than silicon in the visible region. In the same Figure 8, we notice that absorption peaks of ZrSO start at 2.5 eV. The absorption peaks of ZrSO are also observed at 2.6 eV, 3 eV, and 3.59 eV. Among these four non-silicon materials, the absorption coefficient of ZrSO is smaller than those of the other three; this is due to the wideband gap of ZrSO.

4. Conclusions

We employed band gap calculations based on GGA on a pool of 1000 materials in order to identify twenty-seven possible candidates for photovoltaic applications. Among these candidates, four promising materials that had direct band gaps were chosen, and in-depth analysis was carried out to check the utility of these compounds for photovoltaic applications. We have presented a set of first-principle calculations employing the hybrid functional HSE06 and utilized to compute the electronic structures and effective masses of the four chosen materials, namely, $TlBiS_2$, Ba_3BiN, Ag_2BaS_2, and ZrSO. The BSE method was employed to calculate the optical properties. Our study provided rational insights into the electronic structure and optical properties of these four non-silicon materials. These four materials exhibit a direct band gap in the range of 1.10 eV to 2.60 eV.

The main advantage with $TlBiS_2$, Ba_3BiN, and Ag_2BaS_2 is that all three materials have direct band gaps and higher absorption coefficients than the widely-used photovoltaic material silicon in the visible region. Among these three materials, $TlBiS_2$ and Ba_3BiN have better optical properties than Ag_2BaS_2. ZrSO is the least preferable photovoltaic material because of the fact that its absorption properties are inferior to those of silicon. Nevertheless, we have shown that there is a significant difference in the GGA and HSE06 calculation for ZrSO. The phonon calculations revealed that $TlBiS_2$, Ba_3BiN, Ag_2BaS_2, and ZrSO are dynamically stable, as no imaginary frequencies were observed. Our elastic constant calculations illustrate that the compounds are mechanically stable. The calculated G/B values are greater than 0.5, confirming the brittle nature of these materials. Our detailed studies of the electronic, structural stability, mechanical stability and optical properties of these four materials show them to be potential candidates for photovoltaic application.

Supplementary Materials: The following are available online at http://www.mdpi.com/1996-1944/11/10/2006/s1, Table S1: Calculated GGA band gap values for 30 compounds with lattice parameters; Table S2: Calculated structural parameters and atomic positions of $TlBiS_2$, Ba_3BiN, Ag_2BaS_2, and ZrSO; Figure S1: Calculated total energy as a function of unit cell volume for cubic- and tetragonal-ZrSO; Figure S2: Crystal structures for (a) cubic-ZrSO; (b) tetragonal-ZrSO. The legends for the different kinds of atoms shown in the illustration; Figure S3: Total and site projected density of states of Ba_3BiN. The Fermi level is set to zero and marked by a vertical dotted line; Figure S4: Total and site projected density of states of Ag_2BaS_2. The Fermi level is set to zero and marked by a vertical dotted line; Figure S5: Total and site projected density of states of ZrSO. The Fermi level is set to zero and marked by a vertical dotted line.

Author Contributions: Conceptualization, M.R., D.V. and P.V.; Methodology, M.R., D.V. and P.V.; Software, M.R., P.V. and D.V.; Validation, P.V., M.R., F.B. and D.V.; Formal Analysis, M.R.; Investigation, M.R., D.V. and P.V.; Resources, M.R., P.V.; Data Curation, M.R. and P.V.; Writing-Original Draft Preparation, M.R.; Writing-Review & Editing, D.V., P.V. and F.B.; Visualization, M.R. and P.V.; Supervision, D.V., P.V.; Project Administration, D.V.; Funding Acquisition, D.V.

Funding: This research was funded by Western Norway University of Applied Sciences grant number 23300.

Acknowledgments: The authors gratefully acknowledge the Western Norway University of Applied Sciences for financially supporting the project (23300) and UNINETT Sigma2 for computing facilities of project numbers NN2867K and NN2875K, which have been used to conduct the calculations presented in this article, and further acknowledge Vishnukanthan Venkatachalapathy for fruitful discussions.

Conflicts of Interest: The authors declare no conflict of interest.

References

1. Unold, T.; Schock, H.-W. Nonconventional (non-silicon-based) photovoltaic materials. *Annu. Rev. Mater. Res.* **2011**, *41*, 297–321. [CrossRef]
2. Shockley, W.; Queisser, H.J. Detailed balance limit of efficiency of p-n junction solar cells. *J. Appl. Phys.* **1961**, *32*, 510–519. [CrossRef]
3. Goetzberger, A.; Hebling, C.; Schock, H.-W. Photovoltaic materials, history, status and outlook. *Mater. Sci. Eng. R Rep.* **2003**, *40*, 1–46. [CrossRef]
4. Bube, R.H. Materials for photovoltaics. *Annu. Rev. Mater. Sci.* **1990**, *20*, 19–50. [CrossRef]
5. Birkmire, R.W.; Eser, E. Polycrystalline thin film solar cells: Present status and future potential. *Annu. Rev. Mater. Sci.* **1997**, *27*, 625–653. [CrossRef]
6. Mitchell, K.W. Status of new thin-film photovoltaic technologies. *Annu. Rev. Mater. Sci.* **1982**, *12*, 401–413. [CrossRef]
7. Boer, K.; Rothwarf, A. Materials for solar photovoltaic energy conversion. *Annu. Rev. Mater. Sci.* **1976**, *6*, 303–333. [CrossRef]
8. Rasukkannu, M.; Velauthapillai, D.; Vajeeston, P. Computational modeling of novel bulk materials for the intermediate-band solar cells. *ACS Omega* **2017**, *2*, 1454–1462. [CrossRef]
9. Rasukkannu, M.; Velauthapillai, D.; Vajeeston, P. A first-principle study of the electronic, mechanical and optical properties of inorganic perovskite Cs_2SnI_6 for intermediate-band solar cells. *Mater. Lett.* **2018**, *218*, 233–236. [CrossRef]
10. Hellenbrandt, M. The inorganic crystal structure database (ICSD)—Present and future. *Crystallogr. Rev.* **2004**, *10*, 17–22. [CrossRef]
11. Ponniah, V. *Density Functional Theory Based Database (DFTBD)*; University of Oslo: Oslo, Norway, 2013.
12. Rasukkannu, M.; Velauthapillai, D.; Ponniah, V. A promising high-efficiency photovoltaic alternative non-silicon material: A first-principle investigation. *Scr. Mater.* **2018**, *156*, 134–137. [CrossRef]
13. Kresse, G.; Furthmüller, J. Efficient iterative schemes for ab initio total-energy calculations using a plane-wave basis set. *Phys. Rev. B* **1996**, *54*, 11169. [CrossRef]
14. Perdew, J.P.; Burke, K.; Ernzerhof, M. Generalized gradient approximation made simple. *Phys. Rev. Lett.* **1996**, *77*, 3865. [CrossRef] [PubMed]
15. Dudarev, S.; Botton, G.; Savrasov, S.Y.; Szotek, Z.; Temmerman, W.; Sutton, A. Electronic structure and elastic properties of strongly correlated metal oxides from first principles: LSDA+ U, SIC-LSDA and EELS study of UO_2 and NiO. *Phys. Status Solidi A* **1998**, *166*, 429–443. [CrossRef]
16. Kresse, G.; Furthmüller, J. Efficiency of ab-initio total energy calculations for metals and semiconductors using a plane-wave basis set. *Comput. Mater. Sci.* **1996**, *6*, 15–50. [CrossRef]
17. Liechtenstein, A.; Anisimov, V.; Zaanen, J. Density-functional theory and strong interactions: Orbital ordering in Mott-Hubbard insulators. *Phys. Rev. B* **1995**, *52*, R5467. [CrossRef]
18. Heyd, J.; Scuseria, G.E. Efficient hybrid density functional calculations in solids: Assessment of the Heyd–Scuseria–Ernzerhof screened Coulomb hybrid functional. *J. Chem. Phys.* **2004**, *121*, 1187–1192. [CrossRef] [PubMed]
19. Paier, J.; Marsman, M.; Kresse, G. Dielectric properties and excitons for extended systems from hybrid functionals. *Phys. Rev. B* **2008**, *78*, 121201. [CrossRef]
20. Aroyo, M.I.; Perez-Mato, J.M.; Capillas, C.; Kroumova, E.; Ivantchev, S.; Madariaga, G.; Kirov, A.; Wondratschek, H. Bilbao Crystallographic Server: I. Databases and crystallographic computing programs. *Z. Krist. Cryst. Mater.* **2006**, *221*, 15–27. [CrossRef]
21. Aroyo, M.I.; Kirov, A.; Capillas, C.; Perez-Mato, J.; Wondratschek, H. Bilbao Crystallographic Server. II. Representations of crystallographic point groups and space groups. *Acta Crystallogr. Sect. A Found. Crystallogr.* **2006**, *62*, 115–128. [CrossRef] [PubMed]

22. Aroyo, M.I.; Perez-Mato, J.; Orobengoa, D.; Tasci, E.; De La Flor, G.; Kirov, A. Crystallography online: Bilbao crystallographic server. *Bulg. Chem. Commun.* **2011**, *43*, 183–197.
23. Togo, A.; Oba, F.; Tanaka, I. First-principles calculations of the ferroelastic transition between rutile-type and $CaCl_2$-type SiO_2 at high pressures. *Phys. Rev. B* **2008**, *78*, 134106. [CrossRef]
24. Togo, A.; Tanaka, I. First principles phonon calculations in materials science. *Scr. Mater.* **2015**, *108*, 1–5. [CrossRef]
25. Monkhorst, H.J.; Pack, J.D. Special points for Brillouin-zone integrations. *Phys. Rev. B* **1976**, *13*, 5188. [CrossRef]
26. Shannon, R.D. Revised effective ionic radii and systematic studies of interatomic distances in halides and chalcogenides. *Acta Crystallogr. Sect. A Cryst. Phys. Diffr. Theor. Gen. Crystallogr.* **1976**, *32*, 751–767. [CrossRef]
27. Gäbler, F.; Kirchner, M.; Schnelle, W.; Schwarz, U.; Schmitt, M.; Rosner, H.; Niewa, R. (Sr_3N) E and (Ba_3N) E (E = Sb, Bi): Synthesis, crystal structures, and physical properties. *Z. Anorg. Allg. Chem.* **2004**, *630*, 2292–2298. [CrossRef]
28. Steinbrenner, U.; Simon, A. Ba_3N–a new binary nitride of an alkaline earth metal. *Z. Anorg. Allg. Chem.* **1998**, *624*, 228–232. [CrossRef]
29. Bronger, W.; Lenders, B.; Huster, J. $BaAg_2S_2$, ein Thioargentat im $CaAl_2Si_2$-Strukturtyp. *Z. Anorg. Allg. Chem.* **1997**, *623*, 1357–1360. [CrossRef]
30. McCullough, J.D.; Brewer, L.; Bromley, L. The crystal structure of zirconium oxysulfide, ZrOS. *Acta Crystallogr.* **1948**, *1*, 287–289. [CrossRef]
31. Jellinek, F.; Songstad, J.; Viljanto, J.; Seppälä, P.; Theander, O.; Flood, H. A Tetragonal Form of Zirconium Oxide Sulfide, ZrOS. *Acta Chem. Scand.* **1962**, *16*, 791–792. [CrossRef]
32. Singh, B.; Lin, H.; Prasad, R.; Bansil, A. Topological phase transition and quantum spin Hall state in $TlBiS_2$. *J. Appl. Phys.* **2014**, *116*, 033704. [CrossRef]
33. Ullah, I.; Murtaza, G.; Khenata, R.; Mahmood, A.; Muzzamil, M.; Amin, N.; Saleh, M. Structural and Optoelectronic Properties of X_3ZN (X = Ca, Sr, Ba; Z = As, Sb, Bi) Anti-Perovskite Compounds. *J. Electron. Mater.* **2016**, *45*, 3059–3068. [CrossRef]
34. Krishnapriyan, A.; Barton, P.T.; Miao, M.; Seshadri, R. First-principles study of band alignments in the p-type hosts BaM_2X_2 (M = Cu, Ag; X = S, Se). *J. Phys. Condens. Matter* **2014**, *26*, 155802. [CrossRef] [PubMed]
35. Fonari, A.; Sutton, C. Effective Mass Calculator for Semiconductors. 2015. Available online: https://github.com/afonari/emc (accessed on 2 July 2018).
36. Van Zeghbroeck, B. *Principles of Semiconductor Devices*; Colarado University: Denver, CO, USA, 2004.
37. Ashcroft, N. *ND Mermin Solid State Physics WB Saunders Company*; Saunders College: Philadelphia, PA, USA, 1976.
38. Nye, J.F. *Physical Properties of Crystals: Their Representation by Tensors and Matrices*; Oxford University Press: Oxford, UK, 1985.
39. Hill, R. The elastic behaviour of a crystalline aggregate. *Proc. Phys. Soc. Sect. A* **1952**, *65*, 349. [CrossRef]
40. Reuss, A. Berechnung der fließgrenze von mischkristallen auf grund der plastizitätsbedingung für einkristalle. *ZAMM J. Appl. Math. Mech.* **1929**, *9*, 49–58. [CrossRef]
41. Pugh, S. XCII. Relations between the elastic moduli and the plastic properties of polycrystalline pure metals. *Lond. Edinb. Dublin Philos. Mag. J. Sci.* **1954**, *45*, 823–843. [CrossRef]
42. Gajdoš, M.; Hummer, K.; Kresse, G.; Furthmüller, J.; Bechstedt, F. Linear optical properties in the projector-augmented wave methodology. *Phys. Rev. B* **2006**, *73*, 045112. [CrossRef]
43. Yang, L.-M.; Vajeeston, P.; Ravindran, P.; Fjellvåg, H.; Tilset, M. Revisiting isoreticular MOFs of alkaline earth metals: A comprehensive study on phase stability, electronic structure, chemical bonding, and optical properties of A–IRMOF-1 (A = Be, Mg, Ca, Sr, Ba). *Phys. Chem. Chem. Phys.* **2011**, *13*, 10191–10203. [CrossRef] [PubMed]
44. Albrecht, S.; Reining, L.; Del Sole, R.; Onida, G. Ab initio calculation of excitonic effects in the optical spectra of semiconductors. *Phys. Rev. Lett.* **1998**, *80*, 4510. [CrossRef]
45. Bokdam, M.; Sander, T.; Stroppa, A.; Picozzi, S.; Sarma, D.; Franchini, C.; Kresse, G. Role of polar phonons in the photo excited state of metal halide perovskites. *Sci. Rep.* **2016**, *6*, 28618. [CrossRef] [PubMed]

46. Rohlfing, M.; Louie, S.G. Electron-hole excitations in semiconductors and insulators. *Phys. Rev. Lett.* **1998**, *81*, 2312. [CrossRef]
47. Aspnes, D.E.; Studna, A. Dielectric functions and optical parameters of Si, Ge, GaP, GaAs, GaSb, InP, InAs, and InSb from 1.5 to 6.0 ev. *Phys. Rev. B* **1983**, *27*, 985. [CrossRef]

materials

MDPI

Article

Properties of Novel Non-Silicon Materials for Photovoltaic Applications: A First-Principle Insight

Murugesan Rasukkannu [1,*], Dhayalan Velauthapillai [1], Federico Bianchini [2] and Ponniah Vajeeston [2]

[1] Department of Computing, Mathematics, and Physics, Western Norway University of Applied Sciences, Inndalsveien 28, 5063, Bergen, Norway; vdh@hvl.no

[2] Department of Chemistry, Center for Materials Science and Nanotechnology, University of Oslo, Box 1033 Blindern N-0315, Oslo, Norway; federico.bianchini@smn.uio.no (F.B.); ponniah.vajeeston@kjemi.uio.no (P.V.)

* Correspondence: rmu@hvl.no Tel.: +47-5558-7786

Received: 18 September 2018; Accepted: 11 October 2018; Published: 17 October 2018

Table S1. Calculated GGA band gap values for 30 compounds with lattice parameters.

S.No	Chemical formula	Space group	Pearson symbol	Lattice Parameter(computed)			Energy gap (in eV)	Type of band gap
				a	b	c		
1	$TlBiS_2$	R-3m(166)	hR4	7.817			0.5055	Direct
2	$BaGe_2$	*Pnma* (62)	oP24	6.860	9.196	11.678	0.5235	Indirect
3	Gd_2S_3	*Pnma* (62)	oP20	3.930	10.580	10.790	0.526	Direct
4	$GaTlTe_2$	*I*4/*mcm* (140)	tI16	7.020			0.5618	Indirect
5	GeP	*C*2/*m* (12)	mS24	7.990		9.350	0.5719	Direct
6	Ca_2CuFeO_3S	*P*4/*nmm* (129)	tP16	3.88		14.94	0.6339	Indirect
7	$Fe_2Ga_2S_5$	*P*-3*m*1 (164)	hP9	3.690		15.570	0.6558	Indirect
8	$Ca_2Fe_2O_5$	*Pnma* (62)	oP36	5.538	5.6589	14.885	0.6614	Direct
9	Ba_3BiN	*P*6$_3$/*mmc*(194)	hP10	7.770		6.805	0.6705	Direct
10	Cu_2GeZnS_4	*I*-42*m* (121)	tI16	6.552			0.6729	Direct
11	$CdCu_2GeS_4$	*Pmn*2$_1$ (31)	oP16	6.359	6.627	7.779	0.6863	Direct
12	$CdGeP_2$	*I*-42*d* (122)	tI16	6.838			0.6942	Direct
13	$ZnSnP_2$	*I*-42*d* (122)	tI16	7.0146			0.6984	Direct
14	$CdMn_2O_4$	*I*4$_1$/*amd* (141)	tI28	6.5092			0.7017	Indirect
15	Ag_2BaS_2	*P*-3*m*1 (164)	hP9	4.4251		7.2810	0.7161	Direct
16	$CuKZrS_3$	*Cmcm* (63)	oS24	7.3557		9.8515	0.7388	Direct
17	$CuFeO_3SSr_2$	*P*4/*nmm* (129)	tP16	3.9557		15.7502	0.7516	Indirect
18	$KMnNaO_2$	*Cccm* (66)	oS40	6.8241		7.1011	0.7749	Direct
19	Cu_2GeS_4Zn	*Pmn*2$_1$ (31)	oP16	6.2223	6.5706	7.4744	0.7798	Direct
20	Fe_2MnO_4	*Fd*-3*m* (227)	cF56	6.1012			0.7842	Indirect
21	MnO_3Sr	P63/mmc(194)	hP20	5.5350		9.2802	0.8325	Indirect
22	Cu_2GeMnS_4	*Pmn*2$_1$ (31)	oP16	6.2986	6.5754	7.6952	0.886	Indirect
23	ZrSO	*P*4/*nmm* (129)	tP6	3.6280		6.4154	0.8964	Direct
24	$Mn_2Na_{14}O_9$	*P*-3 (147)	hP25	6.7098		9.4004	0.9245	Indirect
25	$FeGeO_3$	*C*2/*c* (15)	mS40	6.7799		5.2895	0.9459	Indirect
26	$K_3Ni_2O_4$	*Cmcm* (63)	oS36	5.5013		10.6834	1.0845	Indirect
27	$MnNaO_2$	*Pmmn* (59)	oP8	5.8575		6.7005	1.1331	Indirect

The initial structural parameters of a thousand compounds were directly taken from the ICSD database[1], and then GGA band gap for thousand non-silicon compounds were calculated in our DFTB database[2]. These are multinary compounds including conductors, semiconductors, and insulators. Among these thousand non-silicon compounds we considered twenty-seven of them with GGA band gap values in the range of 0.5–1.1 eV (Table S1). Among these twenty-seven compounds, we identified fourteen compounds as direct band gap semiconductors and thirteen as indirect band gap semiconductors. We carried out a study on both electronic and optical properties of twenty-seven semiconductors (both direct and indirect). Our study on the optical properties of the semiconductor

materials showed that four direct band gaps among the twenty-seven materials had higher absorption coefficients in the visible region. Due to the space constraint, the optical properties of all the twenty-seven semiconductors are not presented in the supporting information part

Table S2. Calculated structural parameters and atomic positions of $TlBiS_2$, Ba_3BiN, Ag_2BaS_2, and ZrSO.

Phase	Lattice parameter						*Atomic positions*
	a	***b***	***c***	***α(deg)***	***β(deg)***	***γ(deg)***	
$TlBiS_2$ -R-3m ;166	7.817(7.711[a])			30.83	30.83	30.83	[a]Bi(3a): 0.000 0.000 0.000 [a]Tl(9d): ½ ½ ½ [a]S(36i) : 0.237 0.237 0.237
Ba_3BiN-$P6_3/mmc$;194	7.770 (7.6128[b])		6.805 (6.6805[b])	90	90	120	[b]Ba(6h): 0.1605 -0.1605 ¼ [b]Bi(2d): 1/3 2/3 ¾ [b]N(2a): 0.000 0.000 0.000
Ag_2BaS_2- *P*-3*m*1 ;164	4.4251(4.3861[c])		7.2810(7.1942[c])	90	90	120	[c]S(2d) : 1/3 2/3 0.25296 [c]Ba(1a) : 0.000 0.000 0.000 [c]Ag(2d) : 1/3 2/3 0.62252
ZrSO-P4/nmm; 129	3.6280		6.4154	90	90	90	[d]Zr(*2c*): 0, ½, 0.1950 [d]S(*2c*): 0, ½, 0.6330 [d]O(*2a*): 0, 0, 0
ZrSO-$P2_13$; 198	5.6960						[e]Zr(*4a*): 0.071, 0.071, 0.071 [e]S(*4a*): 0.3335, 0.3335, 0.3335 [e]O(*4a*): 0.6535, 0.6535, 0.6535

[a]Reference [3]; [b]Reference [4]; [c]Reference [5]; [d]Reference [6]; [e]Reference [7].

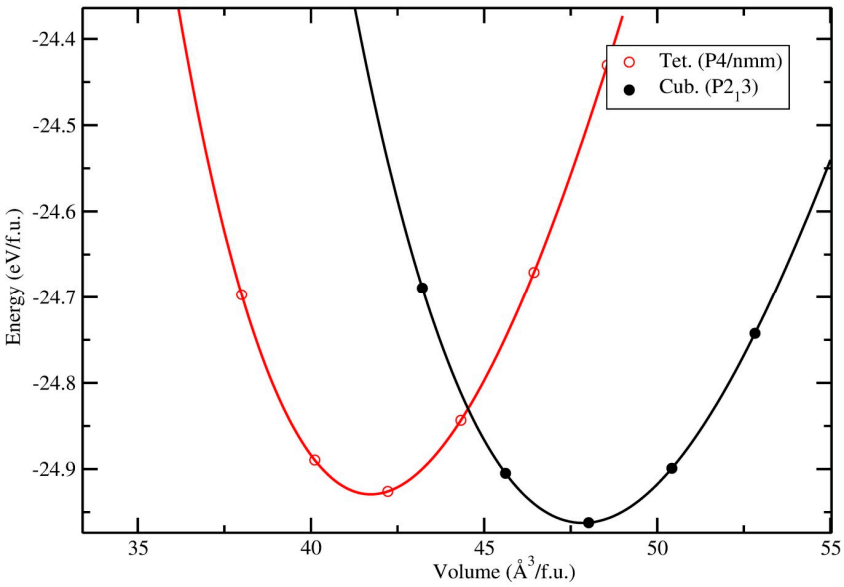

Figure S1. Calculated total energy as a function of unit cell volume for cubic- and tetragonal-ZrSO.

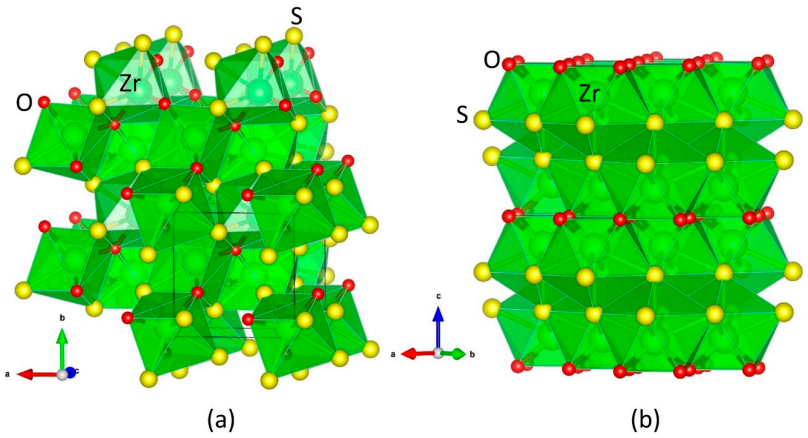

Figure S2. Crystal structures for (**a**) cubic-ZrSO; (**b**) tetragonal-ZrSO. The legends for the different kinds of atoms shown in the illustration.

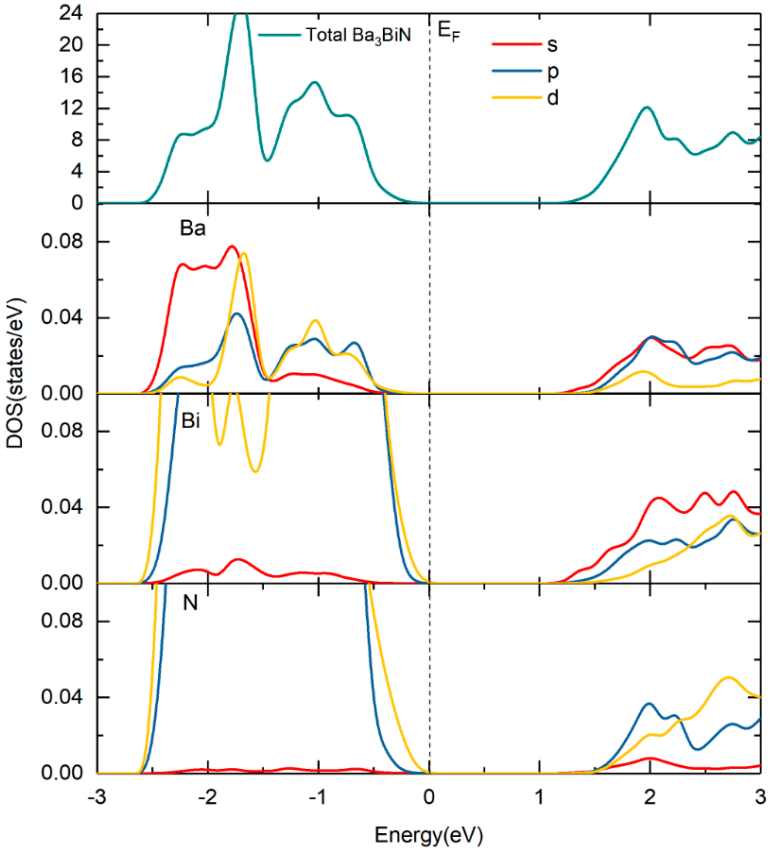

Figure S3. Total and site projected density of states of Ba_3BiN. The Fermi level is set to zero and marked by a vertical dotted line.

The total and site projected density of states of Ba_3BiN, Ag_2BaS_2, and ZrSO are presented in Figure S3, S4 and S5 respectively. From S3, we observe that the valence band derived from Bi-**p** and hybridized Bi-*d* states and conduction bands are mainly composed of Bi-*s* and Ba-*s* states. From Figure S4, we observe that the valence band maximum is derived from S-*p* states and the conduction band derived from Ag-*s* states. In the case of ZrSO, we observe that the valence bands derived from S-*p* states, and conduction bands derived from O-*s* states as shown in Figure S5.

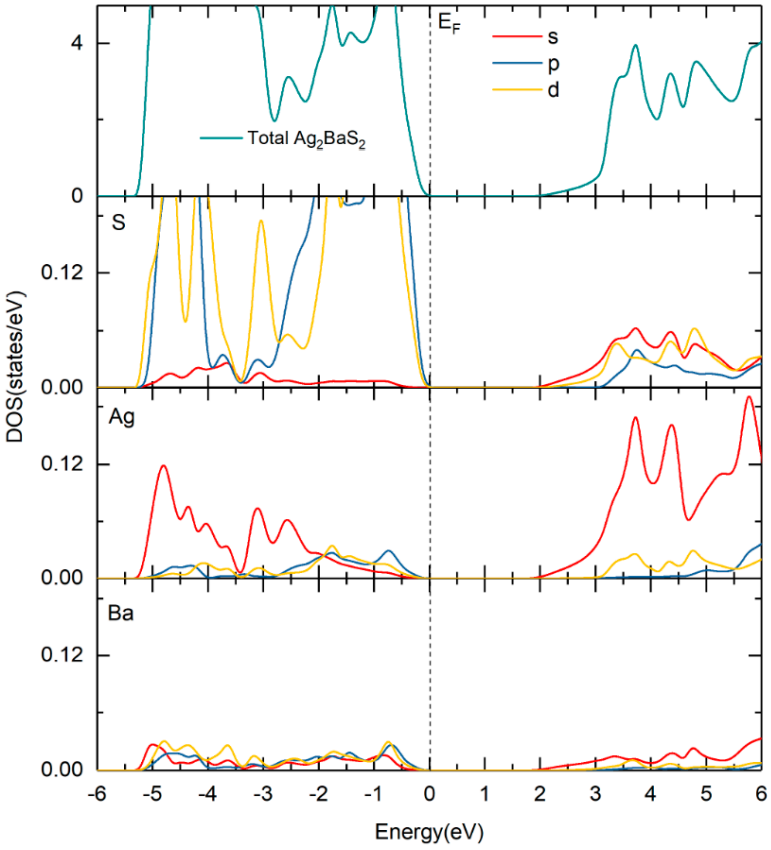

Figure S4. Total and site projected density of states of Ag_2BaS_2. The Fermi level is set to zero and marked by a vertical dotted line.

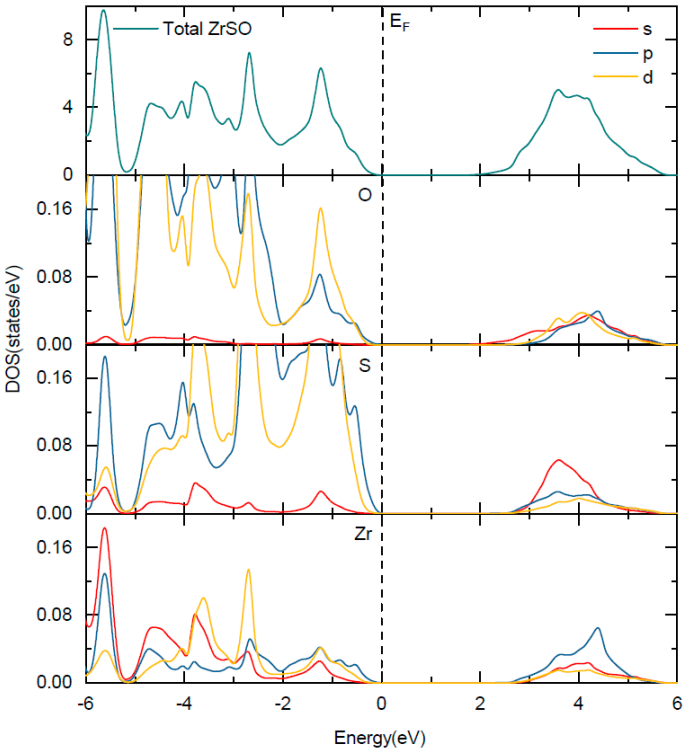

Figure S5. Total and site projected density of states of ZrSO. The Fermi level is set to zero and marked by a vertical dotted line.

References

1. Hellenbrandt, M. The inorganic crystal structure database (ICSD)—present and future. *Crystallogr. Rev.* **2004**, *10*, 17–22.
2. Ponniah, V. *Density Functional Theory Based Database (DFTBD)*. University of Oslo, Norway, 2013.
3. Özer, M.; Paraskevopoulos, K.; Anagnostopoulos, A.; Kokou, S.; Polychroniadis, E. Large single-crystal growth and characterization of the narrow-gap semiconductor. *Semicond. Sci. Technol.* **1996**, *11*, 1405.
4. Gäbler, F.; Kirchner, M.; Schnelle, W.; Schwarz, U.; Schmitt, M.; Rosner, H.; Niewa, R. (Sr3N) E and (Ba3N) E (E= Sb, Bi): synthesis, crystal structures, and physical properties. *Zeitschrift für anorganische und allgemeine Chemie* **2004**, *630*, 2292–2298.
5. Bronger, W.; Lenders, B.; Huster, J. BaAg2S2, ein Thioargentat im CaAl2Si2-Strukturtyp. *Zeitschrift für anorganische und allgemeine Chemie* **1997**, *623*, 1357–1360.
6. Jellinek, F.; Songstad, J.; Viljanto, J.; Seppälä, P.; Theander, O.; Flood, H. A Tetragonal Form of Zirconium Oxide Sulfide, ZrOS. *Acta Chem. Scand.* **1962**, *16*, 791–792, doi:10.3891/acta.chem.scand.16-0791.
7. McCullough, J.D.; Brewer, L.; Bromley, L. The crystal structure of zirconium oxysulfide, ZrOS. *Acta Crystallogr.* **1948**, *1*, 287–289.

Chapter 11

Publication V

A promising high-efficiency photovoltaic alternative non-silicon material: A first-principle investigation

Murugesan Rasukkannu[1], Dhayalan Velauthapillai[1], Ponniah Vajeeston[2]

[1]*Western Norway University of Applied Sciences, Department of Computing, Mathematics and Physics, Inndalsveien 28, Box 5063, Bergen, Norway*

[2]*Center for Materials Science and Nanotechnology, Department of Chemistry, University of Oslo, Box 1033 Blindern N-0315, Oslo, Norway*

Published in

Scripta Materialia

(Elsevier)

Vol. 156 **2018**, Page 134-137

Scripta Materialia 156 (2018) 134–137

Contents lists available at ScienceDirect

Scripta Materialia

journal homepage: www.elsevier.com/locate/scriptamat

Regular article

A promising high-efficiency photovoltaic alternative non-silicon material: A first-principle investigation

Murugesan Rasukkannu [a,*], Dhayalan Velauthapillai [a], Vajeeston Ponniah [b]

[a] Western Norway University of Applied Sciences, Department of Computing, Mathematics and Physics, Inndalsveien 28, Box 5063, Bergen, Norway
[b] Center for Materials Science and Nanotechnology, Department of Chemistry, University of Oslo, Box 1033, Blindern, N-0315 Oslo, Norway

ARTICLE INFO

Article history:
Received 8 July 2018
Received in revised form 19 July 2018
Accepted 20 July 2018
Available online xxxx

Keywords:
HSE06
PV materials
Hybrid density function
$TlBiS_2$
Non-silicon solar cell material

ABSTRACT

We demonstrate by means of first-principle calculations that the band structure of $TlBiS_2$ characterizes this material as a promising candidate for photovoltaic applications. Two calculation hybrid functional models are used, one including the spin-orbit coupling and one neglecting it. These calculations show that $TlBiS_2$ has a direct band gap of 1.10 eV in the absence of spin-orbit coupling and 0.67 eV for spin-orbit coupling. The absorption peaks appear in the visible region with a consequently high absorption intensity for both without and with spin-orbit coupling. We show how computational modeling of $TlBiS_2$ can substantially enrich the understanding of photovoltaic properties.

Silicon devices are currently the dominating technology for photovoltaic applications. More than 80% of the solar cell modules installed worldwide are based on either mono or multi-crystalline silicon. However, silicon exhibits an indirect band gap, resulting in a low absorption coefficient [1]. The research community has thus been making efforts in studying alternative materials for photovoltaic applications. Ternary, binary, multinary materials and compounds such as copper zinc tin sulfide, characterized by direct band gap and high absorption coefficient, are of utmost interest for photovoltaic application. The desirable features of alternative materials are high photon conversion efficiencies and low production cost. The chalcogenide-structured narrow band semiconducting compounds with general valence types III-V-VI_2, V_2-VI_3 (where III = Al, Ga, In, Tl; V = P, As, Sb, Bi; VI = Se, Te, S) have been investigated due to their application as topological insulator [2–6] and have not been widely investigated in solar cell. Topological insulators are innovative materials represent an ideal platform for nanoelectronics, optoelectronics and photonics [5–9].

The relative cost and scarcity of Ga and In have motivated a drive for alternative materials for photovoltaic applications. Thallium-bearing ternary semiconductors have been investigated in optoelectronics [10], but not extensively studied in photovoltaics due to the toxicity of thallium. However, $TlBiS_2$ have strong absorption coefficient with an optimum band gap, resulting in high efficiency for the photovoltaic process. $TlBiS_2$ crystallizes with a chalcogenide-structure, and it exhibits a narrow band gap with valence band and conduction bands located at Γ and F-point of the Brillouin zone [2]. The electronic properties of $TlBiS_2$ are already well studied using *ab initio* calculations under the generalized gradient approximation (GGA) [2, 11]. However, accurate Heyd-Scuseria-Ernzerhof (HSE06) and Bethe-Salpeter equation (BSE) calculation have not yet been used to explore its photovoltaic properties. This is addressed here by calculating the electronic band structure and optical properties of III-V-VI_2 compound (III = Tl, V = Bi, VI = S), as well as the effective masses.

Total energies have been calculated by the projected augmented plane-wave (PAW) implementation of the Vienna *ab initio* simulation package (VASP) [12, 13]. Structural optimization calculations are performed using the Perdew-Burke-Ernzerhof (PBE) version of the generalized gradient approximation (GGA) of the exchange-correlation functional [14]. The convergence threshold for self-consistent calculations is set to 10^{-6} eV, the atomic positions and lattice were fully optimized by minimizing the stress tensor and the Hellman-Feynman forces using the conjugate-gradient algorithm with a force convergence threshold of 10^{-3} eV $Å^{-1}$. We used the hybrid non-local exchange-correlation functional of Heyd-Scuseria-Ernzerhof (HSE06) to calculate the electronic structure [15]. The spin-orbit coupling was included in the calculations with non-collinear spins. In the HSE06 method, the screened parameter is set to 0.2 $Å^{-1,}$ and 30% of the screened Hartree-Fock (HF) exchange is mixed with the PBE exchange functional [16]. The cut-off energy for the plane-wave basis set is 600 eV, and we use a 10 × 10 × 10 Γ-centered Monkhorst-pack **k**-point mesh to sample the Brillouin zone [17]. This setup is maintained for both PBE and HSE06 calculations. Solving of the Casida's equation is an alternative,

* Corresponding author.
E-mail addresses: rmu@hvl.no (M. Rasukkannu), vdh@hvl.no (D. Velauthapillai), ponniahv@kjemi.uio.no (V. Ponniah).

https://doi.org/10.1016/j.scriptamat.2018.07.027
1359-6462/

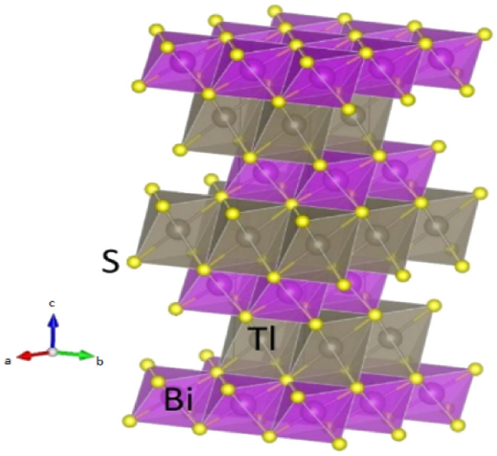

Fig. 1. Crystal structures for $TlBiS_2$. The labels for the different kinds of atoms are shown in the illustration.

well-established approach for calculating the dielectric function [18]. For both GW and the Bethe-Salpeter equation (BSE), we have summed the contributions over a number of $8 \times 8 \times 8$ **k**-points grids, shifted with respect to each other to reproduce $16 \times 16 \times 16$ Γ-centered grid. For all these calculations, a plane-wave cutoff of 410 eV has been used.

The structure of $TlBiS_2$ is closely related to ABQ_2-type compounds (A = monovalent atom, B = trivalent atom and Q = chalcogen) and can be derived from a simple NaCl-type lattice by a rhombohedral distortion along the [111] direction, corresponding to the c axis of the primitive hexagonal arrangement. The sum of the ionic radii for a coordination number (CN) of 6 is 2.87 Å for Bi^{3+}/S^{2-} and 3.34 Å for Tl^{+}/S^{2-} [$r(Bi^{3+}) = 1.03$ Å, $r(Tl^{+}) = 1.50$ Å and $r(S^{2-}) = 1.84$ Å] [19]. The experimentally determined and the theoretically derived values of the bond length are in good agreement for Bi—S, but for the Tl—S distance is underestimated by about 5.3%. The considered system has a rhombohedral crystal structure with four atoms in the primitive unit cell. The space group is D5 3d (R-3m, SG no. 166). The conventional hexagonal unit cell has 12 atoms corresponding to three formula units in which the layers are stacked in the order Tl-S-Bi-S along the z-axis. Each Tl (Bi) layer is sandwiched between the two S layers so that the bonding between all the layers is strong, and the material is essentially three-dimensional. Our calculated lattice parameters and the atomic positions are in good agreement with the experimental findings. The crystal structure of $TlBiS_2$ is presented in Fig. 1.

The band gap of the photoactive semiconductors determines the upper bound on the short-circuit current and open-circuit voltage. A large-band gap cell has a larger open-circuit voltage, and lower short-circuit current than a small-band gap cell. Thus, it absorbs fewer solar photons than a small-band gap cell. However, the detailed-balance limiting efficiency of an ideal solar cell of optimal band gap $E_g = 1.4$ eV is 32%. In real cells, thermalization loss occurs because the solar resource used has a broad energy spectrum, and it poorly matches the band gap, resulting in lower efficiencies below the detailed-balance limit [20]. Since the efficiency of solar cell is highly dependent on the band gap of material, the use of electronic band structure presents itself as a promising opportunity for engineering the material for photovoltaic applications. Fig. 2a shows the HSE06 band structure of $TlBiS_2$ without spin-orbit coupling. The valence band maximum (VBM) and the conduction band minimum (CBM) are located at the Γ **k**-point, characterising $TlBiS_2$ as a direct band gap semiconductor. The calculated HSE06 band gap between VBM and CBM is 1.1 eV. It is approximately equal to the silicon band gap, but of a different type. Bahadur Singh et al., used GGA calculation and showed that $TlBiS_2$ is a direct band gap semiconductor at Γ **k**-point, with a band gap of 0.64 eV [11]. The comparison between the present results using HSE06 with these previous GGA results [11] suggests that band gap of $TlBiS_2$ is larger by approximately 0.46 eV. It is well known that calculations using GGA underestimate the band gap value, while the HSE06 screened hybrid functional is very successful in accurately calculating it. At the F **k**-point, the band gap between VBM and CBM is 1.42 eV. The electronic structure studies of $TlBiS_2$ are identified, the direct band gap and 1.1 eV band gap for the solar cell application.

The spin-orbit coupling (SOC) is strongest for heavy elements, where the electrons acquire large velocities in the proximity of the nucleus. It may be suspected that a strong SOC effect, characteristic of heavy Bi, might be involved in affecting the properties of the material under examination. Therefore, we compare our previously obtained HSE06 band structure with results including the SOC. We may expect that the effect of SOC is of major importance for the distributions of the near-Fermi electronic states. Fig. 2b shows the HSE06 band structure of $TlBiS_2$ with spin-orbit coupling. In $TlBiS_2$, both the valence band maximum (VBM) and conduction band minimum (CBM) are located at the Γ **k**-point. Thus, $TlBiS_2$ is once again found to be a direct band gap semiconductor. The calculated HSE06 band gap between VBM and CBM is 0.67 eV. When we include SOC, the band gap shrinks significantly, and a similarly large energy shift is obtained for all bands throughout the Brillouin zone. Similar phenomena were observed by Bahadur Singh et al., when they band structure calculation including SOC, where the band gap was shown to shrink from 0.64 eV to 0.26 eV at Γ [11]. At the F **k**-point, the band gap between VBM and CBM is 1.16 eV. From Fig. 2a and Fig. 2b, we observe that the presence of SOC introduces large energy shift for all band, and the band gap values shrink

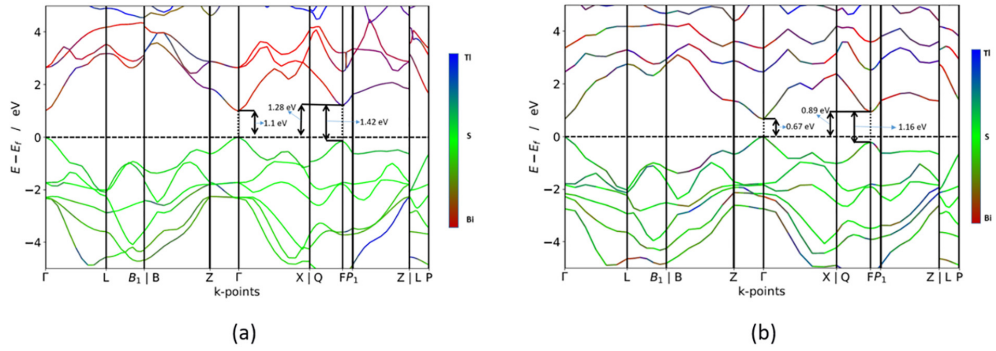

Fig. 2. Calculated HSE06 electronic band structure of $TlBiS_2$ (a) without spin-orbit coupling (b) with spin-orbit coupling. The Fermi level is set to zero.

Table 1
The calculated effective mass of $TlBiS_2$, effective masses of light holes (m^*_{lh}), heavy holes (m^*_{hh}) and electrons (m^*_e).

Compound	Plane directions	HSE06		
		$m^*_{lh}\cdot m_e$	$m^*_{hh}\cdot m_e$	$m^*_e\cdot m_e$
$TlBiS_2$	110	0.182	0.224	0.154

significantly at the Γ and F **k**-points. We found that the effect of SOC is of major importance for the distributions of the near-Fermi electronic states. The accurate HSE06 band structure calculations revealed that the inducing of SOC significantly reduces the band gap, thus influencing the optical properties.

The calculation of the effective mass (EM) is crucial in a detailed study of the energy levels in solar devices. The conductivity of the effective masses of electrons and holes perturbs the mobility, electrical resistivity, and free-carrier optical response in photovoltaic applications. To this end, we have employed the effective mass calculator (EMC) [21]. This algorithm is based on a finite difference method, and it is not a fitting band algorithm [21]. The effective masses of $TlBiS_2$ calculated by HSE06 are listed in Table 1. We noted that the EM holes are heavier than the EM of electrons. This result can be understood from the fact that the VB is derived from S-*p* state, less dispersed compared to the CB derived from Bi-*p* states. The EM of electron photovoltaic materials such as silicon (Si) and gallium arsenide (GaAs) are $0.26m_e$ and $0.12m_e$ [22] respectively. The calculated EM of electrons of the $TlBiS_2$ is $0.154m_e$, the EM of the electron is low for $TlBiS_2$ compare to Si. Hence, $TlBiS_2$ have remarkably large electron mobility.

The knowledge of the optical properties is crucial for the study of solar cell materials, as it allows describing their absorption properties. To investigate the optical behavior of $TlBiS_2$, we used the optical dielectric function $\varepsilon(\omega) = \varepsilon_1(\omega) + i\varepsilon_2(\omega)$, the fundamental quantity of the optical properties. It is defined as the linear response of the system to electromagnetic radiation, which controls the propagation of radiation in a medium. Here, $\varepsilon(\omega)$ is connected to the interaction between photons and electrons. Its imaginary part $\varepsilon_2(\omega)$ can be derived from the inter-band optical transitions by summing over unoccupied states using the equation [23], the real part $\varepsilon_1(\omega)$ of dielectric function can be derived from the $\varepsilon_2(\omega)$ by the Kramer-Kronig relationship [23, 24]. The absorption coefficients $\alpha(\omega)$ can be calculated from $\varepsilon_1(\omega)$ and $\varepsilon_2(\omega)$ [23, 24]. The calculated imaginary part of the dielectric function and absorption coefficients of $TlBiS_2$ compound is presented in Figs. 3 and 4 respectively. In general, the inclusion of excitonic effects treated within the Bethe-Salpeter equation (BSE) framework is in better agreement with the experimental absorption spectra [25] [26] [27]. The calculated dielectric functions can be further improved by averaging over multiple grids using BSE without and with SOC [27].

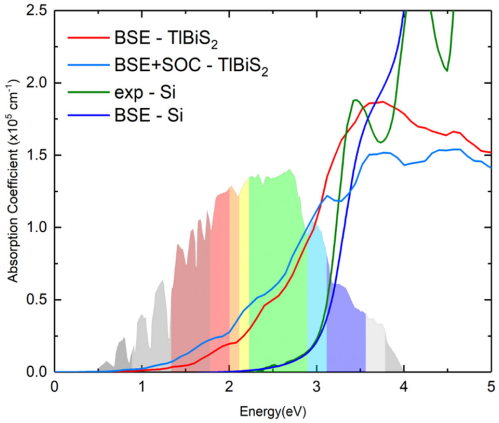

Fig. 4. Calculated absorption coefficient of $TlBiS_2$. (Colour code: red – BSE absorption coefficient of $TlBiS_2$ without SOC, light blue – BSE absorption coefficient of $TlBiS_2$ with SOC, green – experimental absorption coefficient of Silicon, blue – BSE absorption coefficient of Silicon.) (For interpretation of the references to colour in this figure legend, the reader is referred to the web version of this article.)

According to the directional dependency of $\varepsilon_1(\omega)$ and $\varepsilon_2(\omega)$, $TlBiS_2$ is a highly isotropic medium. This is due to same lattice parameters along all directions. In Fig. 4, the dielectric function of the $TlBiS_2$ without and with SOC is plotted against the photon energy. These results illustrate the shift of the optical band gap due to spin-orbit effects. Moreover, the slope of $\varepsilon_2(\omega)$ near the band gap is smaller for SOC effect. This is due to reduced number of critical states in the CB and split bands in the CB when SOC is considered (as shown in Fig. 2b). The main band gap is located at the Γ **k**-point, but the secondary band gap at the F **k**-point observed independently from the presence of SOC, leads to further contributions to the optical absorption of $TlBiS_2$. In comparison, the optical absorption $\varepsilon_2(\omega)$ of $TlBiS_2$ for BSE with SOC is higher than $\varepsilon_2(\omega)$ of $TlBiS_2$ for BSE without SOC calculation in the infrared region. This is due to the low electronic band gap of $TlBiS_2$ with SOC effect at Γ **k**-point.

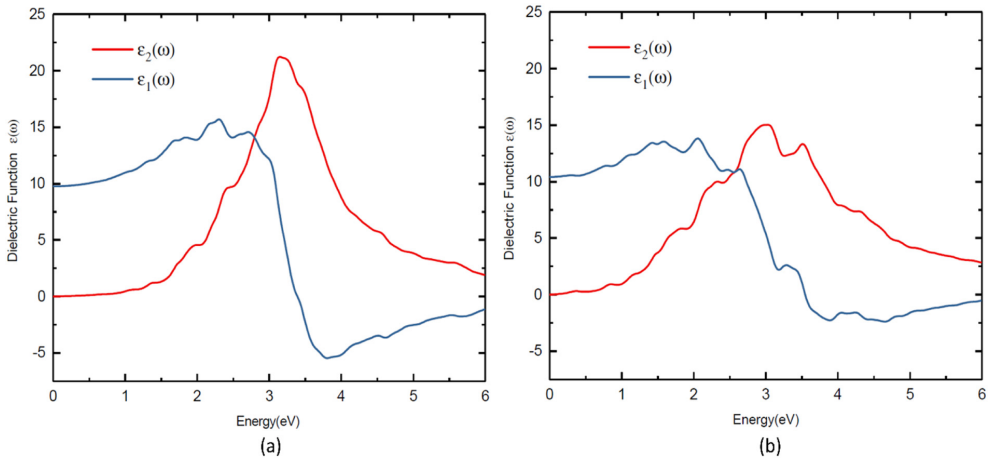

Fig. 3. The calculated dielectric function of $TlBiS_2$ (a) without SOC, (b) with SOC.

However, the calculated BSE with SOC optical absorption of $TlBiS_2$ is lower than optical absorption of $TlBiS_2$ for BSE without SOC in the ultraviolet region. This is due to the large electronic band gap of $TlBiS_2$ without SOC effect at Γ and F **k**-points.

The absorption coefficients $\alpha(\omega)$ can be calculated from $\varepsilon_1(\omega)$ and $\varepsilon_2(\omega)$ [23, 24]. Fig. 4 shows the optical absorption coefficient for $TlBiS_2$ calculated using the BSE without SOC method. For comparison, we plotted the experimental and the BSE absorption coefficient of silicon. It can be seen that the absorption coefficient of silicon presents similar values for both experiment [28] and theoretical calculation [18]. The absorption can occur only when the photon energy is larger than the band gap of the material. Since the electronic band gap of $TlBiS_2$ without SOC effects is 1.10 eV and it is a direct band gap, $TlBiS_2$ exhibits an absorption starting at 1.08 eV. From Fig. 4, the absorption peaks of $TlBiS_2$ are observed at 1.08 eV, 1.32 eV, 2 eV, 2.45 eV and 3.6 eV for BSE calculation without SOC. When the photon energy is about 3.6 eV, the α of $TlBiS_2$ reaches the maximum. Since the electronic band gap with SOC effect of $TlBiS_2$ is 0.67 eV and it is direct band gap, $TlBiS_2$ exhibits an absorption starting at 0.71 eV. From Fig. 4, the absorption peaks of $TlBiS_2$ are observed at 1.17 eV, 1.81 eV, 2.32 eV, 3.116 eV and 3.78 eV for BSE calculation with SOC. These results illustrate the redshift of the optical band gap of $TlBiS_2$ with spin-orbit effects due to the reduced number of critical states and split bands in the CB. However, the absorption coefficient of $TlBiS_2$ with SOC effects is higher than the absorption coefficient of $TlBiS_2$ without SOC effects in the visible region. This is due to the secondary band gap of 1.16 eV at F **k**-point, shrinks band gap and split bands in the CB.

For silicon, the α values become significant only after 2.5 eV and become large enough only at 3.3 eV. This is because silicon has an indirect band gap, resulting in a low absorption coefficient in the visible region. However, it can be seen that absorption coefficient of $TlBiS_2$ is perfectly matched to the visible region for both BSE without and with SOC effects. The reason behind the high absorption coefficient of $TlBiS_2$ without SOC effect is the direct band gap at the Γ and the F **k**-points with optimum band gap. Hence, we proposed that the $TlBiS_2$ exhibit large absorption for both without and with SOC in the visible region across the solar spectrum, thus meeting one of the important prerequisites for efficient solar to electrical energy conversion.

In summary, first-principle calculations employing the hybrid HSE06 and BSE method were utilized to compute the electronic structures, effective masses and optical properties of the $TlBiS_2$ compound. The HSE06 calculated electronic structures without and with SOC effect confirmed that the $TlBiS_2$ exhibits a direct band gap, with a value of 1.10 eV and 0.67 eV respectively, at the Γ **k**-point. The HSE06 calculated electronic structures without and with SOC effect confirmed that the $TlBiS_2$ exhibits a direct band gap, with a value of 1.42 eV and 1.16 eV respectively, at the F **k**-point. Thus, the absorption peaks exhibited a high absorption intensity in the visible region. For the very first time, absorption spectra of $TlBiS_2$ based on BSE without and with SOC effects calculation is reported in this paper. It is shown that $TlBiS_2$ is more efficient absorption material than silicon. Our detailed studies of electronic and optical properties of the ternary chalcogenide material reveal that $TlBiS_2$ is a potential candidate for photovoltaic application, especially for the development of multi-junction solar cells.

Acknowledgment

The authors gratefully acknowledge the Western Norway University of Applied Sciences (23300) for financially supporting and NOTUR for computing facilities with the project numbers NN2867K and NN2875K, which have used to conduct the calculations presented in this article.

References

[1] T. Unold, H.-W. Schock, Annu. Rev. Mater. Res. 41 (2011) 297–321.
[2] Q. Zhang, Y. Cheng, U. Schwingenschlögl, Sci. Rep. 5 (2015) 8379.
[3] C. Lamuta, D. Campi, A. Cupolillo, Z. Aliev, M. Babanly, E. Chulkov, A. Politano, L. Pagnotta, Scr. Mater. 121 (2016) 50–55.
[4] X. Fu, Q. Ding, Z. Xu, T. Zhu, Q. Yu, Z. Zhang, Scr. Mater. 135 (2017) 10–14.
[5] W. Tang, A. Politano, C. Guo, W. Guo, C. Liu, L. Wang, X. Chen, W. Lu, Adv. Funct. Mater. (2018) 1801786.
[6] C. Lamuta, A. Cupolillo, A. Politano, Z.S. Aliev, M.B. Babanly, E.V. Chulkov, L. Pagnotta, Nano Res. 9 (4) (2016) 1032–1042.
[7] A. Politano, G. Chiarello, Z. Li, V. Fabio, L. Wang, L. Guo, X. Chen, D.W. Boukhvalov, Adv. Funct. Mater. 28 (23) (2018) 1800511.
[8] A. Politano, L. Viti, M.S. Vitiello, APL Mater. 5 (3) (2017) 035504.
[9] L. Viti, D. Coquillat, A. Politano, K.A. Kokh, Z.S. Aliev, M.B. Babanly, O.E. Tereshchenko, W. Knap, E.V. Chulkov, M.S. Vitiello, Nano Lett. 16 (1) (2015) 80–87.
[10] Z.S. Aliev, F.J. Zúñiga, Y.M. Koroteev, T. Breczewski, N.B. Babanly, I.R. Amiraslanov, A. Politano, G. Madariaga, M.B. Babanly, E.V. Chulkov, J. Solid State Chem. 242 (2016) 1–7.
[11] B. Singh, H. Lin, R. Prasad, A. Bansil, J. Appl. Phys. 116 (3) (2014) 033704.
[12] G. Kresse, J. Furthmüller, Phys. Rev. B 54 (16) (1996) 11169.
[13] G. Kresse, D. Joubert, Phys. Rev. B 59 (3) (1999) 1758.
[14] J.P. Perdew, K. Burke, M. Ernzerhof, Phys. Rev. Lett. 77 (18) (1996) 3865.
[15] J. Heyd, G.E. Scuseria, J. Chem. Phys. 121 (3) (2004) 1187–1192.
[16] A.V. Krukau, O.A. Vydrov, A.F. Izmaylov, G.E. Scuseria, J. Chem. Phys. 125 (22) (2006) 224106.
[17] H.J. Monkhorst, J.D. Pack, Phys. Rev. B 13 (12) (1976) 5188.
[18] J. Paier, M. Marsman, G. Kresse, Phys. Rev. B 78 (12) (2008) 121201.
[19] R.D. Shannon, Acta Crystallographica Section A: Crystal Physics, Diffraction, Theoretical and General Crystallography, 32 (5) (1976) 751–767.
[20] W. Shockley, H.J. Queisser, J. Appl. Phys. 32 (3) (1961) 510–519.
[21] A. Fonari, C. Sutton, Effective Mass Calculator for Semiconductors, 2015.
[22] B. Van Zeghbroeck, Colarado University, 2004.
[23] M. Gajdoš, K. Hummer, G. Kresse, J. Furthmüller, F. Bechstedt, Phys. Rev. B 73 (4) (2006) 045112.
[24] L.-M. Yang, P. Vajeeston, P. Ravindran, H. Fjellvåg, M. Tilset, Phys. Chem. Chem. Phys. 13 (21) (2011) 10191–10203.
[25] S. Albrecht, L. Reining, R. Del Sole, G. Onida, Phys. Rev. Lett. 80 (20) (1998) 4510.
[26] M. Rohlfing, S.G. Louie, Phys. Rev. Lett. 81 (11) (1998) 2312.
[27] M. Bokdam, T. Sander, A. Stroppa, S. Picozzi, D. Sarma, C. Franchini, G. Kresse, Sci. Rep. 6 (2016) 28618.
[28] D.E. Aspnes, A. Studna, Phys. Rev. B 27 (2) (1983) 985.

Chapter 12

Publication VI

First-principle calculation of high absorption-$TlGaTe_2$ for photovoltaic application

Murugesan Rasukkannu[1], Dhayalan Velauthapillai[1], Ponniah Vajeeston[2]

[1]*Western Norway University of Applied Sciences, Department of Computing, Mathematics and Physics, Inndalsveien 28, Box 5063, Bergen, Norway*

[2]*Center for Materials Science and Nanotechnology, Department of Chemistry, University of Oslo, Box 1033 Blindern N-0315, Oslo, Norway*

Submitted to

Scripta Materialia

(Elsevier)

Chapter 13

Publication VII

Bandgap engineering in $CsSn_xPb_{(1\_x)}I_3$ and their influence on light absorption

Håkon Eidsvåg[1], Murugesan Rasukkannu[1], Dhayalan Velauthapillai[1], Ponniah Vajeeston[2]

[1]*Western Norway University of Applied Sciences, Department of Computing, Mathematics and Physics, Inndalsveien 28, Box 5063, Bergen, Norway*

[2]*Center for Materials Science and Nanotechnology, Department of Chemistry, University of Oslo, Box 1033 Blindern N-0315, Oslo, Norway*

Published in

Materials Letters

(Elsevier)

Vol. 218 **2018**, Page 253-256

Materials Letters 218 (2018) 253–256

Contents lists available at ScienceDirect

Materials Letters

journal homepage: www.elsevier.com/locate/mlblue

Featured Letter

Bandgap engineering in $CsSn_xPb_{(1-x)}I_3$ and their influence on light absorption

Håkon Eidsvåg [a], Murugesan Rasukkannu [a], Ponniah Vajeeston [b,*], Dhayalan Velauthapillai [a]

[a] Western Norway University of Applied Sciences, Department of Computing, Mathematics and Physics, Inndalsveien 28, Box 5063, Bergen, Norway
[b] Center for Materials Science and Nanotechnology, Department of Chemistry, University of Oslo, Box 1033 Blindern N-0315, Oslo, Norway

ARTICLE INFO

Article history:
Received 17 January 2018
Accepted 5 February 2018
Available online 6 February 2018

Keywords:
$CsPbI_3$
$CsSnI_3$
$CsSn_{0.5}Pb_{0.5}I_3$
Bandgap engineered solar cells
Simulation and modelling
Solar energy materials

ABSTRACT

We present first-principle computational modelling of the perovskite $CsSn_xPb_{(1-x)}I_3$ (x = 0, 0.5 and 1), aimed at increasing the efficiency of perovskite photovoltaics. Using density functional theory calculations with a hybrid functional, we predict that both $CsPbI_3$ and $CsSnI_3$ are stable structures with direct bandgaps, suitable for photovoltaic application. On the other hand, the stable structure of $CsSn_{0.5}Pb_{0.5}I_3$ exhibits an indirect bandgap, which could work as a direct bandgap due to the short electron-hole distance. The results of this study demonstrates that through bandgap engineering, we can obtain larger photon absorption ranges and higher efficiencies for perovskite based photovoltaics.

1. Introduction

In the last few years perovskite-based photovoltaics has emerged as a possible solution to the world's energy problem, having now reached efficiencies as high as 22.1% [1]. The current research is focused on methylammonium lead trihalide perovskites ($MAPbX_3$; MA = $CH_3NH_3^+$, X = Cl, Br, I) and metal halide perovskites (ABX_3; A = Cs, Rb, B = Sn, Pb, Ge, X = Cl, Br, I), with the aim of increasing the efficiency and solve the instability issue of perovskites [2,3]. Especially $CsPbI_3$ and the lead free $CsSnI_3$ have shown great potential. One of the main solutions for increasing efficiency is the doping of the perovskites, as this can have a major effect on many electronic properties. However, bandgap engineering in combination with theoretical simulations of perovskites seems to gather little attention from the research community.

With this in mind, this article proposes a new perovskite configuration, which combines $CsPbI_3$ and $CsSnI_3$ to improve the bandgap and the absorption range. The idea is to utilise simultaneously the two different absorption ranges, 675–750 nm and 875–1050 nm for $CsPbI_3$ and $CsSnI_3$ respectively, to achieve a higher absorption efficiency. We show through density functional theory (DFT) simulations that bandgap engineering of $CsSn_xPb_{(1-x)}I_3$ is possible in a solid solution. Furthermore, we investigate and compare the structural stability of $CsPbI_3$, $CsSnI_3$ and $CsSn_{0.5}Pb_{0.5}I_3$.

2. Methods and approaches

The total energies have been calculated by the projected augmented plane-wave (PAW) implementation of the Vienna ab initio simulation package (VASP) [4]. For the exchange-correlation functional part, we used the Perde-Burke-Ernzerhof (PBE) version of the generalized gradient approximation (GGA) [5]. The ionic coordinates are fully optimised using an energy converged threshold of a 10^{-6} eV per atom. We used the hybrid nonlocal exchange-correlation functional of Heyd-Scuseria-Ernzerhof (HSE06) to calculate the electronic structure and optical properties. In the HSE06 method, the screened parameter is set to 0.2 $Å^{-1}$ and 30% of the screened Hartree-Fock (HF) exchange is mixed with the PBE exchange functional [6]. The cut-off energy for the plane-wave basis set is set to 600 eV, and we use a $10 \times 10 \times 10$ Γ-centred Monkhorst-pack **k**-point mesh for sampling the Brillouin zone. These settings are used in both PBE and HSE06 calculations for α-$CsSnI_3$. We used a similar density of **k**-points and energy cut-off to estimate total energy as a function of volume for all the structures considered in the present study.

3. Results and discussion

3.1. Structural description and relative stability

$CsSnI_3$ is a unique phase-change material that exhibits four polymorphs [7]. Two polymorphs are stable at room temperature: one has a one-dimensional double-chain structure and is yellow in

* Corresponding author.
E-mail address: ponniahv@kjemi.uio.no (P. Vajeeston).

https://doi.org/10.1016/j.matlet.2018.02.021
0167-577X/

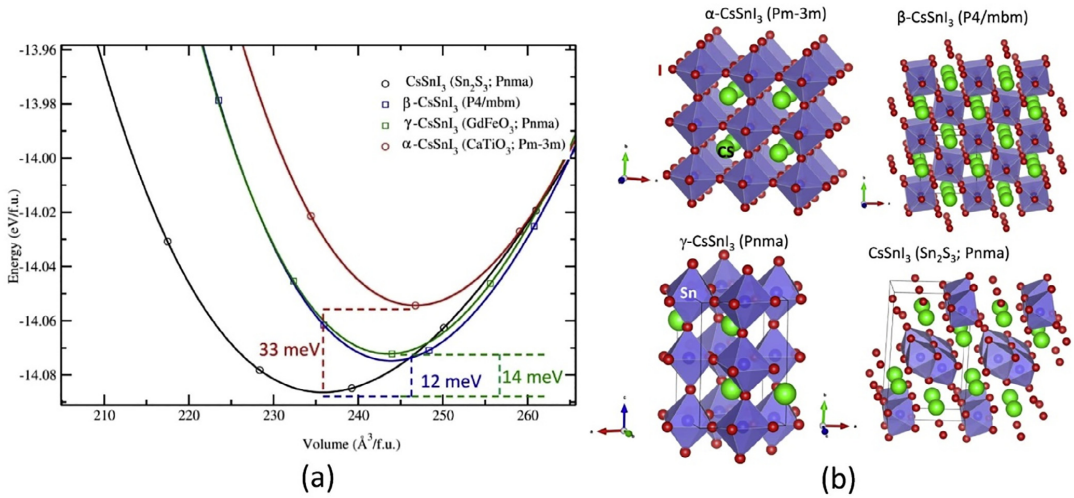

Fig. 1. (a) Calculated total energy (per formula unit; f.u.) as a function of the volume of the unit cell for the different polymorphs of $CsSnI_3$. The involved energy differences between the different polymorphs are indicated. (b) Crystal structure of $CsSnI_3$ polymorphs. The illustration contains legends for the different atoms.

color (Y-$CsSnI_3$; Sn_2S_3-type), and another has a three-dimensional perovskite structure (see Fig. 1b) and is black in color (γ-$CsSnI_3$). When heated above 425 K, the Y phase transforms to a black cubic perovskite phase (α-$CsSnI_3$), which, on subsequent cooling, converts to a black tetragonal phase (β-$CsSnI_3$) at 426 K (instead of Y) and a black orthorhombic phase (γ-$CsSnI_3$) at 351 K. In order to understand the relative stability of these four phases we have calculated the total energy as a function of unit-cell volume, which are displayed in Fig. 1a. Among the considered structures, the Sn_2S_3-type atomic arrangement is found to have the lowest total energy. The calculated ionic positions and lattice parameters for the four phases are found to be in good agreement with experimental findings [3]. It is interesting to note that the energy difference between α-, β-, γ- and Y-$CsSnI_3$ is very small, and hence, one can easily modify one polymorph into another by application of moderate temperature or pressure. This is in agreement with the work of Chung et al. [3] who found that $CsSnI_3$ stabilize in four different structures depending upon the synthesis method/condition and temperature. Similarly, for the $CsPbI_3$ and $CsSn_{0.5}Pb_{0.5}I_3$ phases, our theoretical energy-volume curves shows that both of them stabilize in orthorhombic structures with the Pnma space group (α-phase; Sn_2S_3-type). At ambient conditions $CsPbI_3$ crystallize in an orthorhombic structure, which at high temperature is transformed into a cubic ($CaTiO_3$-type) structure [8]. The energy difference between the two phases of $CsPbI_3$ is 0.15 eV and the calculated structural parameters are in good agreement with the experimental findings [8]. The crystal structure of $CsSn_{0.5}Pb_{0.5}I_3$ is currently unknown and the present study predict that at ambient conditions $CsSn_{0.5}Pb_{0.5}I_3$ crystallizes in an orthorhombic Sn_2S_3-derived structure.

3.2. Nature of electronic structure and related properties

The calculated band structures for the low-energy structures are shown in Fig. 2, highlighting the relevant points in reciprocal space. $CsSnI_3$ is found to have three polymorphs with direct bandgaps (Y-, α- and β-$CsSnI_3$) and one with an indirect bandgap (γ-$CsSnI_3$). The polymorphs with direct bandgaps are suitable for photovoltaic application due to the efficient electron-hole transport. For $CsPbI_3$ we observe a direct bandgap at the Γ point, indicating the reason why it is a successful perovskite solar cell material. For $CsSn_{0.5}Pb_{0.5}I_3$ an indirect bandgap is observed, due the valence band maximum (VBM) being found between Y-H and Γ-X while the conduction band minima (CBM) is between Z-D. However, we found that the electron/hole jump distance is minimum at Z-D. Furthermore, the energy difference between the

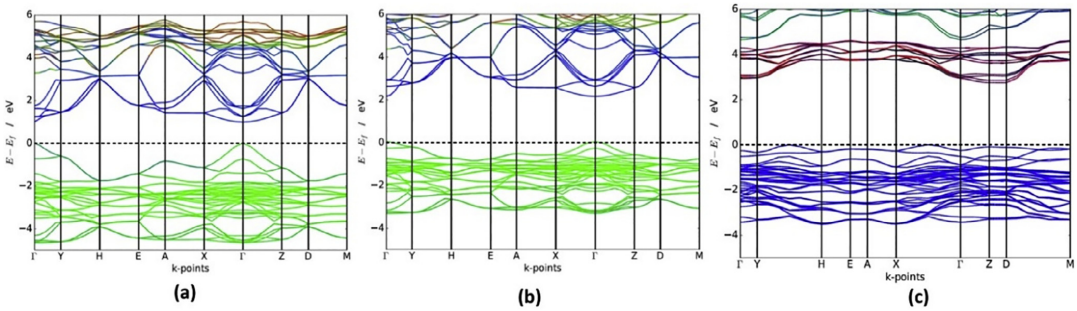

Fig. 2. Calculated band structures at the HSE06 level of the stable orthorhombic structures of (a) $CsSnI_3$, (b) $CsPbI_3$ and (c) $CsSn_{0.5}Pb_{0.5}I_3$.

VBM and the band energy in the Z-D is ca 0.001 eV. This makes it possible for this compound to function as a direct bandgap material. This bandgap properties require further research to understand how it works in the real condition. Table 1 summarizes the band parameters obtained from the calculated band structures of studied compounds.

3.3. Optical properties

Fig. 3 shows the absorption coefficients and the imaginary part of the dielectric function for the three perovskites and their stable polymorphs. The peak for Y- $CsPbI_3$ seen at 3.5 eV is in agreement with experimental literature. When lead is substituted with Sn, we get the expected red shift in absorption coefficient [9]. For $CsSn_{0.5}Pb_{0.5}I_3$ we anticipated an absorbance coefficient with a maximum in between the other two. However, we found the maximum peak to be blue shifted compared to that of both $CsSnI_3$ and $CsPbI_3$. In addition, we found the maximum peak value for $CsSn_{0.5}Pb_{0.5}I_3$ to be higher than that of the other two perovskites.

Moving on to the imaginary part of the dielectric function, we see once again that by combining $CsSnI_3$ and $CsPbI_3$ into $CsSn_{0.5}Pb_{0.5}I_3$ the maximum peak position is shifted towards higher energies (blue shifted) instead of being found in between the maximum peaks of $CsSnI_3$ and $CsPbI_3$ respectively. The

Table 1
Calculated bandgap values, space groups, Mulliken population and BOP for the perovskites based on the two different approximations.

Phase	Space group	Bandgap (eV)		Type of bandgap	Mulliken population charges	BOP
		GGA	HSE06			
α-$CsSnI_3$	*Pm*-3*m*	0.500	0.870	Direct	Cs: 0.61, Sn: 0.08, I: −0.23	0.47 (Sn-I)
Y-$CsSnI_3$	*Pnma*	0.650	1.017	Direct	Cs: 0.66, Sn: 0.26, I1: −0.39, I2: −0.17, I3: −0.17	−0.56 (Sn-I) 0.33 (Sn-i) −1.69 (Cs-I)
β-$CsSnI_3$	*P*4/*mbm*	0.671	1.060	Direct	Cs: 0.66, Sn: 0.19, I1: −0.23, I2: −0.31	0.16 (Sn-I)
γ-$CsSnI_3$	*Pnma*	2.030	2.670	Indirect	Cs: 0.58, Sn: 0.25, I1: −0.35, I2: −0.24	−0.10 (Sn-I) −0.30 (Cs-I)
$CsPbI_3$	*Pnma*	1.500	2.170	Direct	Cs: 0.69, Pb: 0.47, I1: −0.25, I2: −0.42, I3: −0.49	−0.64 (Pb-I) −0.62 (Cs-I)
$CsPbI_3$	*Pm*-3*m*	1.503	2.0934	Direct	Cs: 0.67, Pb: 0.48, I: −0.34	−0.58 (Pb-I) −0.81 (Cs-I)
$CsSn_{0.5}Pb_{0.5}I_3$	*Pnma*	2.05	2.713	Indirect/direct	Cs: 0.68 to 0.71, Sn: 0.25, Pb: 0.47, I: −0.26 to −0.48	0.25 (Sn-I) 0.08 (Sn-I) −0.73 (Pb-I) −1.37 (Cs-I) −1.05 (Cs-Pb)

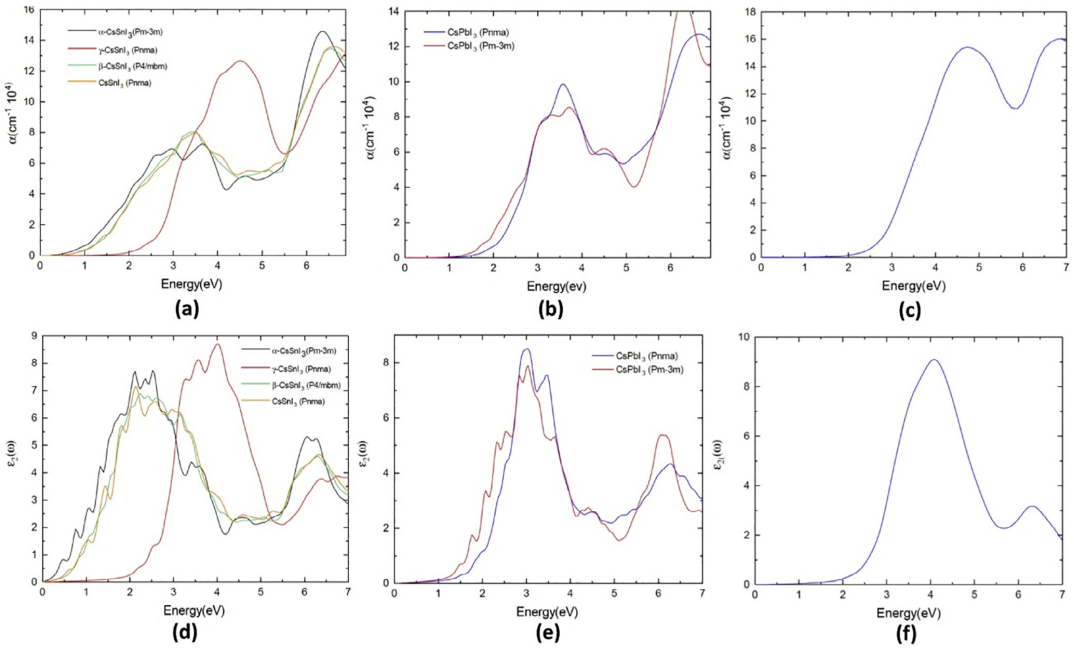

Fig. 3. Calculated absorption coefficients for (a) different polymorphs of $CsSnI_3$, (b) $CsPbI_3$ and (c) $CsSn_{0.5}Pb_{0.5}I_3$, and imaginary part of the complex dielectric function for (d) different polymorphs of $CsSnI_3$, (e) $CsPbI_3$ and (f) $CsSn_{0.5}Pb_{0.5}I_3$. We used HSE06 for these calculations.

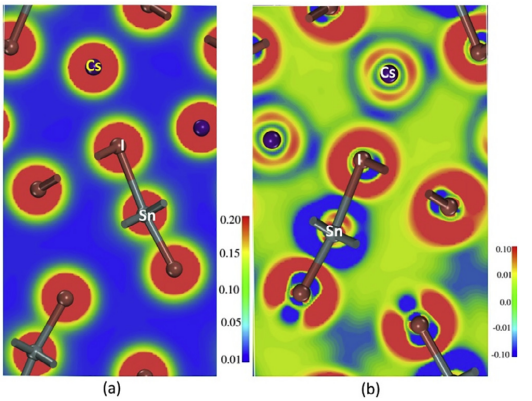

Fig. 4. Calculated valence-electron-density map (a), and (b) charge transfer plot for Y-$CsSnI_3$.

maximum value rises from 7.6 ω and 8.5 ω for $CsSnI_3$ and $CsPbI_3$ respectively to 9.2 ω for $CsSn_{0.5}Pb_{0.5}I_3$. This indicates that electromagnetic radiation will travel further into the material before being absorbed.

3.4. Chemical bonding

Based on the charge distribution plots for $CsSnI_3$ reported in Fig. 4, it is clear that the electrons resides around the individual atoms. Furthermore, the spherically-shaped charge distribution indicates that the bonding between Sn – I, Sn – Cs and Cs – I is primarily ionic. The charge transfer map reveals a polar character to the compound with depletion of charge around the Cs and Sn atoms. Although Mulliken analysis is more qualitative than quantitative it has proven useful in the analysis of chemical bonds [10]. Our bond overlap population (BOP) values are low, which supports our findings of ionic binding. $CSPbI_3$ displays the same ionic trend, with an even stronger charge depletion around the Cs and Pb atoms. The BOP analysis confirms the ionic bonding with its low values. However, for $CsSn_{0.5}Pb_{0.5}I_3$ we have the charge primarily distributed around the Sn and I atoms with little charge around Cs and Pb. Once again, we get low BOP values indicating an ionic nature of the bonds. The charge transfer plot indicates towards a slight polar character as charge gathers around the I atoms, however in general the atoms share the charge.

The Mullikan population charges for the Cs site is around +0.65e for all three compounds, confirming what is seen in the charge distribution plot that Cs does not fully donate its one valence electron to I, Pb or Sn in any of the configurations. For I the charges varies from −0.17e to −0.49e depending on the configuration, while Pb and Sn is consistent over the various configurations with charges of around 0.47e and 0.25e respectively. In other words, Cs, Pb and Sn all donate parts of their valence electrons to the I atoms.

4. Conclusion

In conclusion, we demonstrated that $CsSnI_3$ could be stabilized in four different polymorphs, three of which contain a direct bandgap ideal for photovoltaic applications. By adding Pb to the perovskite to create $CsSn_{0.5}Pb_{0.5}I_3$, we found that although this the new perovskite has an indirect bandgap, it could work as a direct bandgap material due to the lower electron-hole distance in the Z-D region. In general, we found that by combining $CsSnI_3$ and $CsPbI_3$ we got a new compound with different electronic and optical structure in addition to different chemical bonding. Based on this it could be viable to combine various compounds in an attempt to end up with an optimal compound for photovoltaic applications.

Acknowledgements

The authors gratefully acknowledge the Western Norway University of Applied Sciences for financially support, and the Research Council of Norway for providing the computer time at the Norwegian supercomputer facilities (under the project numbers NN2867K and NN2875k). The authors also acknowledge F. Bianchini for fruitful discussions.

References

[1] X. Qiu, B. Cao, S. Yuan, X. Chen, Z. Qiu, Y. Jiang, Q. Ye, H. Wang, H. Zeng, J. Liu, M. G. Kanatzidis, From unstable $CsSnI_3$ to air-stable Cs_2SnI_6: a lead-free perovskite solar cell light absorber with bandgap of 1.48 eV and high absorption coefficient, Sol. Energy Mater. Sol. Cells 159 (2016) 227–234.
[2] M. Ahmad, G. Rehman, L. Ali, M. Shafiq, R. Iqbal, R. Ahmad, T. Khan, S. Jalali-Asadabadi, M. Maqbool, I. Ahmad, Structural, electronic and optical properties of $CsPbX_3$ (X = Cl, Br, I) for energy storage and hybrid solar cell applications, J. Alloy. Compd. 705 (2017) 828–839.
[3] I. Chung, J.H. Song, J. Im, J. Androulakis, C.D. Malliakas, H. Li, A.J. Freeman, J.T. Kenney, M.G. Kanatzidis, $CsSnI_3$: semiconductor or metal? High electrical conductivity and strong near-infrared photoluminescence from a single material. High hole mobility and phase-transitions, J. Am. Chem. Soc. 134 (20) (2012) 8579–8587.
[4] G. Kresse, J. Furthmüller, Efficient iterative schemes for ab initio total-energy calculations using a plane-wave basis set, Phys. Rev. B 54 (16) (1996) 11169–11186.
[5] J.P. Perdew, K. Burke, M. Ernzerhof, Generalised gradient approximation made simple, Phys. Rev. Lett. 77 (18) (1996) 3865.
[6] J. Heyd, G.E. Scuseria, Efficient hybrid density functional calculations in solids: assessment of the Heyd-Scuseria-Ernzerhof screened Coulomb hybrid functional, J. Chem. Phys. 121 (3) (2004) 1187–1192.
[7] K. Yamada, S. Funabiki, H. Horimoto, T. Matsui, T. Okuda, S. Ichiba, Structural phase transitions of the polymorphs of $CsSnI_3$ by means of rietveld analysis of the X-ray diffraction, Chem. Lett. 20 (5) (1991) 801–804.
[8] D.M. Trots, S.V. Myagkota, High-temperature structural evolution of caesium and rubidium triiodoplumbates, J. Phys. Chem. Solids 69 (10) (2008) 2520–2526.
[9] T.C. Jellicoe, J.M. Richter, H.F. Glass, M. Tabachnyk, R. Brady, S.E. Dutton, A. Rao, R.H. Friend, D. Credgington, N.C. Greenham, M.L. Bohm, Synthesis and optical properties of lead-free cesium tin halide perovskite nanocrystals, J. Am. Chem. Soc. 138 (9) (2016) 2941–2944.
[10] R.S. Mulliken, Electronic population analysis on LCAO–MO molecular wave functions, J. Chem. Phys. 23 (10) (1955) 1833–1840.

Graphic design: Communication Division, UiB / Print: Skipnes Kommunikasjon AS

uib.no

ISBN: 978-82-308-3580-7